Innovative radionuclides production for theranostics applications from commercial cyclotrons and nuclear reactors coupled with mass separation technology

Roberto Formento-Cavaier

UNIVERSITE MATIERE BRETAGNE MOLECULES LOIRE ET MATERIAUX

UNIVERSITÉ DE NANTES

THESE DE DOCTORAT DE

L'UNIVERSITE DE NANTES
COMUE UNIVERSITE BRETAGNE LOIRE

ECOLE DOCTORALE N° 596
Matière, Molécules, Matériaux
Spécialité : Physique Nucléaire

Par
Roberto FORMENTO CAVAIER

Innovative radionuclides production for theranostics applications from commercial cyclotrons and nuclear reactors coupled with mass separation technology

Thèse présentée et soutenue à Nantes, le 12/02/19
Unité de recherche : SUBATECH

Rapporteurs avant soutenance :

Klaus WENDT	Professeur, Johannes Gutenberg-Universität Mainz (DE)
Mikael JENSEN	Professeur, Technical University of Denmark (DK)

Composition du Jury :

Président :	Ulli KÖSTER	Professeur associé, Université Grenoble Alpes
Examinateurs :	Thierry STORA	Chercheur, Conseil Européen pour la Recherche Nucléaire (CH)
	Arnaud GUERTIN	Chargé de Recherches, Institut Mines-Télécom
Dir. de thèse :	Ferid HADDAD	Professeur, Université de Nantes, Directeur du GIP Arronax
Co-dir. de thèse:	Ilyes ZAHI	Ingénieur de recherche, Advanced Accelerator Applications
	Thomas SOUNALET	Chargé de Recherches, Centre National de la Recherche Scientifique

Acknowledgments

Being part of a European project such as MEDICIS-PROMED is a gift, as the working conditions are over the average PhD students' ones, allowing better access to trainings, material and travels. This translates in faster development of personal knowledge and easier expertise network development, if well applied. Thus, I am really grateful for the opportunity that was given me.

In those three years I have met a great deal of people, I have been in numerous facilities. Therefore, the list of acknowledgements should be incredibly long. I will summarize as follow.

First of all, I would like to thank Luca Maciocco who was the first to believe in me and hired me three years ago. Unfortunately, we spent together only few months. I wish it had been more.

I had the chance to have a great thesis director such as Ferid Haddad. I grew exponentially with him both under personal and professional point of views. I think he was the perfect person for me to prepare myself for my future steps. Besides his full agenda, he always found the time to dedicate to me. I appreciate every moment spent together and hope to continue working together in the future. I really appreciate everything did for me, I will be eternally grateful. We are also a great team on the football pitch, what else?

As it was a multitasking thesis, all of my supervisors were fundamental as they were bringing different expertise. Ilyes Zahi was the perfect link between the company and the academic environment, supporting me a lot in this navigation between the two worlds. I appreciate also all the time spent to let me further improve on different aspects. Thomas Sounalet, instead was precious in the chemistry support I needed along those three years, substituting Nathalie Michel which had to leave from my supervisors after some months. Thank you all, a lot.

Coming back to the project, I have to thank Thierry Stora to have shaped this idea several years ago and Cristina Ferrari for her great support. Furthermore, I would like to thank him, and also the CERN team (Nhat-Tan *et. al.*, too many names to cite!) to have welcomed me and supported me for more than 6 months for my secondment at CERN. I really appreciate our moments at work, at coffee breaks, at O'Brasseur, at coffee breaks, at skiing, at coffee breaks, at futsal, etc…

On the same line, I would like to thank the LARISSA team at JGU Mainz for the warm welcome in the cold Mainz, and the support during the almost two months I have spent there. Particular thanks to Klaus Wendt, "mon rapporteur", and Vadim Gadelshin. It was a pleasure to have worked with you and obtained amazing results from our experiences.

Thank you Ulli Köster, for the constant support along the three years. I have learnt a great deal of things from you. It was great to have your expertise always available, as well as your hints and your great ideas.

Thank you Mikael Jensen, “mon rapporteur”, to have warmly welcomed me in Denmark and be supportive. I hope to have the chance to continue learning from you in the future.

It was an honor to have such expertise among my PhD jury.

Thanks to the MEDICIS-PROMED ESRs for the nice time spent together during conferences, trainings, meetings and so on. It seems to me yesterday that we were starting with the kick-off week in Villars. When you will be famous noble prices, please remember me.

I would like to thank all the Arronax employees for the three years spent together. The office mates (Mostafa, Estelle, Elodie, Mateusz, …); la compagna di merenda, di sfoghi, di caffè e di numerose avventure, grazie mille del supporto/sopporto Maddalena; the sport team (Cecile, Celine, Cyrille, Julien, ...) which allowed me to limit my final overweight; and all the others.

Thanks to the AAA colleagues, for the support from the other AAA sites. In particular, thanks to Maurizio Mariani, who haven’t fired me even though I showed up to an important meeting with a big black and red eye, after the participation at the orange fight (Ivrea carnival). I am pleased to have the chance to continue working for AAA, which became in the meanwhile a Novartis company, a great condition for aiming a brilliant future.

Thanks to the Subatech support, in particular to the Arnauds.

I would like to give an enormous thank you to my family, which made a huge effort in supporting me, always, in particular with their economical effort, in order to let me complete my formation path as best as possible. Without them, I would have never been here to write those words.

Last but not least, I would like to thank my gorgeous girlfriend who has been next to me, no matter the distance, no matter the difficulties. She is the main fuel of my daily happiness.

Non si smette mai di apprendere, never give up.

Table of contents

Introduction

Formally, war was declared to cancer more than forty years ago when U.S. President Richard Nixon (1913 – 1994) signed the National Cancer Act in 1971. The trigger was that cancer became the second death cause in USA. From Nixon's declaration, the National Cancer Institute was established carrying out the national effort against cancer by creating the National Cancer Program. Different ways of treating cancers were developed and tried over the years worldwide. In this work, the use of radiations for the diagnosis and the treatment of cancer diseases is considered. Indeed, nowadays the interest on radiopharmaceuticals in nuclear medicine is in continuous growth. A major achievement is the allowance to determine the tumor accumulation in the targeted tissue by molecular imaging such as Positron Emission Tomography (PET) and Single Photon Emission Computed Tomography (SPECT). The first one is based on the detection of the two photons emitted at 511 keV from the annihilation of a positron emitted during the β+ decay, while the second one is based on the detection of the photons emitted, ideally ranging between 100 and 200 keV. These are already consolidated applications considering the large use of fluorine-18 for PET and technetium-99m for SPECT.

In addition to the imaging, some radiopharmaceuticals are used for the treatment of tumors. The therapy exploits charged particle (β-, α and Auger electrons) emitters. Without few exceptions (e.g. the use of I-131 for the treatment of thyroidal tumors), it is necessary to vectorize the radionuclides to target the cells of interest and avoid unnecessary irradiations of healthy tissues. This can be done by using the proper vector and chelate. The energy released during the decay will cause the destruction of cells. Electrons and α particles are emitted with different energies, usually electrons mean energy in beta decay are in a range between 100 and 600 keV, while α particles are more energetics (of the order of 5 MeV). Besides this energy difference, the fact that mass and charge are not the same implies that interaction with matter is very different, as alpha particle are strongly interacting with matter. These facts lead to a very different Linear Energy Transfer (LET, the amount of energy released over a given distance) and different mean free path inside the tissue: very short for α particles and longer for electrons. For these reasons, the dose needed for the treatment will have to be optimized for each isotope depending on the decay type of a radionuclide.

At the moment, only few radionuclides are exploited for medical application. Often the reason is the lack of production of considerable quantities of some of them, or the lack of a production method. Widening the fleet of radionuclides which can be used could allow setting up new possibilities to treat cancer. Indeed, the different characteristics of them can be suitable for different application and sometimes can be complementary each other. One example is the use

of a beta emitter radionuclide for the treatment of large tumor cluster, complemented by the injection of a alpha emitter nuclide which can treat locally the tumor cells left.

The initial aim of this work was to go through all known radionuclides and found those that can be used for medical applications, with a particular attention to those allowing the application of the theranostics concept. Theranostics, is a treatment strategy that combines therapy and diagnosis that goes into the direction of personalized treatment. By doing imaging prior to the treatment, it is possible to select patients that will respond to a given treatment, to make dosimetry prior to therapy and to define the activity to inject. One strategy consists on identifying elements having two different radionuclides: one used for imaging, the other one for therapy.

After the selection of the innovative radionuclides of interest, a thorough analysis of a new large-scale production method is analyzed for them. The notions and experimental steps from the initial development to the proof of principle are given.

In the first chapter, a brief historical introduction is given with focus on the breakthrough event of the nuclear medicine history. Furthermore, the introductive notions necessary for the understanding of the concept and the working method considered in the rest of the thesis are presented. Among them, the radionuclides production from cyclotrons, nuclear reactors are illustrated as well as the mass separation technology and the resonant laser ionization, which combined are necessary for the selective production of a single nuclide from a mixture of different radionuclides not chemically separable.

The second chapter contains the procedure used to select the radionuclides of interest for the production in this thesis among all the radionuclides with interesting properties for medicine. Nuclear medicine application such as PET and SPECT for diagnosis and the treatment application in particular beta and alpha therapy are presented. Finally, the three elements chosen for the production are introduced.

Sometimes theoretical data are not suited for thorough radionuclides production analysis. It happens indeed that they can largely overestimate the values. One example is the cross-section of Tb-149 from the irradiation with a proton beam of a natural gadolinium target. Consequently, the experimental cross-section is evaluated with the stacked foil method, as well as all the other cross-section for the detected terbium co-produced during the same irradiation. For the obtained cross-section which can be found in literature already performed experiments, the values are compared; for the others, it is the first time that they are evaluated in the considered range of energy.

In chapter four are discussed the steps needed to the development of the production method for terbium radionuclides. The development of two different targets one for Tb-149 and one for Tb-152 and Tb-155 have been investigated. The simulations and the experiments performed toward the realization of the proof of principle are given. In particular the experimental study of

the release of terbium from a mixture of terbium gadolinium solution and its mass separation, as well as the development of a resonant laser ionization scheme for terbium have been performed. The details of the future proof of principle are given.

Analogously to the chapter four, in chapter five, a similar analysis has been done for the production of Sc-47. In this case only the theoretical analysis has been reported.

In the final chapter, the production of very high specific activity Er-169 is presented. It has been produced at ILL nuclear reactor (Grenoble, FR) and the irradiated sample has been mass separated at CERN-MEDICIS facility. The experimental study of the release and mass separation of erbium, as well as the development of a resonant laser ionization scheme for erbium path the ways to the first production. The performed proof of principle represents a world premiere. Nevertheless, the possible amelioration of the efficiency of the process are discussed.

CHAPTER-1

Radioactivity and radionuclides production

In this chapter, the breakthrough historical events related to the discovery of the radioactivity and the developments toward the medical applications of radiation are illustrated. Furthermore, the notions on radioactivity, radioactive decay modes and particles interaction with matter are given.

The identification of radionuclides is discussed. The experimental methods for characterizing the type of radioisotopes which will be useful to understand the thesis work are described here. The different method for radionuclides production is introduced with focus on cyclotrons, reactors and mass separation technologies, as well as resonant laser ionization technique for isotope separation, which are discussed more in details in the following chapters.

1.1 History

1.1.1 Discovery of x-rays

The dawn of the discovery of radioactivity coincides with the X-rays discovery by Wilhelm Conrad Röntgen (1845 - 1923) at the University of Würtzburg in Germany in 1895. (1) He was studying electric discharges in glass tubes filled with various gases at very low pressure. Röntgen shielded a Crookes' tube with black paper. Darkening the room, he detected a brilliant fluorescence. He found out that a piece of paper painted with a fluorescent dye up to two meters from the tube glow when high voltage between the electrodes of the Crookes' tube is applied. Later he realized that this radiation could not only penetrate black paper but also thicker blocks of wood, books and even his hand. In the dark room, he observed shadows of the bones in his own hand on a photographic film. (2) At that point, he decided to make a special Christmas gift to his wife. He kept hiding his secret discovery to his colleagues for weeks, then he asked his wife to follow him in the lab. It was a cold day that 22nd of December 1895. Röntgen's wife positioned her hand between the tube and the screen. The first x-ray radiography was done, clearly of a married female. (Figure 1)

Figure 1: first x-ray radiography ever done worldwide by Röntgen in 1895

Röntgen published his discovery in Nature in January 1896. (3) The French mathematician Henri Poincaré (1854 - 1912) noticed the publication. He had the intuition that X-ray emissions and fluorescence are strongly correlated. Poincaré presented then his idea at the Académie des Sciences in Paris the 20th of January 1896. He suggested that the X-ray emission might be the result of the fluorescence of the used glass in which cathode rays were produced at low pressure, and that this phenomenon might be a general effect of fluorescence. Within the audience there was a very interested professor of applied physics in the department of Natural History at the Paris Museum, Henri Becquerel (1852 - 1908). He was already working on fluorescence and thought he could adapt his usual experimental setup following Poincaré's talk. As a matter of fact, he wanted to test his fluorescent source, potassium-uranyl sulfate, a uranium salt, on a photographic plate in a sunny day. Indeed, the light of the sun was believed of fundamental importance as the fluorescence consists in the re-emission of light at different frequencies of the absorbed light. When he set the experiment, the sunlight was intermittent, and he didn't expect to find a good image. Nevertheless, the obtained image was even better than what he thought. Becquerel then assumed that the emission continued in the dark too. He tried to replicate the experiment leaving the system in the dark for long time, and it kept imprinting the photographic plates through the black paper. Not only paper, he found out that those rays were able to cross thin metallic foils too. Therefore, he believed he discovered a new type of rays, different from the previously discovered x-rays, which he named uranic rays. During new studies, he discovered that those rays exhibited reflection, refraction and polarization. (4)

Those years were prolific for physics discoveries. At that time, indeed, Becquerel believed that the Zeeman effect was more promising and in April 1897 he decided to give up on his uranic rays. Nonetheless, it raised the interest of other great scientists. One of his students looking for a PhD subject wanted to go deeper in uranic rays and continue Becquerel work. She was Marie

Sklodowska-Curie (1867 - 1934), a Polish physicist married with Pierre Curie (1859 - 1906), French physicist. She intended to investigate all existing elements in the search of radiating ones. She did similar tests to Becquerel ones, applying the electric method instead of the photographic method. Furthermore, she studied many different natural elements through this method and she found out that uranium and thorium were the most actives ones. The outcome was similar, meaning that the effect was not only belonging to uranium but to other elements too. In particular, she highlighted that those unknown rays are emitted by the heaviest elements in nature, which was found later that this is due to the short-range nuclear forces, not able to compensate the Coulomb repulsion between protons in high atomic number nuclei. Marie Curie then, in her thesis manuscript, refers to the name she used for defining those types of element, which was later adopted worldwide, radioactive: « Nous dirons que l'uranium, le thorium et leurs composés émettent des rayons de Becquerel. J'ai appelé radioactives les substances qui donnent lieu à une émission de ce genre. Ce nom a été depuis généralement adopté.” (4)

Figure 2: Marie Sklodowska-Curie immortalized working in her laboratory in Paris. (5)

Figure 3: Marie Sklodowska-Curie and her daughter Irene Joliot-Curie at the Institute of radium in 1921. (5)

In 1898, Marie and Pierre Curie isolated fractions of pitchblende, a type of uranic ore composed by around 60% of uranium, and found out that some of those fractions contained more radioactivity than pure uranium. They expected to detect radioactivity corresponding to 0.6 g of uranium isolating 1 g of mineral. Surprisingly the activity was much higher than what they thought. In July of that year, after numerous chemical separations of tons of pitchblende, they discovered an element with a radioactivity 400 times greater than an equal amount of uranium. They named it polonium after Marie's native country, Poland. Later that same year, they discovered another new element, radium. (6)

In parallel, the discovery of x-rays unlocked the path to a new world, medical imaging. By 1896 the first scientific journal on medical imaging was edited. It was Archives of Clinical Skiagraphy, name derived from the greek σκιά which means shadow. X-rays were suddenly brought to therapy too. In 1896, Victor Despeignes unsuccessfully tried to treat stomach cancer. Nevertheless, from the explosion of the use of x-ray the harmfulness of the radiation emerged. For this reason, in 1898 the first radiation protection studies were performed by a specific committee set by Röntgen. (7)

In 1900, the two German scientists Giesel and Wakhoff found that the rays emitted by radium had a destructive action on the epidermal. (8) (9) After reading their paper, Pierre Curie placed a radium sample for 10 hours on his arm for studying its effect on the skin. "He was most enthusiastic about the appearance of an erythema which covered a surface of about 6 cm^2 of his skin. Later a wound became visible which healed after a lapse of 4 months, but not without leaving a mark behind. Henry Becquerel reacted in a very different way. He traveled to London where he had to address the Royal Society. There was a tube containing radium chloride in his waistcoat

pocket and on arriving home in Paris he discovered a wound on his chest produced by the radiation emitted by the radium sample. He was very much upset and reproached the Curies to have discovered a substance which emitted a radiation having such an unpleasant effect." (8) (9)

Despite this, other scientists were trying to go deeper in the newly discovered uranic rays. One of them was Ernest Rutherford (1871 - 1937), New Zealander physicist. In 1911 investigating with James Chadwick (1891 - 1974) the absorption of uranium radiation by an increasing aluminum thickness, he concluded that there were at least two distinct types of radiation. One that is very readily absorbed, which will be termed for convenience the α radiation, and the other of a more penetrating character, which will be termed the β radiation. (10) Later Frederick Soddy (1877 – 1956) coined the concept of radioisotopes, referring to those nuclides localized in the same spot in the periodic table having indistinguishable chemical properties. (11)

1.1.2 Artificial available radionuclides

Georges Charles de Hevesy (1885-1966), working under Rutherford at the Cavendish Laboratory in 1911, developed the idea that a radioactive substance, chemically bonded with a stable substance and indistinguishable, could be used as an indicator of the latter. Nevertheless, this concept of radiotracer couldn't be applied to medicine due to the lack of non-toxic natural radioisotopes at that time. Along with the invention of the cyclotron dated back 1930 by Ernest O. Lawrence (1901 – 1958), new radioisotopes artificially produced became available. In 1929, Lawrence observed that potassium ions crossing a metallic tube in which an alternate voltage was applied, were accelerated and exit the tube with an exit energy equal to the double of the initial one. From that, he developed the concept of the cyclotron and in the years '30s several cyclotrons accelerating particles beam between 80 keV and 100 MeV were built around the world.

In parallel Irene Joliot-Curie (1887 - 1956), daughter of Marie Curie, and her husband Frédéric Joliot-Curie (1900 – 1958) discovered that irradiating an aluminum foil with the high energy alpha emission of a polonium solution, it generated positron emissions from the metal. Also, those emissions were not stopped by removing the polonium solution, but decreased exponentially with time. They succeeded in obtaining the same results with boron and magnesium, measuring their half-life and proving the transmutation of nuclei with the alpha particle capture. They called these new isotopes radionitrogen, radiosilicon, radiophosphorus. (12) They suggested that those elements, and more, could be produced when irradiating materials with other particles like proton, deuteron and neutron.

In the thirties the Italian group "I Ragazzi di via Panisperna", coordinated by Enrico Fermi (1901 - 1954), were very active with their researches in nuclear physics, leading e.g. to the discovery of slow neutrons. One thought was also that one of the scientists of the group, Ettore Majorana (1906 – disappearance 1938) discovered the neutron before James Chadwick (1891 – 1974), but never published his work. Another scientist of the group, Emilio Segré (1905 - 1989) during one

of his trips to Berkeley noticed a molybdenum deflector of the cyclotron which was substituted and store as waste. Wondering whether he could find other elements, in particular the element 43, he asked to bring the radioactive piece with him in Italy. With the agreement of Lawrence, Segré travelled back to Italy with the molybdenum deflector in his luggage. Then together with the professor in mineralogy Carlo Perrier (1886 – 1948), they were able to isolate the element number 43 from the radioactive material, and they gave the name technetium from the Greek meaning artificial, as it was the first artificial discovered element. (13) Tc-99m was then identified as useful isotope for nuclear imaging available by bombarding a molybdenum target with deuteron beams, but its short half-life was not ideal for a convenient medical use. However, in the fifties the idea of producing the parent nuclide, Mo-99, with a long half-life acting as a generator of Tc-99m emerged, spreading its use for clinical applications. From the discovery of technetium, other artificial elements were discovered as well as a larger number of radioisotopes for each element was clearer. This allowed having available a larger number of radionuclides with physical properties of interest for medical and many other applications. It was from that time that researchers started to develop new molecules and radiopharmaceuticals aimed to support the diagnostic and treatment of diseases as primary concern.

1.2 Radioactive decays

The world is a combination of fundamental particles. The early 19th century vision of the atom as the smallest and indivisible elementary particle was replaced, after the discovery of the neutron, by the thought that proton, neutron and electron were the smallest fundamental particles constituting the atoms. Later, with the particle acceleration and detection technology evolving and related improvements, it was found that protons and neutrons were made up by the so-called quarks. The standard model was elaborated in the second half of the 20th century. However, it is still incomplete as some further explanations have to be found in order to complete the particles theory. A fundamental particle is characterized by mass, electric charge and spin. Particles with half-integer spin are called fermions and those with integer spin are called bosons. (14) Up to now, fermions, divided into six quarks and six leptons were discovered. Neutrons and protons are bound states of quarks, while electrons and neutrinos are part of leptons family. Photons instead are classified in the bosons family. The antiparticles are considered appertaining at the same family.

1.2.1 Radioactivity and Bateman equation

Radioactivity is the spontaneous disintegration of a nucleus that transfers into another nucleus while emitting particles or electromagnetic radiation. The most common forms of radiation emitted have been traditionally classified as alpha (α), beta (β), and gamma (γ) radiation. Radioactive processes are usually quoted as decays. The probability per unit time that a given

radionuclide will decay is called decay constant and is denoted by the symbol λ. The main physical quantity is the activity A representing the number of disintegrations per unit time. The activity is measured in Becquerel (Bq), which corresponds to one decay per second. An alternative unit of measure of the activity is the Curie (Ci) corresponding to the activity of 1 g of Ra-226 and is equivalent to 3.7E10 Bq. The activity is related to the decay constant by the equation:

$$A(t) = -\frac{dN}{dt} = \lambda N(t) \quad (1)$$

where N(t) is the number of radioactive nuclei in the sample at time t. Integrating equation (1) one can obtain the equation (2), which substituted in (1) gives (3):

$$N(t) = N(0) * e^{-\lambda t} \quad (2)$$

$$A(t) = \lambda N(0) * e^{-\lambda t} \quad (3)$$

Where N(0) is the initial number of nuclei at time t=0. Another important quantity is the half-life. It is the time $T_{1/2}$ when the initial number of nuclides is decreased by half: $N(T_{1/2})=N(0)/2$. Substituting in equation (3) it gives:

$$\frac{N(0)}{2} = N(0) * e^{-\lambda T_{1/2}} \quad (4)$$

$$T_{1/2} = \frac{ln\,2}{\lambda} \quad (5)$$

When an atom decays, it become a daughter nuclide. Therefore, the population of the parent nuclide decreases with time while the population of the daughter nuclide increases. If the daughter is radioactive, the population evolution in time will depend on the decay constant of the parent and the decay constant of the daughter nuclides. It can be calculated by the following equation. Considering an atom "a" which decays to his daughter "b", the variation of number of daughter nuclides N_b in time is:

$$\frac{dN_b}{dt} = -\lambda_b N_b + \lambda_a N_a \quad (6)$$

Substituting (2) in (6) one can obtain (7). Its integration in time gives (8):

$$\frac{dN_b}{dt} = -\lambda_b N_b + \lambda_a N_{a0} e^{-\lambda_a t} \quad (7)$$

$$N_b = N_{b0} e^{-\lambda_b t} + \frac{N_{a0}\lambda_a}{\lambda_b - \lambda_a}(e^{-\lambda_a t} - e^{-\lambda_b t}) \quad (8)$$

Where N_{a0} and N_{b0} are the number of atoms of the species a and b at time t=0. This equation is known as the Bateman equation. It can be completed and applied to a decay chain adding further daughter elements. In the following figure is presented an example of relative population evolution of: a parent radionuclide, b first daughter radionuclide, and c second daughter stable nuclide). Initially, the mixture contains only the parent radionuclide.

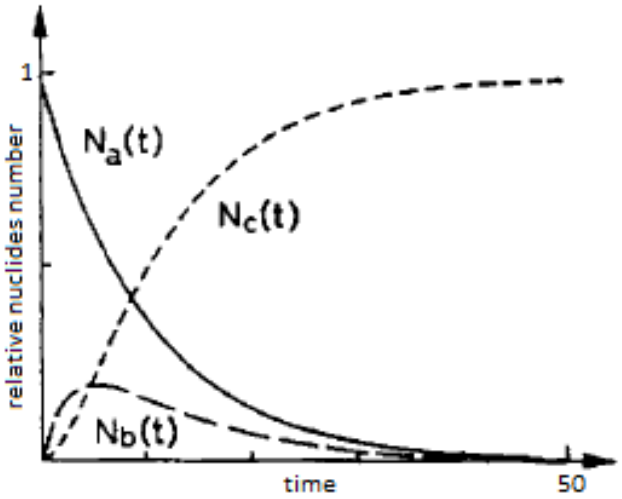

Figure 4: example of relative population evolution for a decay chain involving the parent nuclide a, the daughter b and the stable grand-daughter c. (15)

1.2.1.1 Specific activity

Very often radionuclides occur in a mixture of nuclides of the same element, some being stable, others radioactive. A very important quantity is the fraction of the activity of the radionuclide over the total mass of a considered sample. This is called specific activity. The specific activity for a given radionuclide x in Bq/mg can be calculated as follows:

$$A_s = \frac{A_x}{m_{tot}} \qquad (9)$$

Where A_s is the activity of the radionuclide in Bq and m_{tot} is the total mass of the sample in mg. Considering a sample containing three isotopes x, a, b of the same element, this can be rewritten as:

$$A_s = \frac{\lambda N_x}{m_a + m_b + m_x} \qquad (10)$$

In the ideal situation where the sample is composed only by the radionuclide x the specific activity is:

$$A_{s,x} = \frac{\lambda N_x}{m_x} = \frac{\lambda}{m_x}\frac{N_A m_x}{M_x} = \frac{\lambda N_A}{M_x} \qquad (11)$$

Where N_A is the number of Avogadro in (atoms/mol) and M is the molar mass in (mg/mol). This is the theoretical specific activity, thus the maximum specific activity achievable for a given radionuclide.

1.2.2 The atom

Atoms are composed of protons and neutrons bonded together within the nucleus and electrons, which follow specific orbits around the atom nucleus. Electrons have mass 9.1E-31 kg

and charge e = - 1.6E-19 Coulombs; protons have a mass of 1.7E-27 kg and a positive charge with the same magnitude as the electrons one; the neutrons mass is 1.7E-27 kg and are electrically neutral. The number of protons of an atom, the atomic number Z, gives the name to each individual element. The overall number of protons and neutrons is giving the atomic mass A. The conventional writing for atomic mass and atomic number of an atom X is the following:

$$_{Z}^{A}X$$

An atom with the same atomic number having a different atomic mass is called isotope. Currently 118 elements have been discovered both natural occurring and artificially produced. Elements could have one or more stable isotope, and several non-stable isotopes which can be artificially produced or present in nature from the decay of a parent isotope or coming from specific minerals and from cosmic rays. Stable nuclei (in black in Figure 5) only occur in a very narrow band in the N/Z plane close to the line N=Z corresponding to the light nuclei region as shown in Figure 5.

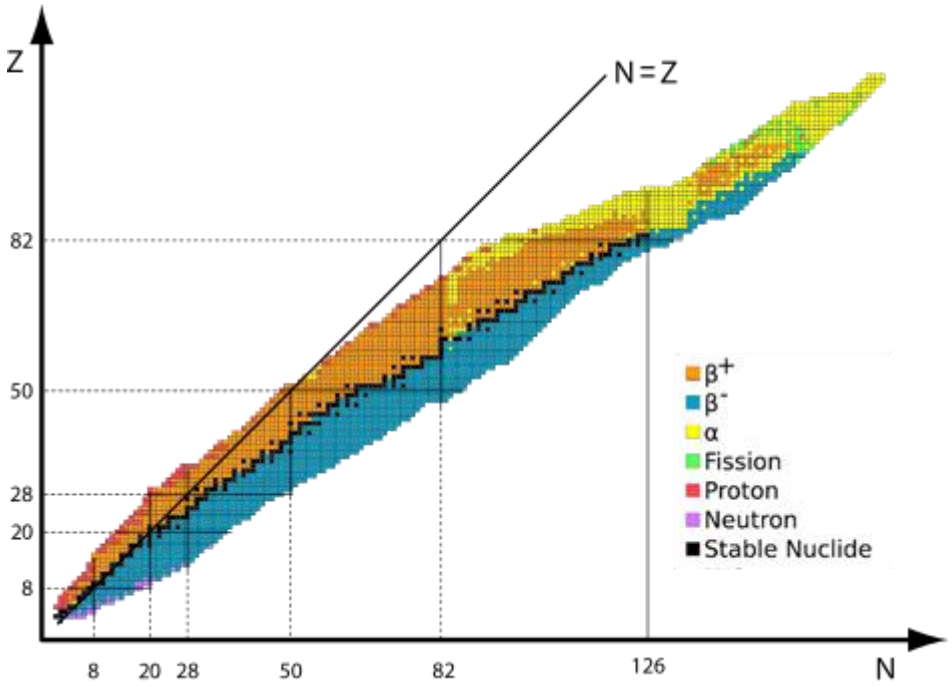

Figure 5: chart of nuclides. The distribution of stable nuclei occurring in nature (in black) compared to the N=Z line. (16)

The state of a nucleus corresponding to the lowest energy is called nuclear ground state. When the nucleus instead has more energy than the ground state it is in an excited state. A nucleus does not remain in an excited state, but decays to lower energy states either reaching the ground state or decaying to a daughter nucleus.

1.2.3 Decay modes of nucleus

Nuclear decays could happen from an excited nucleus through the excess energy release or by spontaneous emission. Several decay modes can happen, they are listed hereafter with their decay schemes presented in *Figure 6*. Furthermore, some nuclei could have different decay branches, corresponding to different decay daughter, or different energy branches, corresponding to different excited level of the same daughter nucleus. The probability of a given decay mode and a given decay energy is called branching ratio, usually indicated in percentage.

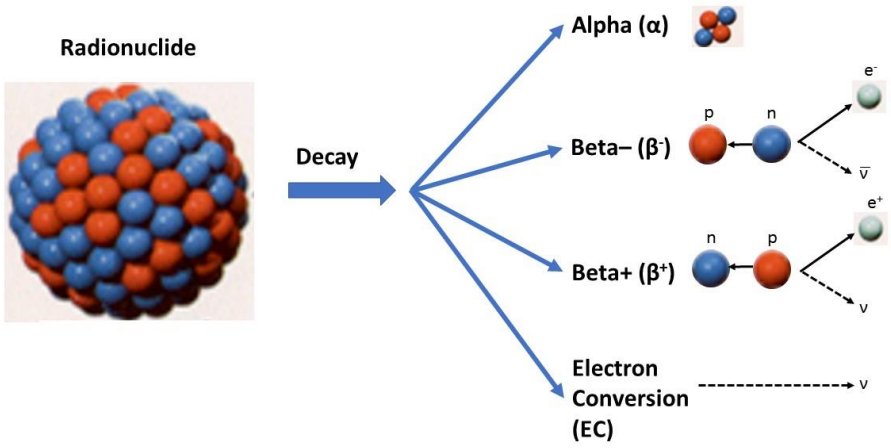

Figure 6: radionuclides decay modes scheme.

1.2.3.1 Alpha Decay α

Alpha (α) particles are nucleus of helium He-4, therefore they are composed by 2 protons and 2 neutrons bonded together. During an α decay an atom with atomic mass A and atomic number Z decays in a nuclide with atomic mass A-4 and atomic number Z-2.

$$ {}^{A}_{Z}X \rightarrow {}^{A-4}_{Z-2}Y + {}^{4}_{2}He $$

Alpha particles are emitted from the nucleus with a specific energy with its respective probability of emission. Each emission presents a mono-energetic spectrum. This particularity allows the characterization of an alpha source by detecting the emitted particles energies. The average emission energy is between 3 and 7 MeV. The process of alpha decay can be found mostly in high atomic number nuclides as increasing the mass number the electrostatic repulsive forces increase more rapidly than the cohesive nuclear force.

1.2.3.2 Beta decay β-

Beta β- decay consists in the emission of an electron from the decay of a neutron in a neutron-rich nucleus. The neutron converts in a proton, emitting an electron and an antineutrino: $n \rightarrow p + e^- + \bar{\nu}$. During a β- decay an atom with atomic mass A and atomic number Z decay in a daughter nuclide with atomic mass A and atomic number Z+1, resulting in an isobaric (same atomic mass) transition.

$$ {}^{A}_{Z}X \rightarrow {}^{A}_{Z+1}Y + e^- + \bar{\nu} $$

The spectrum of β- decay is continuous (*Figure 7*), therefore the main quantities are the maximum and the average electron energies. This effect is related to the co-emission of an electron and an antineutrino which share the total available energy. After most of β- decays, the daughter nucleus is left in an exited state leading to the emission of other radiation.

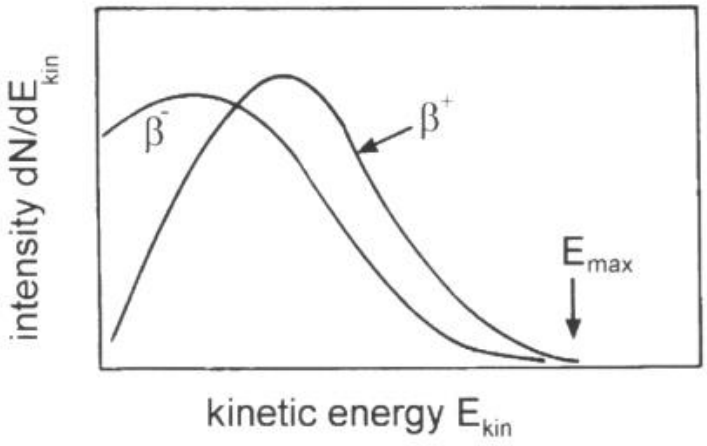

Figure 7: energy spectrum of electron β- and positron β+ emission. (17)

1.2.3.3 Beta decay β+

The antiparticle of the electron is called positron (β+). It has the same mass of the electron but opposite charge. Beta β+ decay consists in the emission of a positron from the decay of a proton in a proton-rich nucleus. The proton converts in a neutron, emitting a positron and a neutrino electron: $p \rightarrow n + e^+ + \nu$. During a β+ decay an atom with atomic mass A and atomic number Z decay in a daughter nuclide with atomic mass A and atomic number Z-1, resulting in an isobaric transition as for β- decay.

$$ {}^{A}_{Z}X \rightarrow {}^{A}_{Z-1}Y + e^+ + \nu $$

As for electron emissions, positron emissions present a continuum spectrum (*Figure 7*), caused by the co-emission of a positron and a neutrino. When a positron is ejected from the parent nucleus the daughter nucleus shed an orbital electron to balance the charge. This phenomenon is energetically possible only with a threshold energy of 1.022 MeV, in other terms only if the

mass of the parent nucleus exceeds the mass of the daughter nucleus by at least two times the electron mass at rest.

1.2.3.4 Electron Capture (EC)

The electron capture is a competitor of the β^+ decay, indeed are involved the same parent nucleus with atomic number Z and the same daughter nucleus with atomic number Z-1. It consists in a capture of an atomic orbital electron in proton-rich nuclides: $e^- + p \rightarrow n + \nu$. The hole in the atomic shell left by the captured electron is filled by another electron of an outer shell. The energy is released as x-rays and Auger electrons. Auger electrons are monoenergetic and their typical energy is few keV or lower. This process has no threshold energy. Indeed, for $\Delta E \leq 1.022$ MeV only EC decay mode is present, whereas for $\Delta E > 1.022$ MeV EC and β^+ decay modes could happen as they are in competition.

1.3 Particles interaction with matter

When particles or electromagnetic waves are emitted from a nucleus, distinct effects are governing the interaction with matter. The effects depend on the type of emission and the matter of interaction. Particles can be divided in non-charged particles, such as neutrons and photons, and charged particles, such as alpha and beta particles. Charged particles are strongly interacting with matter while is more challenging to stop non-charged particles as shown in Figure 8.

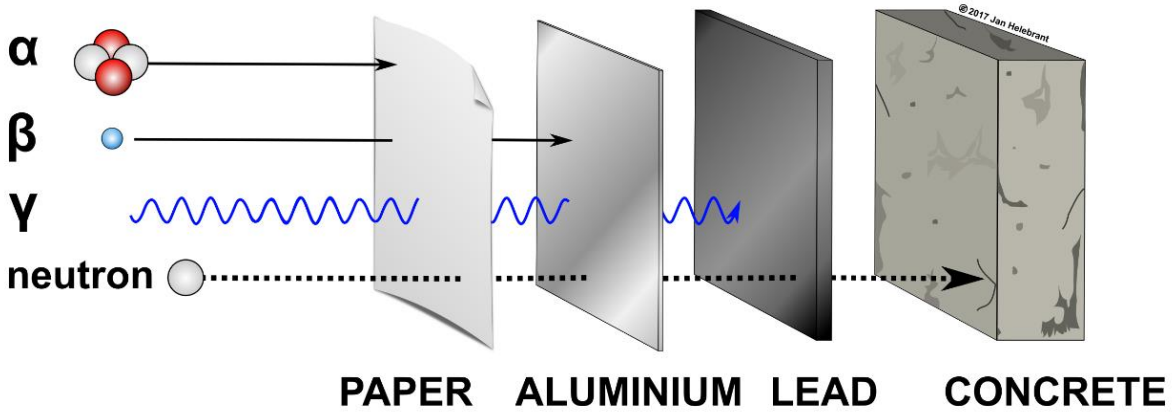

Figure 8: penetrating power of different types of radiation. (taken from www.openclipart.org)

The path travelled by an alpha particle emitted from a radionuclide in air is only few centimeters and alpha particles can be simply stopped with a paper foil. Beta particles are more penetrating than alpha particles. They have an average range of around 1 meter in air and they can be stopped with for example thin metallic foils. Gamma rays can be stopped by a thick layer of an heavy element such as lead, while neutron can be stopped for example by concrete blocks. Indeed, larger material layers are needed to stop neutron as they interact only with the atom nuclei. The

interaction with matter for alpha, beta and gamma particles is described in the following paragraphs.

1.3.1 Electromagnetic waves interaction with matter

Gamma rays are short wave-length electromagnetic radiation following a radionuclide decay. Gamma ray emission typical energies are in the range from 70 keV to 3 MeV in radioactive decays. Gamma rays are emitted after a decay when the daughter nuclide is in an excited state. Usually gamma rays allow the identification of an atom through their detection, as many radionuclides have a typical gamma emission spectrum. Gamma rays interact with matter by three main ways (Figure 9):

- photoelectric effect (interaction with electrons)
- Compton effect (interaction with electrons)
- pair production. (interaction with nuclei)

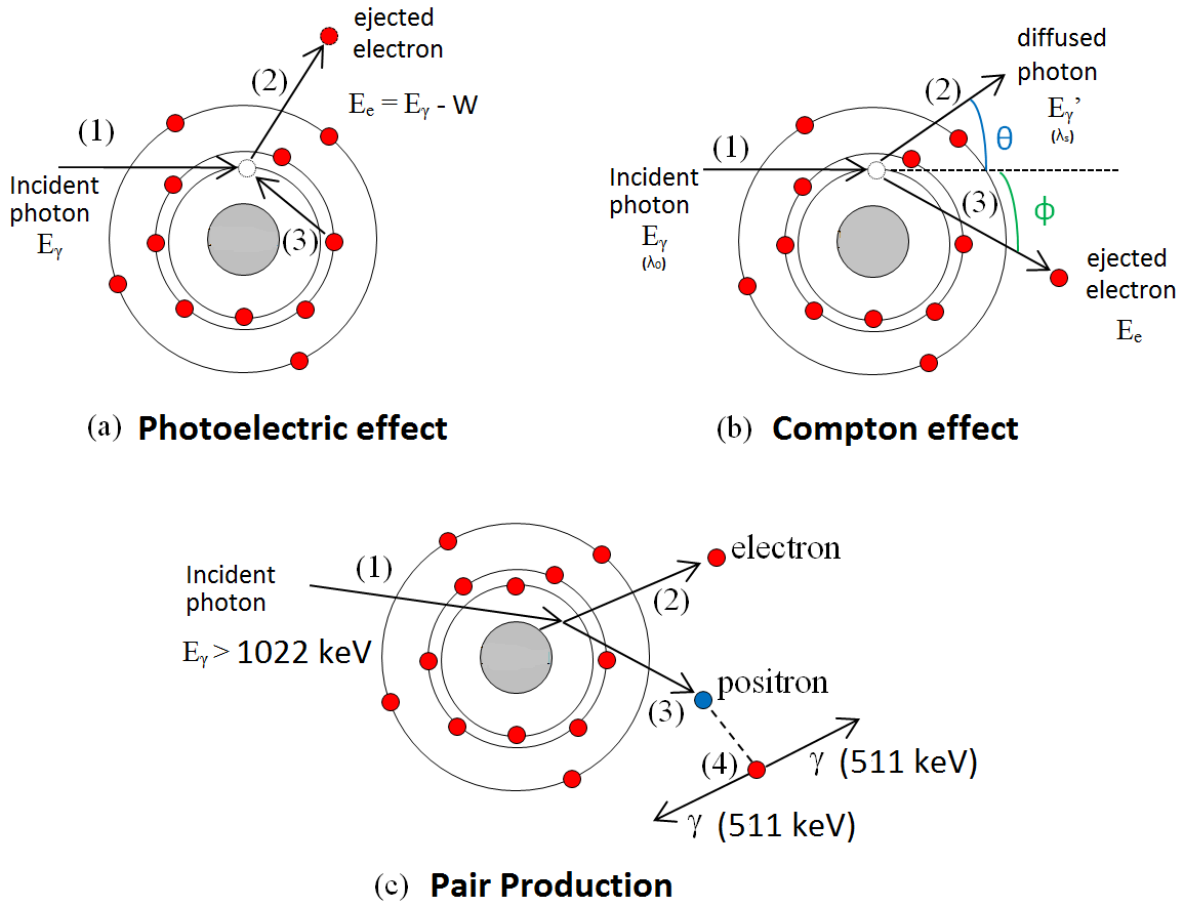

Figure 9: main interactions of gamma rays with matter. (9a) Photoelectric effect scheme; (9b) Compton effect scheme; (9c) Pair Production scheme. (18)

1.3.1.1 Photoelectric effect

Max Planck (1858 - 1947) suggested that the energy carried by electromagnetic waves could only be released in packets of energy, photons, in his work on black body radiation. Albert Einstein (1879 - 1955) applied Plank's statement to explain the photoelectric effect. (19) A photon of frequency ν carries energy hν (E_γ), where h is Planck's constant. If it strikes an electron inside matter, it can transfer all its energy to the electron. The latter then is ejected from the atom with an energy of $E_e = E_\gamma - E_b$, where E_b is the binding energy. The vacancy then is filled by an outer shell electron. The excess energy is released as X-ray or Auger electron emission. The scheme of the process is represented in Figure 9a.

The photoelectric effect is predominant for low-energy photons and in high-Z materials. An example of the photoelectric effect energy range compared to the other effects is given in Figure 10.

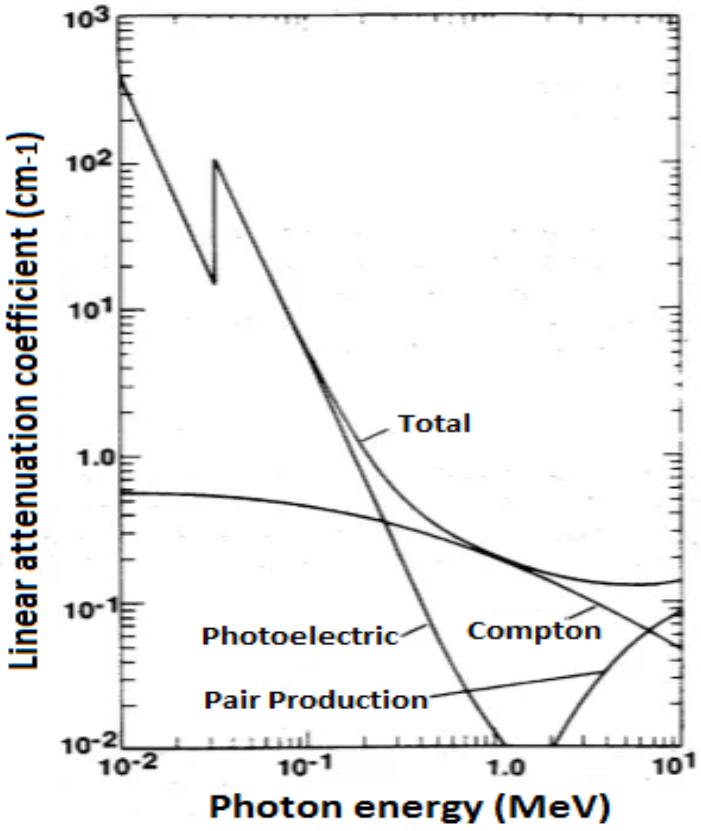

Figure 10: example of linear attenuation coefficient (of NaI) showing the contributions of photoelectric absorption, Compton scattering and pair production. Taken from (20)

1.3.1.2 Compton effect

Following the wave theory, it is supposed that an incident wavelength with frequency ν_0 on an electron almost at rest, would let the electron absorb energy from the wave and re-radiate

electromagnetic wave of a frequency $\nu_s < \nu_0$. Arthur Compton (1892 – 1962) found that the wavelength of the scattered radiation does not depend on the intensity of incident radiation, but it depends on the angle of scattering and the wavelength of the incident beam. The wavelength of the radiation scattered λ_s at an angle θ is given by:

$$\lambda_s = \lambda_0 + \frac{h}{m_0 c}(1 - cos\,\theta) \qquad (12)$$

where m_0 is the rest mass of the electron and λ_0 the wavelength of the incident radiation. The constant $\frac{h}{m_0 c}$ is known as the Compton wavelength of the electron and it corresponds to 0.0024 nm. The scheme of Compton effect is shown in Figure 9b. Compton scattering is the predominant effect in the energy range around 1 MeV (Figure 10). Nevertheless, the scattered photons by Compton effect have different energy. When characterizing a radioactive source by detecting the gamma spectrum, Compton effect can be the main source of background noise.

1.3.1.3 Pair Production

The pair production, which is schematically presented in Figure 9c, consists in a photon transformation in an electron-positron pair after the interaction with a nucleus. The threshold photon energy for this phenomenon is 1022 keV, corresponding to the energy necessary to create a pair of e^-/e^+ at rest. The generated positron after slowing down by interacting with the electrons of the medium, annihilates with an electron in two gamma rays having the same energy, 511 keV, and opposite direction. This effect is predominant at high energies as shown in Figure 10.

1.3.2 Heavy charged particles interaction with matter

In the following, we consider as heavy particles protons and alpha particles, to distinguish them from light charged particles such as electrons and positrons. Interactions of heavy charged particles in matter causes a loss of energy and the deflection of the particle from its incident direction. They can be registered following inelastic collisions with atomic electrons of the materials and elastic scattering from nuclei. Other rarer events are the emission of Cherenkov radiation (emission of photons occurring when charged particle travels faster than the speed of light in matter), nuclear reactions, bremsstrahlung (emission of electromagnetic waves from the scattering in the electric field of a nucleus). The collisions with electrons are the main cause of the energy degradation of alpha particles in matter. Even though the transferred energy per collision is small, the number of collisions per unit path in a dense media is large. For this reason, sometimes, thin layers can stop particles. Elastic scatterings are less frequent than inelastic scattering. In this case, very low energy is transferred, as usually the atoms of the material are heavier than the considered incident particles. To estimate the mean loss of energy of heavy charged particles inside the matter the stopping power (dE/dx) has to be considered. In order to describe this quantity, Bethe and Bloch have derived the equation:

$$-\frac{dE}{dx} = 2\pi N_A r_e^2 m_e c^2 \rho \frac{Z}{A}\frac{z^2}{\beta^2}\left[\ln\left(\frac{2m_e\gamma^2 v^2 W_{max}}{I^2}\right) - 2\beta^2\right] \qquad (13)$$

Where:

- N_A is the Avogadro's number
- r_e is the electron radius (2.817E-13 cm)
- m_e is the electron mass in g
- ρ is the density of the absorbing material in g/cm^3
- Z atomic number of the absorbing material
- z is the charge of incident particle
- β is the ratio v/c of the incident particle
- γ is given by $1/\sqrt{1-\beta^2}$
- I is the mean excitation potential
- W_{max} is the maximum energy transfer in a single collision

Usually two correction factors are added to the previous equation: the density effect correction δ; the shell correction C. This results in the following equation:

$$-\frac{dE}{dx} = 2\pi N_A r_e^2 m_e c^2 \rho \frac{Z}{A}\frac{z^2}{\beta^2}\left[\ln\left(\frac{2m_e\gamma^2 v^2 W_{max}}{I^2}\right) - 2\beta^2 - \delta - 2\frac{C}{Z}\right] \qquad (14)$$

1.3.3 Light charged particles interaction with matter

Electrons and positrons similarly to heavy charged particles, passing through matter undergo to a collisional energy loss. Moreover, due to their small mass, the bremsstrahlung effect is much more important. The effect of bremsstrahlung is remarkable at energies above few MeV, and above few tens of MeV this is the main effect. The critical energy from which bremsstrahlung starts to become predominant was approximately determined by Bethe and Heitler:

$$E_c = \frac{1600\, m_e c^2}{Z} \qquad (15)$$

The energy loss by electrons and positrons in matter is composed by the collision term and the emission of radiation term:

$$\left(\frac{dE}{dx}\right)_{TOT} = \left(\frac{dE}{dx}\right)_{COL} + \left(\frac{dE}{dx}\right)_{RAD} \qquad (16)$$

For the collision energy loss, the given Bethe-Bloch formula should be simplified and adapted to the smaller mass of the incident particles. In addition, as the incident particle is the same as the collided particle, the formula should take into account the indistinguishability of the two particles.

$$-\frac{dE}{dx} = 2\pi N_A r_e^2 m_e c^2 \rho \frac{Z}{A}\frac{1}{\beta^2}\left[\ln\left(\frac{\tau^2(\tau+2)}{2\left(\frac{I}{m_e c^2}\right)^2}\right) - F(\tau) - \delta - 2\frac{C}{Z}\right] \quad (17)$$

where τ is the kinetic energy of the particle and F(τ) is a function that depends on the incident particle, whether it is an electron or a positron.

Finally, as previously described for the pair production, a positron after slowing down annihilates, this is the effect which generates two gamma rays of 511 keV emission.

1.4 Radiation detection

The phenomena of interaction between radiation emission from a radioactive source and a detector material allow the measurement of the radiation. The detection of radiation includes the identification of its nature, the number of detected radiation per seconds and the measure of the energy of radiation. A detection system is composed by a detector layer, where the interaction of radiation with the latter for ionization of atomic excitation provokes an electric or light signal. In this work the detection of gamma rays and alpha particles are treated.

1.4.1 Gamma spectrometry

As most of the known radionuclides have a characteristic gamma spectrum, it is possible to perform gamma spectrometry to identify the composition of a radioactive source with specific detectors. A detector should have several characteristics:

- Sensitivity: produce measurable signal for given type of particle and energy. It depends on the cross-section of the ionizing reactions and on the surrounding noise.
- Response: the relation between the output given by the detector and the energy of the particle and the time needed for the signal creation and analysis (dead time)
- Detection efficiency: ratio between the number of detected particles and the number of emitted particles
- Energy resolution: the ΔE between two detectable energies in terms of Full Width at Half Maximum (FWHM)

The type of gamma detector used for the characterization of the samples analysis done in this work, as well as the activity measurements from the stacked foils for cross-sections evaluations is the High Purity Germanium (HP Ge), a semiconductor detector. Indeed, this type of detector provides the suitable characteristics for those applications. At GIP ARRONAX two different gamma detectors have been used, namely Recherche and Arrofixe (Figure 11).

Figure 11: layout of the HP-Ge detector Recherche on the left, layout of the HP-Ge detector Arrofixe on the right at GIP ARRONAX

Detectors are cooled with liquid nitrogen based cryogenic system usually at 77 K. The detector cooling reduces the thermal generation of charge carriers. Otherwise, the leakage current induced noise would be too high (21). The detectors have a lead shielding in order to reduce as much as possible the natural radioactivity background, which is cladded with a copper layer to reduce the background caused by the x-ray generated by the interaction of the emitted gamma rays from the radioactive source to detect and the lead layer (Figure 11).

The interaction of the emitted gamma rays with the germanium detector causes the creation of electron-hole pairs. The number of electron-hole pairs is governed by the average energy spent by the particle to produce a single electron-hole pair. Applying a high tension on the semiconductor, the created charges are attracted by the positive electrode where they are collected. The charges produce a measurable current, proportional to their energy. The signal passes through a pre-amplifier and an amplifier. An analog-to-digital converter transforms the amplified signal in a number proportional to the energy deposited on the semiconductor. The number are assigned to a determined channel, which correspond to a small energy range, by a multi-channel analyzer. This allows obtaining a spectrum of the recorder signals.

1.4.1.1 Gamma spectrometry analysis

In this work, the control of the multichannel analyzer has been performed with LVis software (22), which allows exporting the obtained signal in a format compatible with other software for the analysis of the obtained spectrum. A histogram is given with x-axis corresponding to the channel numbers, proportional to the energy of the gamma rays, and y-axis the number of counts for each channel. In order to assign the channel to the particle energy in the channel the detector must be calibrated in energy with a known source. The calibration will be also needed for the quantification of the activity from the counts obtained in order to take into account the efficiency of counting.

The obtained spectrum with file extension ".chn", were saved and analyzed with FitzPeaks (23). The following procedure has been followed for the spectrum analysis:

- Peak search: identification of peaks presents in the recorded spectrum
- Peak fitting: adjustment of the peak with a Gaussian function as suitable representation of peaks detection. Each peak fitting was visually checked, when the peak was not well fitted, a further manual adjustment was performed (ex. division of a non-properly fitted Gaussian in two or more Gaussians corresponding to different peaks emitted at very close energies)
- Energy calibration: allows linking the radiation energy to a channel number (1.4.1.2 Energy calibration)
- Efficiency calibration: allows linking the detected counts to the activity of the radioactive source (1.4.1.3 Efficiency Calibration)
- Peak area determination: integration of the fitted peaks to obtain the total counts number for each peak
- Nuclides identification and quantification: a specific library has been made, containing all the potential nuclides contained in the source. When a peak was non-identified by the software, a manual research was made to identify the possible provenience of the peak. In case it was corresponding to a nuclide missing in the library the analysis was done once more with the updated library.

When samples were counted at other facilities detectors, such as CERN and ILL, the calibration curves were provided. In those cases, the analysis was performed with GENIE2000 (24) software. The libraries were made from nuclear data present on NNDC database. (25)

1.4.1.2 Energy calibration

The source used for calibrations is a sealed Eu-152 source (half-life 13.54 years), certificated at 3.437 kBq the 26/11/2008 at 12h UTC from LEA-CERCA (AREVA). The source has been counted for

one week in Recherche and Arrofixe at the same distance as the evaluated sample in order to keep the same geometry. The Eu-152 gamma lines used for the calibrations are listed in the following table. Indeed, Eu-152 has been chosen as calibration source due to the wide energy range of its emitted gamma rays energy, covering the energy range of the detectors (up to 2 MeV) and suitable for the energy of the gamma rays emitted from the nuclides analyzed in this work.

Table 1: list of Eu-152 source gamma ray energies and associated intensities used for the calibration of the detectors. (25)

E (keV)	I (%)
121.78	28.5 ± 16%
244.69	7.5 ± 4%
344.28	26.6 ± 20%
411.12	2.2 ± 13%
778.9	12.9 ± 8%
867.37	4.2 ± 3%
964.08	14.5 ± 7%
1085.87	10.1 ± 5%
1112.07	13.7 ± 8%
1299.14	1.6 ± 11%
1408	20.9 ± 9%

With the calibration source, for which the peaks present in the spectrum are perfectly know, it is possible to associate one energy to a given channel. In the following figures are presented the energy calibrations obtained for both detectors Recherche and Arrofixe.

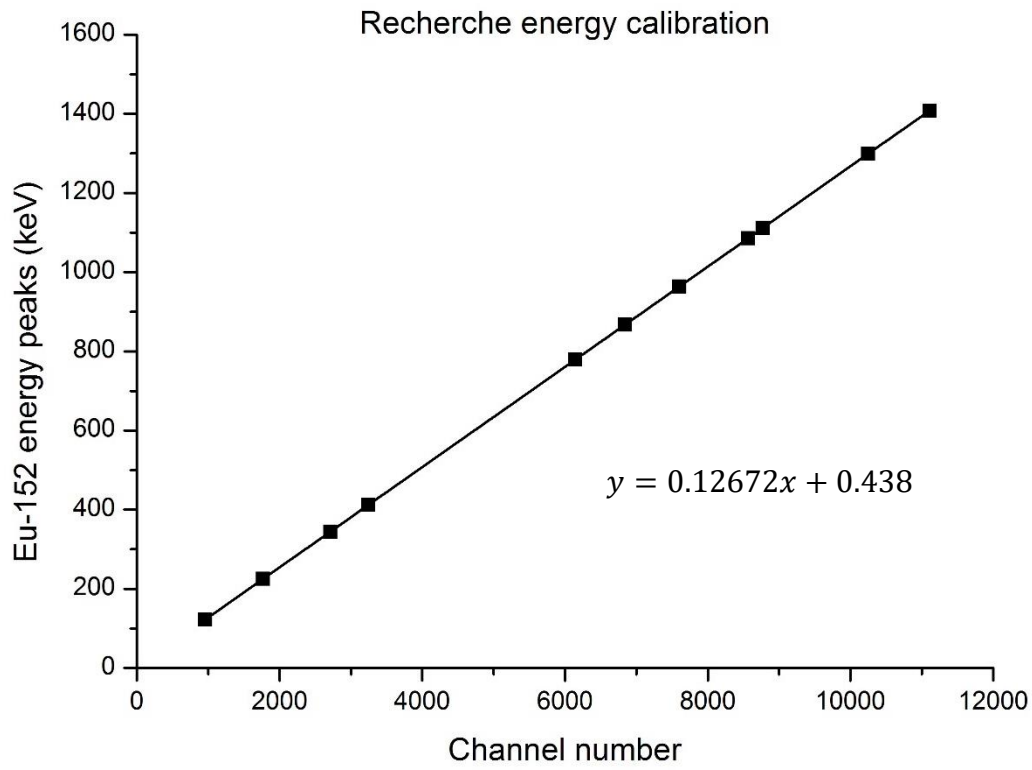

Figure 12: energy calibration curve for Recherche detector

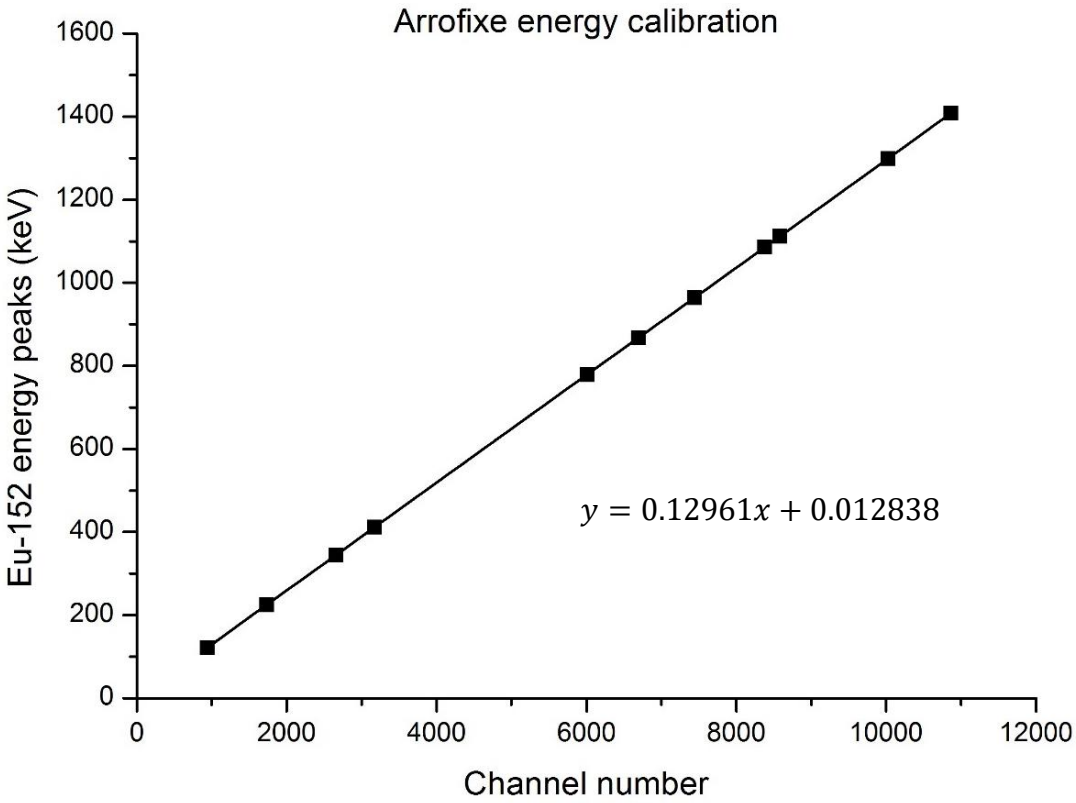

Figure 13: energy calibration curve for Arrofixe detector

1.4.1.3 Efficiency Calibration

Once the energy of the peaks is obtained, it is necessary to apply the efficiency calibration which takes into account the geometry effect, solid angle, self-attenuation and detector efficiency. For that purpose, an efficiency calibration of a known source has to be performed. The calibration source has a geometry similar to the one of our measured samples, therefore the detected solid angle is the same. Positioning the calibration source at the right distance with the eventual shielding is possible to perform the calibration. As some effects depend on the energy of the radiation, it is also necessary to use a calibration curve with γ radiation with the energy spread along the whole energy range. For this purpose, the Eu-152 source already used for the energy calibration has been used. In this case, the geometry of the source must be as close as possible to the one of the measured samples. The distance of the sample from the detector induced a rather small cascade summing correction, which was neglected.

The efficiency of detection of a detector is referred to the number of counts detected for a determined energy peak and the total number of gamma rays emitted by a radioactive source at that specific energy. For a given gamma emission line at the energy E emitted from a radionuclide and considering that the half-life of the radionuclide used for the calibration is long compare to the duration of the calibration run, the overall efficiency ε(E) is given by:

$$\varepsilon(E) = \frac{C}{BR\,(E) * t * A} \qquad (18)$$

Where C is the total number of counts detected at the energy E, BR(E) is the branching ratio of the considered gamma emission, t is the measurement time (s) and A is the activity of the radionuclide present in the radioactive source (Bq). In the following figure are presented the efficiency calibration curves obtained for the two detectors, with the polynomial function of order 4 used for the interpolation. As one can see from the figures, below around 100 keV the results are not fully reliable, however this is out of the range of the analyzed samples.

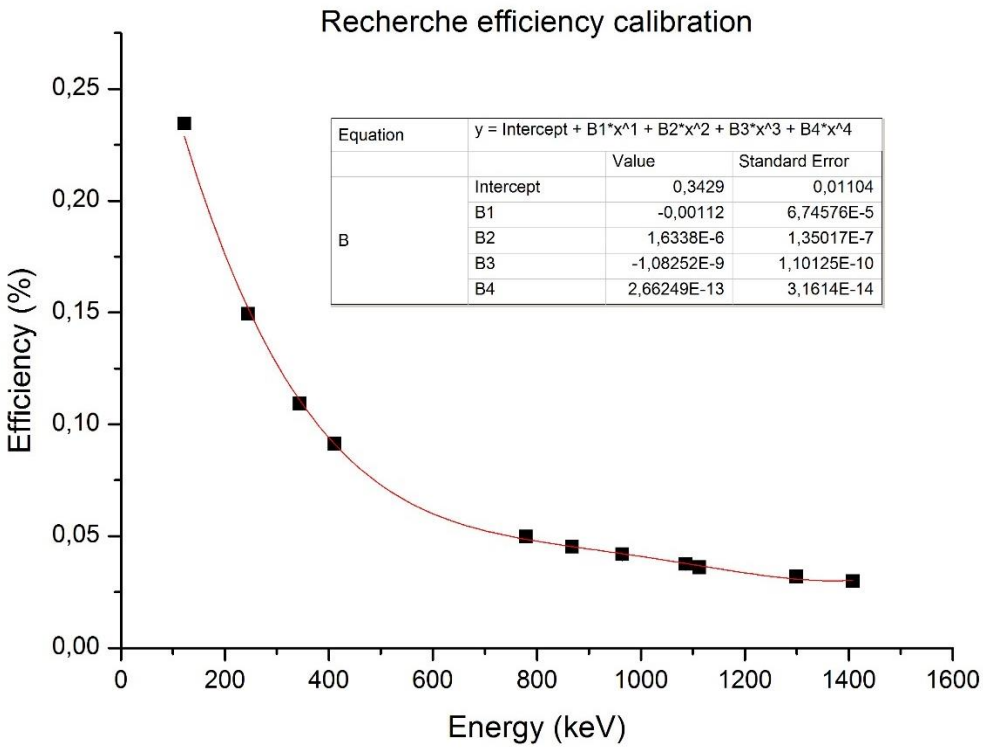

Figure 14: efficiency calibration curve for Recherche detector

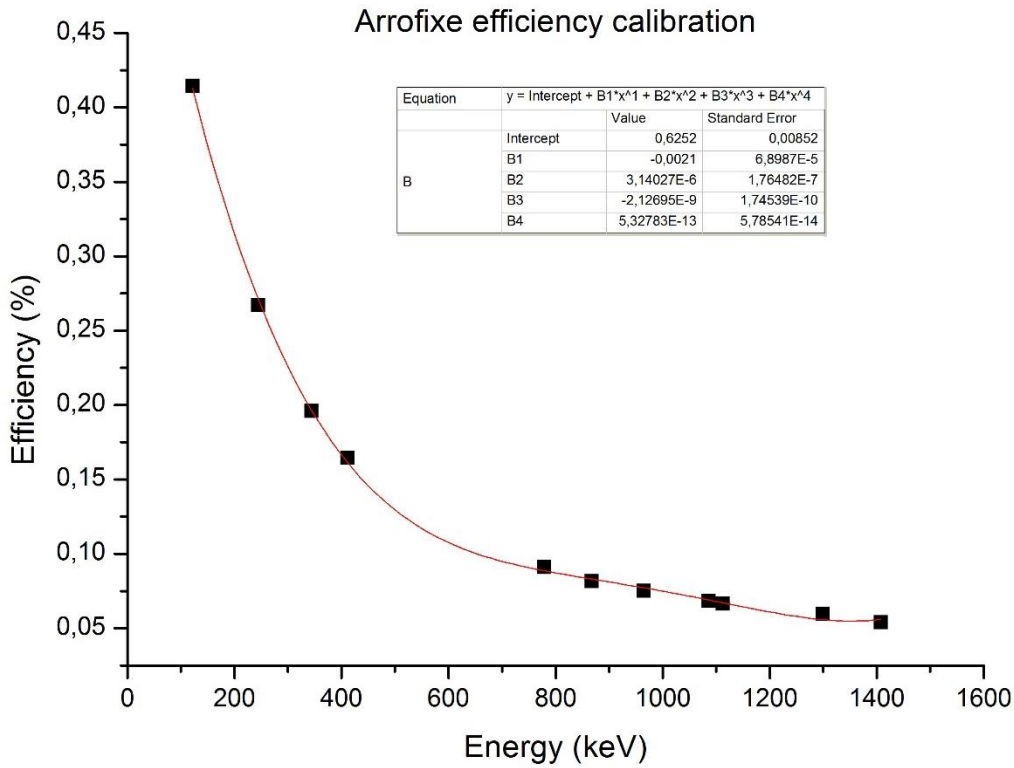

Figure 15: efficiency calibration curve for Arrofixe detector

1.4.2 Alpha spectrometry

For alpha emitters it is sometimes easier to use α-spectrometry. Indeed, it may happen that the radionuclide has no gamma rays or low energy or low intensity gamma ray difficult to determine. Also, it could happen that the background is too high leading to poor measurement or no-unique gamma rays are detectable with enough statistic for the quantification of a single radionuclide. In case of the stacked foils measurements performed in this work, the quantification of Tb-149 (α-emitter with half-life 4.112 hours) has been performed with an alpha spectrometer. The detector used at GIP ARRONAX is a Passivated Implanted Planar Silicon (PIPS) detector Alpha Series A of Canberra. It has a minimum active thickness greater than 140 µm, which is sufficient for the full absorption of alpha particles of up to 15 MeV. The principle of particle detection of the PIPS is similar to the HPGe, indeed the number of electron-hole created is directly proportional to the energy of the stopped particle. Nevertheless, the low leakage current helps minimizing peak shift with temperature variation, not requiring a detector cooling. The electric field in this region sweeps the electrons to the positive electrode and the holes to the other. A preamplifier integrates the charge pulse and with a multichannel analog-to-digital converter, the count rate versus the energy output is obtained.

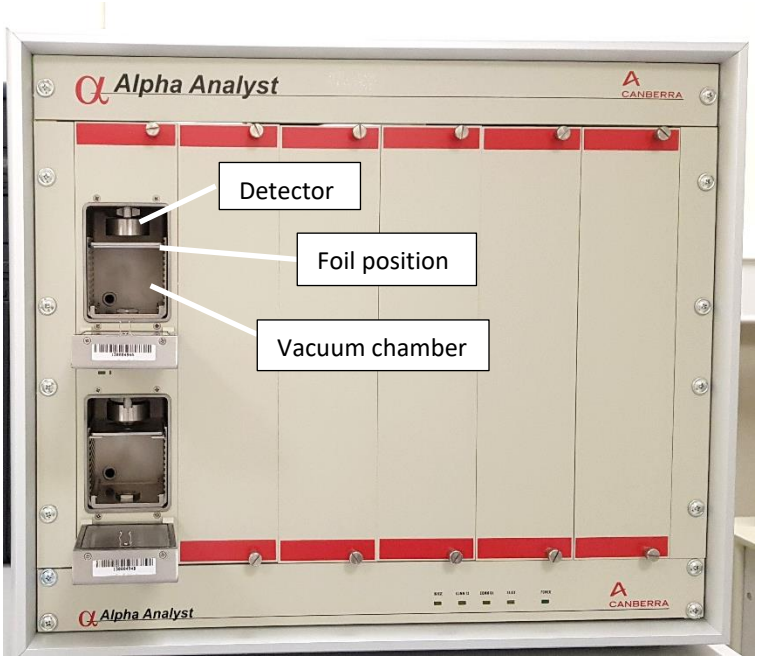

Figure 16: passivated Implanted Planar Silicon (PIPS) detector Alpha Series A of Canberra used at GIP ARRONAX

As alpha particle interacts strongly with matter (1.3.2 Heavy charged particles interaction with matter) it is necessary to work under vacuum. A mechanical pump is providing the vacuum inside the used module which contains two chambers.

In order to evaluate the activity of the produced radionuclides, the following equation has been used:

$$A = \frac{C*\lambda}{BR*\varepsilon*(1-e^{-\lambda t_m})} * e^{\lambda t_d} \quad (19)$$

Where:

- C is the integrated area of the detected peak. It has been determined summing all the contributions related to the peak area summing all the counts in that region
- BR is the branching ratio of the considered alpha emission
- ε is the detector efficiency
- t_m is the measurement time in s
- t_d is the time passed between the EOB and the starting of the measurement in s
- λ is the radioactive constant of the measured isotope in s^{-1}

1.4.2.1 Energy calibration

The energy and efficiency calibration curves of the detector at the considered distance have been measured with a certificated multi-alpha emitter source composed of Pu-239, Am-241 and Cm-244 at 364 α/s 2π steradian on the 16/06/2011 at 12h UTC from LEA-CERCA (AREVA).

The calibration source was characterized at the moment of the calibration. Indeed, it fundamental to consider the decay of the radionuclides during the time elapsed between the certification and the calibration. The activity values for each radionuclide present in the calibration source are presented in Table 2.

Table 2: Multi-α calibration source composition

Radionuclide	Energy (MeV)	Activity (Bq)	Half-life (y)
Pu-239	5.147	184.4 ± 5%	24110
Am-241	5.479	264.9 ± 8%	432.6
Cm-244	5.793	205.9 ± 8%	18.1

Similarly to what was described for the gamma spectrometry, given the known activities of each peak present in the calibration source, it is possible to associate one energy to a given channel. In the following figures are shown the energy calibrations made for both chambers used in the alpha detector.

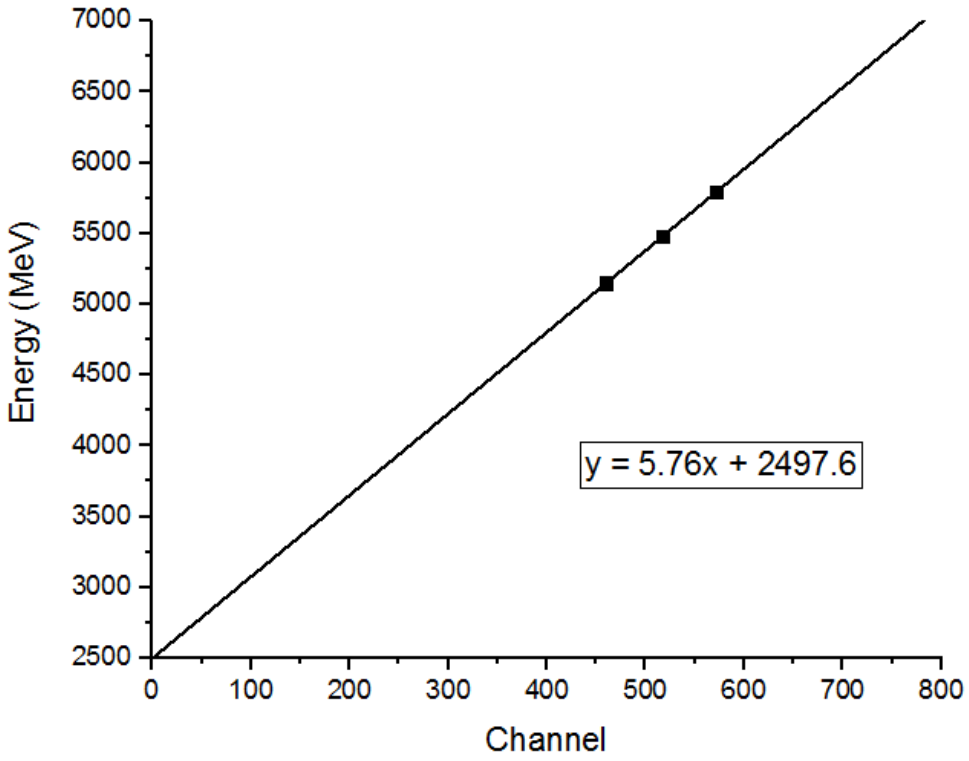

Figure 17: energy calibration for the chamber #1 of the alpha detector used

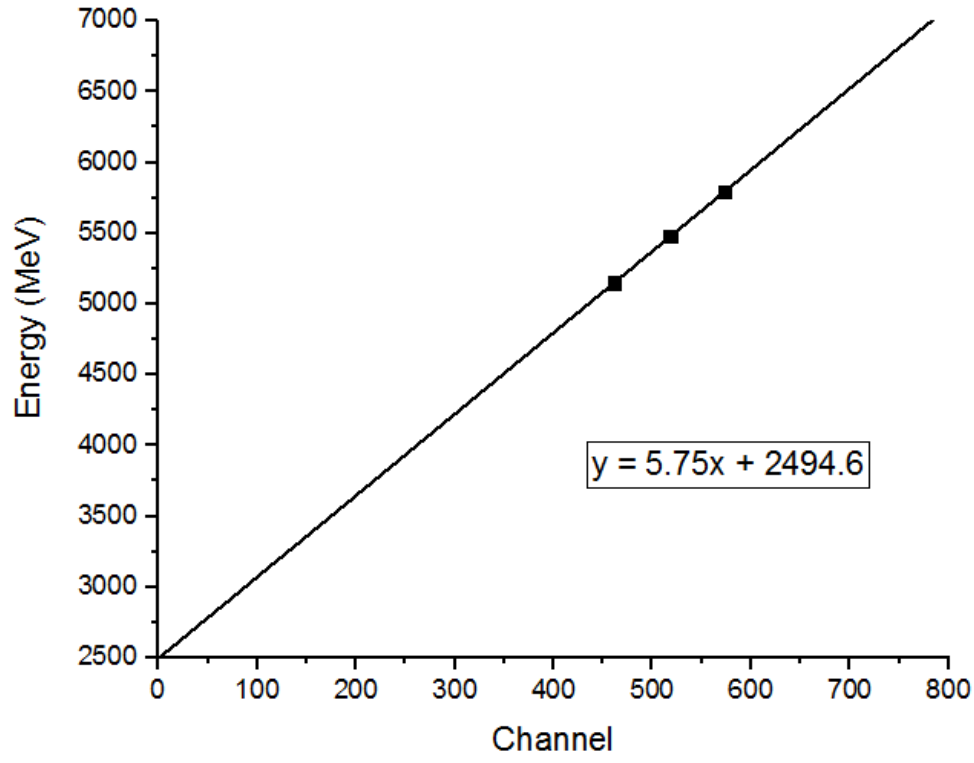

Figure 18: energy calibration for the chamber #2 of the alpha detector used

1.4.2.2 Efficiency calibration

After the energy calibration, an efficiency calibration is needed to take into account the geometry effects, self-attenuation and detector efficiency. As for the gamma spectrometry, the calibration source has a geometry close to the one used for the measured sample, therefore the detected solid angle is supposed to be the same. The multi-α source has been counted in both of the used chamber. The efficiency values obtained are presented in Figure 19 and Figure 20. The efficiency is then assumed constant for all the energy range of the measurement (2.5 to 7 MeV). The obtained values are 24.5 % for the first chamber and 25.2% for the second chamber. The spectrum obtained with the calibration source is given in Figure 21. It clearly shows 3 peaks that are associated to the 3 radionuclides present in our radioactive source.

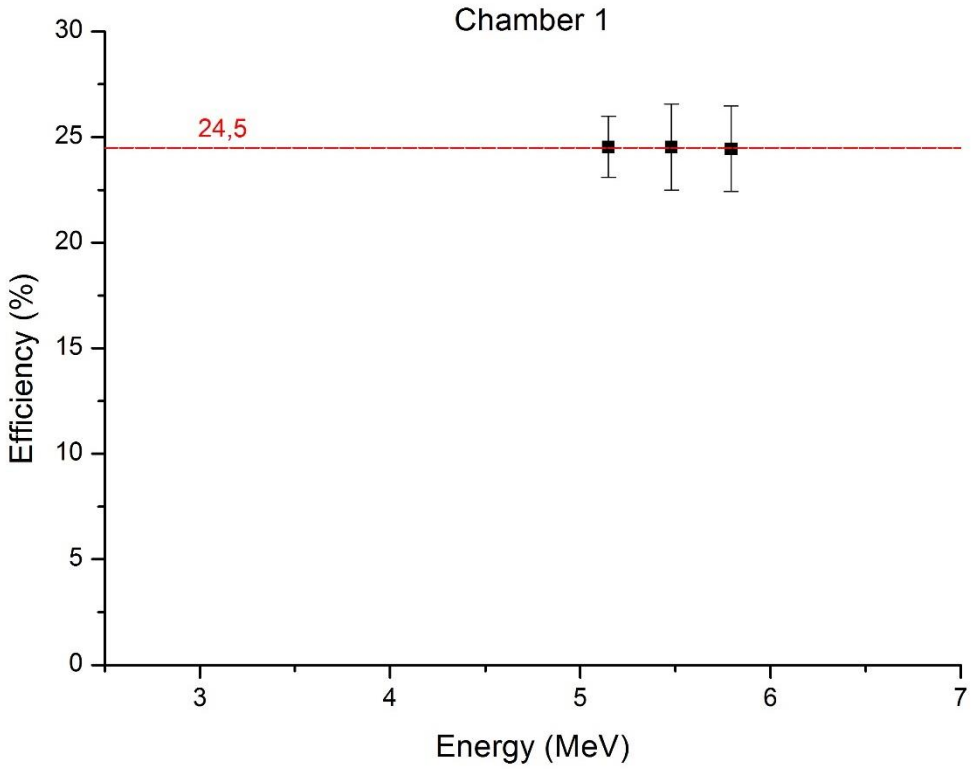

Figure 19: efficiency calibration for the chamber #1 of the alpha detector used

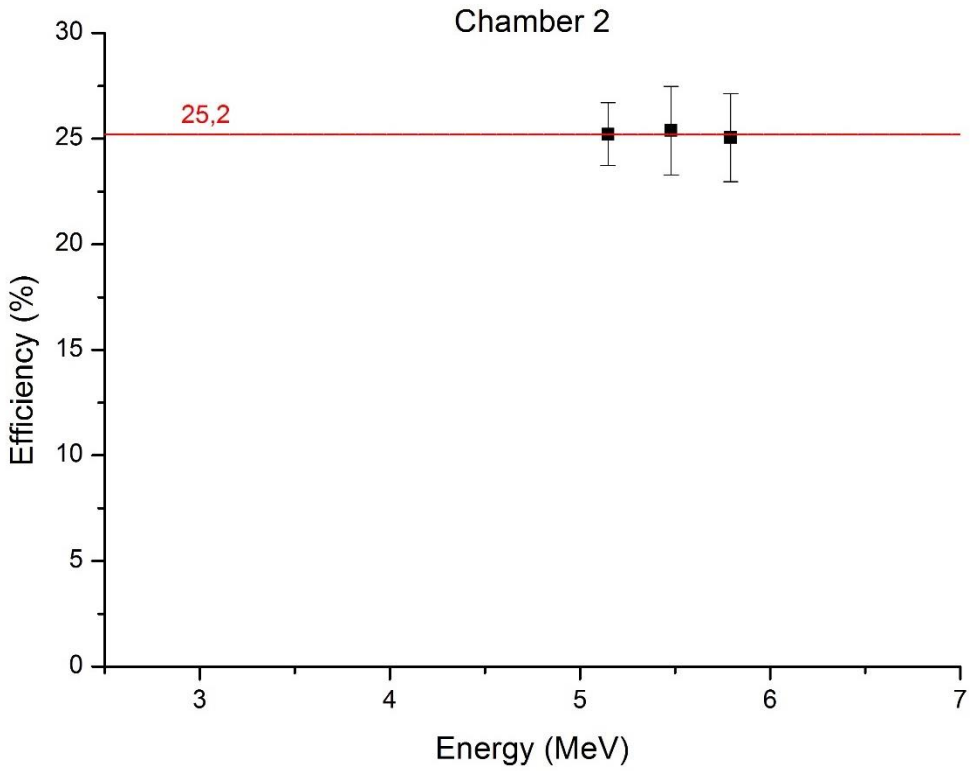

Figure 20: efficiency calibration for the chamber #2 of the alpha detector used

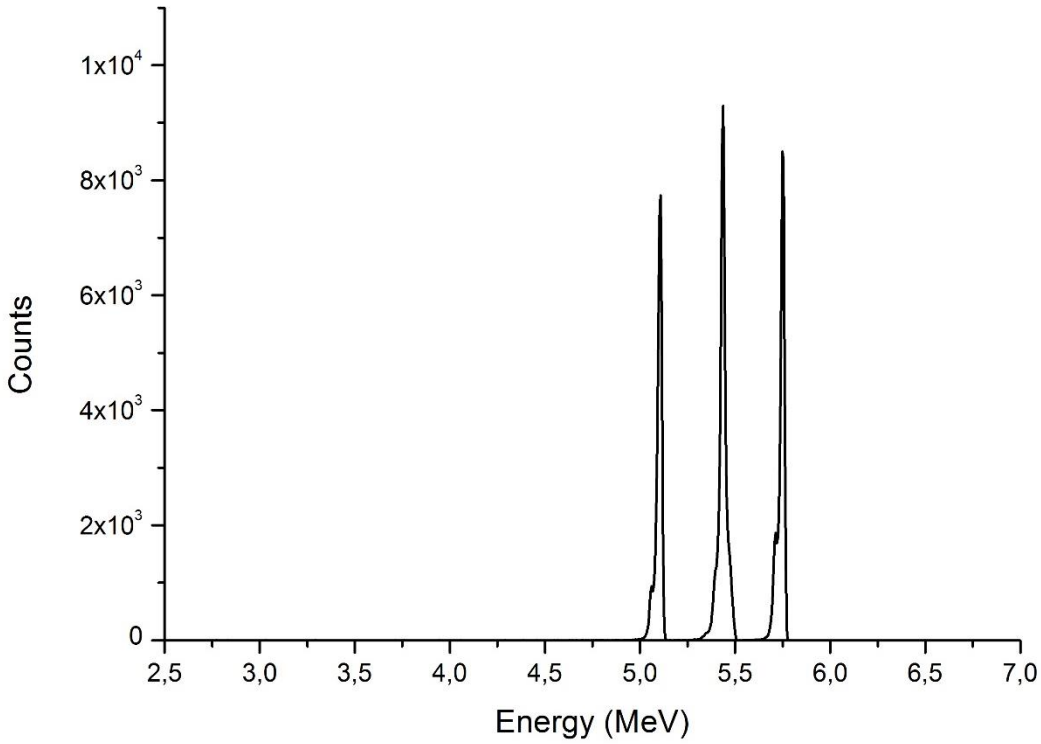

Figure 21: multi-alpha calibration source spectrum for chamber #1

1.5 Production of radionuclides

In the previous paragraph the natural radioactivity is presented. Nevertheless, the natural occurring radionuclides are limited to the natural decay chains daughters and few others (e.g. K-40 and C-14). For producing radionuclides artificially, nuclear reactions must be performed with collision of a projectile with a target nucleus. Any type of projectile could be used (e.g. n, γ, p, α, heavy ions). The interaction between the beam and the target lead to different reaction, depending on the nature and the energy of the beam.

Considering a target with area A (cm^2) and thickness x (cm) containing N atoms per unit volume and a uniform monodirectional particle beam of intensity I (particles/s), the interaction rate in the entire target is defined as follows:

$$Interaction\ rate = \sigma INAx \qquad (20)$$

Where σ is known as cross-section and it is usually measured in barns (b). One barn is equivalent to 1E-24 cm^2. The cross-section is thus a conventional area representing the target area seen by the particle beam as the probability of having the interaction projectile-target atoms. Rewriting equation (20):

$$\sigma = \frac{Interaction\ rate}{INAx} \qquad (21)$$

Since NAx is the total number of target atoms, it follows that σ is the interaction rate per unit of atom number in the target and per unit of intensity of the incident beam.

Nuclear reactions respect the conservation of charge, conservation of momentum and conservation of energy. The latter can be used to predict whether a reaction is energetically possible. Considering a nuclear reaction involving a radionuclide Y, a projectile pr is shot to a target X with the particle(s) ejected ej; it can be represented as X(pr,ej)Y or in alternative $\mathrm{X} + \mathrm{pr} \rightarrow \mathrm{ej} + \mathrm{Y}$. The energy before the reaction is given by the kinetic energy and the rest mass energy of X and pr, the energy after the reaction is given by the kinetic energy of the projectile and the rest mass energy of ej and Y. A balance of the energy at rest of the initial and final state of the reaction can be evaluated in the following equation:

$$E_X + E_{pr} + M_X c^2 + M_{pr} c^2 = E_{ej} + E_Y + M_{ej} c^2 + M_Y c^2 \qquad (22)$$

Rearranging the formula

$$(E_X + E_{pr}) - \left(E_{ej} + E_Y\right) = [\left(M_{ej} + M_Y\right) - \left(M_X + M_{pr}\right)]c^2 \qquad (23)$$

Where the differences of the total kinetic energies before and after the reaction is known as Q value. It represents the amount of energy available in the center of mass of the collision.

$$Q = [\left(M_{ej} + M_Y\right) - \left(M_X + M_{pr}\right)]c^2 \qquad (24)$$

From the Q-value, the threshold energy for a reaction to occur can be estimated from the following equation:

$$E_{th} = Q\left[\frac{(M_X + M_{pr})}{M_X}\right] \quad (25)$$

The combination of beam type, energy and target material opened up the access to a great deal of artificial nuclides.

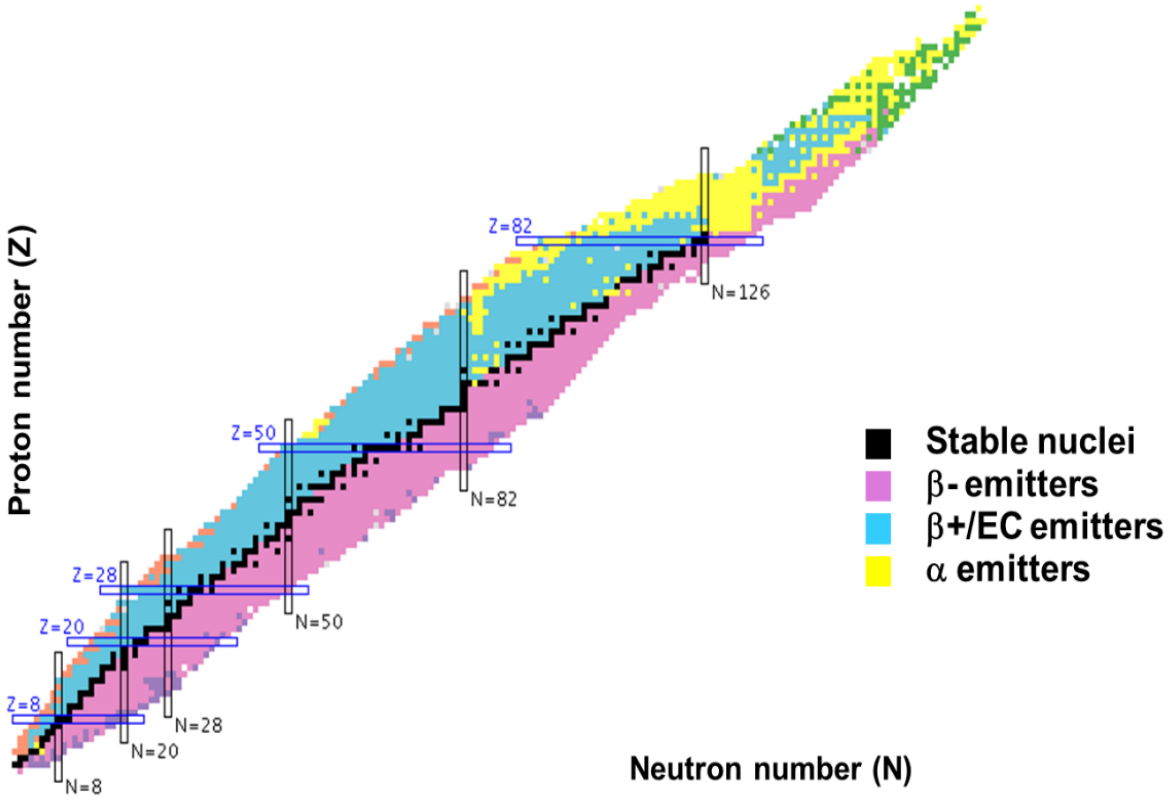

Figure 22: nuclides chart taken from Nucleonica. (26)

The most useful tool in radionuclides production is the radionuclides table (Figure 22), which allows a quick understanding of the possible production for a radionuclide. Usually, but not exclusively, the proton rich radionuclides for imaging (in blue) are produced in accelerators, while neutron rich radionuclides for therapy (in rose) are mostly produced in reactors. Those are the two main ways for producing nuclides in large scale. In Figure 23 is presented the scheme on how to read the nuclides table in Figure 22 considering the main nuclear reactions for radionuclides production. Considering a projectile incident of a stable target, when the projectile hit the nucleus another nucleus is formed for a brief time. After that particles are ejected. In Figure 22 one can predict what will be the produced nucleus for a given reaction.

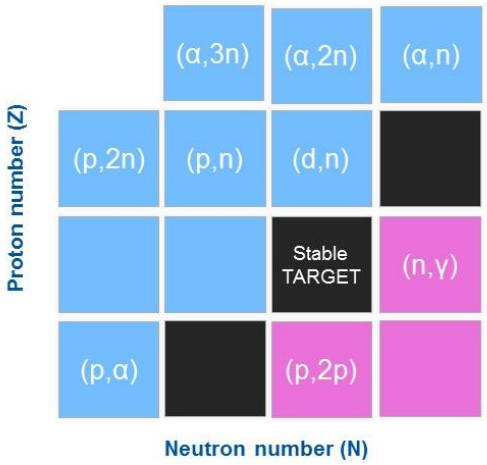

Figure 23: scheme of how-to-read the nuclides table considering some main nuclear reactions starting from a stable target. In the parenthesis the first letter is associated to the projectile, the second to the ejectile(s).

1.5.1 Radionuclides production in reactors

Reactor produced radionuclides represent a large percentage of the total production because of different factors. Reactors can offer simultaneous irradiation of several samples, large initial investment but economy of each production, possibility to produce a wide variety of neutron rich radioisotopes and in some cases better production efficiencies due to the large cross-section at thermal neutron energy (e.g. for Lu-176 is 2100 barn).

The first nuclear reactor in the world was the Chicago Pile-1 (CP-1). It was built in 1942 at the University of Chicago in the west basement of the American football stadium, under the supervision of Enrico Fermi, Italian physicist, and the collaboration of Leo Szilard (1898 - 1964). It was part of the Manhattan Project (1939 – 1946), program of research and development for the American nuclear bomb during World War II. The state of art of the technology at that time imposed to use natural uranium as fuel and graphite as moderator, indeed the pile of graphite block gave the name to the CP-1. From that moment on, several reactors were constructed in the world based on different technologies. Indeed, different technologies combining fuel materials (as natural or enriched uranium, thorium, etc.) with moderators (heavy water, graphite, etc.) and cooling fluids (CO_2, liquid metals, etc.) have been developed and tested along the years. In 2003 around 300 research reactors were operating of which around 70 dedicated to the production of radionuclides (27).

Research reactors designed for radionuclides production are quite different from power reactors developed for electricity production. Indeed, the constraints are different. As thermal power extraction is not needed and the neutron flux should be maximized, compact designs considering moderate water cooling pressures have been developed. In case of thermal reactors with uranium fuel, the neutron flux can be maximized with a higher U-235 enrichment level.

Indeed, natural uranium is composed by 99.3% of U-238 and only 0.7% of U-235, the latter being the fissile material needed. Fissile material is a material that can be induced to fission with thermal neutrons with a high probability; as in a fission reaction multiple neutron are emitted, this allows the sustaining of the chain reaction in a nuclear reactor. Power reactors use usually 3-5% enriched U-235 fuel, whereas research reactors usually between 20-93% enriched U-235. Furthermore, the loading and unloading of the target material inside the vessel of the reactor should be simplified. For producing the wanted radionuclides, the selected target material is sealed in primary ampoules to be irradiated, mostly made of quartz used in high-flux reactors. In pool-type reactors, the loading and unloading of targets can be performed from the top of the pool using simple devices. The ampoules are loaded in specially designed irradiation jigs and then positioned in predetermined locations in the core for irradiation. Most of the reactor produced radioisotopes, are produced through the neutron activation process. It consists in the (n,γ) reaction and it usually has a very high cross-section in thermal neutron region. However, along the years one of the main radionuclides produced in reactors was Mo-99, parent of Tc-99m used for SPECT applications, produced by thermal neutron induced fission of U-235. Indeed, Tc-99m-based diagnostic represent around 80% of all nuclear medicine procedures, corresponding to 30-40 million examinations worldwide every year. (28) Several nuclides produced in reactors are used for different applications. The main ones, suitable for medical uses, are summarized in the following table.

Table 3: list of main reactors produced medical radioisotopes ordered by increasing A.

Nuclide	Half-life (d)	Application
Mo-99	2.75	Tc-99m generator for SPECT
I-131	8.02	β^- therapy
Sm-153	1.93	β^- therapy
Ho-166	1.12	β^- therapy
Er-169	9.39	β^- therapy
Lu-177	6.65	β^- therapy
Re-186	3.72	β^- therapy
Th-227	18.7	Ra-223 generator for α-therapy

When a radionuclide is produced through the neutron capture of the target material, there are two different scenarios. The first include the irradiation of an isotope of the same element of the produced radionuclide (ex. Lu-176 target for Lu-177 production). The second method is the indirect way, which consist in producing the parent radionuclide (ex. Yb-176 target irradiation for producing Yb-177 that decays in Lu-177). In the first case, the produced radionuclide is an isotope

of the target element. Therefore, it cannot be isolated using chemistry from the target material, leading to a mixture of radioactive and stable isotopes. To characterize the product, one can refer to the specific activity. In the second case, as the radionuclide of interest and the target nuclides correspond to different elements, chemical separation is possible, leading to very pure product and consequently high specific activity.

In order to estimate the yield achievable for reactor produced radionuclides, knowing the irradiation parameters and the amount of target material irradiated, the equation (26) is given. It is valid assuming that other nuclear reactions are not significant, and the target is not destroyed during irradiation.

$$A = \phi * \sigma * \frac{N_A * m}{M} * (1 - e^{-\lambda t_{irr}}) \qquad (26)$$

Where:

- ϕ is the average thermal neutron flux in n/s/cm^2
- σ is the cross-section of neutron capture reaction for thermal neutron in b
- $\mathrm{N_A}$ is the Avogadro's number
- m is the mass of the irradiated target in g
- M is the molar mass in g/mol
- t_{irr} is the irradiation time in s
- λ is the radioactive constant of the measured isotope in s^{-1}

In nature some of the 80 known elements with stable isotopes have only a single stable isotope. The others have several stable isotopes with a specific percentage composition. Therefore, in most of those cases for obtaining the highest yield, enriched material has to be considered unless specific conditions are met. For example, the high difference in the cross-section of the reactions involved or important difference or the half-life of the produced radionuclides.

1.5.2 Radionuclides production in cyclotrons

The accelerator production of radioisotopes reached a key point with the construction of the first cyclotron.

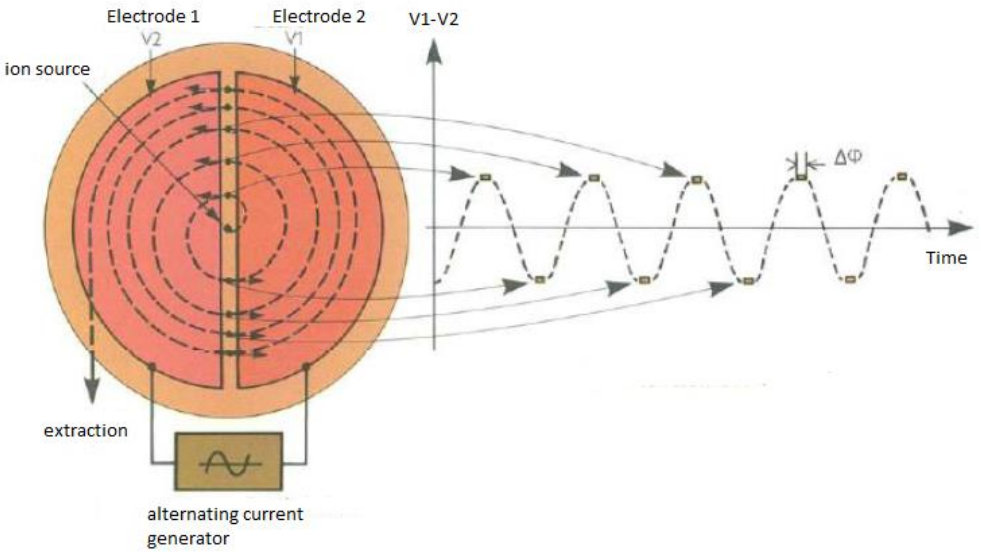

Figure 24: simplified cyclotron scheme

The principle of functioning of a cyclotron is quite simple (Figure 24). An alternating potential difference is applied to two separated cavities, the so-called 'dees' from their original D-shape, positioned in a vacuum chamber. Charged particles are injected in the center of the cyclotron from an ion source. If the particles are charged negatively, they are attracted and accelerated toward the positive cavity. Then after an half period,T/2, the polarity is changed, and the particles are attracted to the other cavity. In each Dee there is a magnetic field perpendicular to the axial plane which causes the charge to follow a half-circle. The polarity change in the Dees causes the acceleration of the particle. At each half period, the particle receives a kick and is accelerated, thus the particle moves along a spiral path of increasing radius. When it comes near the edge, it is taken out using either a deflector plate or a stripper foil depending on the charged of the particle. In particular, the frequency of the applied voltage must match the particle's cyclotron resonance frequency as shown in equation (27): where B is the magnetic field strength, q is the electric charge of the ion and m is the relativistic mass of the charged particle.

$$\frac{1}{T} = \nu_c = \nu_a = \frac{qB}{2\pi m} \qquad (27)$$

Thanks to the high energy charged particles and the high beam current available in cyclotrons, it is possible to produce important quantities of a wide range of radionuclides, in particular proton rich nuclides. A large number of new cyclotrons have been installed for isotope production in the last decade. Some low energy cyclotrons are dedicated to the production of a single isotope such as F-18, other cyclotrons are more dedicated to the research on innovative radionuclides. The actual total installations worldwide are around 1200, of which about 250 cyclotrons are in Europe. Depending on the energy and the type of accelerated particles in the cyclotron, as well as the

suitable target material, specific radionuclides are producible. A list of radionuclides produced in cyclotron is given in Table 4.

Table 4: list cyclotron produced radionuclides for application and cyclotron energy range

Radionuclide	***Half-life***	***Cyclotron***	***Reaction***	***Application***
F-18	*1.83 h*	*≤ 18 MeV*	*O18(p,n)F18*	*PET*
Sc-44	*3.97 h*	*≤ 18 MeV*	*Ca44(p,n)Sc44*	*PET/ β+γ*
Cu-64	*12.7 h*	*≤ 18 MeV*	*Ni64(p,n)Cu64*	*PET/β-therapy*
Ga-68	*1.13 h*	*≤ 18 MeV*	*Zn68(p,n)Ga68*	*PET*
Sr-82	*25.3 d*	*≤ 70 MeV*	*natRb(p,x)Sr82*	*PET*
Tc-99m	*6 h*	*≤ 30 MeV*	*Mo100(p,2n)Tc99m*	*SPECT*
In-111	*2.8 d*	*≤ 18 MeV*	*Cd111(p,n)In111*	*SPECT*
Tl-201	*3 d*	*≤ 30 MeV*	*Tl203(p,3n)Pb201*	*SPECT*
At-211	*7.2 h*	*≤ 30 MeV*	*Bi209(α,2n)At211*	*α-therapy*
Ac-225	*10 h*	*> 70 MeV*	*natTh(p,x)Ac225*	*α-therapy*

Usually thick targets are irradiated in cyclotrons. This implies an important beam particle energy loss in the target which cannot be neglected and is, eventually, challenging for the cooling system. For estimating the radionuclides production in a cyclotron, the equation (28) is given:

$$A = \phi * \frac{X * N_A * \rho}{M} * \left(1 - e^{-\lambda t_{irr}}\right) * \int_{E_{OUT}}^{E_{IN}} \frac{\sigma(E)}{\frac{dE}{dx}} dE \qquad (28)$$

Where:

- ϕ is the current of the accelerated beam in particles/s
- X is the enrichment of the material
- N_A is the Avogadro's number
- ρ is the density of the target in g/cm^3
- λ is the radioactive constant of the measured isotope in s^{-1}
- $\sigma(E)$ is the cross-section of the considered reaction in cm^2
- E_{IN} is the incident beam energy in the target in MeV
- E_{OUT} is the exit beam energy from the target in MeV
- $\frac{dE}{dx}$ is the stopping power of the particle beam in the target

1.5.2.1 GIP ARRONAX

GIP (Group of Public Interest) ARRONAX is a public entity with private accounting aimed at the production of innovative radionuclides and radiopharmaceuticals for research and clinic. ARRONAX stands for Accelerator for the Research in Radiochemistry and in Oncology in Nantes Atlantique X. The last X was put on purpose. Indeed, its positioning at the end allow composing ARRONAX being a tribute to Jules Verne, French writer born in Nantes (France). ARRONAX is the

name of the fictitious marine biologist main character of his novel Twenty Thousand Leagues Under the Sea (1870). The facility, situated near Nantes, hosts an IBA C70 cyclotron (Figure 25). Its main characteristics are the possible acceleration of several different particles at middle- high energies and high currents. In

Table 5 are resumed ARRONAX cyclotron characteristics.

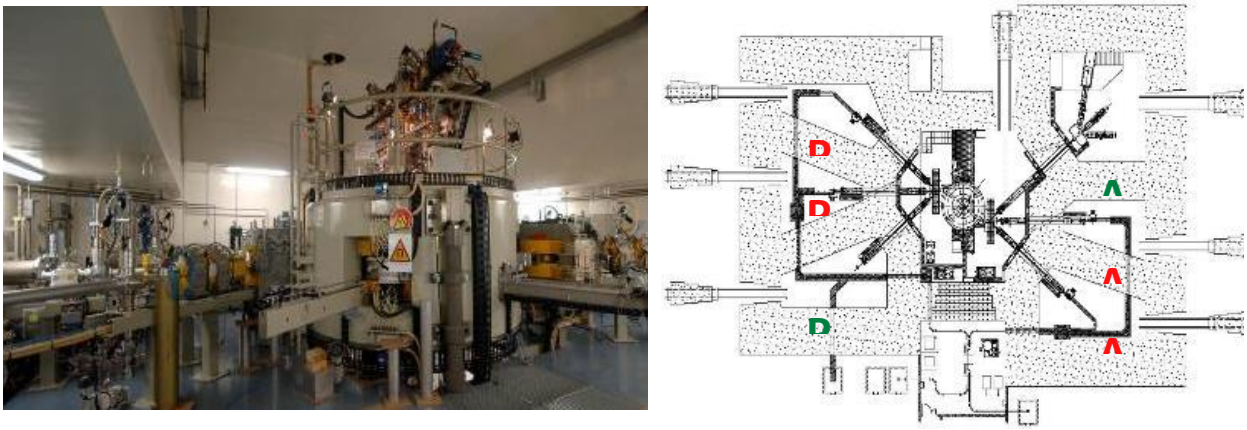

Figure 25: on the left, the C70 cyclotron in his bunker is shown whereas on the right, it is the layout of ARRONAX cyclotron

Table 5: characteristics of ARRONAX cyclotron

Beam	***Accelerated particles***	***Energy range (MeV)***	***Intensity (eμA)***	***Dual beam***
Proton	*H-*	*30-70*	*<375*	*Yes*
	HH+	*17*	*<50*	*No*
Deuteron	*D-*	*15-35*	*<50*	*Yes*
Alpha	*He++*	*68*	*<70*	*No*

ARRONAX can deliver beams in six different bunkers. Four vaults are dedicated to radionuclide production and equipped with an irradiation station connected to the hot cells via an automatized rabbit system (P2, P3, A1, A2). One vault contains a neutron activator installed in collaboration with AAA within the TheraneaM project. The last one, namely the AX vault, is used for basic research in radiolysis, radiobiology and physics. This vault hosts three beam lines, namely AX1, AX2, AX3, where beams can be provided up to 1μA (29). Regarding the presented stacked foils measurements for cross-section evaluations, the beam line considered will always be AX3. The main nuclides produced in ARRONAX on a regular basis for commercial purpose or research are Sr-82, Cu-64, At-211 and Sc-44. The group is also active in the research of innovative isotopes production. One example is described in this work consisting in the use of mass separation technology after the production in cyclotron to access those radionuclides which are not available

at enough purity for clinical use. This is due to the isotopic contamination which leads to low purity products, as for example the co-presence of Sc-46 for Sc-47 production from titanium targets.

1.5.3 Electromagnetic isotope separation

The mass separation technique consists in the use of an electromagnetic field to differentiate the trajectory of ions with different atomic mass. To achieve that, several steps are necessary. The first consists in the vaporization of a material to get a gas which is ionized to be slightly accelerated. This allows conveying the ions to an electromagnetic field where the separation happens. Finally, the ions having same mass over Z ratio can be collected after the exit from the magnetic field. The scheme of principle is presented in Figure 26, however the components are not in scale.

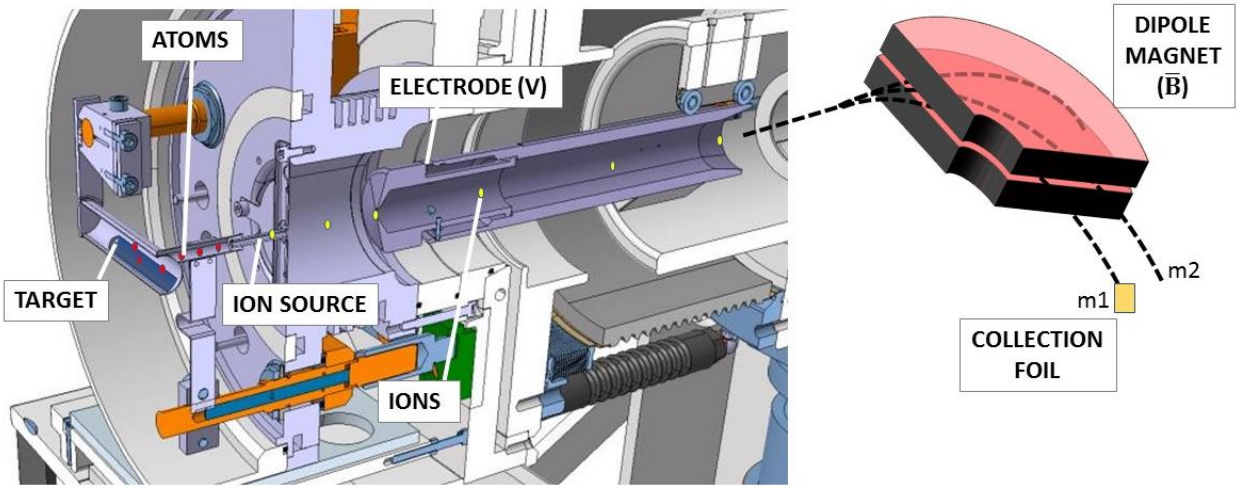

Figure 26: scheme of mass separation technology. The components are not in scale.

The ions having mass m and velocity v carrying a charge q acquire a kinetic energy equal to qV, it can be described by the equation (29):

$$qV = \frac{1}{2}mv^2 \qquad (29)$$

Applying a magnetic field B and an electric field E, the behavior of charged particles in an electromagnetic field is governed by Lorentz equation:

$$\bar{F} = q\bar{E} + q\bar{v}x\bar{B} \qquad (30)$$

Equation (29) shows that a charged particle immersed in a magnetic field is subjected to a force perpendicular to the vector of the magnetic field and its velocity vector. This results in a rotational motion around the magnetic field lines. Considering the physical magnitudes, equating the magnetic force to the centrifugal force one can obtain:

$$qvB = \frac{mv^2}{r} \quad (31)$$

$$r = \frac{mv}{Bq} = \frac{m}{Bq} * \sqrt{\left(\frac{2qV}{m}\right)} = \frac{\sqrt{2qVm}}{Bq} \quad (32)$$

Where r is the radius of the particle followed in its rotation. Considering two different nuclides with masses m1 and m2, their radius will be r1 and r2. If they have the same charge and velocity, the ratio of the different radius is proportional to the square root of the ratio of the masses of the ions.

$$\frac{r1}{r2} = \sqrt{\frac{m1}{m2}} \quad (33)$$

This shows that ions having different masses are following different radius in given electromagnetic fields. For this reason, optimizing the magnet shape, dimensions, bending radius and magnetic field intensity, as well as distance of the collection point, it is possible to separate ions with a specific mass.

The principle of the considered mass separation is to use a dipole magnet and to collect a specific mass while damping the others in the dipole zone. Depending on the characteristic of the magnet, as e.g. its bending angle, it is possible to define a very important quantity for the comparison of different installations, the mass resolving power R. It is the ratio $R = \frac{m}{\Delta m}$ which can be assumed constant over a wide range of masses.

The dipole separates the ions coming from the ionizer. Different ionization modes can be used: surface ion sources, electron bombardment, plasma discharge, radiofrequency discharge, laser ion sources. In this thesis only two types will be considered, surface ion sources and lasers ion sources.

1.5.3.1 Surface ionization

Surface ionization is a relatively simple technique for ionizing elements with low ionization potential, up to 7 eV, such as lanthanides and few other elements. Depending on the chosen ionizer material, it can positively ionize or negatively ionize. In this work only the positive ionization is discussed. It is based on the loss of one electron from one atom following a collision with a hot metal surface. In Figure 27 the scheme of the surface ionization method is presented. The material of the ion source should be accurately selected according to its work function Φ which should be the highest possible. The most often used materials are tantalum, tungsten, molybdenum and rhenium. For predicting the ionization of a surface ion source, the Saha-Langmuir equation is used (30):

$$\frac{n_+}{n_0} = \left(\frac{g_+}{g_0}\right) exp\left(\frac{(\phi - W)}{kT}\right) \quad (34)$$

Where:

- n_+ Is the ions flux exiting the surface in 1/cm2
- n_0 Is the neutrals flux exiting the surface in 1/cm2
- $g_+$and g_0 are statistical weights for the ionic and atomic ground states respectively
- ϕ is the work function in eV
- W is the ionization potential in eV
- k is the Boltzmann's constant (8.617E−5 eV/K)
- T is the operating temperature in K

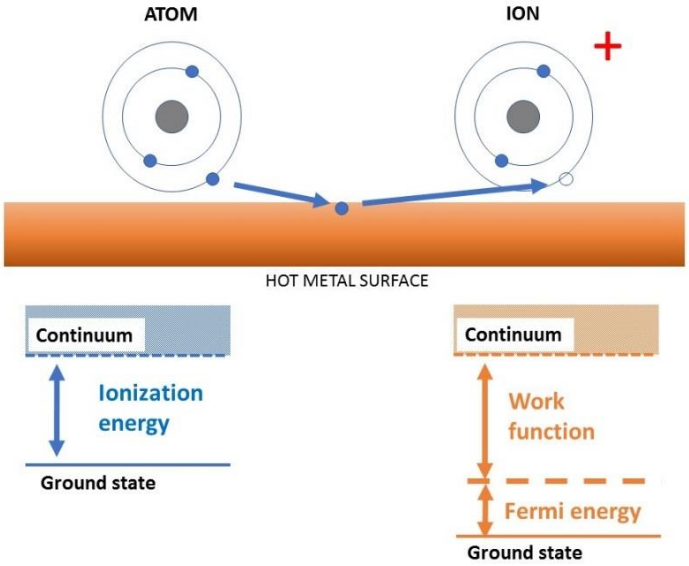

Figure 27: surface ionization scheme reproduced from (31)

The work function is the distance from the Fermi level to the continuum. In general, the first ionization energy increases as we go from left to right across a row and decreases as we go down in a column of the periodic table.

The efficiency of the surface ionization $\varepsilon_{s,i}$ is given by:

$$\varepsilon_{s,i} = \frac{n_+}{n_+ + n_0} = \frac{1}{1 + \frac{1}{\left(\frac{g_+}{g_0}\right) exp\left(\frac{\phi - W}{kT}\right)}} \qquad (35)$$

In a hot cavity, the efficiency could reach very high values if the inner diameter is small compared to the internal surface. The ionization efficiency of a hot cavity can be described by combining two different factors. The factor ω is the probability that an atom entering in the ion source leaves the latter as an ion; k is the average number of atom collisions on the wall before escaping through the exit. This is considered in the following equation:

$$\varepsilon_{ion} = \frac{\varepsilon_{s,i}\omega k}{1 - \varepsilon_{s,i}(1 - \omega k)} \qquad (36)$$

The factor ωk strongly depends on the geometry and the properties of the material at the working temperature. It can be determined experimentally testing several known samples. For the factor k, it has been found for similar geometries that a theoretical value of 33 coming from the ratio of the inner surface to the cross-section area of the hot-cavity was overestimating the experimental values (32). Calculating k for the considered ISOLDE/MEDICIS geometry, as the ionizer internal surface area (331 mm^2) divided by the orifice aperture (diameter 3.1 mm), gives around 44. Another work based on ISOLDE ionizers, claim that the probability ω is between 0.1 and 0.5, giving a range of ωk between 4 and 20 (33).

Furthermore, at working temperatures between 2150 and 2200 (°C) in literature can be found different ranges of work function values for each material. Hereafter are considered 4.3 eV for tantalum, 4.5 eV for tungsten and 5 eV for rhenium (34) (35). The first two materials are currently the most used, mainly because the manufacturing and handling are easier than in the case of rhenium. The statistical weights for the ionic (g_+) and atomic (g_0) states have been calculated from NIST database (36) from the atomic and ionic ground state as 2J+1. From NIST database are taken the ionization potential for each element too.

An example of efficiency values considering a mid-value of ωk=10 are given in Table 6 for some elements discussed later in this work.

Table 6: theoretical surface ionization efficiency (%) considering different ionizer materials. The calculated efficiencies refer to the ionization of terbium, gadolinium, erbium, scandium and titanium.

	Tb	**Gd**	**Er**	**Sc**	**Ti**
W	1,34	0,40	0,41	0,03	0,01
Ta	0,51	0,16	0,15	0,01	0,002
Re	13,50	4,53	4,37	0,37	0,10

As shown in Table 6, even though they could be considered the maximum theoretical efficiencies, they are quite low. Nevertheless, those values must be experimentally verified, as dependent on many factors. In particular, different values of the considered ionizer work function and the factor ωk could strongly affect the efficiency obtained.

The overall off-line mass separation efficiency ε depends on the type of the experiment. In the case of the off-line mass separation, after irradiating a starting material in a cyclotron or a nuclear reactor, the target is dissolved with acid and evaporated in order to deposit the mixture of radionuclides on a support. After that, the support is inserted into the target unit for the mass separation. Therefore, the overall efficiency of mass separation is given by:

$$\varepsilon = \varepsilon_{rel} \cdot \varepsilon_{ion} \cdot \varepsilon_{sep} \cdot \varepsilon_{tr} \qquad (37)$$

Where:

- ε_{rel} is the release efficiency of an atom from the target material to the ion source
- ε_{ion} is the ionization efficiency
- ε_{sep} is the mass separation efficiency
- ε_{tr} is the transport efficiency of the ions from the ionizer to the collection point

ε_{sep} and ε_{tr} are usually close to 100% not influencing the overall efficiency. As the target material consists in a mixture of radionuclides deposited as salt on a high melting point temperature support material, the ε_{rel} is usually very high. Indeed, when heating the target container to temperatures around 2000 (°C) an important mass of the target is evaporated.

1.5.3.2 CERN-MEDICIS facility

Since the first experiment in ISOLDE facility at CERN dating back 1967, researchers started to develop unique competences on on-line radionuclides production through the mass separation technique. Nowadays the facility is aimed at producing radionuclides for a wide range of studies in fundamental and applied physics. The proton synchrotron booster at CERN, which will be soon upgraded to 2 GeV, until December 2018 provided a 1.4 GeV proton beam to ISOLDE. During ISOLDE target unit irradiations up to 50% of the total CERN proton beam is used. Within the ISOLDE program, radionuclides for medical applications corresponds to a small part of the available beam time. These radionuclides are thus not available all the time, slowing down the potential use of them. In order to dedicate an entire facility to the production of radionuclides for medical use, a spin-off of ISOLDE has been completed at CERN: MEDICIS (Figure 28). MEDICIS, is using parasitically almost 85% of the total incident beam on the ISOLDE target which does not interact and goes through the target. This is done by the positioning of MEDICIS target downstream of the ISOLDE one (Figure 28) and the set-up of a new off line mass separator (37). The aim of MEDICIS is to produce batches of innovative radionuclides for new imaging and therapy protocols in cell and animal models. Unique sets of radionuclides as terbium and scandium can be produced with high specific activity and high purity. The produced radionuclides will be collected on metallic foils positioned into a new collection chamber and prepared for shipment in the chemical laboratory being build inside the facility. The collected batches will be sent without additional costs to hospitals and research centers for in-vitro and in-vivo studies. A fully automated area not accessible during MEDICIS operations comprises the mass separator bunker, the robot and the target station for moving targets (37).

After the irradiation, the target will move on a railway system to a station for a fully automated transfer to storage, to the off-line mass separator or in position for the chemical treatment pre-disposal.

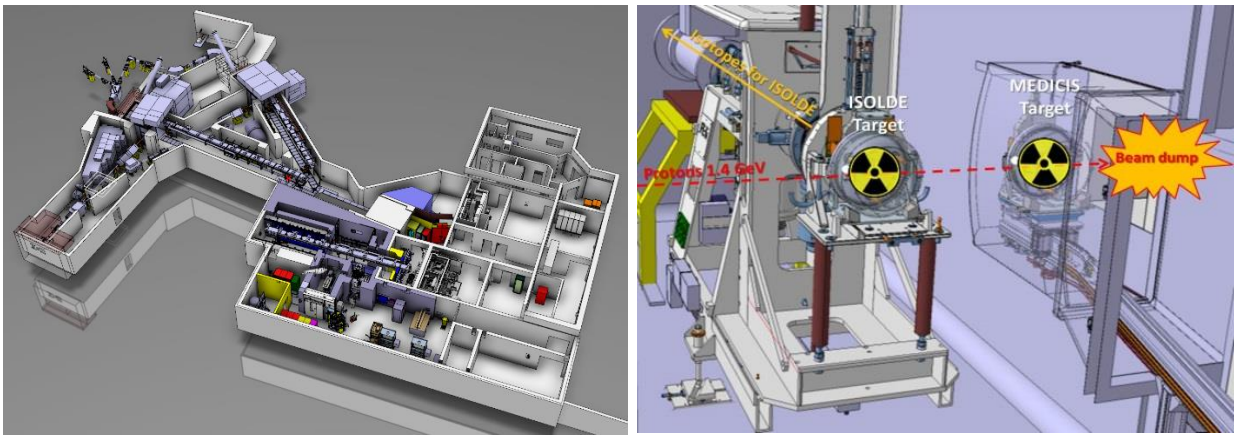

Figure 28: on the left outlook of the CERN-MEDICIS facility; on the right MEDICIS target positioning related to the ISOLDE one.

The first demonstration run of the facility was performed in December 2017 with the irradiation of a tantalum target and the production of 200 Bq of Tb-155. The first proof of concept demonstration was the production of Er-169 in May 2018. It consisted in the mass separation of an external erbium source irradiated at the ILL nuclear reactor (Grenoble, France), which will be discussed in detail in chapter 6.

1.5.3.3 MEDICIS target

The target units used for MEDICIS irradiations are the same as the ones used in ISOLDE for the starting phase. Nevertheless, the proton beam passing through the ISOLDE target is diverging. As no ion optical component can be installed between the two targets to focus the beam, MEDICIS target is not receiving the entirety of the beam. For this reason, a new design of the target has been developed. The main feature is the four times bigger target container which allows a bigger target surface catching the total beam. The target unit is composed by a target container with the target material rolled foils inside, an ion source, eventual gas leak, mass markers and electrical connections depending on the specific experiment. The target material depends on the desired radionuclides, it could be rolled tantalum foils for the production of terbium isotopes, rolled titanium foils for the production of scandium isotopes, uranium or thorium carbides for the production of high Z isotopes.

Some components of the target are manufactured at CERN in the ISOLDE/MEDICIS workshop and the others are purchased from external contractors. They are assembled in the so-called clean room. Indeed, it is important to work in a clean environment not to contaminate the target (e.g. with Ca, La, etc.). The components are assembled on the predefined ISOLDE target unit aluminum base (Figure 29). Every component is cleaned with acid, then washed with demineralized water, and finally cleaned with ultrasonic bath immersed in ethanol. When

extracted from the alcoholic bath they are blown with argon jet and then installed in the target unit.

Figure 29: ISOLDE/MEDICIS target unit assembling. On the left the predefined base; in the middle tantalum components; on the right the target container and surface ion source.

Once the target assembled, its temperature behavior is calibrated. The target container and the line are gradually heated, and their temperatures are taken using a pyrometer. The temperature calibration is fundamental to know the operating temperature during the mass separation run. It is monitored by the current flowing through the target container and the ion source, with two separated circuits. Next step is to test the target in this offline laboratory Offline1. In the laboratory there is an offline mass separator used for evaluating the efficiencies of the ion sources and confirming the absence of contamination. Is it also a way to test the correct target assembling, in order to avoid unexpected failures once it is mounted online for the irradiation or mass separation, such as the vacuum test and the separation test.

1.5.3.4 MEDICIS working mode

The tested targets are brought to MEDICIS and positioned at the loading point. The robot moves the target on the target station, where it can be sent to the irradiation position, in the back of the HRS ISOLDE target. The irradiations are planned in accordance with ISOLDE schedule. After the irradiation the target is moved back from the irradiation point to the target station. From there the robot can transfer the target to the decay position or to the mass separator front end. This

mass separator consists in two main parts: the front end (FE) and the mass separator (MS). The FE is the area where the target is positioned and linked to the extraction line. The MS consists in the magnet and the collection spot. FE and MS are connected through a Faraday cup chamber and a valve. The MEDICIS magnet is coming from the Leuven Isotope Separator On Line facility coupled to the CYCLONE 110 cyclotron at Louvain-la-Neuve. It was built to produce and study short-lived radioactive isotopes for fundamental research in nuclear physics starting in 1975 and was shut down in 2014. The characteristic of MEDICIS magnet (Figure 30) are shown in the following table:

Table 7: characteristics of MEDICIS mass separator magnet

	MEDICIS magnet characteristics
Mass resolving power	1500
Bending angle	55°
Power consumption	130 kVA
Power supply	250 A / 35 V
Exit ports	3 ports: +45°; 0°; -30°

Figure 30: magnet of the MEDICIS mass separator in its dedicated bunker. Only the exit line at 0° is used.

As reported in Table 7 MEDICIS separator could potentially have three collection points, However, only the central one (0°) is used, as only one extraction line is installed.

Once the target installed on the FE, the valve FE/SEP is opened and the vacuum pump is started. Working pressures are around 10^{-7} - 10^{-6} mbar. Once the vacuum is achieved, the cooling system is activated, and the line is gradually heated to the nominal value, whereas the target is gradually heated below the release temperature of the wanted radionuclide. When the temperatures are reached, the mass separator is calibrated to set the magnet to the current corresponding to the selected mass and to optimize the beam profile. The calibration consists in optimizing all the optical components, as Einzel lens and deflectors, the extraction electrode and slit position. This is performed with a known mass close to the one of interest and allows having the best beam profile of the selected mass. Once the setup is ready, the target is then ramped up to the nominal value that depends on the target material, and it is kept there until the end of the run. The current of the ion beam collected on the collection foil have a peak when reaching the maximum temperature. At that moment, indeed the release of the atoms shall be at maximum. Then the release of the atoms at constant temperature decreases exponentially with time. When the required activity has been collected, the foils are removed from the collection chamber and prepared for the shipment to research centers. When the chemical laboratory will be operational, foils will be chemically treated in MEDICIS and the extracted radionuclides will be shipped to collaboration partners and hospitals.

After the first commissioning phase, MEDICIS is ramping up to the nominal working mode. The second phase starting from beginning of 2019 involves the installation of a chemical laboratory for the chemistry of the irradiated target. Furthermore, it involves a new laser installation for the laser ionization, upgrading the already existent surface ionization system.

1.5.3.5 Laser ionization

A LASER (Light Amplification by Stimulated Emission of Radiation) is a device which produces electromagnetic waves by stimulated emission. The atoms that are present in the lasing medium are excited by an external energy source. Optical amplification is achieved by the resonance of these atoms. Through an arrangement of mirrors in a laser resonator, a powerful amplified beam of light is generated. The laser light is coherent as each photon emitted has the same phase as the initial photon who induced the emission, the phase is maintained in time and space; it is characterized by a single wavelength, a single-color light that is known as monochromaticity; it emits the radiation in one direction; in this way a high intensity beam of well-defined wavelength is generated. As the potential applications of lasers are numerous, several different types of laser have been developed. Grouping the types of lasers depending on the lasing medium, there are six categories: solid-state lasers, liquid state lasers, gaseous state lasers, chemical laser, free electron laser and semiconductor laser.

In order to generate a laser beam, in general three components are required: a gain or amplifying medium, a pumping system and an optical resonance cavity. The gain or amplifying

medium is the active medium (gaseous, crystal or liquid) which emits the laser light. On this medium is depending the wavelength of the emitted radiation. The pumping system provides the energy to the active medium inducing pumping into an excited state (e.g. Penning effect, electric discharge, resonant energy transfer). The optical cavity, or resonator typically consists of mirrors between which a coherent beam of light travels in both directions, reflecting back on itself so that an average photon will pass through the gain medium repeatedly before it is emitted from the exit aperture if it is not lost to diffraction or absorption. A frequency doubling, or second harmonic generation, can be obtained when photons are interacting with a non-linear medium. Two incident photons of frequency ω could generate a photon with frequency 2ω and corresponding to half wavelength.

As solid state lasers Titanium-doped sapphire crystal (Ti^{3+}:Al_2O_3) based lasers (Ti:Sa) are widely used. Indeed, it is a prominent active laser medium which allows the construction of tunable solid-state lasers with extremely large tuning range. As the liquid lasers the dye lasers are the most used. They use organic dyes dissolved in liquid solvent as gain medium.

Lasers are used for a wide range of applications. Within medical applications they can be used in biology, which is a subject not discussed in this work, and for isotopes separation. The interest in separating isotopes comes from World War II, when the need of nuclear fuel for nuclear power plants and the request to construct the nuclear weapons was demanding enriched fissile uranium U-235. Nevertheless, with the invention of lasers, around the 1970 techniques as AVLIS (Atomic Vapor Laser Isotope Separation) and MLIS (Molecular Laser Isotope Separation) were developed. They were based on selective multistep photoionization in an atomic or molecular vapor stream. (38) More recently the Magnetically Activated and Guided Isotope Separation (MAGIS) technique was proposed. (39) Its principle is to use optical pumping by lasers to change the internal state of the atoms and their response to a magnetic field.

In addition to conventional ion sources, laser ionization can provide a complementary method for improving both the selectivity and the overall ionization efficiency. The principle is based on the interaction of the resonant absorption of laser beam photons by the outermost electron of the atom. If the absorbed energy is greater than its binding energy, the electron will be ejected and the atom will be in an ionization state. The ionization potential is the energy necessary to free the less bounded electron in an atom. To give this amount of energy to an electron it may require one to several excitation steps (

Figure 31). The different excitation levels for each element allow the selective ionization of an element, contrarily to the properties of the conventional ionization techniques.

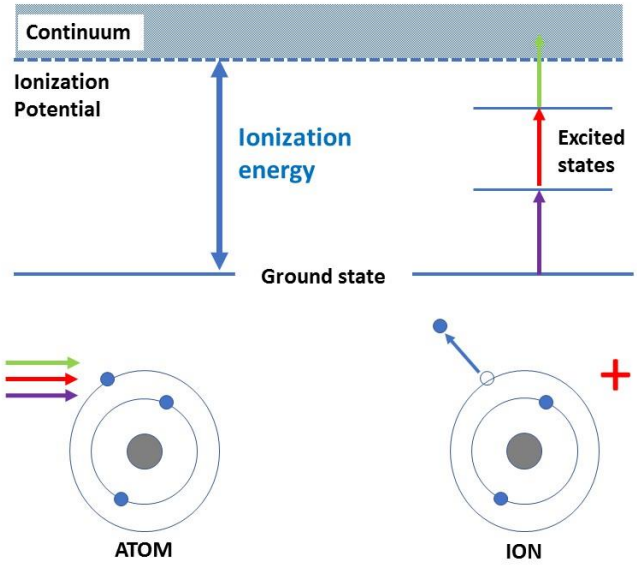

Figure 31: laser ionization scheme reproduced from (31)

With laser ionization technique, it is possible to ionize elements or compound with a ionization potential up to 10 eV and even higher, well above the surface ionization which is up to 7 eV. The laser beams are sent to the center of a hot cavity. The surface ionizer discussed before can be used as atomizer cavity (31).

Three possible laser ionization modes are possible:

- Resonant ionization via autoionizing states: the autoionizing state is an electron configuration located above the ionization potential. It is thus situated in the continuum, being formed by a two-electron excitation (Figure 31).
- Non-resonant ionization: the transition to the continuum is provided by non-resonant photon absorption from a laser wavelength corresponding to a photon energy exceeding the difference between the ionization potential and the upper state energy of the excitation scheme.
- Ionization via Rydberg states: a Rydberg state is an excitation level below but close to the ionization potential. When an atom is in a Rydberg level, it can easily be ionized by collisions with other atoms or by applying an electric field.

In this work resonant laser ionization schemes and their efficiencies were studied at JGU Mainz with LARISSA group within MEDICIS-PROMED collaboration, with the goal of transferring this technique to CERN-MEDICIS. The experiments were performed with the RISIKO (Resonance ionization spectroscopy in collinear geometry) mass separation installation. As shown in Figure *32* the atoms are vaporized in a hot cavity where laser beams are sent in the opposite direction, in

which the ions are extracted. Then they are accelerated to 30 kV by an extraction electrode and after beam-shaping the ions enter into the magnet. There the species with different mass are spatially separated and detected via a Faraday cup after a slit aperture that transmit only a selected mass range, Δm.

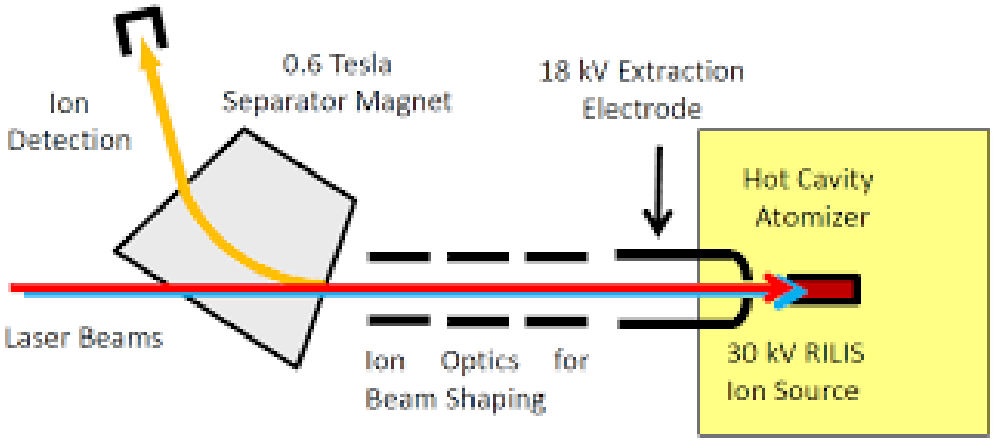

Figure 32: layout of RISIKO mass separator at JGU Mainz. *(40)*

At JGU Mainz in the LARISSA group, two different mass spectrometers are available: RISIKO and MABU. The separator used for the present analysis is RISIKO, which has a higher mass resolution compared to the compact system MABU (R=1000 and R=200 respectively), and only slightly lower than the CERN-MEDICIS mass resolution. The separator is actually almost identical to the one recently installed at CERN-MEDICIS. The separator operates at vacuum pressures in the 10E-7 mbar region. It uses a similar ion source frontend and initial beam-shaping ion optic geometry to the CERN-MEDICIS separator. The laser beam enters the vacuum vessel through a window on the magnet (Figure 33) and is focused into the entrance of the ionizer tube.

The ion source chosen is a tantalum surface ion source, because of its high melting point and good machinability. It has an inner diameter of 2.5 mm and a length of 35 mm. The tool for holding the sample is the so-called mass marker. It is a tantalum capillary tube which is inserted at the rear entrance of the ion source in order to have the best release possible without diffusion losses. Inside the mass marker the sample is inserted as a rolled thin metallic foil. On this foil it has been previously deposited and dried the liquid standard solution of the wanted element. Once the mass separator frontend is prepared, and a sufficient vacuum is reached, the experiment can be performed. The ion source is ramped up to 280 A (about 2000 °C) and the mass marker is gradually heated up to 100 A (about 2000 °C). The aim is to let the solution evaporate, diffuse in the ion source where the laser beams ionize the atoms of the wanted radionuclides.

In Figure 34 is shown the layout of the front end. Each part has been aligned with a telescope positioned after the magnet window. Particular attention has been given to the alignment in

order to have the laser beams as accurate as possible into the center of the ion source for optimizing the overall extraction efficiency.

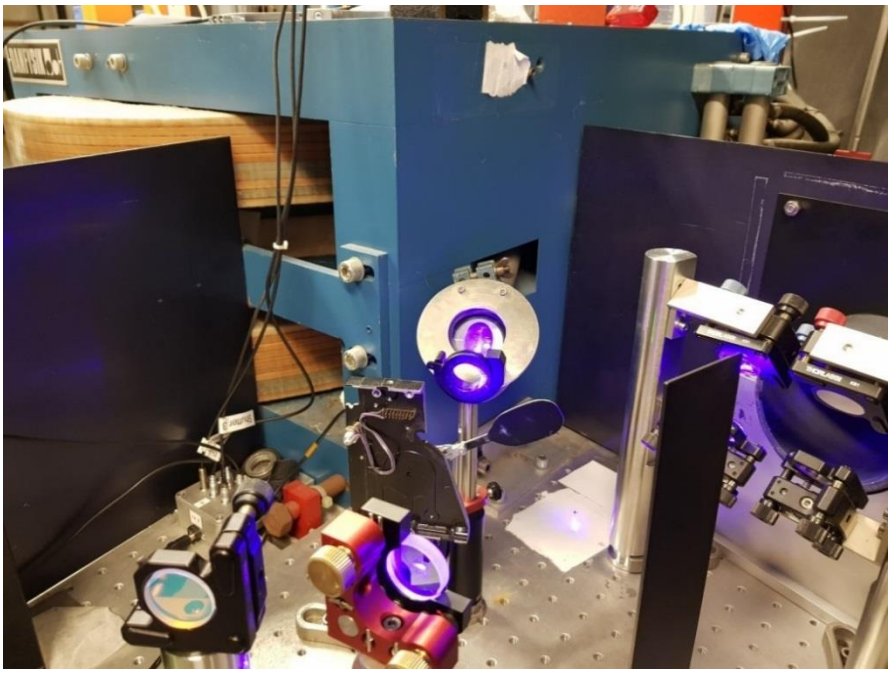

Figure 33: magnet window for the laser entrance in the mass separator

Figure 34: view of the experimental setup with the opened front end of the RISIKO mass separator

On the RISIKO laser table three Ti:Sa (titanium:sapphire) lasers have been installed in the three cavities (Figure 35). Mirrors and lenses have been placed on the table to focus and to direct the laser beams to the magnet window.

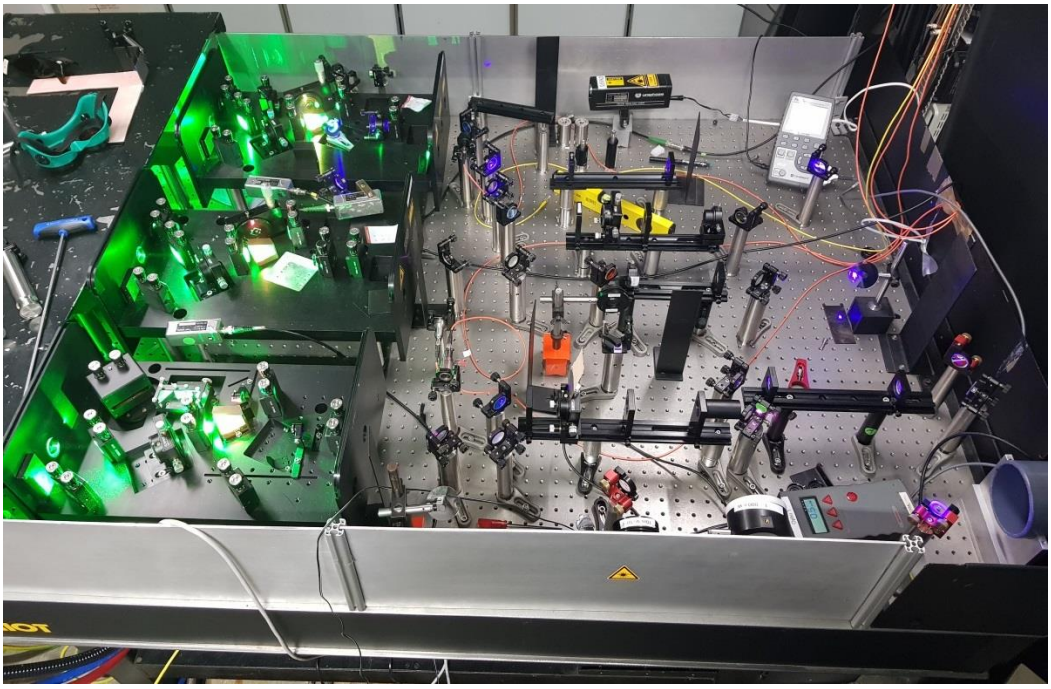

Figure 35: laser setup, view of the RISIKO laser table. On the left with green shade there are the three cavities

Laser beams are optimized regarding wavelength, intensity, timing and direction, tuned depending on the isotopes of interest. Several experiments were performed to study lanthanides' laser ionization schemes and their efficiencies, in particular for terbium and erbium as illustrated in dedicated chapters.

A similar new laser installation will be available at CERN-MEDICIS starting from 2019, allowing the laser ionization and potentially increase the production yields of the facility.

CHAPTER-2

Radionuclides for theranostics applications

In this chapter receptor-targeted radiopharmaceuticals for diagnostic and therapy applications, as well as the concept of theranostics are presented. A list of innovative isotopes has been drawn and some nuclides with relevant characteristics have been selected for the thorough large-scale production analysis. For the selected radionuclides the current state of art of the production will be discussed.

The method developed for this analysis is detailed, focusing on the main different steps: beam and target characteristics, target development including cross-section measurements, numerical simulations and experimental tests.

2.1 Radionuclides for medicine

As seen in the first chapter, the currently known radionuclides have different physical properties; half-life, emission type, decay chain. Those characteristics can be exploited in nuclear medicine. Indeed, by making compromises between the physical decay properties, the radiochemistry, the biodistribution and the production logistic, we can find relevant indication for both imaging and therapy. Potential indications range from physiologic studies, for diagnosis or treatment of cancer. Tumors can be of different forms, either solid tumors or liquid tumors as hematologic malignances. Solid tumors are groups of abnormal cells forming lumps or growths. They can start in any of the cells in our bodies. Tumors grow and behave differently, depending on whether they are cancerous (malignant), non-cancerous (benign) or precancerous. Cancerous tumors that spreads from the first place it started, called the primary tumor, to a new part of the body is called metastatic cancer. When cancer cells spread and develop into new tumors, the new tumors are called metastases. Non-cancerous tumors don't spread to other parts of the body. Precancerous cells are abnormal cells that may develop into cancer if they aren't treated. Hematologic cancers instead, begin in blood-forming tissues, such as the bone marrow, or in the cells of the immune system. Examples of hematologic cancer are leukemia, lymphoma, and multiple myeloma.

Radionuclides can be one of the best weapons against such diseases. Of great importance is to determine the most suitable conditions to use radionuclide: determination of the medical aim, choice of the radionuclide, definition of the injectable molecule and targeting mechanism. Few radionuclides can be introduced in the human body as they are, thanks to their chemical properties to bound to specific human cells. One example is the use of iodine for thyroid diseases. In most cases, radionuclides (RN in Figure 36) must be attached to a carrier molecule using a chelate and a linker. A chelating agent is a substance whose molecules can form several bonds to a single atom or ion, also defined as multidentate ligand. When using a carrier molecule, the suitable biological target must be found for clinging the tumor cells while sparing the healthy cells. This is possible using peptides or antibodies that have preferential uptake into specific receptor and by choosing those that targets receptors more frequently present in tumor cells rather than in healthy ones.

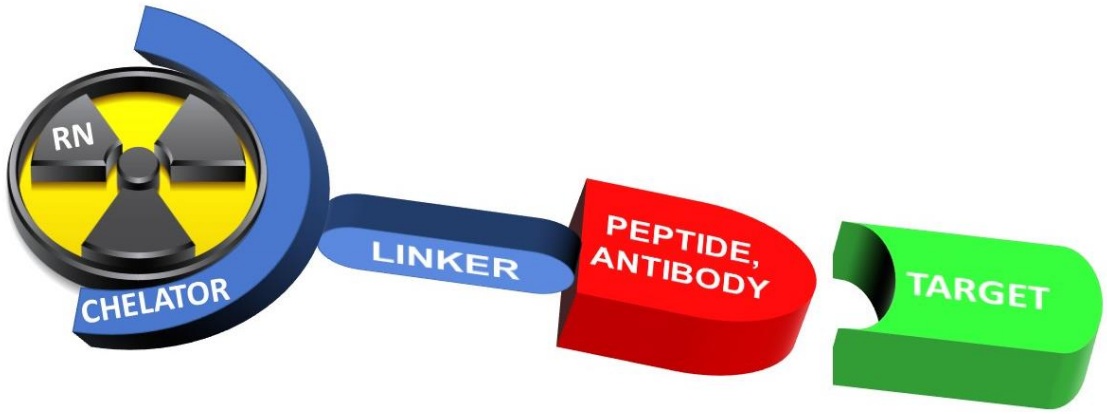

Figure 36: scheme of a radiopharmaceutical, composed by a radionuclide, a chelator, a linker, a peptide or antibody.

2.1.1 Imaging applications of radionuclides

Medical imaging refers to a variety of technologies used to see inside the human body to diagnose and monitor medical diseases, determine how to treat them, follow-up on treatment efficacy and representing the function of some organs or tissues. In other terms, each type of imaging technology gives different information about the area of the body being studied or treated, related to possible disease, injury, or the effectiveness of medical treatment. Molecular nuclear imaging is a non-invasive technique. It is a functional imaging technique, as it provides information on the function of the organs. It is based on the use of radionuclides having the following characteristics: radiation should be detected outside patients, therefore high penetrating radiation such as gamma ray should be considered; the co-emissions should be as low as possible to reduce the dose to patients and doctors; the energy range of the emitted photons should be well suited and corresponding to the detectable energies of the existing detectors.

The current main radiodiagnostic applications are the Single Photon Emission Tomography (SPECT) and the Photon Emission Tomography (PET). Both techniques can be coupled with other imaging techniques such as Computed Tomography scan using x-ray (CT scan) and Magnetic Resonance Imaging (MRI). This will allow improving the obtained information adding an information on the morphology of the organs.

2.1.1.1 Single Photon Emission Tomography

SPECT technology is based on the detection of a single gamma ray emitted from a radioactive source. Gamma rays are emitted when nuclei in excited levels release energy to reach the ground level. The gamma ray emitted should have a sufficient energy to be detected outside the body and not too high to be correctly detected by available devices. This implies the optimal gamma ray energy be in the energy range of around 70 keV and 250 keV. This derives from the historical developments of SPECT detectors for the detection of the gamma emitted by Tc-99m (140 keV), which is the most used radionuclide in molecular nuclear imaging. Therefore, the efficiency of

detection decreases at increasing photon energies. In the bottom of Table 8 are presented the main radionuclides currently used for SPECT applications.

2.1.1.2 Positron Emission Tomography

The PET is based on the detection of the 511 keV gamma rays. As explained in the first chapter, they are emitted from the annihilation of a positron, following a β^+ emission. Indeed, this process generates two gamma rays with the same energy, 511 keV, with opposite directions. The patient after the administration of the drug is laid down on the bed and positioned inside a ring of detectors. In Table 8 are presented the main radionuclides currently used for PET applications. For future applications, particular interest is the $\beta^+\gamma$ imaging (41). The principle of this method is to detect the two 511 keV photons and one high energy gamma ray simultaneously emitted.

Table 8: list of the main radionuclides used for PET and SPECT applications. The 511 keV gamma rays derives from positron emissions.

Nuclides	Half-life	Main gamma ray energy (keV)	Application
F-18	1.83 h	511 (193.5 %)	PET
Sc-44	3.97 h	511 (188.5 %)	PET/$\beta^+\gamma$
Cu-64	12.7 h	511 (35.2 %)	PET
Ga-68	1.13 h	511 (177.8%)	PET
Rb-82	1.25 m	511 (190.9 %)	PET
Tc-99m	6 h	140.5 (89%)	SPECT
I-123	13.2 h	158.9 (83.3%)	SPECT

2.1.2 Therapeutic applications of radionuclides

The objective of using radiation for tumor treatment is to deposit localized energy for killing tumor cells. Thus, charged particles are used as strongly interacting with matter. Radiotherapy can be achieved in many different ways. One way is to use external beams. This method consists in accelerating the beam to a specific energy determined to maximize the energy deposition at the tumors sites considering body and organ penetration. This is the case for example for common radiotherapy, protontherapy and the hadrontherapy, which exploits beams of gamma rays, protons and carbons respectively. Another way is to inject into the patient a boron-based drug for targeting specific tumor cells and irradiate this tumor zone with a neutron beam after incorporation of a large quantity of boron inside the tumor cells. The reaction of the neutron captured by boron nucleus causes the emission of a high energy alpha particle B10(n,α)Li7, releasing high amount of energy in a very short range (<10µm) of human tissue (42). This is called Boron Neutron Capture Therapy (BNCT).

Furthermore, in the receptor targeted radiotherapy a localized dose needs to be deposited in a malignant or inflammatory tissue to achieve the desired therapeutic effect. The radiopharmaceutical is injected in the body and must specifically target tumor cells in order to reduce as much as possible the side effects on healthy cells. The decay of the radionuclide releases energy through radiation. The nature of the radiation implies a different distance range and a different energy deposition, both related to the so-called linear energy transfer (LET). LET is the amount of energy transferred by an ionizing particle per unit distance, it can be measured in keV/µm. Alpha particles have a very short range in human tissue and very high energy deposition compared to beta particles. Thus, LET is much higher for alpha compared to beta particles.

To determine the therapeutic effectiveness one important parameter is the Relative Biological Effectiveness (RBE). It is defined as the ratio of a dose from standard radiation to produce a given biological effect (D_{st}) to the dose from test radiation to produce the same biological effect (D_{test}). As standard radiation has been defined the dose delivered by Co-60 gamma rays. The RBE is defined as follows:

$$RBE = \frac{D_{st}}{D_{test}} \qquad (38)$$

RBE depends on many factors as organ, cell, injected dose and LET. The higher the LET the higher is the RBE up to an LET of around 200 keV/µm. Above that value, the LET of the incident radiation is higher than the what needed for killing a cell, therefore the RBE decreases (Figure 37).

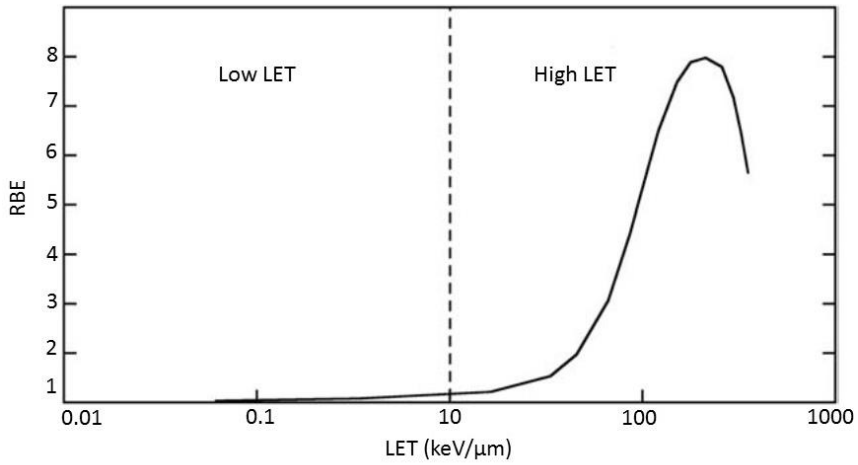

Figure 37: variation of RBE in function of LET of the emitted radiation, taken from (43)

2.1.2.1 β⁻-therapy

The low LET of beta particles implies a longer path in human tissues. For this reason, they are mainly used for macrocluster tumor cells treatments. However as the β^- emission energies are

different for each radionuclide, in Table 9 and in Figure 38 are presented the average energies of emission as a function of the maximum path traveled in human tissues.

Table 9: electron path in human tissues associated to the mean energy of the emitted electrons for the main β- emitters used in nuclear medicine. The 511 keV gamma rays derives from positron emissions.

Radionuclide	Half-life (d)	<E> (keV)	Average range (mm)	Eγ (keV)
P-32	14,3	695	2,6	-
Sc-47	3,3	162	0,3	159
Cu-64	0,5	190	0,4	511
Cu-67	2,6	141	0,2	185
Sr-89	50,5	587	2,0	-
Y-90	2,7	933	3,8	-
Sn-117m	13,8	72	0,1	159
I-131	8	181,9	0,4	364
Sm-153	1,9	224	0,5	103
Ho-166	1,1	665	2,4	81
Tb-161	6,89	154	0,3	75
Lu-177	6,7	134	0,2	208
Er-169	9,4	100	0,1	-
Re-186	3,7	347	1,0	137
Re-188	0,7	763	2,9	155

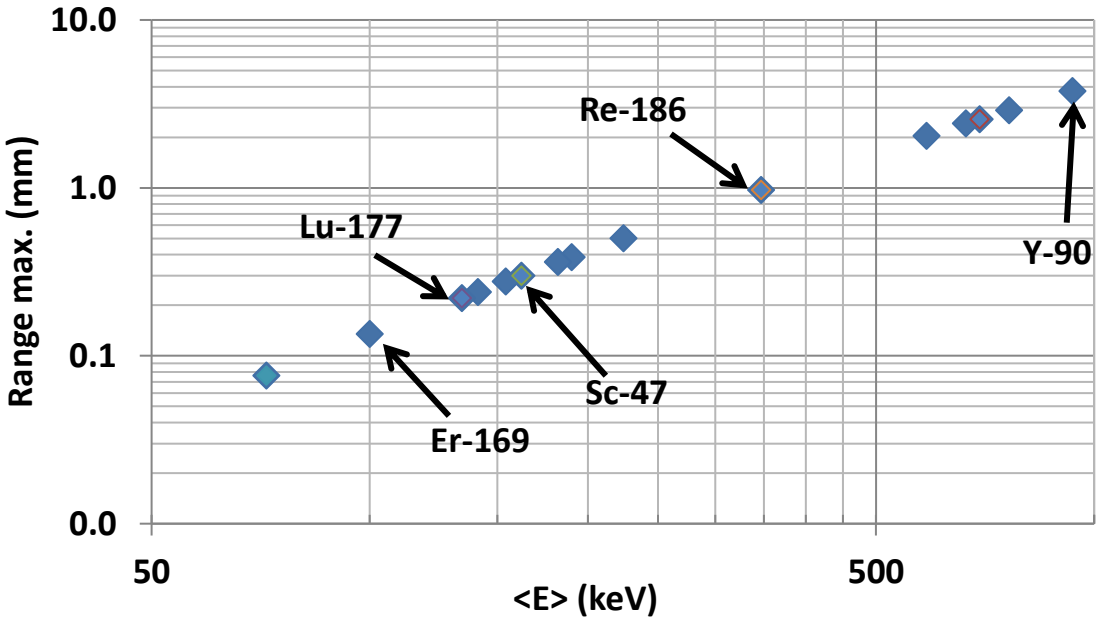

Figure 38: electron path in human tissues associated to the mean energy of the emitted electrons for the main β- emitters used in nuclear medicine.

Most of the presented radionuclides are currently produced in nuclear reactors. Nowadays the β^- emitter of reference for the receptor targeted radiotherapy of NeuroEndocrine Tumors (NET) is Lu-177. From Figure 38, it is possible to see that it is on the left side of the graphic, meaning lower β^- energies and shorter path in the human cells compared to other β^- emitters with suitable characteristics for medical applications. However, this different physical characteristic is of key importance for the future improvement towards the personalized treatment, selecting the suitable energy for each specific disease allows optimizing the treatment effect.

2.1.2.2 α-therapy

Alpha particles as they are heavier and carry a higher charge, have a higher LET and travel shorter path in the human tissues. This high release of energy in a very narrow zone can be exploited for treatments of microcluster of tumor cells. However, the emission of such high energy particles causes an important recoil effect of the nuclei. Indeed, depending on the physical state and location of the nuclei, when an alpha emission happens, the nuclei receive a kick in the opposite direction of the alpha emission. As much energetic is the emission, as more important is the recoil effect which should be taken into account (44).

In Table 10 are presented the main α-emitters of interest for medical applications. The main physical properties are given, as well as the current production routes.

Table 10: list of the main α-emitters physical characteristics and production methods

Radionuclide	Half-life	Decay mode	α Energy (keV)	Production route(s)
Terbium Tb-149	4.12 h	α (16.7 %) ε (83.3 %)	3967 (16.7%)	Spallation + mass separation / accelerator (70 MeV)
Astatine At-211	7.21 h	α (41.8%) ε (58.2%)	5869 (41.8%)	Accelerator (30 MeV) / Spallation + mass separation
Bismuth Bi-212	60.55 m	α (35.94%) β^- (64.06 %)	6050 (25%) 6090 (9.7%)	Generator (Pb-212)
Bismuth Bi-213	45.61 m	α (2.2%) β^- (97.8 %)	5875 (1.96%)	Generator (Ac-225)
Radium Ra-223	11.43 d	α (≈100%) ^{14}C (≈0%)	5606 (25%) 5716 (52%)	Generator (Th-227) / Spallation + mass separation / Reactor
Actinium Ac-225	9.99 d	α (≈100%) ^{14}C (≈0%)	5790 (8.6%) 5792 (18%) 5830 (51%)	Accelerator (18 MeV) / Generator (Th-229) / Spallation + mass separation / Reactor

At-211 can be produced in cyclotrons with 28-30 MeV alpha beam on a bismuth target Bi209(α,2n)At211. The energy of the alpha beam should be optimized to maximize the production of At-211 while reducing as much as possible the co-production of At-210 that decays in the dangerous Po-210. As an alternative, Rn-211 generator could be produced with high energetic proton beam on thorium or uranium targets or using lithium beam interacting on a bismuth target.

Bismuth Bi-213 and Bi-212 are both characterized by a short half-life of approximately one hour. For this reason, they are usually provided by a generator production. Bi-213 can be obtained from a Ac-225/Bi-213 generator, whereas Bi-212 can be obtained from a Ra-224/Pb-212 generator, Pb-212 being used as an in-vivo generator for the daughter Bi-212. Ra-224 can be obtained from Th-228 sources.

Radium Ra-223 (11.43 days half-life) could be obtained by the production of the Ac-227/Th-227 generator by irradiation of natural thorium target with high energy proton beams (45). An alternative production technique is based on the Ac-227/Th-227 generator by irradiation of Ra-226 target in reactor (226Ra(n,γ)227Ra → Ac-227 → Th-227→ Ra-223); very high energy proton beam on a uranium or thorium target and mass separation. Xofigo® (radium Ra 223 dichloride), which is a radiopharmaceutical developed by Bayer, is based on the properties of Ra-223. It received the FDA approval in 2013 for the treatment of patients with castration-resistant prostate cancer (CRPC) and symptomatic bone metastases.

Actinium Ac-225 (almost 10 days half-life) is characterized by a rapid decay cascade, leading to stable Bismuth-209. It can be obtained from different ways: in cyclotrons by 18 MeV proton irradiation of radium Ra-226 target (226Ra(p,2n)225Ac); by neutron irradiation of radium Ra-226 target (226Ra(n,2n)225Ra → Ac-225); high energy proton beam on a uranium or thorium target and mass separation; natural decay of Th-229. Actinium-225 can be also be used as a parent radionuclide for the production of a 225Ac/213Bi generator. An alternative production method is through bremsstrahlung irradiation, from electron linacs, of a Ra-226 target. The reaction Ra226(γ,n)Ra225 lead to the production of Ra-225 (half-life 14.9 d), parent of Ac-225.

Tb-149, compared to the other α-emitters is only available in small quantities from very high energy proton beam irradiation on a tantalum target and mass separation. A thorough analysis regarding the production of Tb-149 will be presented in the next paragraphs.

2.1.2.3 Auger electron therapy

One attractive option for therapeutic applications is the use of Auger electrons. When a collision with atomic electrons cause the emission of an electron, the vacancy is filled by an outer shell electron. This can cause the emission of x-rays or Auger electrons. Auger electron's energy is fixed and does not have a continuum spectrum as the beta emissions. Most of Auger electrons have very low energies, around 10-20 keV, with very short ranges in biological tissues, up to 1 μm. This cause an extremely localized energy deposition, which could damage the DNA of the tumoral cells,

it occurs within the cell DNA. Examples of Auger emitter are Sn-117m and Er-165. Auger electrons emission can potentially play a complementary role in β^-therapy too. Indeed, studies are currently ongoing with β^- emitters having an important co-emission of Auger electron. One example is Tb-161 (46).

2.1.3 Theranostics concept

Of continuous increasing relevance is the theranostics concept. It refers to the coupling of diagnostic and therapy with the same vector in order to go in the direction of a personalized treatment for each patient. Using the same vector for both imaging first and therapy then, allows reaching the target organ in the same way and with the same efficiency. Using the information from the diagnostic agent, the patient response can be inferred as well as the stage of the disease. If the treatment can be applied, a dosimetry study can help defining the best dose to use. After treatment, a follow-up could be made with eventual additional use of the diagnostic agent.

Thus, theranostics can be achieved in different ways. One way is to pair two radionuclides of the same element (e.g. Sc-44 and Sc-47); another method is the coupling of two radioisotopes of different chemical elements having similar chemical properties (e.g. Ga-68 and Lu-177); or using only one radioisotope for both purposes (e.g. Cu-64).

Although the term was coined by John Funkhouser in 1998 (47), theranostics has been applied years back. In 1939, I-131 produced at Berkeley cyclotron (USA) was used for thyroid investigations by Hamilton and Soley (48), which studies were based on autoradiography and external counting techniques rather than imaging (7). Successively in 1941 the physicist Saul Hertz administrated the first dose of I-131 to a patient at Massachusetts General Hospital for treatment of hyperthyroidism (49). During the years many new isotopes were made available and used in clinic. More recently, the company Advanced Accelerator Applications developed the first theranostics couple of radiopharmaceuticals for receptor vectorized theranostics, pairing diagnostic products NETSPOT® (gallium Ga-68 dotatate) in the US and SomaKit TOC® (gallium (Ga-68) edotreotride) in Europe, and the radioligand therapy, Lutathera® (USA: lutetium Lu-177 dotatate; Europe: lutetium (Lu-177) oxodotreotide), which is approved for use in Europe and the United States respectively end of 2017 and early 2018 (50).

2.2 Radionuclides selection for theranostics

In this work, the study of new production methods is proposed to make certain innovative radionuclides more available with better purity for nuclear medicine. The identification of the suitable radionuclides has been performed searching for theranostics radionuclides among the ones already used in medicine or with suitable characteristics for future medical applications. Indeed, sometimes the lack of radionuclide production availability hinders its medical application.

Starting from the nuclear chart of elements, (25) the selection of the radioisotopes with favorable characteristics for theranostics applications is made respecting some criteria, defined from the literature on radioisotopes production, imaging (PET and SPECT) and therapy. Those criteria can be then modified and the list of the selected radioisotope of interest can be reevaluated if in the future new challenges, technologies and requirements will be considered. Some radionuclides already in use do not fulfill our criteria, but they have been added to the list of elements of medical interest taken from the bibliography (27), (37), (51).

The defined criteria with, in brackets, the total number of radionuclides that satisfy all the criteria until that point, are presented hereafter.

- Suitable half-life: 10 m < $T_{1/2}$ < 10 d (232). This criterion allows an initial wider analysis and will be refined later in this report in order to consider the labeling time, the transportation, the time needed to the radiopharmaceutical to reach the organ target and a decay time not too long that is not an issue for radioprotection purpose considering the activity inside the patient body.
- Decay type: gamma rays, β^+, β^-, α emitters (232).
- Branching ratio: we set up a minimal value of 10% that corresponds to 20% for the intensity of the 511 keV photons coming from β+ decay. (171)
- Emission of γ with energy E > 1500 keV must be lower than 1% to limit the radiation safety constraints on patients and staff. (138)
- For imaging we want a limited co-emission (lower than 5%) in the window of analysis of the cameras. This window corresponds to ±100 keV around 511 keV for PET and between 70 and 250 keV for SPECT. This concerns especially PET rather than SPECT applications. (121)
- Decay to stable daughter elements or long-lived daughters only except for the radionuclides used as generators. (70)
- Production must be with proton beam with energy lower than 70 MeV considering available commercial accelerators. This criterion will be later enlarged to reactor produced radionuclides too, in particular the one which cannot be currently produced at sufficiently high specific activity.
- Stable target to limit constraints associated to the preparation and handling of a radioactive target, of a different chemical species from the produced radioisotope to permit extraction with high specific activity.

The criterion of the minimum half-life was initially set to a low value that allows to have a better general overview, then this criterion has been refined to a minimum half-life of 3 h, which is a good value for radioisotopes used for imaging, but it is still low for therapy. In addition, there are already two isotopes with half-life lower than 3h that are widely used (F-18 and Ga-68, the latter obtained from cyclotron direct production or a generator system from its mother Ge-68). As written above,

this radionuclides half-life must allow the labeling, the transportation and permit the radiopharmaceutical to reach the targeted organ; following this, the total amount of isotopes with favorable characteristics goes down to 51. Furthermore, radioisotopes that do not respect all the criteria, but have already been used in medicine and have a good potential pair of the same element, have been considered as well. One example is Tb-149 that has not been considered in a first stage due to the unstable daughters generate by its decay. It was reconsidered in a later stage following the actual applications of the others interesting terbium radionuclides.

From the list of 51 radionuclides mentioned above, one should distinguish between their intended indication and their type of suitable coupling whenever it is possible and requested. Then for each radioisotope mentioned below one should consider the state of art of the production methods, applications and problems already encountered from other researchers. In the next sections, we will briefly describe our results and comment them for the theranostics applications.

2.2.1 Radionuclides pairs of the same elements

Table 11 presents the list of all the possible couples of radionuclides of the same element that can be used for theranostics based on the selected criteria.

Table 11: list of possible radionuclides pairs of the same element for theranostics with relative characteristics. The 511 keV gamma rays derives from positron emissions. (25)

Element	*Isotope*	*Half-life*	*γ energy [keV] (%)*		*β- mean energy [keV] (%)*		*α energy [keV] (%)*	*Comments*
Scandium	Sc-43	3,89 h	511 (176%)					Selected for further studies
	Sc-44	3,97 h	511 (188%)	1157 (100%)				
	Sc-47	3,35 d	160 (68%)		142 (68%)	204 (32%)		
Copper	Cu-61	3,33 h	511 (123%)					
	Cu-64	12,70 h	511 (35%)		191 (38%)			
	Cu-67	61,83 h	93 (16%)	184 (48%)	141 (100%)			
Arsenic	As-72	26,00 h	511 (176%)					Already available from some research centers
	As-77	38.79 h	239 (1.6%)		138 (1.6%)	229 (97%)		
Yttrium	Y-86	14,74 h	511 (64%)	515 (5%)				Y-90 available from Sr-90 produced from reactor
	Y-90	64,05 h			933 (100%)			
Iodine	I-124	4,17 d	511 (45%)	602 (63%)				Limitation from radioprotection by the γ rays emitted
	I-131	8,02 d	364 (81%)		191 (90%)			
Terbium	Tb-149	4,12 h	511 (14%)				3.97 (16.7)	Selected for further studies
	Tb-152	17,50 h	511 (41%)					
	Tb-155	5,32 d	105 (25%)	86 (32%)	AUGER			
	Tb-161	6,89 d			137 (26%)	157 (65%)		

From this list, one can notice that Y-90 can is being already produced from reactor (through the Sr-90 generator), as well as I-131 with satisfactory radioactive purity and specific activity. This means they are not economically attractive for a production using cyclotrons. Scandium, copper, arsenic and terbium instead have at least a potential couple of radionuclides of interest for theranostics that currently are not available in large quantities. These are good candidates.

Concerning scandium, Sc-44 and Sc-43 have good properties for PET applications and Sc-47 that can be used for treatment can form suitable couples. The most interesting copper radionuclides to study are Cu-64 and Cu-67 that have both good characteristic for diagnosis and therapy respectively, while Cu-61 can also be used for PET applications. Even if they are still in a research phase, arsenic radionuclides have some potentially interesting characteristics for theranostics purposes: As-72 for PET applications (alternatively As-71 or As-74 can be considered) and As-77 for therapeutic applications. Terbium is the unique element that presents a poker of interesting radionuclides for theranostics: Tb-161 for β- and Auger electron therapy, Tb-149 for both α therapy and PET diagnosis, Tb-152 for PET and Tb-155 for SPECT applications.

2.2.2 Radionuclides pairs of different elements

Another way for theranostics is coupling radionuclides of different elements. In this case the choice is less straightforward. First of all, it strongly depends on the chemical compatibilities and the suitability of labelling the two radionuclides to the same vector (peptides or antibodies). This means that different combinations are possible and with further studies some new couples could become of interest for the future. Table 12 shows the possible couples within the radioisotopes considered.

Table 12 - list of possible radionuclides pairs of different elements for theranostics.

Couples	Diagnosis	Therapy	Application
Ga-68 / Lu-177	Ga-68	Lu-177	PET
Ga-68 / Lanthanides	Ga-68	Lanthanides	PET
Sc-44 / Lanthanides	Sc-44	Lanthanides	PET
Tc-99m / Re-186	Tc-99m	Re-186	SPECT
Tc-99m / Re-188	Tc-99m	Re-188	SPECT

Ga-68 / Lu-177 is the first theranostics pair for peptide receptor radionuclide therapy application commercially available. As previously presented, the recent EMA (European Medical Agency) and FDA (Food and Drug Administration) approval of Lutathera made available a theranostics pair for GEP-NET (Gastro-Entero-Pancreatic - NeuroEndocrine Tumors) therapy. Lu-177 and Re-188 can be produced by reactors, as well as Tc-99m obtained through molybdenum Mo-99 generator, which means they are not economically attractive for a production with cyclotrons as mentioned before.

Finally, other lanthanides radionuclides have good properties for therapy, but not for diagnosis, as for example Er-169. Nevertheless, it is possible to use Sc-44/Er-169 or Ga-68/Er-169 theranostics couples. For this reason, Er-169 has been added to the list.

2.2.3 Single radionuclides for therapeutic follow-up

Finally, the last category of theranostics radionuclides is the one that contains all the radionuclides that potentially allow both therapy and imaging. One has to keep in mind that the dose injected into patients for imaging is different from the one used for therapy. This implies that in this last category if the radionuclide has a high branching ratio for imaging radiation, it will be suited for diagnosis, but it will give a higher dose to the patient and staff during therapy. If the imaging radiation for a radionuclide has instead a low branching ratio, diagnosis will not be feasible, but it will be possible to follow the patient after the treatment (Table 13).

Table 13: list of possible single radioisotopes for theranostics.

Element	Imaging	Therapy	Medical tracking
Sc-47	Yes / SPECT	Yes	Yes
Cu-64	Yes / PET	Yes	Yes
Cu-67	Yes / SPECT	Yes	Yes
I-131	Yes / SPECT	Yes	Yes
Tb-149	Yes / PET	Yes	Yes
Sm-153	Yes / SPECT	Yes	Yes
Ho-166	Yes / SPECT	Yes	Yes
Lu-177	Yes / SPECT	Yes	Yes

2.2.3.1 Other radionuclides

Some of the remaining radionuclides are already used for well tested applications such as brachytherapy in clinical trials as for example Ho-166 which can be produced from nuclear reactor (52) (53) or neutron activator driven by cyclotron (54).

Other radionuclides have favorable characteristic for imaging or therapy, but do not have a pair for theranostics applications yet: palladium (Pd-109), silver (Ag-111) and heavier elements (Ir-194, Ir-195, Pt-197).

Other nuclides as alkali or noble gases, cannot be stably linked to a receptor, examples are potassium (K-42 and K-44) and xenon (Xe-133). These are not considered in this work.

2.2.4 List of radionuclides of interest for production

Based on the presented radionuclides scouting, considering nuclear reactor produced radionuclides too, a list of potential interesting innovative radionuclides has been made. Considering the thesis timescale and resources, only few of them are selected for developments

studies. In particular scandium, terbium and erbium elements are selected considering the actual technology and future potential needs. In this work the radionuclides presented in Table 14 will be analyzed for the large-scale production with commercial cyclotrons and nuclear reactors.

Table 14: list of selected radionuclides for production analysis.

Element	Radionuclide	Application	Comments
Scandium	Sc-47	Therapy	reactor and 70 MeV accelerator
Terbium	Tb-149	Therapy / PET	High energy mass separator / 70 MeV accelerator
	Tb-152	PET	High energy mass separator / 70 MeV accelerator
	Tb-155	SPECT	High energy mass separator / 70 MeV accelerator
Erbium	Er-169	Therapy	production via reactor

Scandium has been chosen because Sc-44 is a diagnostic agent with an already well identified production route. As mentioned before, it could be used as diagnostic couple of therapeutic lanthanides. Nevertheless, Sc-47 is the natural diagnostic pair of Sc-44, but a suitable production method has not been identified yet. The main issue is the potential co-production of Sc-46 (half-life 84 d), a long-lived contaminant.

Terbium is the most interesting element for MEDICIS-PROMED project for its radionuclides with optimal properties for medical applications, Tb-149, Tb-152, Tb-155 and Tb-161. Whereas Tb-161 can be produced in reactor, a large-scale production method is currently missing for the other three radionuclides. In particular an efficient production route for Tb-149 is missing.

Nevertheless, the cyclotron production of terbium and scandium radionuclides, as it will be shown in the next chapters, is challenging. One reason is the co-production of radionuclides of the same element of the wanted one. Those cannot be separated with the conventional chemical separation method. The selected way to overcome this issue is to consider the mass separation of the irradiated target with the use of CERN-MEDICIS mass separator.

Finally, the production of Er-169 from reactor will be considered. For this production route, the irradiation conditions are already the optimal ones. Nevertheless, currently it can only be produced at low specific activities, diluted in the stable Er-168. For this reason, the use of the mass separation is considered, and the analysis is presented in chapter 6. This will serve as a proof of principle of the proposed method, which potentially can be applied to other radionuclides with the same problematic of Er-169, such as Sm-153. Er-169 was mainly chosen as test isotope for its longer half-life, allowing an easier development.

2.3 Production method choice and analysis

The development of the production method for a radionuclide is an iterative process, starting from the investigation of the state of art of the production methods already existing, passing through the definition of target material and beam characteristics, target development and the target validation, ending with a production method definition.

The first step is to select a production route. This can be performed with the comparison of the cross-section of the governing reactions and the associated yields, as well as the co-produced contaminants, allowing the evaluation of the best potential starting material. After that it has to be verified whether a separation method is needed (chemical separation or physical separation) and whether the needed method is available or possible to develop. Once the previous step is identified, a target development method should be defined to fulfill them. If this results not feasible the previous step must be reassessed. The defined targetry then should be economically feasible, indeed sometimes enriched material is required and it could be too expensive for the production, therefore a compromise on the maximization of the production and the cost should be found.

One key step on the analysis is the cross-sections comparison. The experimental cross-sections are taken from EXFOR (55) if available, otherwise Talys software (56) has been used to calculate them. Sometimes happens that some cross-sections are not available and the one calculated with Talys are not fully trustable as they could largely differ from the experimental cross-section. In those cases, experiments for the evaluation of the experimental cross-sections have been foreseen. With the considered cross-sections a production yield analysis is made. The yield analysis along this thesis have been made with the Radionuclides Yield Calculator (RYC) program developed at ARRONAX and freely available (57). The yield calculation is based on the thick target yield calculation equation previously presented in chapter 1.

This analysis should be repeated with any potential target/beam combination. Thus, the higher production yield is evaluated as well as purity, cost and availability of the target, leading to the configuration which represents the best compromise between those parameters. The selected target material should be dimensioned and defined for a performant and safe irradiation configuration. Therefore, depending on the chemical form of the starting material and the known targetry techniques, the best theoretical configuration is defined. It should be tested for the mechanical and thermal stresses, and especially the ones coming from beam induced thermal power deposition into the target material. Indeed, the thermal load depends on the beam characteristics and irradiation conditions. For this reason, Computational Fluid-Dynamics (CFD) simulations have been done, allowing to define the feasibility of the irradiation and eventually the

optimal irradiation condition. The simulations scan help in the target design process. If a solution is not found, the process should be repeated with another target/beam configuration.

In the next paragraphs the state of art of the production for the selected radionuclides are presented to give a thorough overview of the possible improvements to be made within this thesis work.

2.3.1 Scandium Sc-47 production

Scandium is the lightest transition metal belonging to the third group of the periodic table. It has hexagonal structure and, under proper conditions, it forms insoluble hydroxides, fluorides and oxalates, similarly to the lanthanides. (58) Scandium was discovered in 1879 by Lars Fredrik Nilson, a Swedish chemist, by separation from rare earth mixtures in euxenite and gadolinite. The name scandium derives from Scandinavia. It occurs in association with lanthanides in uranium ores and several minerals. The only known concentrated sources of this element are thortveitite, euxenite, and gadolinite. The principal uses of scandium are in Sc-Al alloys for different applications such as structural parts in airplanes and in solid oxide fuel cells. Minor amounts of scandium are also used in variety of other applications including electronics, lasers, and lighting. Further uses are: in oxides as a catalyst and in making ceramic parts; in sulfates in very dilute aqueous solutions is used in agriculture as a seed treatment to improve the germination of corn, peas, wheat, and other plants. The abundance of scandium in the Earth's continental crust is remarkable, with average values of 31, 19, and 14 ppm for the lower, middle, and upper crust, respectively. (59)

Scandium has atomic number 21 and up to nowadays 23 isotopes are known, namely one stable Sc-45, six neutron-deficient and sixteen neutron-rich. (25) Among them, a triplet of isotopes raised interest in medicine due to their physical properties suitable for theranostics applications: Sc-43 for PET, Sc-44 for PET and $\beta^+\gamma$ photoimaging, Sc-47 for β^- therapy. The $\beta^+\gamma$ photoimaging is a potential new feature of PET diagnosis technique (41), detecting a high energy gamma in addition to the two 511 keV gamma. Therefore, it is very important to detect the energy and direction of the high energy gamma ray. One way is to use Compton scattering, which effect is enhanced for gamma rays around 1 MeV as shown in the first chapter. The research of optimal detectors is still ongoing, for this reason this can still be considered at a research level only. Table 15 resumes the main physical properties of scandium medical radionuclides.

Table 15: main physical properties of scandium radionuclides for medical applications. The 511 keV gamma rays derives from positron emissions.

Radioisotope	**Sc-43**	**Sc-44**	**Sc-47**
Half-life	3.89 h	3.97 h	3.35 d
Decay mode and branching ratio	β^+ (88%)	β^+ (94%)	β^- (100%)
Main γ emission (keV)	372.9 (22.5%) 511 (176.2%)	511 (188.5%) 1157 (99.9%)	159.4 (68.3%)
Mean/maximum β⁻ emission (keV)	N/A	N/A	142.6/440.9 (68.4%) 203.9/600.3 (31.6%)

Scandium radionuclides are raising increasing interest in medicine. This is mainly due to the theranostics couples available, namely Sc-43/Sc-47 or Sc-44/Sc-47. Furthermore, an identified possibility is that Sc-44 can be a diagnostic agent which could be potentially used in parallel or in place of Ga-68 as the diagnostic partern of radiolanthanides such as Lu-177. Indeed, the longer half-life could enable a better patient-specific pre-therapeutic dosimetry before peptide receptor radionuclide therapy with the lanthanide pair.

The clinical application of Sc-47 is still far from ideal due to the lack of regular availability of sufficient quantity batches. One production route is the indirect production with the neutron activation of 46Ca(n,γ)Ca47 then using Ca-47/Sc-47 generator process. Ca-47 has 4.5 days half-life and decays β- in Sc-47. This route is followed by high-flux reactors such as ILL. (60) Nevertheless, the prohibitive cost of highly enriched Ca-46, its limited availability and its maximum enrichment level available on the market (around 25%), as well as the low thermal neutron cross-section of the reaction (0.74 b), make this route not exploited yet for large scale production, even though is the only method to avoid the co-production of Sc-46. A different way to produce Sc-47 is with 25 MeV electron linacs as Mamtimin *et. al.* proposed at Idaho Accelerator Center (61). Considering the photoactivation of Ti-48 targets (Ti48(γ,p)Sc47)), their theoretical assessment they can achieve potentially a specific activity of 100 MBq/mg. Another explored way to produce Sc-47 is to use fast neutron beams. It is possible to irradiate enriched titanium Ti-47 oxide targets ((n,p) reaction) as made at Brookhaven (High Flux Beam Reactor) and Oak Ridge (High Flux Isotope Reactor). Is it also possible to irradiate titanium and vanadium targets for producing Sc-47 via spallation reactions, as made at Brookhaven National Laboratory (BNL, Brookhaven Linac Isotope Producer) and Los Alamos National Laboratory (LANL, Isotope Production Facility), and higher energy facilities such as TRIUMF and CERN (62) (63). Furthermore, at Brookhaven National Laboratory (BLIP accelerator), different targets materials have been irradiated for Sc-47 such as vanadium and enriched Ti-48 (64). Also, a Coordinated Research Project (CRP) coordinated by IAEA on the production of Sc-47 with cyclotrons irradiating enriched Ti-48 is ongoing. (65)

In this chapter, the large-scale production of the scandium theranostics couple is analyzed with focus on the production of Sc-47, as the diagnostic ones can already be produced in large quantities and high purity. The proposed production method is based on commercial high-energy and high current cyclotron facilities such as the 70 MeV ones, followed by mass separation technology. ARRONAX cyclotron and CERN-MEDICIS mass separator are considered for this study.

In the next chapters the comparison of the cross-section and relative yield for proton irradiation of titanium and proton irradiation on calcium are presented, aiming to evaluate a suitable target design for Sc-47 production.

2.3.2 Terbium radionuclides production

Terbium discovery is related to the erbium one. Carl Gustaf Mosander succeeded in separating erbia and terbia from gadolinite starting material in 1843. From erbia and terbia the elements erbium and terbium were isolated. Terbium has been used for more than a century because of the green fluorescence under ultraviolet light of its trivalent salts, such as $Tb_2(SO_4)_3$, in lamps and monitors; combined with europium blue and red emitting salts they allow to have a wide range of colors. (66) Terbium found its applications in biology too: fluoroimmunoassays and supramolecular luminescent sensors. The first one has been developed for studying the primary production of iron in oceans and the carbon cycle. The second one consists in the design of sensitizing ligands providing highly emissive complexes with enough stability and aqueous solubility for practical applications. (67) Another application is the use in Terfenol-D composites, consisting in terbium dysprosium and iron alloys, which has the largest room temperature magnetostriction. (68)

Terbium has atomic number 65 and up to nowadays thirty-five terbium isotopes are known, namely one stable, twenty-one neutron-deficient and thirteen neutron-rich. (25) Among them, a poker of isotopes raised interest because of their physical properties suitable for nuclear medicine applications: Tb-149 for alpha therapy, Tb-152 for PET, Tb-155 for SPECT and Tb-161 for β^- therapy. Indeed, terbium is the only element which offers one radionuclide for each main medical application, allowing different configuration of the theranostics couple depending on the targeted tumor. Table 16 summarizes the main physical properties of the four terbium medical radionuclides.

Table 16: main physical properties of terbium radionuclides for medical applications. The 511 keV gamma rays derives from positron emissions.

Radioisotope	**Tb-149**	**Tb-152**	**Tb-155**	**Tb-161**
Half-life	4.12 h	17.5 h	5.32 d	6.89 d
Decay mode	α (16.7%) EC (83.3%)	ε (100%)	EC (100%)	β- (100%)
Main γ emission (keV)	164.98 (26.4%) 352.24 (29.4%) 511 (14.2%) 853.43 (15.5%)	271.09 (9.52%) 344.28 (63.5%) 511 (41%) 974.05 (3%)	86.55 (32%) 105.32 (25.1%)	25.65 (23.2%) 48.92 (17%) 74.57 (10.2%)
Mean/max. β- emission (keV)	N/A	N/A	N/A	138/460 (25.7%) 157.4/522 (65%)
α emission (MeV)	3.97 (16.7%)	N/A	N/A	N/A

Terbium radionuclides are currently far from the routine use in clinic, even though Tb-152 has already been tested in human as 152Tb-DOTATOC for a neuroendocrine metastases diagnostic (69). This is mainly due to the lack of isotopes availability. Whereas Tb-161 can be produced in reactors, for the other radionuclides a large-scale production of high specific activity batches has not been developed yet. Often, the main issue is the co-production of unwanted terbium isotopes contaminants. They have a similar or longer half-life and it is not possible to separate them with the conventional chemical separation methods.

2.3.2.1 Terbium Tb-149 production

Tb-149 is the lowest mass alpha emitter, and the only one among the radiolanthanides, with suitable physical properties for receptor-targeted alpha therapy (TAT). It emits short-range α particles at 3.967 MeV with an intensity of 17%. Furthermore, it has a quite long decay chain. It decays into daughters which main decay process is EC. A few very low branching ratio alpha daughters are present too. (Figure 39)

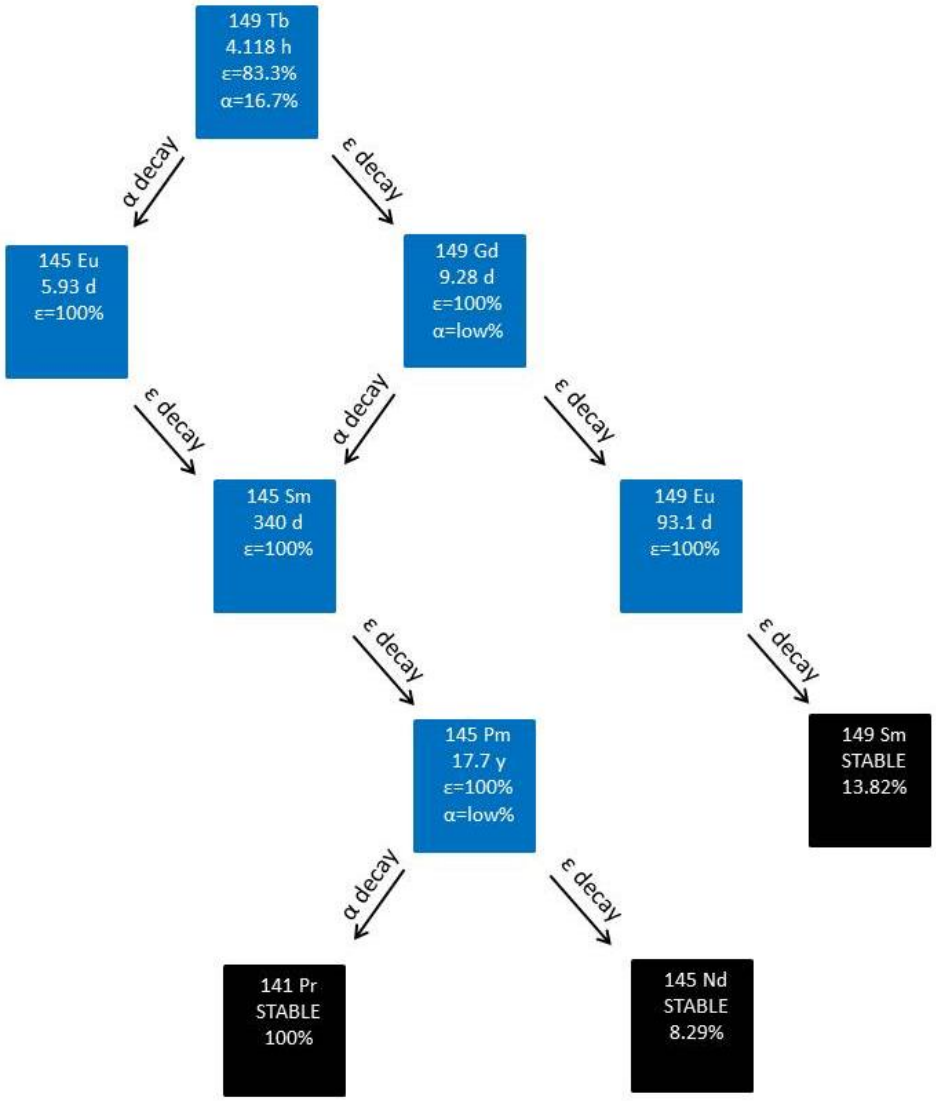

Figure 39: Tb-149 decay chain

2.3.2.2 Tb-152 and Tb-155

As mentioned above Tb-152 and Tb-155 are the diagnostics radionuclides among terbium ones. The PET radionuclide is Tb-152 (half-life 17.5 h) which emits positrons with an average energy of 1.08 MeV and 17% intensity. The SPECT radionuclide instead is Tb-155 (half-life 5.32 d) which decays by electron capture (EC) and emits γ-rays of 86.55 keV (BR=32%) and 105.3 keV (BR=25%). As the current exploited production routes are similar to the ones for Tb-149. Therefore, a general overview is given for all.

2.3.2.3 Existing production routes and workplan

Currently, high specific activity terbium nuclides are produced at CERN in ISOLDE facility with high energy proton beam and mass separation technology. The current batches are available for preclinical studies, but in limited availability (around 15 days of run per year). Indeed, the ISOLDE beam time dedicated to the medical isotopes is very limited. In the near future at the CERN-MEDICIS facility the production could be increased on a regular basis. ISOLDE and MEDICIS use the 1.4 GeV proton beam from the CERN proton synchrotron booster. Nevertheless, the beam is not constantly provided, indeed there are short (every year) and long (occasionally) shutdowns. During those periods the production of terbium should be guaranteed by the mass separation of a target irradiated in another facility with an alternative production method, as the one discussed hereafter.

Other similar facilities which can potentially look to the production of terbium nuclides based on spallation and mass separation have already been operating; those are the Isotope Separator and Accelerator (ISAC) at TRIUMF, Canada's National Laboratory for Particle and Nuclear Physics (Canada) and the Investigation of Radioactive Isotopes on Synchrocyclotron (IRIS), at the Petersburg Nuclear Physics Institute (PNPI, Russia).

Other facilities also are under construction or planned for the next future such as: Radioactive Isotope Beam Factory (RIBF, USA); Belgium Nuclear Research Center's ISOL facility (ISOL@MYRRHA, Belgium); Japan Proton Accelerator Research Complex (J-PARC ISOL, Japan). (70)

Furthermore, other researchers studied the alternative production of Tb-149 from tandem accelerator with heavy ion beams irradiation. Different reactions were studied: 141Pr(12C,4n)149Tb with not satisfactory yields obtained; natNd(12C,xn)149Dy and natNd(12C,xn)152Dy which decay respectively in Tb-149 and Tb-152, but the purity achievable is not high enough; for this reason only in vitro studies were made. (71) (72)

The common point of the presented production routes is the non-sustainable and non-regular production of Tb-149. Thus, a new more reliable production method needs to be found.

At GIP ARRONAX, two different production routes could be investigated for the production of Tb-149. The first one is the irradiation of a gadolinium target with proton beam, the second is the irradiation with an alpha beam of europium target. In the case of the proton route, which is the one considered, new cross-section data are mandatory in the investigated energy route up to 70 MeV. Indeed, experimental cross-section measurement of the reaction natGd(p,x)Tb149 is missing. Whereas for the production of Tb-152 and Tb-155 experimental data are available from Vermeulen et. al. (73), their comparison with Talys calculated cross-section is presenting an important discrepancy. For this reason, the stacked foils experiment for the cross-section measurement for the production of Tb-149 from natural gadolinium has been performed and presented in chapter 3. The obtained data will allow elaborating a thorough analysis for the optimal production route for Tb-149.

In the following chapters then, a new production method based on commercial high-energy and high current cyclotron irradiation, coupled with mass separation technology, is proposed for producing Tb-149, Tb-152 and Tb-155 during CERN-MEDICIS shutdown periods. ARRONAX cyclotron and CERN-MEDICIS mass separator are considered for the analysis.

CHAPTER-3

Cross-section measurements with focus on Tb-149 production from natural gadolinium

As illustrated in the previous chapter, when developing a new production method, it is of fundamental importance to compare different production routes. Sometimes the comparison is not simple as it requires data that are not available from experimental databases for the energy range considered or the data available are not consistent within each other.

In this work the production cross-section associated to natGd(p,x)Tb149 has been investigated in order to be able to make a thorough analysis for the Tb-149 production from commercial cyclotrons. The stacked foils method used for the experiment is illustrated. Production cross-section curves between 70 and 58 MeV, the most interesting energy range for Tb-149 production

from natGd, are presented for different terbium nuclides. For the ones which experimental points were already available in literature, the results of this work are in agreement.

3.1 Stacked foils method

The cross-section measurements performed in this work were done with the so-called stacked foils method. The method consists in irradiating a stack of thin foils. A stack is composed by a target foil, a monitor foil, a catcher foil and a degrader foil and it is repeated N times for the measurements of N experimental points (*Figure 40*). The target foil is made of the starting material of interest for the investigation of beam/target reaction considered. The monitor foil is a foil used to measure the current of the beam along the stack. It is made of an element for which at least one reaction cross-section is well known and certified by IAEA as reference cross-section. The material is chosen depending on the energy range investigated and the reference cross-section behavior in that range. It should be of a different material with respect to the target to avoid the production of the radionuclide under investigation and possible interferences (74). Furthermore, the monitor has the function to catch the eventual recoil atoms from the target foil. In that case the activity of the atoms detected in the monitor will be added to that of the target foil. Then a catcher foil is put only for catching the eventual recoil from the monitor foil to add the eventual fraction of escaped recoil atoms. Finally, a degrader foil is used to decrease the beam energy before the following target foil. The thickness of the foils is chosen to have the suitable number of experimental points in order to properly describe the investigated excitation function. Thus, the thickness of the degrader foil used will vary depending of the desired energy loss. Except for the degrader, as they are thin foils, the energy loss in the foils is negligible compared to the kinetic energy of the incident particles.

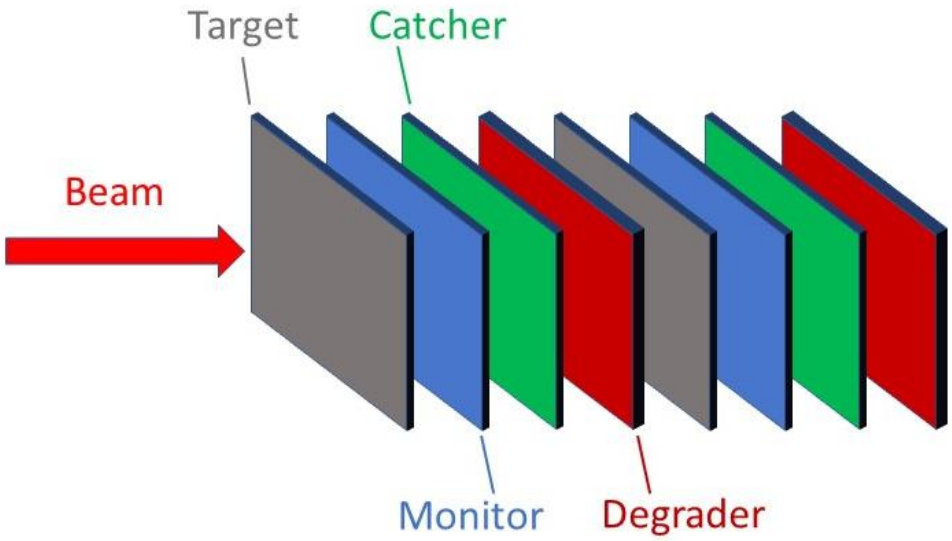

Figure 40: stacked foils method. The order of the stack is target, monitor, catcher, degrader foils repeated N times.

The activity of the produced radionuclides in a thin foil can be calculated as follows:

$$A = \phi * \sigma * \frac{\mathrm{X}*N_A*\rho_A}{M} * (1 - e^{-\lambda t_{irr}}) \qquad (39)$$

Where:

- ϕ is the proton beam current in particles/s
- σ is the reaction cross-section in cm^2
- X is the enrichment of the target (%)
- N_A is the Avogadro's constant in atoms/mol
- ρ_A is the area density of the target in g/cm^2
- M is the molar mass of the target in g/mol
- t_{irr} is the irradiation time in s

In order to evaluate the cross section of new investigated reactions, one has to refer to the reference cross section validated by IAEA. Those are monitor cross sections validated after numerous cross section measurements of the same reaction by different group of researchers. Therefore, the searched cross section is calculated assuming the beam current interacting the target foil is equal to the beam current interacting the monitor foil positioned next to it. Indeed, this is possible because we know the cross section of the monitor reaction and we can measure the activity produced in both the target foil and the monitor foil. Using equation 39, it is possible equalize the expressions of the flux for both the target produced and monitor produced radionuclides. In the following equations, the monitor quantities will be denoted with an apex (ex. ϕ').

$$\frac{A*M}{\sigma*\mathrm{X}*N_A*\rho_A*(1-e^{-\lambda t_{irr}})} = \frac{A'*M'}{\sigma'*\mathrm{X}'*N_A*\rho'_A*(1-e^{-\lambda' t_{irr}})} \qquad (40)$$

where the unknown of the equation is only σ, the cross-section of the investigated reaction. Reorganizing (39) in (40) and erasing the common term N_A one can obtain the formula use for the cross-section estimations:

$$\sigma = \sigma' * \frac{A*M*\mathrm{X}'*\rho'_A*(1-e^{-\lambda' t_{irr}})}{\mathrm{X}*\rho_A*(1-e^{-\lambda t_{irr}})*A'*M'} \qquad (41)$$

The cross-section uncertainty is estimated with the propagation error calculation. Since all the parameters of (41) are independent, the total error is expressed as a quadratic sum and is presented in (42):

$$\frac{\Delta\sigma}{\sigma} = \sqrt{\left(\frac{\Delta\sigma'}{\sigma'}\right)^2 + \left(\frac{\Delta A}{A}\right)^2 + \left(\frac{\Delta A'}{A'}\right)^2 + \left(\frac{\Delta\rho_A}{\rho_A}\right)^2 + \left(\frac{\Delta\rho'_A}{\rho'_A}\right)^2} \qquad (42)$$

The main uncertainties come from the measured activities that are less than 10% in most cases and the uncertainty on the recommended cross-section values. Since no uncertainties are given for the recommended cross-section values, 10% error is taken as an average value from the ones used in the literature (18). It usually derives from the average of the higher error of the experimental points closest to the investigated experimental point for each measured point.

3.1.1 Experimental setup

The target material selected is gadolinium as we are interested in the yield calculations for the production of terbium radionuclide interesting for medicine which can be produced with a 70 MeV cyclotron: Tb-149, Tb-152, Tb-155. Indeed, as discussed in the previous chapter, the considered route to produce terbium radionuclides is to irradiate with proton beam between 30 and 70 MeV a gadolinium target. In literature are available cross-section data only for the production of Tb-152 and Tb-155 from natural gadolinium, while data are scarce and not very accurate for Tb-149 (73) (75). The choice of purchasing very thin gadolinium foils of 2 µm are related to the Tb-149 quantification. Indeed, as Tb-149 is an alpha emitter with 16.7 % branching ratio, in this work the cross-section natGd(p,x)Tb149 is estimated from the foil counting in the alpha detector. Therefore, the thickness of the foils should be as thin as possible for quantifying the produced activity of Tb-149. This is due to the dramatic alpha particle slowing down power in the matter. In a previous test a 25 µm gadolinium foil was irradiated and measured at the alpha spectrometer. The result was a flat peak in the detected energy range up to 3.967 MeV, making the quantification of Tb-149 activity impossible (*Figure 41*). For this reason, after SRIM simulations, it was found that with 2 µm foils a clear peak must be identified. In this case, clear broad peak was obtained (*Figure 42*). The broadening is coming from the energy loss of the alpha particle within the target itself.

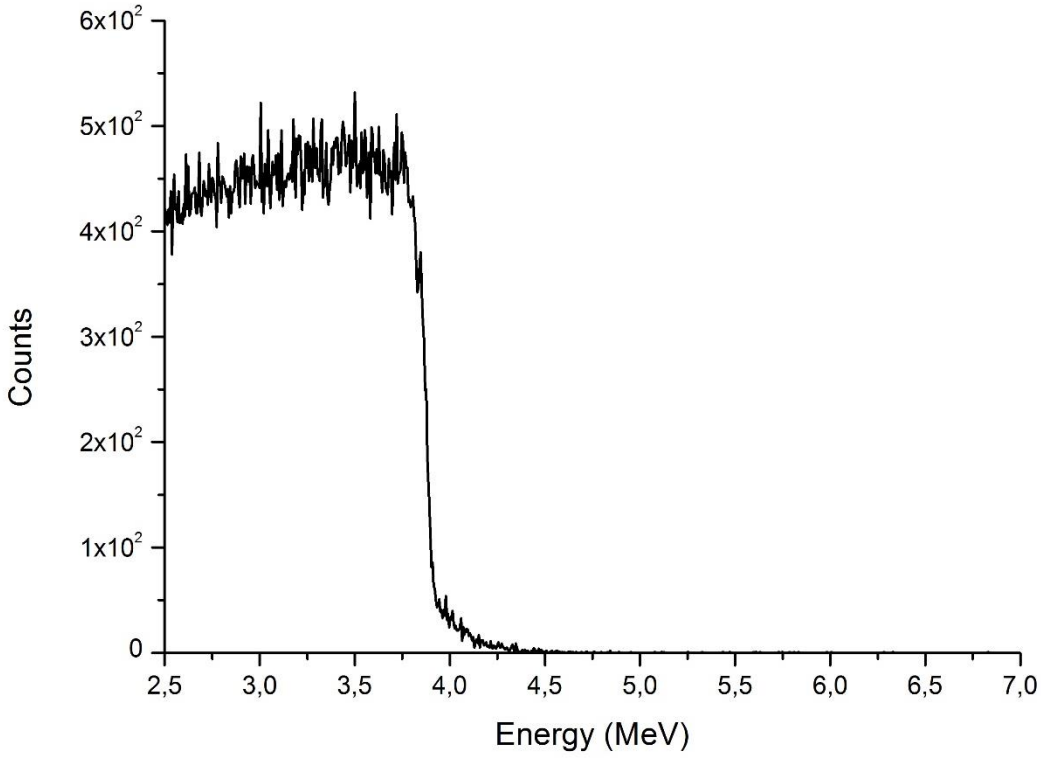

Figure 41: alpha spectrometry spectrum obtained from the measurement of a 25 µm gadolinium foil

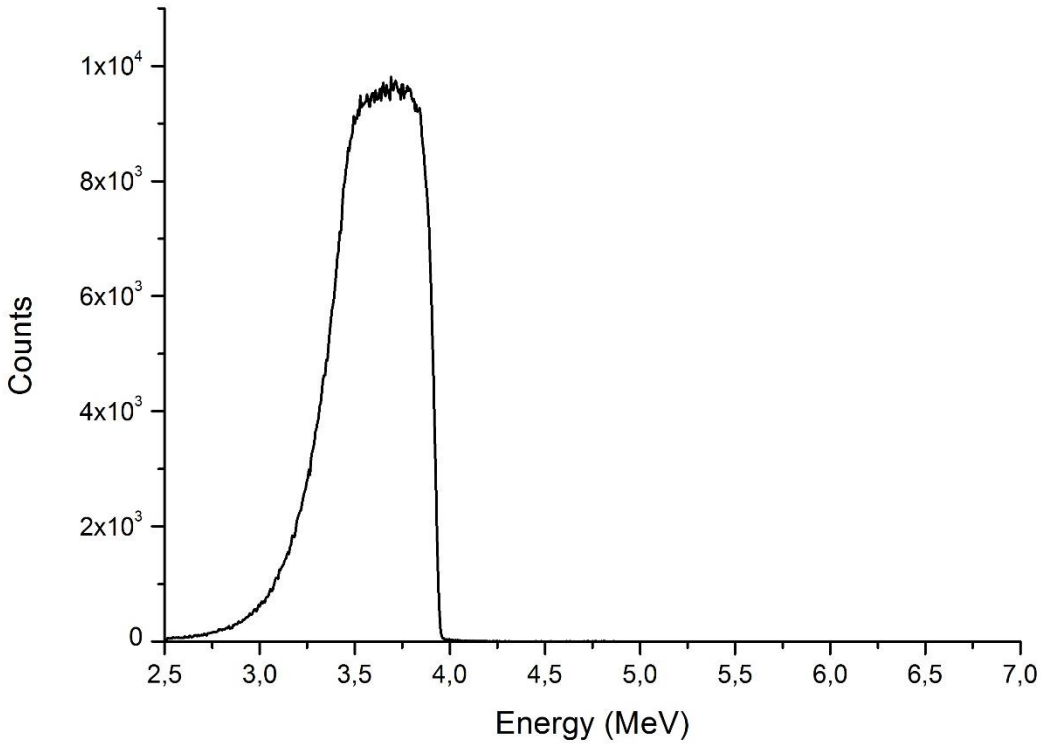

Figure 42: alpha spectrometry spectrum obtained from the measurement of a 2 µm gadolinium foil

The monitor and the catcher foils used were of 10 µm of thickness. From past experiences, this is the optimal thickness for manipulating in an easy way the foils while minimizing the loss of beam energy in the foils.

The chosen monitor for this work is nickel as it presents a suitable cross-section, the natNi(p,x)Ni57 (*Figure 43*), for incident proton beam in the range 30-70 MeV. It presents a quite high cross-section in the considered energy range, allowing to have higher statistic consistency for their activity gamma spectrometry measurement. Furthermore, the considered energy range is after the cross-section peak, which is the zone where the error and the difference between the curves is the highest. Thus, the selected energy range is where the propagation error of the measured cross-section will be lower.

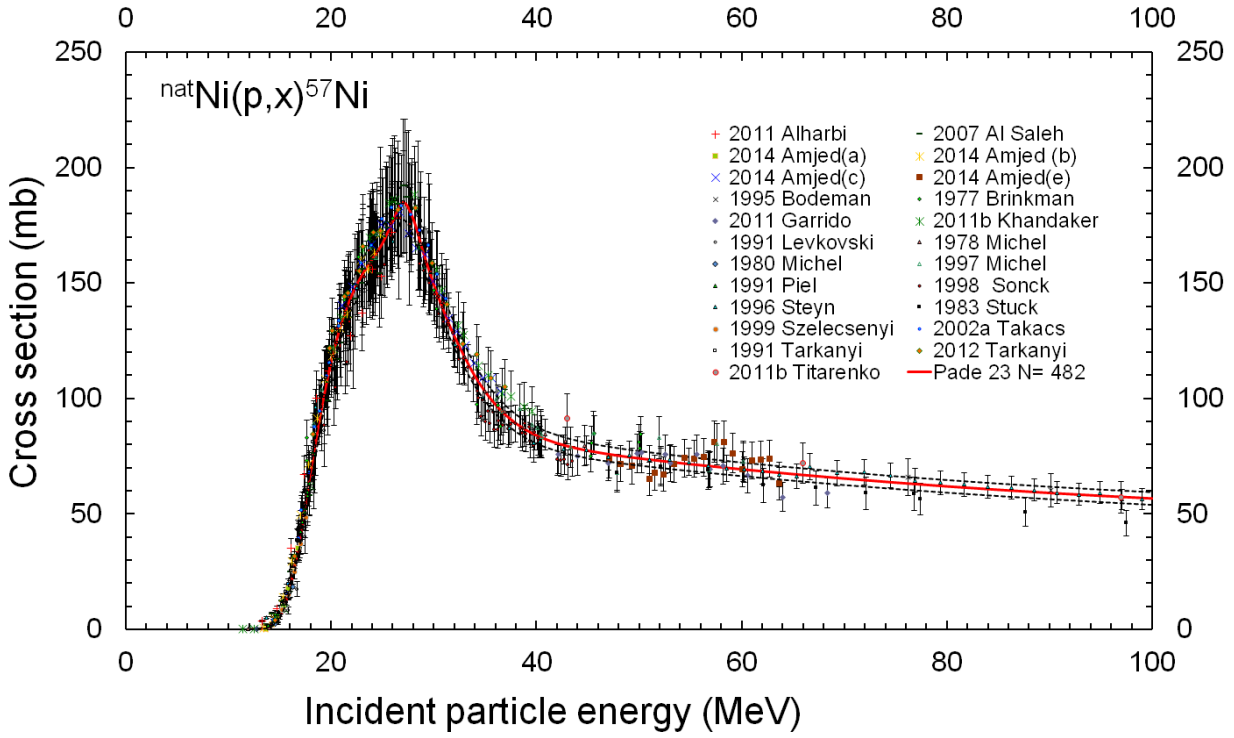

Figure 43: monitor reaction cross-section of reference for the reaction natNi(p,x)Ni57. (74)

Aluminum was chosen as catcher and degrader material. It does not interfere with the target and monitor foil, it is largely available in the laboratory stock, it is not an expensive material and have high thermal conductivity.

The stacked foils system used for the experiment is a system that is placed at the end of the beam line in air. For this reason, a thin Kapton window is used to maintain the vacuum inside the beam line and not to degrade significantly the energy of the beam. The system has been systematically put at 7 cm of distance from the beam line end. For defining the thickness of the degrader to be

used, the energy degradation along the stack is calculated with the software Stopping and Range of Ions in Matter (SRIM) (76). The simulations made with SRIM take into account the beam exit window made of kapton (75 µm thick) and the air layer between the beam line end and the first foil of the stack. The values of beam energy in each foil is given by calculating the average energy of entry and exit of 1000 events (1000 incident protons), then the energy is given by $\frac{E_{IN}+E_{OUT}}{2}$. The energy error is given by the error propagation, considering the initial error of the beam energy of 0.5 MeV for the C70 cyclotron (77).

The foils used for the experiments were purchased from Goodfellow. (78) They are squared foils of 25x25 mm^2 with variable thickness. For the irradiation made in this work the foils presented in *Table 17* have been chosen.

Table 17: foils material and thickness used for the stacked foils experiments done within this work.

Type of foil	material	Thickness (µm)
Target	Gadolinium	2
Monitor	Nickel	10
Catcher	Aluminum	10
Degrader	Aluminum	200 500 800

The thickness of the degrader foils used are 800 µm for the first two experiment, 200 and 500 µm for the third experiment. Those thicknesses guaranty an energy difference between experimental points of 1 to 2 MeV, allowing the elaboration of experimental curves with 9 experimental points.

The first step is to measure accurately each foil thickness. The foils have been scanned with a scanner, to accurately determine the surface, and weighted. The data are elaborated with an internally developed Matlab program at SUBATECH. This allows obtaining accurate values with very small error compared to the 15% - 25% thickness error usually given by the foils provider. Indeed, with the method, the error of the measured thicknesses are between 0.33% and 0.36%. The measured thicknesses and masses of the used target and monitor foils are presented in the following table.

Table 18: thicknesses and masses of the foils used in each experiment

Foil name	1st experiment		2nd experiment		3rd experiment	
	Thickness (µm)	mass (mg)	Thickness (µm)	mass (mg)	Thickness (µm)	mass (mg)
Gd-1	1.9	9.1	2.1	10.5	1.9	9.1
Ni-1	10.8	60.3	10.6	59.3	10.8	60.3
Gd-2	2.01	10.3	2.0	10.2	2.0	10.3
Ni-2	10.8	59.9	10.8	60.6	10.7	59.9
Gd-3	2.0	10.2	1.9	9.8	2.0	10.2
Ni-3	10.6	59.3	10.7	59.9	10.6	59.1
Gd-4	2.0	10.5	2.1	10.5		
Ni-4	10.8	59.6	10.6	59.9		

The catcher foils analysis showed that no other radionuclides than what has been activated in the aluminum foils was present (below the detection limit). This confirmed that the effect of foil sputtering with a proton beam up to 70 MeV was negligible. After weighting, the stack is assembled according to Figure 44.

Figure 44: preparation of the stacked foils, on the left the stack assembling, on the right of the mounted stacked which will be irradiated

The experimental setup must be installed inside the bunker. An Al_2O_3 (known as alumina) disk with geometry similar to the stacked foils is positioned at the irradiation position to take advantage of the fluorescence light emitted when beam strikes the alumina. This allows the suitable beam shaping setup from the control room, verifying that the beam size and shape is adequate at the target position. The alignment of the alumina is achieved by the use of a laser positioned on the wall and calibrated with the center of the beam line (*Figure 45*). When the beam is ready, a beam dump made of aluminum is positioned after the stacked. This will act as beam current monitor too (*Figure 46*). The current readout is performed using a digital current readout located in the experimental room next to the bunker.

Once the irradiation is over, after two hours of cooling time from EOB the stacked is dismounted. In this way the dose received by the manipulation of the stacked foils is reduced as some short-lived radionuclides have decayed, while not losing much of Tb-149, which is the researched radionuclide. Every foil is positioned in a dedicated plastic box and they are counted at gamma and alpha detectors several times for 1 to 12 hours. The foils are also counted many times in order to verify the decay of the detected radioisotopes.

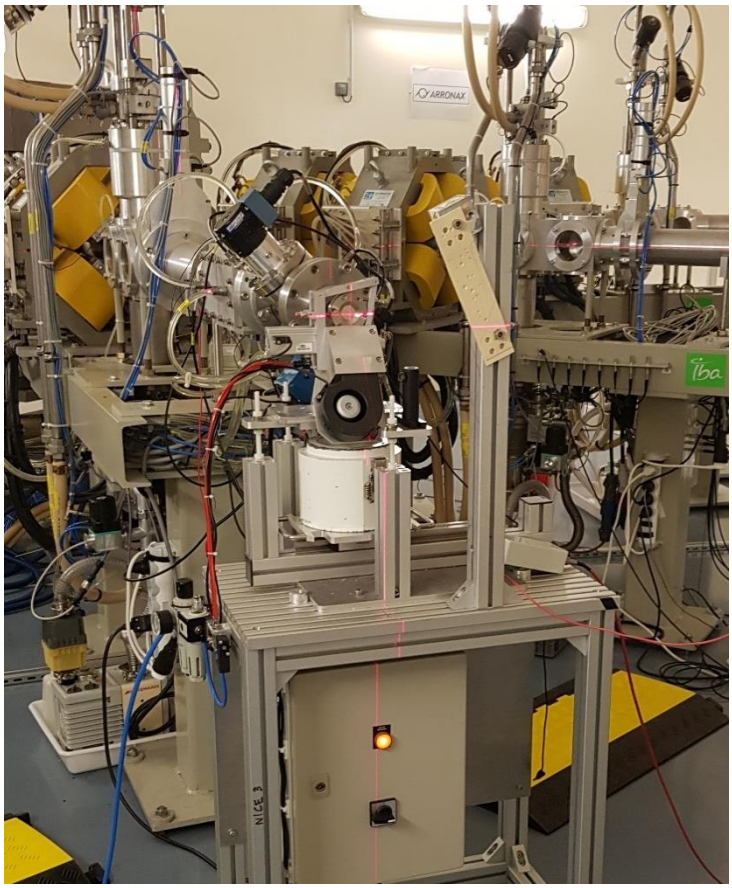

Figure 45: laser alignment before the beam tuning

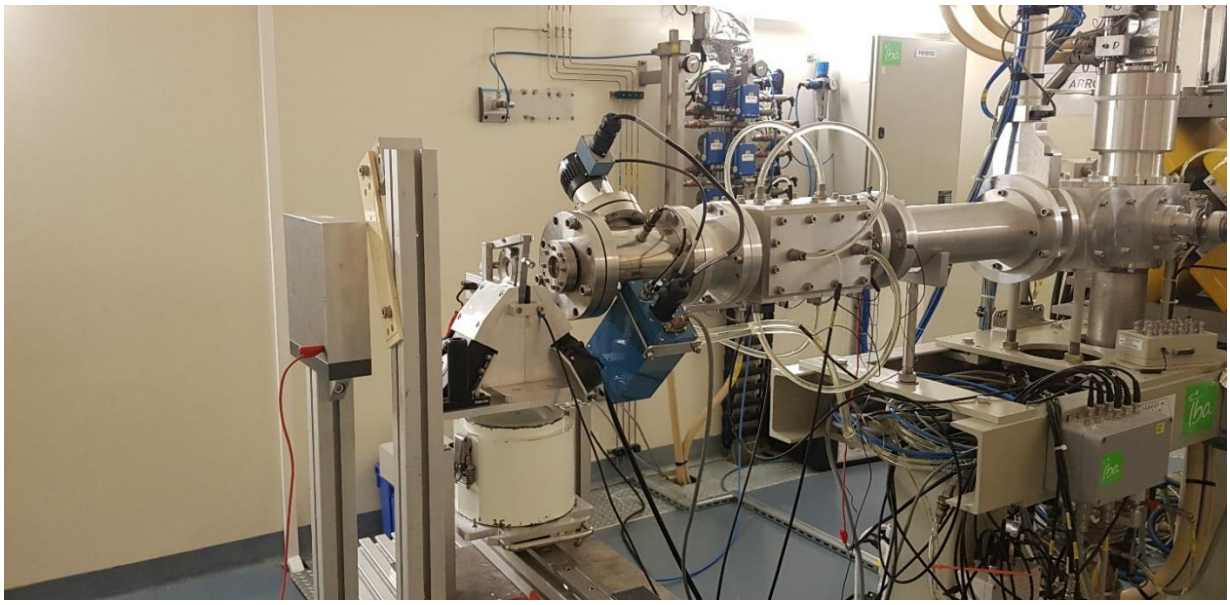

Figure 46: experimental setup for the stacked foils irradiation

3.2 Monitor foils measurement

Two days after each experiment, the monitor foils were counted for 4 to 12 hours. This because the half-life of Ni-57 (35.6 h) allows a longer cooling time for the monitor foils compared to the cooling time of the target foils. The spectrums were analyzed with FitzPeaks, and the Ni-57 activity measured with its error was used to calculate the proton beam current checking the consistency along the stack and the coherence with the beam dump measurement, measured through the instrumented aluminum beam dump. Hereafter are presented the three graphics obtained from the analysis of the three experiments. It is possible to see that the average current for each experiment is in the error bars of each measurement point. For the beam dump 5% error bar has been taken from past experiences already made in ARRONAX (18). Thus, the beam size was small enough, below the aperture of the stacked holding. The straggling of the beam along the stacked could be then neglected.

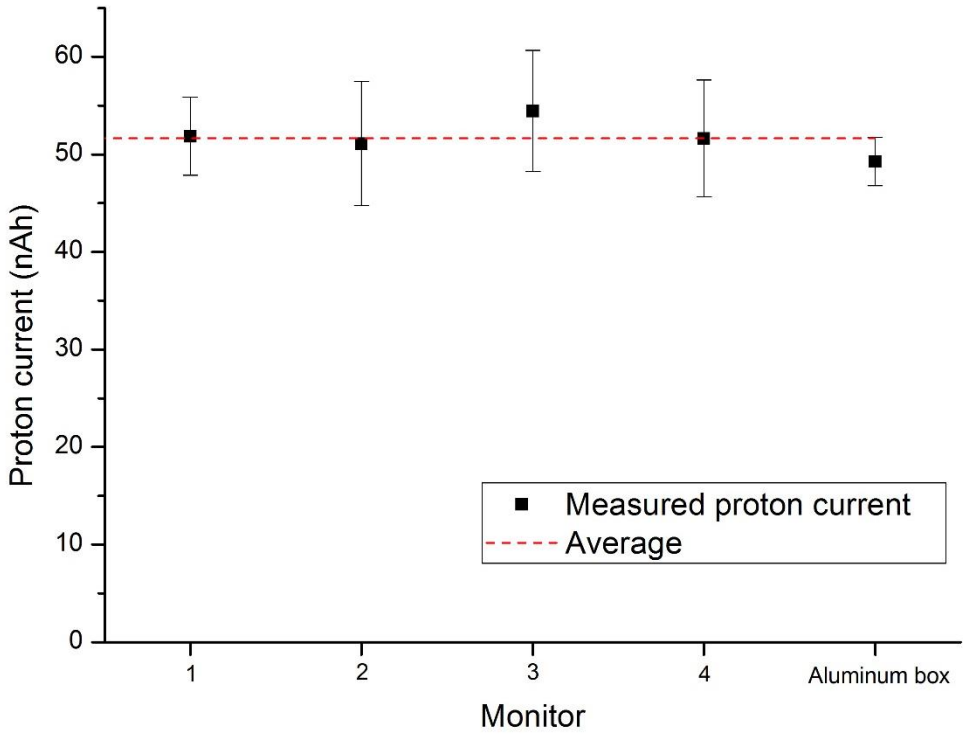

Figure 47: integrated proton current measurement from monitor foils of the first experiment

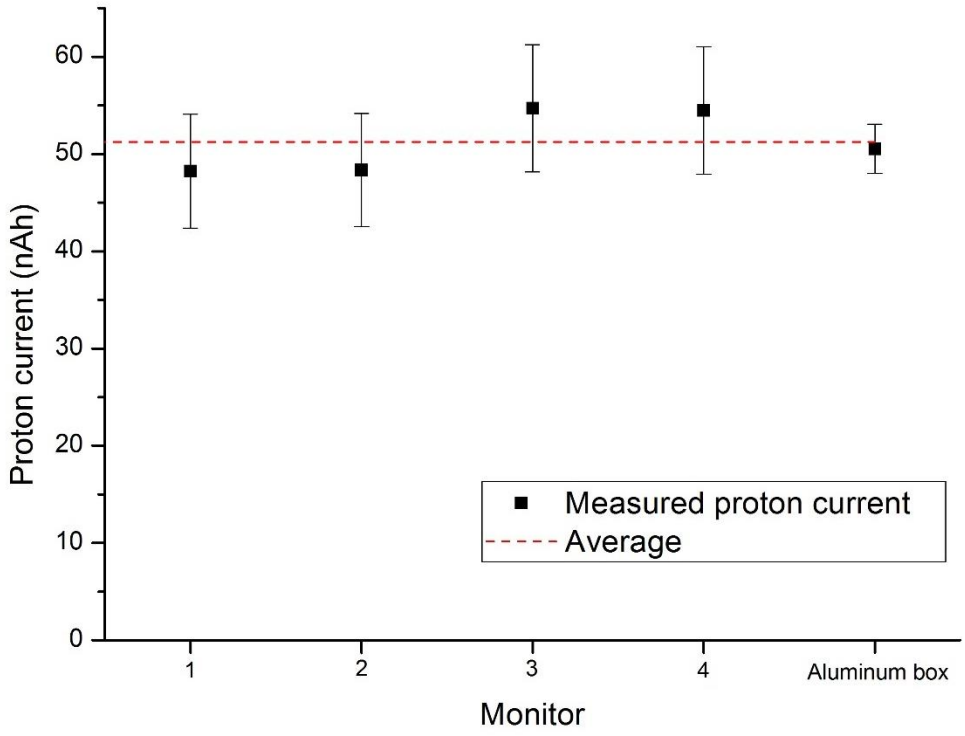

Figure 48: integrated proton current measurement from monitor foils of the second experiment

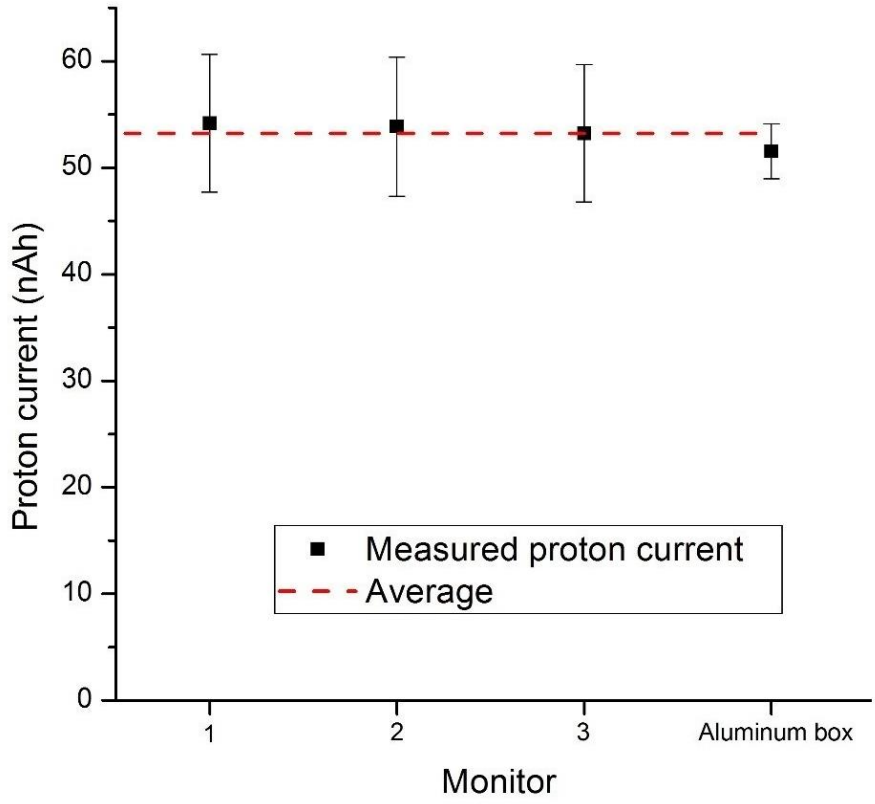

Figure 49: integrated proton current measurement from monitor foils of the third experiment

3.3 Cross-section evaluations

The foils have been counted using the alpha spectrometer for the identification and quantification of exclusively the Tb-149 produced. In parallel, they have been counted at the gamma spectrometer for the identification and quantification of the other terbium radionuclides produced.

With the first counting during the day of the irradiation, short-lived radionuclides such as Tb-149 and Tb-150 can be better quantified, whereas in the following measurements the longer-lived radionuclides can be quantified with more accuracy. The quantification of Tb-149 activity has been made from the peak area obtained with APEX software as explained in the first chapter. It was detected also with gamma spectrometry, however as the error of the activity calculated from the peaks at 165 keV (26.4 %), 388.5 keV (18.4 %), 853 keV (15.5%) is too high, only the alpha spectrometry results are reported.

3.4 Tb-149 cross-section

The Tb-149 cross-section from natural gadolinium with proton beam between 70 and 58 MeV is the main aim of this investigation due to the lack of data. The only experimental points available in the literature for this reaction are made by Mironov *et.al.* (75). In their analysis they used surface-barrier Au-Si detector for the detection of Tb-149 alpha particle emissions. However, their

points are not present in every database. The values used for comparison in this work are taken from Janis 4.0 database in the section proton induced reaction, EXFOR data (79).

The results of the alpha spectrometry can be quantified as Tb-149 has the most energetic alpha emission among the irradiation co-products detectable, namely 3.967 MeV. The list of the alpha emitter potentially co-produced, or generated from decay of other produced radionuclides in the considered beam energy range, are reported in Table 19 with their energy and intensity emission.

Table 19: alpha emitters potentially co-produced with a 70-58 MeV proton beam and natural gadolinium target.

Element	Isotope	Half-life	Energy (MeV)	Branching ratio
Terbium	Tb-149	4,12 h	3,967	16,70%
	Tb-149 m	4,2 m	3,999	0,02%
	Tb-150	3,48 h	3,492	0,05%
	Tb-151	17,81 h	3,407	0,009%
Gadolinium	Gd-148	71.1 y	3,182	100%
	Gd-149	9.28 d	3,016	0,0004%
	Gd-150	1.76E6 y	2,726	100%
	Gd-151	120 d	2,6	0,00%
Europium	Eu-147	24.1 d	2,908	0,0022%
	Eu-148	54.5 d	2,63	0,00%
Samarium	Sm-146	6.8E7 y	2,46	100%

As shown in Table 19 the other alpha emissions are negligible. The only emission more energetic than the one of interest is from Tb-149m. It decays 99.98 % ε in Gd-149 and 0.02% α in Eu-145. Nevertheless, its half-life is 4.2 minutes. As the first foil measurement is made after 2 hours, the contribution of this radionuclide can be considered negligible both due to its intensity and its decay. Particular attention has been made only on Tb-151 emission. Indeed, its energy is situated in the tail of Tb-149 emission, and it smoothly influences the measurement during the last counting, 1 day after EOB. In that case Tb-149 was almost fully decayed and Tb-151 was still quite present. For this reason, to calculate the Tb-149 activity the detected counts were subtracted by the counts generated by Tb-151, which activity was estimated by gamma spectrometry. In order to prevent any source of error due to a potential contamination of the spectrometer chamber, one measurement of the empty chamber was performed after each last measurement of each experiment, thus the background was subtracted. The effect of those two factors was evident because allowed the consistency of the calculated Tb-149 activities along each measurement.

The reactions leading to the production of Tb-149 and their respective threshold energy E_{th} below 70 MeV are listed hereafter:

- Gd152(p,4n)Tb149: E_{th} = 28.4 MeV
- Gd154(p,6n)Tb149: E_{th} = 43.6 MeV
- Gd155(p,7n)Tb149: E_{th} = 50.1 MeV
- Gd156(p,8n)Tb149: E_{th} = 58.7 MeV
- Gd157(p,9n)Tb149: E_{th} = 65.1 MeV

The gadolinium foils have been counted several times in order to verify the half-life of Tb-149 and obtain cross-section values with more statistics. The obtained cross-section values in each of the three experiments are shown in Figure 50.

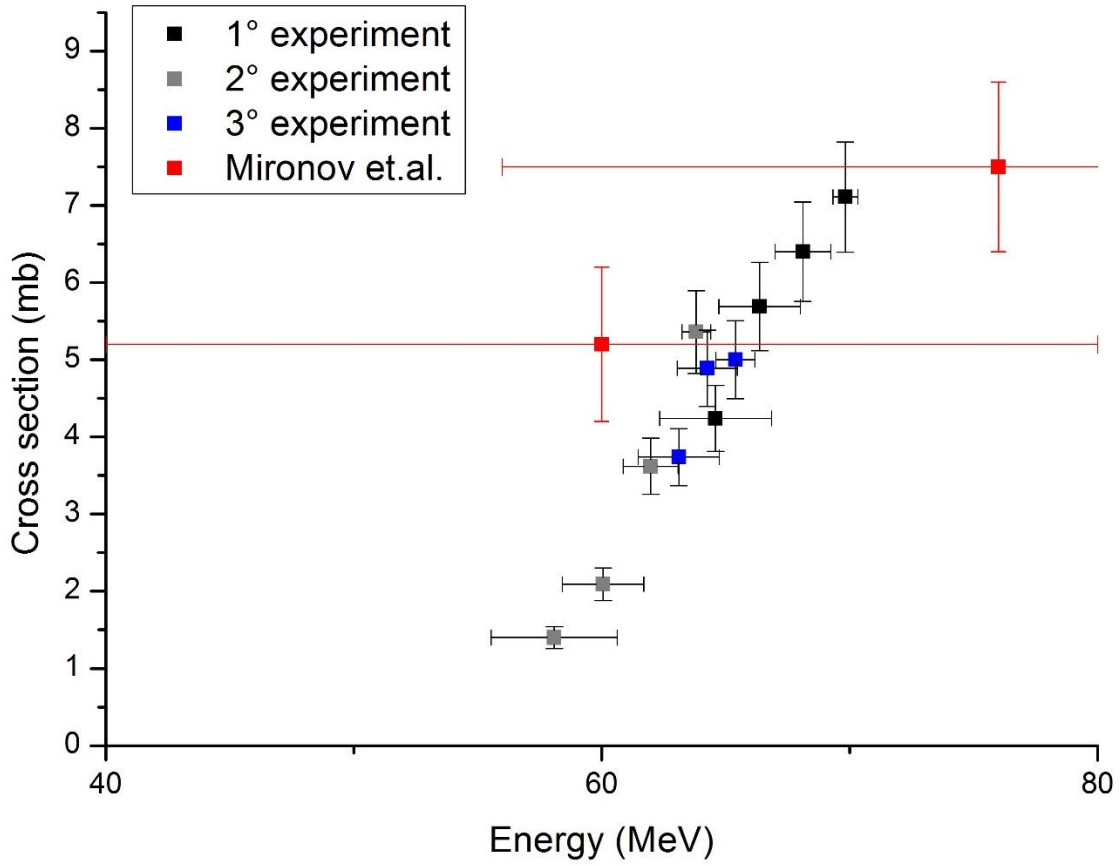

Figure 50: natGd(p,x)Tb149 cross-section

From Figure 50 it is possible to see that the experimental points obtained in this work are within the very large error bars of the experimental points of Mironov *et. al.*. Indeed, their work was performed with a 1.1 GeV proton beam on natural gadolinium target. The beam degradation up to 60 MeV induced them to consider as energy error ±20 MeV for each experimental point. By consequence the error is very small at 1.1 GeV (1.8 %), but it is very high at 60 MeV (33 %). Furthermore, from Figure 50 it is possible to highlight the coherence of the cross-section values within the three experiments.

In the following figure are presented all the experimental points measured in this work and by Mironov *et. al.*; this shows the entire activation curve behavior for the consider reaction.

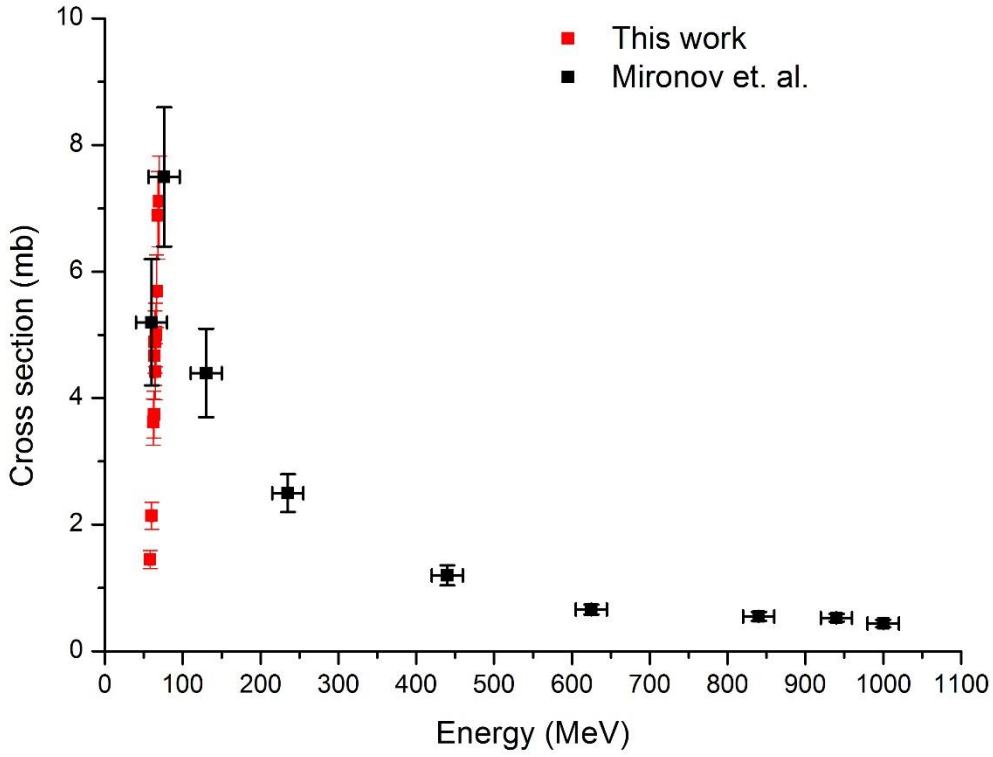

Figure 51: natGd(p,x)Tb149 cross-section points from this work and from Mironov et. al.

Table 20: list of experimental data points for the cross-section natGd(p,x)Tb149

Energy (MeV)	Cross-section (mb)
69.83 ± 0.51	7.11 ± 0.72
68.11 ± 1.13	6.89 ± 0.69
66.37 ± 1.64	5.69 ± 0.57
65.40 ± 0.79	5.00 ± 0.50
64.59 ± 2.26	4.42 ± 0.44
64.26 ± 1.21	4.89 ± 0.49
63.82 ± 0.58	4.67 ± 0.47
63.11 ± 1.64	3.74 ± 0.37
61.98 ± 1.11	3.62 ± 0.36
60.05 ± 1.64	2.14 ± 0.22
58.08 ± 2.55	1.45 ± 0.15

The values of the measured cross-sections are presented in Table 20. As shown in the graphic and in the table the cross-section values are quite low, for this reason a thorough analysis should be

made to evaluate whether this production route can give high enough yields of Tb-149 or enriched starting material should be considered instead.

3.5 Gamma spectrometry results

The terbium radionuclides produced from the natural gadolinium target present a large number of gamma ray emission, often at the same or close energy of other emission from other radionuclides. For this reason, all the produced radionuclides where identified with FitzPeaks. However, as the activity error calculated by the software is usually too high, the activity was estimated from hand calculations after the peak search and fitting done with FitzPeaks. For some radionuclides the activity found for a gamma ray was subtracted by the activity of the radionuclides with the interference gamma ray. The nuclear data for the investigated radionuclides are listed in Table 21. They are all the produced terbium contaminants. Other element's radionuclides are co-produced and were identified. However, as they can be chemically separated or in case of mass separation they are not detected as separate isobars and we don't need their quantification. For the evaluation and comparison of the gamma rays, two databases were used: NNDC database and the Lund/LBNL Nuclear Data Search (25) (80).

Table 21: gamma rays energy and intensity used for the quantification of the activity of the listed radionuclides

Radionuclide	Half-life	Energy (keV)	Intensity (%)
Tb-150	3.48 h	638	72
		496	14,6
Tb-151	17.61 h	251,86	26,3
		287,35	28,3
Tb-152	17.5 h	271,13	8,6
		344,27	65
		586,26	9,4
Tb-153	2.3 d	212	31
Tb-154	21 h	1291,3	6,9
		1123	6,1
Tb-154m	22.7 h	225,9	26,8
Tb-155	5.32 d	180	7,45
		367	1,48
Tb-156	5.35 d	199,21	40,9
		356,42	13,6
		534,32	66,6

The cross-section values obtained, using equation (40) and their error using equation (41), during the whole experimental campaign are resumed in Table 22 and in Table 23 and explained in the next paragraphs. An example of spectrum obtained during one gamma spectrometry measurement is given in the following figure.

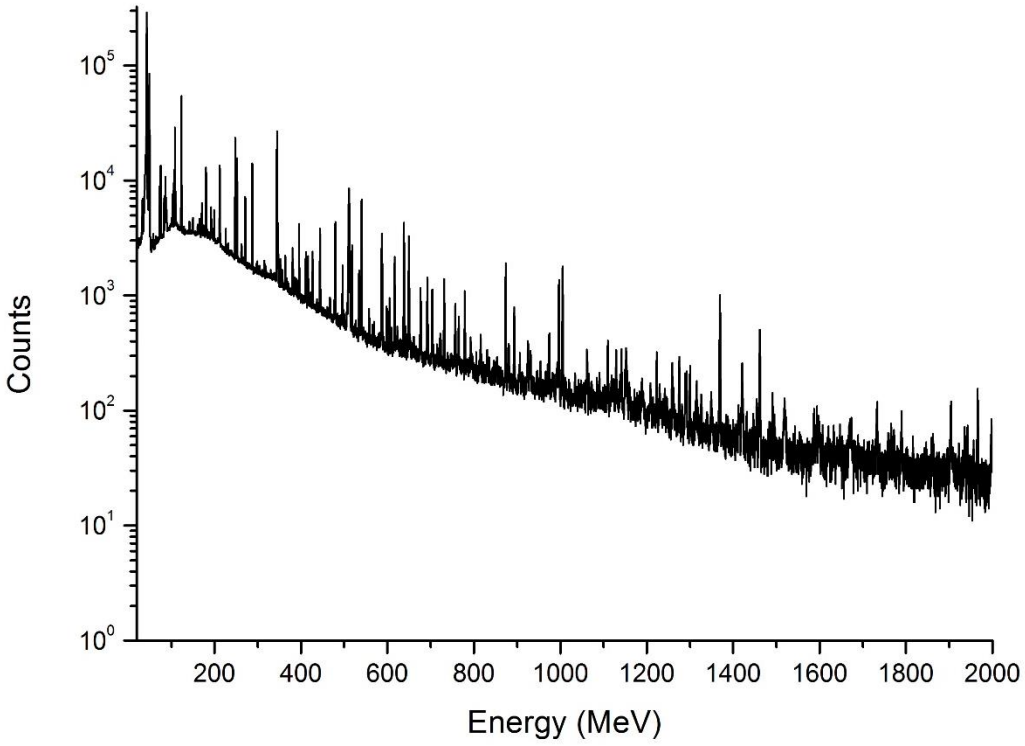

Figure 52: example of a spectrum obtained by gamma spectrometry of one of the target foils

Table 22: measured cross-section values (in mb) for Tb-149, Tb-151, Tb-152 and Tb-153

Energy (MeV)	**Tb-150**	**Tb-151**	**Tb-152**	**Tb-153**
58.2 ± 2.5	21.0 ± 2.1	95.8 ± 9.8	122.3 ± 12.3	171.3 ± 17.4
60.1 ± 1.6	18.3 ± 1.9	83.9 ± 8.9	118.4 ± 12.0	148.3 ± 14.9
62.0 ± 1.1	22.6 ± 2.3	100.6 ± 10.4	118.0 ± 11.6	164.7 ± 17.2
63.8 ± 0.6	27.3 ± 2.8	106.5 ± 10.8	119.5 ± 13.2	167.5 ± 19.3
63.1 ± 1.6	23.3 ± 2.4	105.0 ± 11.3	124.0 ± 14.1	159.0 ± 16.2
64.3 ± 1.2	26.9 ± 2.7	108.1 ± 10.9	121.9 ± 12.3	167.6 ± 17.3
65.4 ± 0.8	20.7 ± 2.4	98.0 ± 10.0	115.3 ± 11.9	146.0 ± 14.8
66.4 ± 1.6	26.4 ± 2.7	107.6 ± 10.9	118.3 ± 11.9	146.7 ± 14.8
68.1 ± 1.1	28.3 ± 2.9	102.3 ± 10.4	117.9 ± 11.9	137.8 ± 14.0
69.8 ± 0.5	30.8 ± 3.1	96.0 ± 9.9	114.0 ± 11.5	123.9 ± 12.9

Table 23: measured cross-section values (in mb) for Tb-154 (total cross-section), Tb-154m2, Tb-155 and Tb-156

Energy (MeV)	Tb-154	Tb-154m2	Tb-155	Tb-156
58.2 ± 2.5	32,9 ± 5,1	9,5 ± 1,4	152,4 ± 15,9	68,8 ± 8,0
60.1 ± 1.6	29,6 ± 3,3	10,4 ± 1,7	117,1 ± 12,2	59,8 ± 6,0
62.0 ± 1.1	34,1 ± 4,1	9,3 ± 1,7	146,9 ± 15,7	67,0 ± 7,3
63.8 ± 0.6	32,8 ± 3,3	9,5 ± 1,3	137,3 ± 14,0	55,7 ± 5,9
63.1 ± 1.6	31,7 ± 4,5	11,5 ± 1,7	138,4 ± 14,1	61,5 ± 7,4
64.3 ± 1.2	38,2 ± 6,0	10,7 ± 1,1	130,4 ± 13,6	60,6 ± 7,3
65.4 ± 0.8	34,5 ± 4,4	12,1 ± 1,3	115,3 ± 12,9	56,3 ± 6,0
66.4 ± 1.6	45,6 ± 6,5	11,7 ± 1,3	135,3 ± 14,0	59,7 ± 6,3
68.1 ± 1.1	45,5 ± 9,0	10,8 ± 1,2	134,6 ± 15,1	54,0 ± 6,3
69.8 ± 0.5	35,3 ± 5,0	10,9 ± 1,4	114,8 ± 11,8	48,7 ± 5,1

3.5.1 Tb-150

Tb-150 (half-life 3.48 h) decays almost 99.95% ε and 0.05% α. Currently no experimental data have been found in the literature and in the databases to compare the experimental point obtained for the reaction natGd(p,x)Tb150. The activity of Tb-150 has been determined by the two peaks at 496 keV (14,6%) and 638 keV (72%). To the total counts obtained analyzing the spectrum, the following contribution have been subtracted to the integrated area of the peaks:

- Peak 496 keV: Tb-151 (0,3%), Tb-152 (0,1%)
- Peak 638 keV: Tb-151 (0,023%), Tb-153 (0,2%)

This can be accurately determined as the radionuclides emitting interference gamma rays can be quantified with unique gamma as it will be shown in the following paragraphs. The two databases used were not in agreement for the gamma ray intensities of Tb-150. Indeed, on LBNL the intensities were a factor 100 lower than the one on NNDC. For this reason, only NNDC database was considered for Tb-150.

Tb-150 has a metastable state which has a very short half-life (5.8 m) hindering his detection. It decays ε in Gd-150. The reactions leading to the production of Tb-150 and their respective threshold energy E_{th} below 70 MeV are listed hereafter:

- Gd152(p,3n)Tb150: E_{th} = 20.6 MeV
- Gd154(p,5n)Tb150: E_{th} = 35.9 MeV
- Gd155(p,6n)Tb150: E_{th} = 42.3 MeV
- Gd156(p,7n)Tb150: E_{th} = 50.9 MeV
- Gd157(p,8n)Tb150: E_{th} = 65.3 MeV

The cross-section curve is presented in Figure 53.

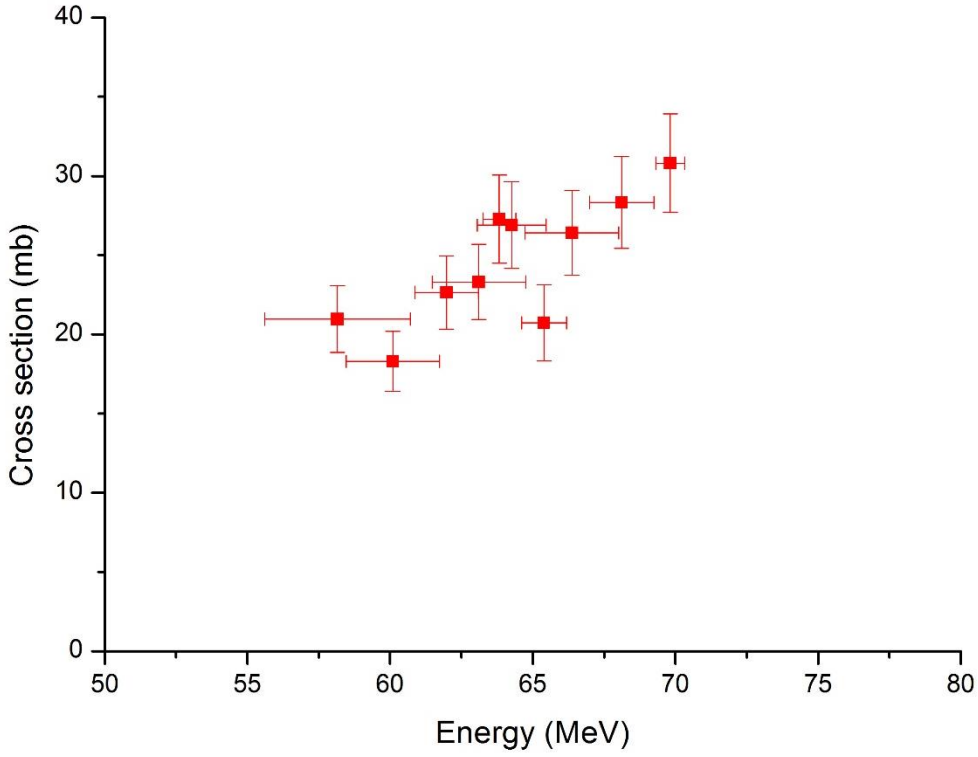

Figure 53: cross-section for the reaction natGd(p,x)Tb150

3.5.2 Tb-151

Tb-151 (half-life 17.6 h) decays 99.991% ε in Gd-151 and 0,009% α in Eu-147. In addition to the ground state, one metastable state (half-life 25 s) is also produced. The metastable state decays rapidly to the ground state by internal transition with branching ratio 93.4 %, and to Gd-151 through ε decays 6.6 %. Due to the short half-live of the metastable state only the cumulative cross-section for the production of the ground state could be measured. Tb-151 could be produced by the following nuclear reactions with the respective threshold energies:

- 152Gd(p,2n)Tb151: E_{th} = 12.0 MeV
- 154Gd(p,4n)Tb151: E_{th} = 27.2 MeV
- 155Gd(p,5n)Tb151: E_{th} = 33.7 MeV
- 156Gd(p,6n)Tb151: E_{th} = 42.3 MeV
- 157Gd(p,7n)Tb151: E_{th} = 48.7 MeV
- 158Gd(p,8n)Tb151: E_{th} = 56.7 MeV.

The experimental results compared to the curve presented by Vermeulen *et. al.* are shown in the Figure 54.

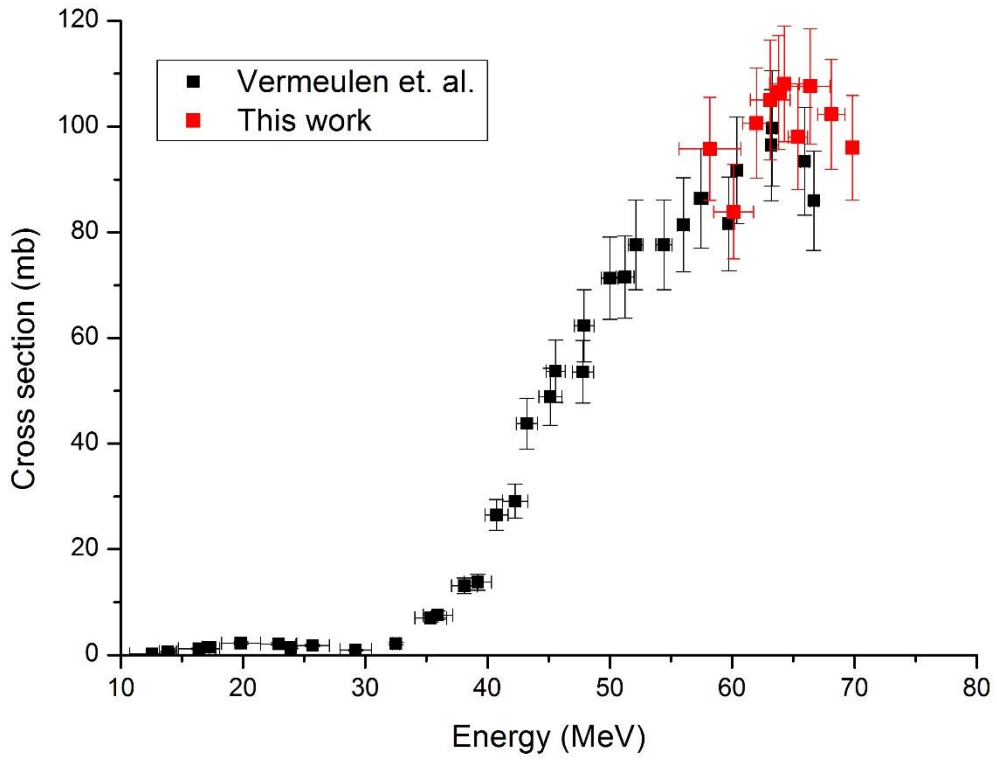

Figure 54: cross-section for the reaction natGd(p,x)Tb151

As shown in Figure 54, the experimental points obtained in this work are in good agreement with the values obtained by Vermeulen *et. al.*. This gives more confidence to the data analysis performed.

3.5.3 Tb-152

Tb-152 (half-life 17.5 h) decays almost 100 % ε in Gd-152 and 7E-7% α in Eu-148. In addition to the ground state, one metastable state (half-life 4.2 m) is also produced. It decays to the ground state by internal transition with branching ratio 78.8 %, and to Gd-152 through ε decays 21.2 %. Due to the short half-live of the metastable state only the cumulative cross-section for the production of the ground state could be measured.

Tb-152 could be produced by the following nuclear reactions with the respective threshold energies:

- 152Gd(p,n)Tb152: E_{th} = 4.8 MeV
- 154Gd(p,3n)Tb152: E_{th} = 20.0 MeV
- 155Gd(p,4n)Tb152: E_{th} = 26.5 MeV
- 156Gd(p,5n)Tb152: E_{th} = 35.1 MeV

- 157Gd(p,6n)Tb152: E_{th} = 41.5 MeV
- 158Gd(p,7n)Tb152: E_{th} = 49.5 MeV
- 160Gd(p,9n)Tb152: E_{th} = 62.9 MeV

The experimental results compared to the curve presented by Vermeulen *et. al.* are shown in Figure 55. Challan *et.al.* (81) investigated the production of Tb-152 too. Nevertheless, their study was based on proton beam up to 18 MeV, which is very far from this work and compared to the values above 30 MeV that part of the curve is negligible. This is mainly due to the low natural abundances of Gd-152 and Gd-154.

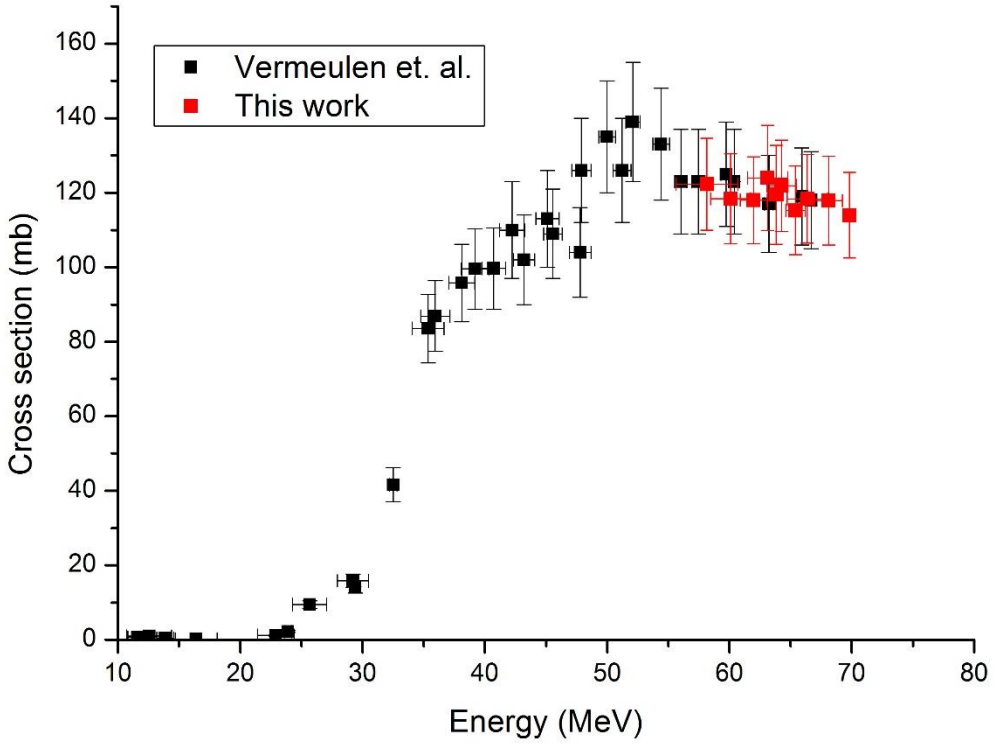

Figure 55: cross-section for the reaction natGd(p,x)Tb152

As presented in Figure 55 the results obtained in this work are in well agreement with the curve made by Vermeulen *et. al*.. From this cross-section is clearly visible the contribution of the different reaction. Indeed, up to 26.5 MeV Tb-152 is produced only from Gd-152 and Gd-154, which are the lowest abundant gadolinium natural occurring isotopes (0.2% and 2.2% respectively). Then after 30 MeV the production from Gd-155 becomes the dominant one. Increasing the energy of the incident beam, other reactions are activated which contribute to the evaluated cross-section, whereas the lower threshold energy reactions decreases in intensity.

3.5.4 Tb-153

Tb-153 (half-life 2.34 d) decays 100 % through electronic conversion in Gd-153 and it has no associated metastable state. Tb-153 could be produced by the following nuclear reactions with the respective threshold energies:

- 152Gd(p,γ)Tb153: E_{th} = 0 MeV
- 154Gd(p,2n)Tb153: E_{th} = 11.3 MeV
- 155Gd(p,3n)Tb153: E_{th} = 17.8 MeV
- 156Gd(p,4n)Tb153: E_{th} = 26.4 MeV
- 157Gd(p,5n)Tb153: E_{th} = 32.8 MeV
- 158Gd(p,6n)Tb153: E_{th} = 40.7 MeV
- 160Gd(p,8n)Tb153: E_{th} = 54.2 MeV

Where the (p,xn) type reactions are the dominant ones for its production. The experimental results compared to the curve presented by Vermeulen *et. al.* are shown in Figure 56.

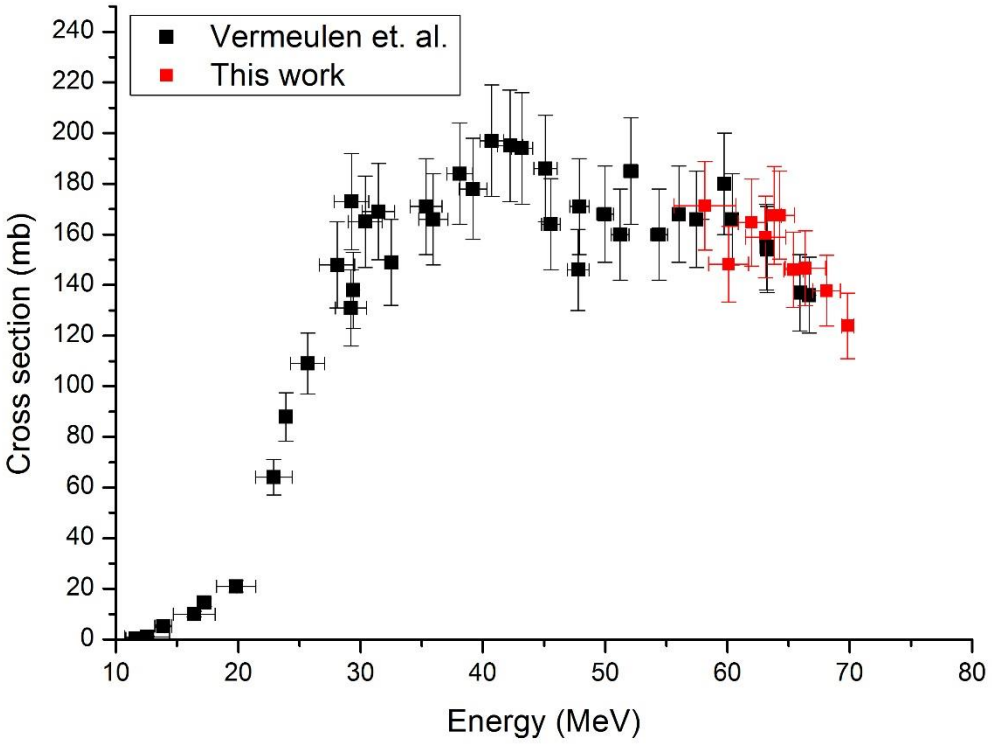

Figure 56: cross-section for the reaction natGd(p,x)Tb153

In Figure 56 is possible to see the well agreement between the experimental points of this work and the curve obtained by Vermeulen *et. al.*. All the experimental points are within the error bars of the other work values.

3.5.5 Tb-154 and Tb-154m2

Tb-154 (half-life 21.5 h) decays prevalently ε, almost 100 % in Gd-154, and less than 0.1 % β- in Dy-154 (very long-lived alpha emitter). It has two metastable states, which order depends on the database of reference, indeed in some database can they be inverted. In this work they are considered as follow: m1 (half-life 9.4 h) which decays ε with BR around 78.2 %, IT around 21.8% and less than 0.1 % β-; m2 (half-life 22.7 h) which decays ε with BR 98.2 % and IT 1.8%. For evaluating the gamma rays of the metastable states only LBNL database has been used as NNDC database reports only gamma ray emission of the ground state. Those 3 levels have very similar and often coincident gamma ray emissions, therefore they have been evaluated by the very few unique gamma rays. For the ground state the cumulative cross-section has been presented in Figure 57. In the literature no data have been found on this reaction, whereas Vermeulen *et. al.* presented the Tb-154m2 cross-section, which is compared with the experimental points obtained in this work in Figure 58. Tb-154m1 was detected by the gamma ray at 540 keV. However, the uncertainty related to the measured activity was very high. For this reason, the obtained result are not presented.

The reactions leading to the production of Tb-154 are presented hereafter with the respective threshold energies:

- 154Gd(p,n)Tb154: E_{th} = 4.3 MeV
- 155Gd(p,2n)Tb154: E_{th} = 10.8 MeV
- 156Gd(p,3n)Tb154: E_{th} = 19.4 MeV
- 157Gd(p,4n)Tb154: E_{th} = 25.8 MeV
- 158Gd(p,5n)Tb154: E_{th} = 33.8 MeV
- 160Gd(p,7n)Tb154: E_{th} = 47.2 MeV

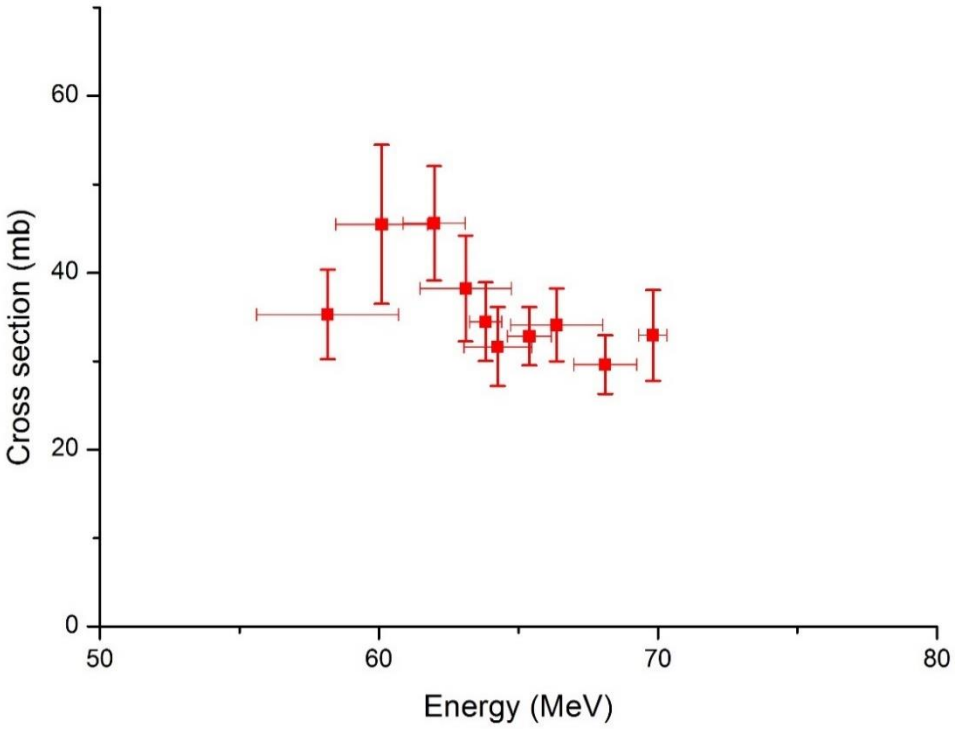

Figure 57: cumulative cross-section for the reaction natGd(p,x)Tb154

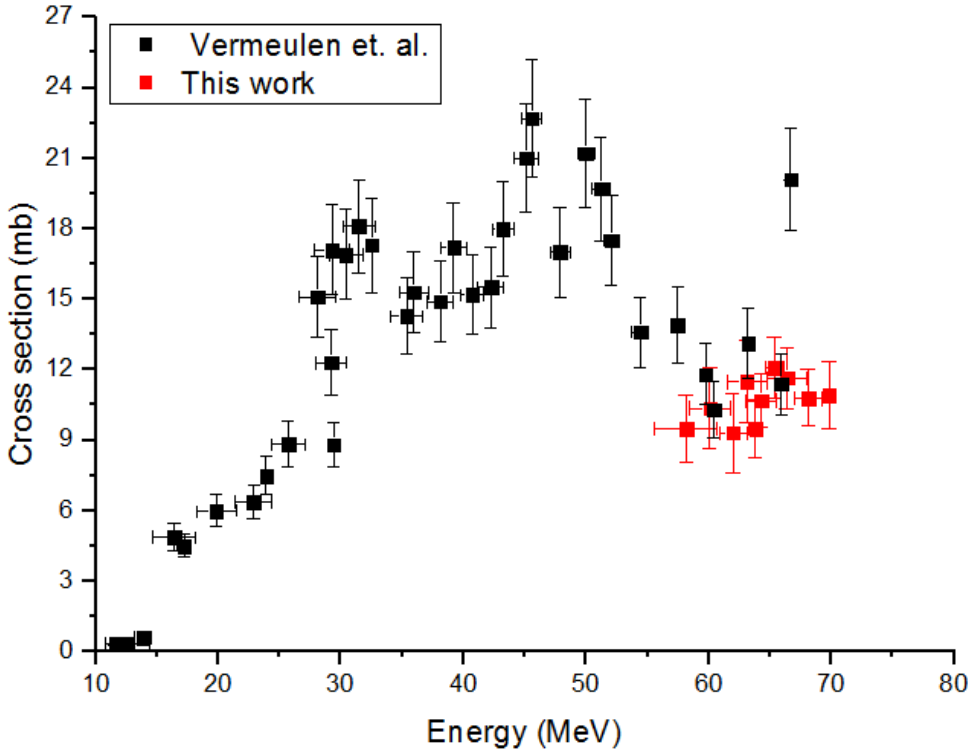

Figure 58: cross-section for the reaction natGd(p,x)Tb154m2

As for the cumulative cross-section of Tb-154 ground state there are no available comparison, only the experimental points obtained in this work are presented. For the Tb-154m2 cross-section, the obtained values are close to the one obtained by Vermeulen *et. al.*, except for one point from their work which seems far away from the curve behavior.

3.5.6 Tb-155

Tb-155 (half-life 5.32 d) decays 100 % through electronic conversion in Gd-155 and it has no associated metastable state. Tb-155 could be produced by the following nuclear reactions with the respective threshold energies:

- 154Gd(p,γ)Tb155: E_{th} = 0 MeV
- 155Gd(p,n)Tb155: E_{th} = 1.6 MeV
- 156Gd(p,2n)Tb155: E_{th} = 10.2 MeV
- 157Gd(p,3n)Tb155: E_{th} = 16.6 MeV
- 158Gd(p,4n)Tb155: E_{th} = 24.6 MeV
- 160Gd(p,6n)Tb155: E_{th} = 38.0 MeV

As for the production of Tb-153, the (p,xn) type reactions are the dominant ones for its production. The experimental results compared to the curve presented by Vermeulen *et. al.* are shown in Figure 59.

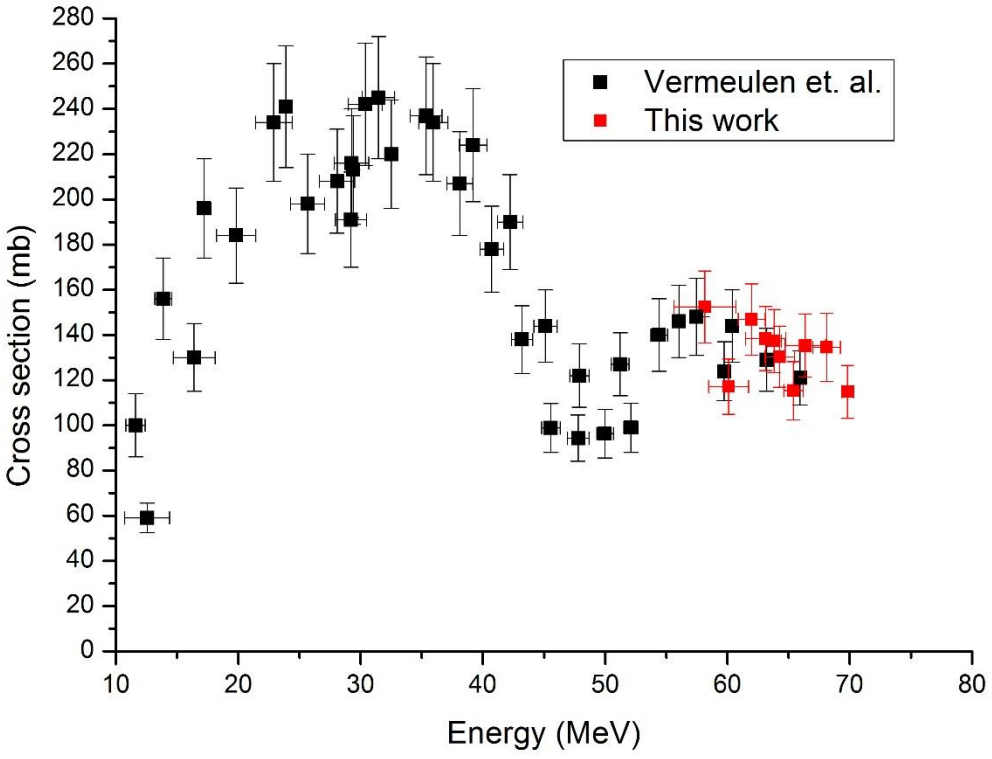

Figure 59: cross-section for the reaction natGd(p,x)Tb155

In Figure 59 is possible to see the well agreement between the experimental points of this work and the curve obtained by Vermeulen *et. al.*.

3.5.7 Tb-156 production

Tb-156 (half-life 5.35 d) decays 100 % ε in Gd-156. It has two metastable states: m1 (half-life 24.4 h) and m2 (half-life 5.3 h) which decays through IT in the ground state. Although they have a half-life allowing their detection, they emits very low energy and low intensity gamma rays, lower than 90 keV. Therefore, they are quite impossible to detect with accuracy due to the very high background and the large incertitude in that range of energy. For this reason, only the cumulative cross-section for the ground state radionuclide has been evaluated.

Tb-155 could be produced by the following nuclear reactions with the respective threshold energies:

- 155Gd(p,γ)Tb156: E_{th} = 0 MeV
- 156Gd(p,n)Tb156: E_{th} = 3.2 MeV
- 157Gd(p,2n)Tb156: E_{th} = 9.6 MeV
- 158Gd(p,3n)Tb156: E_{th} = 17.6 MeV
- 160Gd(p,5n)Tb156: E_{th} = 31.1 MeV

As previously mentioned for other radionuclides, the (p,xn) type reactions are the dominant ones for its production. The experimental results compared to the curve presented by Vermeulen *et. al.* are shown in Figure 60.

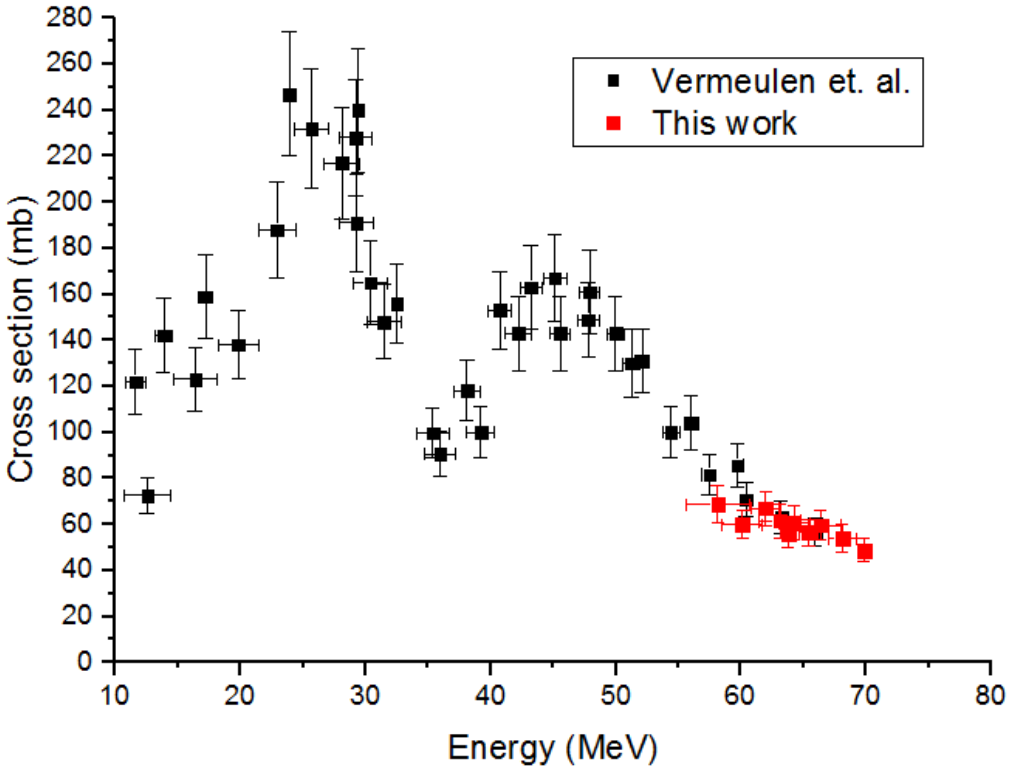

Figure 60: cross-section for the reaction natGd(p,x)Tb156

As for the previously presented cross-section values, the points presented in Figure 60 are in agreement with the curve obtained by Vermeulen *et.al.*. It is possible to see that the curves in the last point at higher energies continues accordingly to the decreasing behavior.

3.6 Conclusion

The experimental evaluation of the cross-section of terbium radionuclides production from natural gadolinium target gave a clear view on the cross-section curve for the production of Tb-149 in the energy of interest of this work. This will allow elaborating a thorough production estimation as well as contaminants estimation verifying whether natural gadolinium can be a suitable starting material or enriched material is strictly needed. The overall cross-section measurement of the other terbium radionuclides, in particular the interesting Tb-152 and Tb-155, confirmed the values already present in literature. Other cross-section has been given for the first time to our best knowledge, as the ones for the cumulative production of Tb-150 and Tb-154. Starting from the experimental cross-sections presented in this chapter, the target development process it is presented in next chapter.

CHAPTER-4

Target developments for large-scale production of terbium radionuclides

In this chapter a new large-scale production method for high specific activity and high purity radionuclides batches is proposed considering the irradiation of a target at ARRONAX cyclotron and the off-line mass separation at CERN-MEDICIS. All the theoretical steps from the target development to the achievable yield are illustrated for the radionuclides of interest listed in Table 14, namely terbium radionuclides Tb-149, Tb-152, Tb-155. The first step for the feasibility study is the target definition. It is an iterative process which takes into account several parameters: availability of the material (natural or enriched), cross-sections of the reactions of interest, achievable yields, cost of the material, target definition and thermal and mechanical resistance of the target.

4.1 Terbium radionuclides production

Among the four terbium isotopes interesting for medical applications, Tb-149, Tb-152 and Tb-155 were selected for the production from commercial cyclotron, in particular at ARRONAX facility. Thus, the selected starting material is initially gadolinium. Gadolinium targets are suitable for proton beam irradiation. The use of proton beam for commercial production allow high maximum current and energy achievable as compared to deuteron and alpha beams or heavier ions. This can guarantee a higher yield achievable with proton beams; furthermore, commercial cyclotrons accelerating deuteron and alpha beams are currently mostly dedicated to research rather than production, nevertheless this could be reconsidered in the future if some radionuclides are commercially needed and only possible to produce with such accelerators (e.g. At-211 produced from 30 MeV alpha beam on bismuth target). Starting from the experimental cross-sections evaluated in the previous chapter a thorough analysis on the best target definition, comparing natural gadolinium with enriched one, is elaborated.

As previously mentioned, currently terbium radionuclides are produced in ISOLDE and MEDICIS facility at CERN with high energy proton beam for the irradiation of tantalum target, combined with mass separation. In order to overcome the limited time at ISOLDE dedicated to medical isotopes, in the near future, the MEDICIS facility will produced on a regular basis once the facility will reach the nominal production rate, allowing their potential availability for clinical trials. Other similar facilities which can potentially look to the production of terbium radionuclides based on spallation and mass separation have already been operating; those are the Isotope Separator and Accelerator (ISAC) at TRIUMF, Canada's National Laboratory for Particle and Nuclear Physics (Canada) and the Investigation of Radioactive Isotopes on Synchrocyclotron (IRIS), at the Petersburg Nuclear Physics Institute (PNPI, Russia). Other facilities are under construction or planned for the next future such as: Radioactive Isotope Beam Factory (RIBF, USA); Belgium Nuclear Research Center's ISOL facility (ISOL@MYRRHA, Belgium); Japan Proton Accelerator Research Complex (J-PARC ISOL, Japan) (70).

Other researchers studied the production of Tb-149 from tandem accelerator with heavy ion beams. Two different reactions were studied: 141Pr(12C,4n)149Tb with not satisfactory yields obtained; natNd(12C,xn)149Dy which decay in Tb-149 but the purity achievable are not high enough, for this reason only in vitro studies were made (72) (82). Another production route investigated is the irradiation with alpha beam of an europium target from commercial cyclotron. However, the low radionuclidic purity of the produced batches require the mass separation. Furthermore, the achievable yields are lower compared to the irradiation of gadolinium targets with proton beams due to the lower beam current available for commercial cyclotrons.

In this work the production of terbium radionuclides from a 70 MeV cyclotron is considered. The co-production of other terbium contaminants implies the use of the mass separation after the

cyclotron irradiation. Nevertheless, compared to high energy facilities, the use of commercial cyclotrons allows exploiting higher beam currents (up to 350 µA compared to 2 µA) accessing higher cross-section of the reaction of interest and limiting the amount of contaminants co-produced resulting in less isobaric contaminants after mass separation.

4.1.1 Starting material: gadolinium

In 1880 the lanthanide gadolinium was isolated by Jean Charles Galissard de Marignac, a Swiss chemist. The name gadolinium derived from Johan Gadolin who in 1787 discovered a new element, yttrium, from gadolinite mineral. It is 6.2 mg/kg abundant in the earth crust. (83) It is commonly used as contrast agent for MRI applications (84). In the nuclear industry gadolinium is used as a neutron absorber due to very high neutron absorption cross-sections of some of its nuclides, in particular Gd-157 (254E3 b). Other applications of gadolinium are in alloys: it can improve the workability and the resistance to high temperatures and oxidation of iron and chromium alloys: It is also used in alloys for making magnets, electronic components and data storage disks. (85) Gadolinium has 7 stable isotopes; the composition is summarized in *Table 24*.

Theoretically, the most suitable way for the production of Tb-149 with a proton beam is to use a Gd-152 target as it is the closest gadolinium isotope and the reaction, Gd152(p,4n)Tb149, is the most favorable. However, its natural abundance is very low, about 0.2 %. As an alternative the reaction Gd154(p,6n)Tb149 can be considered but the natural abundance is only 2.2 %; otherwise Gd-155 and Gd-156 can also contribute to the production of Tb-149 but the cross-section are lower for increasing atomic mass target. Nevertheless, the lower cross-section could be compensated with the higher enrichment level. For this reason, the use of natural gadolinium should be compared with the use of enriched gadolinium. For producing Tb-152 and Tb-155 instead natural gadolinium can be considered. However, one can get higher yields if needed by using enriched targets, such as Gd-152 for producing Tb-152 through Gd152(p,n)Tb152, or Gd-155 for producing Tb-155 through Gd155(p,n)Tb155. In this work, for the production of Tb-152 and Tb-155 only natural gadolinium will be initially considered as starting material, whereas for Tb-149 natural starting material should be compared with enriched ones.

The enriched target material evaluated in this analysis are manufactured by international company suppliers of isotopes such as Trace Sciences International (USA) and Isoflex (Russia). The maximum enrichment level of gadolinium isotopes currently available on the market and the chemical form yield are reported in *Table 24*.

Table 24: properties of the Gadolinium target available on the market in 2018

Isotope	*Natural Abundance*	*Max. Enrichment Level*	*Chemical Form*
Gd-152	*0.20%*	*34%*	*Oxide*
Gd-154	*2.18%*	*67%*	*Oxide / metal*
Gd-155	*14.80%*	*>94%*	*Oxide / metal*
Gd-156	*20.47%*	*≥95%*	*Oxide / metal*
Gd-157	*15.65%*	*88.40%*	*Oxide / metal / chloride*
Gd-158	*24.84%*	*>97.30%*	*Oxide / metal*
Gd-160	*21.86%*	*98.20%*	*Oxide*

From the previous table one can see that almost all nuclides can be purchased under oxide or metallic form, except for Gd-152 and Gd-160 which are currently available only as oxides. The main differences in the properties of the oxide and metal are resumed in the following table:

*Table 25: properties comparison between natural Gadolinium metallic and oxide. *depending on the porosity of the system*

Properties	*Metal*	*Oxide (Gd_2O_3)*
Density [g/cm³]	7.91	7.07
Melting point [°C]	1313	2420
Thermal conductivity [W/mK]	11	0.07 *

Gadolinium oxide has higher fusion temperature compared to metallic gadolinium, but it has a very low thermal conductivity, which depends on the porosity of the target. This implies a more challenging heat removal under irradiation conditions and maybe a more complex target cooling system. Furthermore, the oxide should be encapsulated in a metallic container to be irradiated, while under metallic form it can be irradiated as it is, if properly shaped and compatible to an existing or developed solid targetry system. The encapsulation of pellets of oxides introduces also further complications related to the target chemical treatment after irradiation.

4.1.1.1 Yield evaluations for Tb-149 production

Possible nuclear reactions leading to the production of Tb-149 from gadolinium targets possible with a 70 MeV proton beam have been presented previously (3.4 Tb-149 cross-section). G.F. Steyn *et al.* (86) in their study of feasibility for a large scale production of Terbium radionuclides from a 70 MeV cyclotron, have experimentally measured the cross-section of the reaction Gd152(p,4n)Tb149 and compared with the results obtained with TENDL 2012 and ALICE. They sedimented enriched Gd-152 oxide (30%) on a metallic support. Therefore, they had supposed

that the main reaction leading the production of Tb-149 is Gd152(p,4n)Tb149. Considering a potential enrichment level of 100%, they showed the obtained curve compared to the overestimation of the theoretical codes in the following figure:

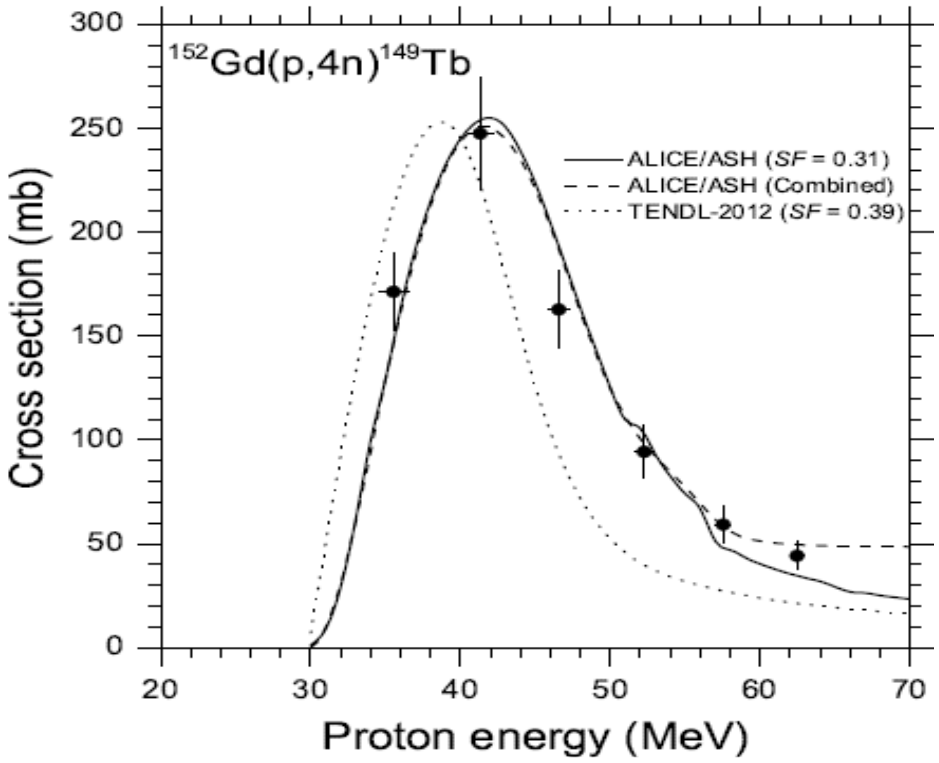

Figure 61: comparison of the cross-section Gd152(p,4n)Tb149 calculated with ALICE, and Talys with the one experimentally obtained (in black dots). (86)

As one can notice, the difference between the cross-section calculated with TENDL 2012 in *Figure 61* from the one calculated by Stein correspond to a Scaling Factor (SF) of 0.39. The analog experimental study is currently missing for enriched Gd-154 excitation function for Tb-149 production.

The theoretical evaluation of the yield achievable for the wanted nuclide in Bq/µA/h (normalized per µA and per hour of irradiation) for different type of enriched targets has been made considering the maximum enrichment available given by Trace Sciences company. The values are: Gd-152 enriched at 34%, Gd-154 enriched at 67%, Gd-155 enriched at 94%, and Gd-156 enriched at 95%. In a previous publication (87) only theoretical evaluated cross-sections were used. In this work a scaling factor of the theoretical cross-sections of 0.39 has been considered assuming the validity of the work of Steyn *et. al.* and the reproducibility to the other similar cross-sections.

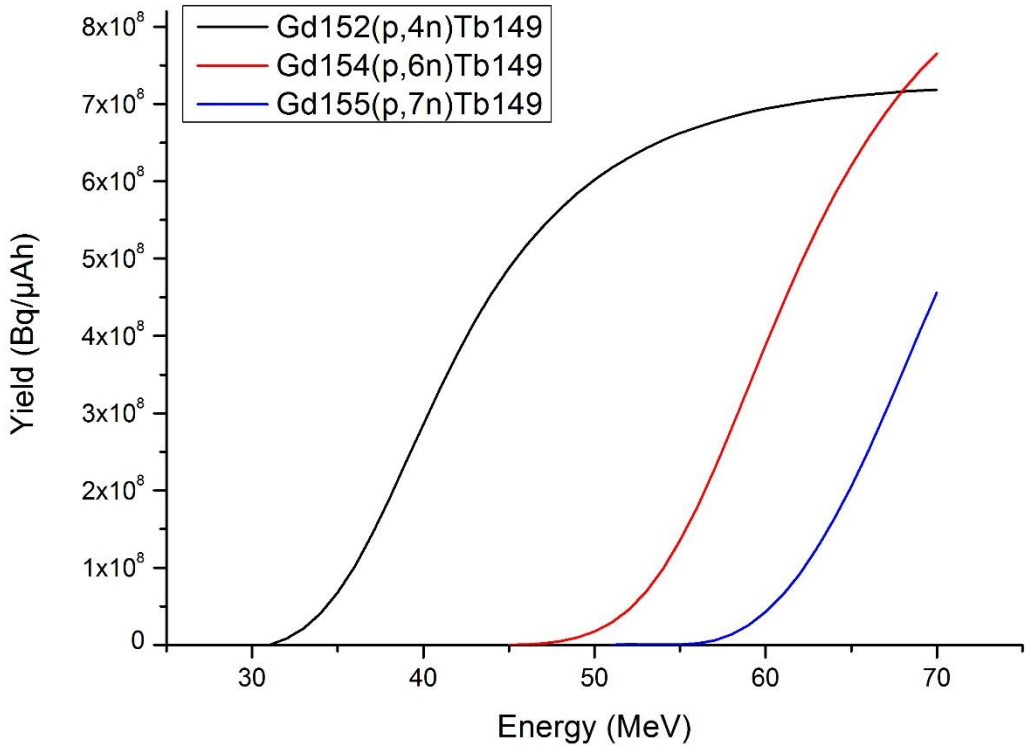

Figure 62: yield comparison for energies ranging from 30 to 70MeV of the reaction of interest for the production of Tb149, considering theoretical cross-sections with a scaling factor 0.39.

In *Figure 62* are presented activation yield curves considering the maximum available enrichment level (*Table 24*) for each considered target. One can notice that the highest yield achievable is for Gd-154 enriched target, 7.6E8 Bq/µAh. Using Gd-152 instead, a similar yield is achievable 7.2E8 Bq/µAh. However, the difference of beam energy is directly proportional to the thickness, meaning that thicker expensive targets are needed for Gd-152 to achieve the same yield (ΔE=22 MeV rather than ΔE=38 MeV). This means lower power deposition (in W) in the target as it is given by the product ΔE*I where I is the beam current (in µA) and lower thermal constraints. Furthermore, a Gd-155 enriched target allows the production of 4.5E8 Bq/µAh with a ΔE of 16 MeV, but with Gd-154 one can achieve the same yield with a thickness corresponding to a ΔE of 11 MeV and with a Gd-152 enriched target a ΔE of 12 MeV is needed. Gd-154 is then chosen as target material as it offers the best trade-off in terms of activation yield and required beam energy range thus lowering the thermal constraint on the target. This consideration is valid with the maximum enrichment available previously considered and the theoretical cross-sections scaled by the factor 0.39. However, if the maximum percentage of the enrichment achievable of Gd-152 will change in the future, or experimental cross-section evaluations with enriched Gd-154 and Gd-155 starting

material will be performed, this will have to be reconsidered. Indeed, considering the maximum enrichment level for each isotope as 100% the yields are presented in the following figure.

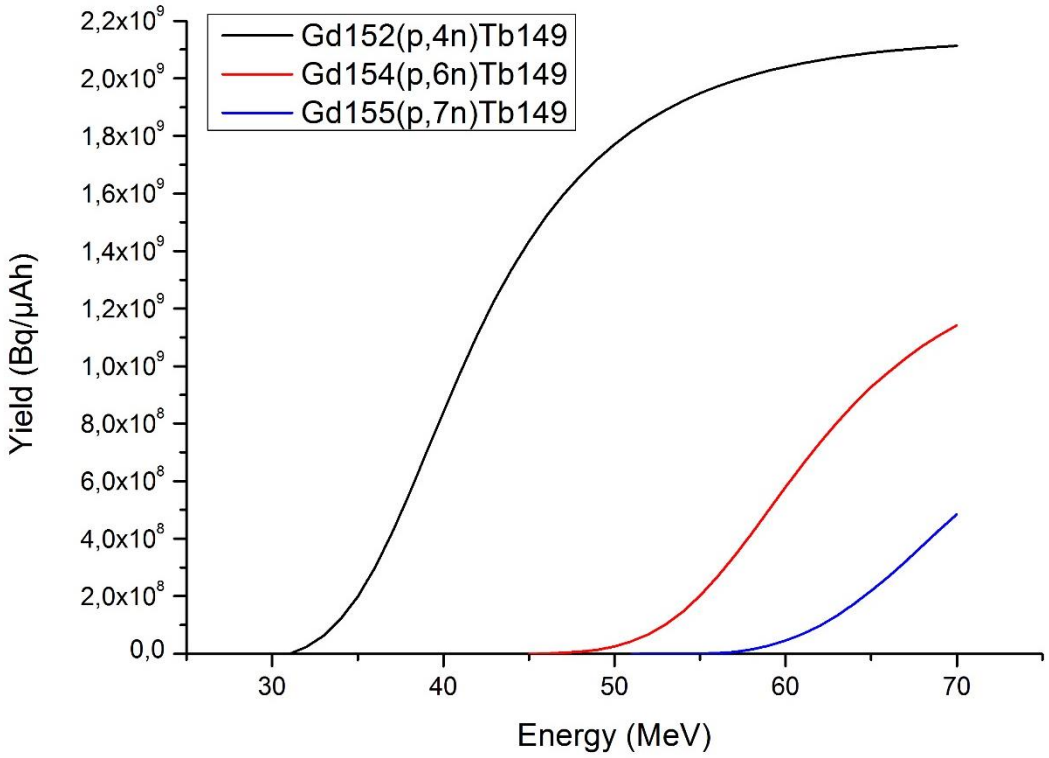

Figure 63: yield comparison for energies ranging from 30 to 70MeV of the reaction of interest for the production of Tb149, considering 100% enriched targets.

It is evident from *Figure 63* that considering a 100% theoretical enrichment level for each isotope, Gd-152 100 % enriched target could allow for example producing 1.8E9 Bq/µAh with a target thickness corresponding to 23 MeV.

The current maximum enrichment levels, the price and the potential radionuclides that can be produced are presented in *Table 26*.

*Table 26: comparison of enriched material of interest price per mg of element considered (mge), coming from Trace Sciences. * refers to 1000 mg quotation*

Isotope	Enrichment	Price/mge (for 100 mg quotation)	Simultaneous potential co-Production
Gd-152	34.8	180 $ *	Tb-149, Tb-152
Gd-154	67.1	30 $	Tb-149, Tb-152
Gd-155	92.8	9.35 $	Tb-149, Tb-152, Tb-155

The choice of the best target material is a balance between several parameters:

- Cross-section: the best material is enriched Gd-152, the worse one is natGd
- Cost: natural material is the most convenient, gadolinium oxide enriched in Gd-154 at 67% is more than six times cheaper than gadolinium oxide 34% enriched in Gd-152
- Target thickness: Gd-154 allows the use of a reduced thickness to achieve similar yields compared to Gd-152

After this first analysis Gd-154 67% enriched target seems to be the most promising target material. Anyway, with any considered gadolinium-based targets, terbium impurities are produced in non-negligible quantities. This requires the use of the mass separation technology after irradiation.

4.1.1.2 Yields for Tb-152 and Tb-155 production

As mentioned above the considerations for the production of Tb-152 and Tb-155 are different compared to the ones previously elaborated for Tb-149. Due to the natural abundances of gadolinium isotopes resumed in *Table 24*, large-scale production of Tb-152 and Tb-155 could be feasible with natural a gadolinium target too, if one considers the mass separation technology to remove the other terbium contaminants co-produced. For this reason, in a first stage only natural gadolinium is considered as it is cheaper and more available rather than enriched material, as well as easier to find in metallic form. From the cross-sections discussed in the previous chapter, the achievable yield has been calculated (Figure 64). It emerges that with a 70 MeV proton beam, the optimal proton beam energy range for the production of both Tb-152 and Tb-155 is between 70 and 30 MeV.

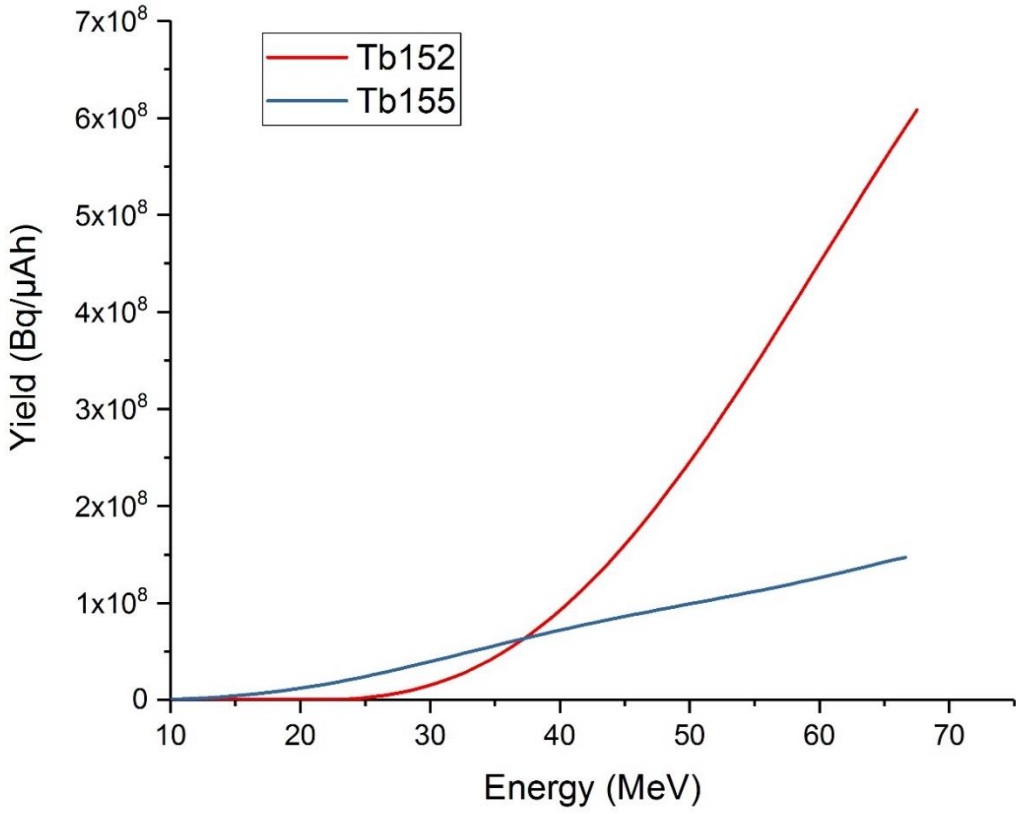

Figure 64: achievable yields for the production of Tb-152 and Tb-155

Natural gadolinium can be purchased in metallic form and several shapes are available. Looking for the existence of a solid targetry system that can be suitable for this application, one system developed by ARRONAX and Subatech has been identified. Thus, the selected targets are 26 mm diameter and 4 mm thickness metallic disks. The targets have been purchased from Goodfellow.

Examples of achievable yields are given for a 4 mm thick target and 70 MeV and 75 µA proton beam:

- For 10 hours of irradiation: Tb-152 = 235 GBq; Tb-155 = 38.2 GBq
- For 24 hours of irradiation: Tb-152 = 441 GBq; Tb-155 = 88.3 GBq

4.1.2 Target development for Tb-149 production

Once the best composition of the starting material is selected the dimensioning of the target is evaluated. Several parameters must be considered: physical state of the target, thickness, physical characteristics, suitable targetry system already available, targetry fabrication method available. Different materials can be irradiated, such as metals, oxides or carbides. Among them metallic targets are preferred due to their usually very high thermal conductivity, requiring a less challenging targetry system and easier cooling system. However, in particular for enriched

material, the metallic target is not available or available in powder form. This requires specific techniques to assemble a target to be mechanically and thermally consistent.

4.1.3 Target thickness

The optimal target thickness required could be calculated from the stopping power of the proton beam in a gadolinium target. Knowing the initial beam energy, it is possible to estimate the projected range, which allows evaluating the target thickness required for the irradiation in the energy range of interest where the cross-section and consequently the yield is the highest. As one can notice from Figure 65 the difference of the projected range of protons in matter between metallic and oxide of gadolinium is quite important.

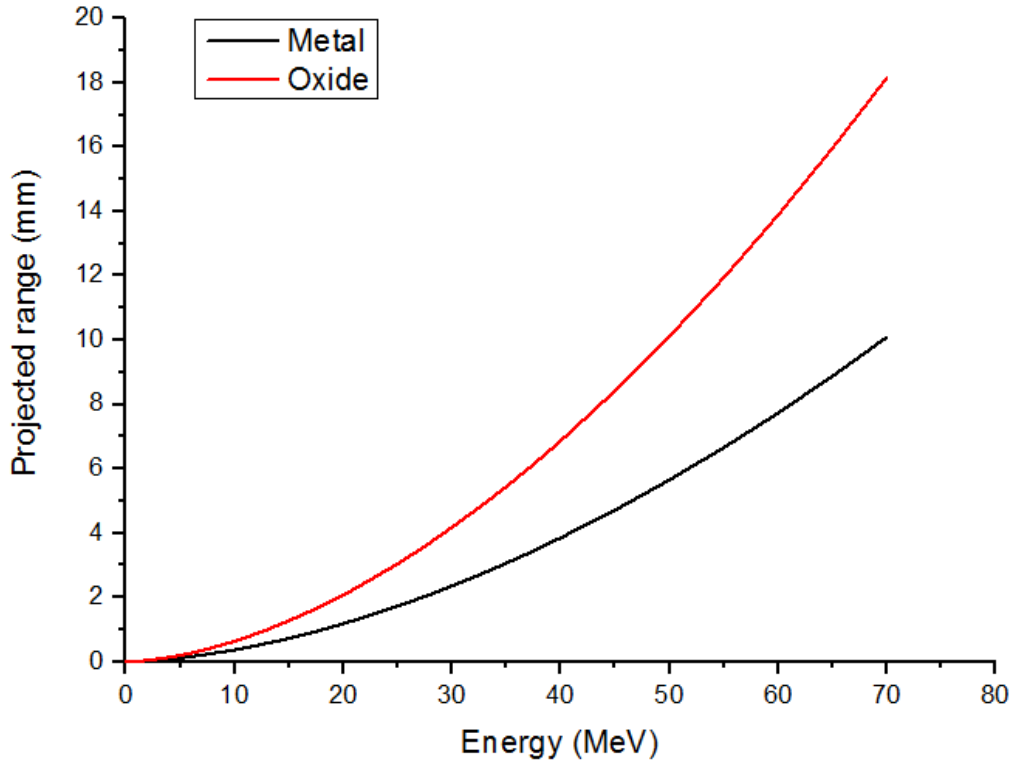

Figure 65: projected range of a beam of proton incident for stable gadolinium isotopes materials.

From *Figure 65* one can see that in order to have the optimal energy window for the production of terbium radionuclides between 30 and 70 MeV, in case of a metallic target around 8 mm of target thickness is required, whereas in order to have the same energy range, around 14 mm target thickness are required for an oxide target. In case of a natural gadolinium target for producing Tb-152 and Tb-155 metallic disks of the diameter of the beam and the suitable thickness are commercially available. Nevertheless, for Tb-149 from enriched target material, capsules of gadolinium oxides could be made but they cannot be irradiated at high proton beam current as

their thermal conductivity is quite low. As metallic targets are preferred, a method to develop it from oxide or metallic enriched powder should be investigated.

4.1.3.1 Target fabrication with enriched gadolinium

Different ways of fabricating an enriched gadolinium target can be investigated:

- *Electrodeposition:* the standard reduction potential of gadolinium Gd^{3+}/Gd is very negative, -2.4 V/SHE (SHE= Standard Hydrogen Electrode), this means that it is impossible to electroplate a gadolinium film starting from an aqueous electrolyte because the reduction of water is very predominant and avoid the reduction from Gd^{3+} to Gd. However, in an organic bath, it is possible to reduce Gd^{3+}. There are two exploitable ways for obtaining a gadolinium film by electrodeposition. The first one is using $GdCl_3$ from gadolinium oxide which is dissolved in HCl. This salt can be dissolved in organic bath such as ethanol (88). The second one is using gadolinium toluensulfonate from gadolinium oxide which is dissolved in p-toluensulfonic acid. This salt is dissolved in aprotic organic solvent, and the supporting electrolyte $(n\text{-}Bu)_4NBF_4$) is added for increasing the conductivity in organic bath (89). The voltage employed during the electrodeposition through the first way is high, more than 60V, meaning it will be challenging and not feasible with the materials already available at ARRONAX. Whereas with the second option the voltage employed is less than 15 V, which can be easily achieved. Therefore, the latter method is the selected one for electroplating experiments at ARRONAX for the initial target development investigation. The work is still in progress.
- *Compression:* it is possible with both gadolinium oxide and metallic gadolinium. The oxide should be encapsulated, for example with a 100 µm layer of stainless steel and cooled with water on both sides. The target geometry is suitable for the already existing targetry system used for the production of strontium Sr-82 from rubidium chloride (RbCl) at ARRONAX. However, the cooling of gadolinium oxide pellets is challenging. Furthermore, smaller disk can be considered, but the mechanical resistance of gadolinium oxide pellets up to 1 mm is poor. As alternative target material GdB_6 could be considered, but currently is not commercially available for enriched gadolinium.
- *Sedimentation:* will not give good thermal conductivity and cause the mechanical instability of the sedimented targets. The author Kovac *et al.* (88) has successfully measured cross-sections, sometimes with high uncertainties and exhibit large scatter. The sedimentation approach is not well adapted for the fabrication of thick targets for large-scale production of Tb-149.
- *Fusion:* metallic gadolinium is suitable, while the oxide has a too high fusion temperature. Drawbacks of this target synthesis approach are the need of a high temperature furnace

to be bought (not available at ARRONAX) and the more expensive cost of the target than the other technics.

For the reasons mentioned above, two different ways for the fabrication of gadolinium target will be considered: electrodeposition and compression of gadolinium oxide. The first one will be the method investigated, while the latter will be a backside plan if electrodeposition will be not satisfactory for thick target fabrication.

4.1.3.2 Electrodeposition of gadolinium

As enriched gadolinium is prevalently available under oxide form, it will be the form considered as starting material with the intent to end up with a deposited layer of enriched metallic gadolinium onto a metallic support. In a first step natural gadolinium has being used to verify the feasibility of the system due to the lower cost of the material, then Gd-152 and Gd-154 enriched oxides will be considered. The main reasons for choosing the enriched oxide rather than the enriched metal are: the price, the availability of the oxides for each of the isotopes constituting natural gadolinium and the less complicated process for the preparation of the organic solution for electrodeposition. The initial target geometry considered is a parallelepiped 10x4x0.1 cm plus a metallic support since it is already an available design used in ARRONAX having dimensions 12x5x0.3 cm. The aimed target thickness previously calculated starting from the stopping power is 4 mm. One of the available systems present at ARRONAX is a slanted target at 15° with respect to the beam axis, this means that 4*sin(15°)=1.035 mm of gadolinium layer thickness should be achieved. As in this case the target is the interface between the vacuum of the beam line and the water cooling itself, it must guarantee the integrity in those conditions. Therefore, the deposited layer should be adherent to the support even under irradiation condition, in order not to fall disrupted in the beam line causing problems in the vacuum system.

Several materials are evaluated as metallic support. They must have good thermal conductivity to remove the deposited heat efficiently. In order to guarantee the feasibility of the system from the thermal point of view, some parameters are fixed *a priori* as irradiation and cooling parameters for evaluating the maximum temperature reached in the system. A first steady-state 1D evaluation is made (ANNEX-C). In *Table 27* are resumed the main outcomes for each material, with a focus of their standard potential. Considering the following parameters:

Irradiation:

- Beam diameter 30 mm
- Beam intensity 100 µA
- Beam energy 70 MeV
- Angle of the target 15°

Cooling parameters:

- Heat transfer coefficient, h=10000 W/m^2K (conservative value)

- Water temperature, T_{bulk}=294 K

Target parameters:

- Thermal conductivity 10.9 W/(mK)
- Thickness 1.2 mm (to have a more conservative case)
- Beam energy loss 20 MeV

Support parameters:

- Thickness 3 mm

Table 27: thermal evaluation for different support material

Element	*Thermal conductivity [W/(mK)]*	*T Fusion [K]*	*Energy loss [MeV]*	*T (target) [K]*	*T (support) [K]*	*T (water) [K]*	*Standard Potential [V/SHE]*
Al	237	934	8	448	408	397	- 0.55
Ti	21	1941	13	594	553	415	- 0.092
Ni	91	1728	30	560	519	477	- 0.250
Cu	401	1357	28	560	558	506	+0.337
Zn	116	693	21	511	510	473	- 0.763
Ta	57.5	3290	50	677	636	550	-
Pt	71.6	2041	50	659	618	549	+1.2
Au	317	1337	50	530	489	477	+1.41

The fusion point of metallic gadolinium is 1314 °C, this means that with every type of support material considered gadolinium doesn't achieve the melting point. Nevertheless, gold seems to have the best thermal performances allowing a higher margin. This is important in case of future upgrade of the beam current needed. Furthermore, gold have a suitable standard potential for electrodeposition process and it is chemically quite stable allowing a possible recovery of the support for multiple uses. For those reasons, gold support is selected in a first stage. Therefore, for the production of Tb-149, the electrodeposition of enriched gadolinium on gold support will be studied. First experiments were performed at GIP ARRONAX, but was electrodeposited only a very thin layer of gadolinium hydroxide. Further experiment will be pursued at GIP ARRONAX to find the best configuration for the deposit of a thick layer.

Once a realistic estimation of the maximum thickness achievable of the gadolinium deposit will be accurately performed, 3-D Ansys simulations for the validation of the thermal and mechanical consistency and irradiation of the considered geometry will be performed.

4.2 Target definition: Tb-152 and Tb-155 production

For producing Tb-152 and Tb-155, instead natural gadolinium could be considered. Thus, differently from the previous analysis for the enriched material, in this case metallic disks can be dimensioned in order to maximize the production preserving their integrity. In this work, the maximum thickness considered is 4 mm based on the targetry systems already existenting at GIP ARRONAX (A.5 ARRONAX targetry). If in the future bigger dimensions will be needed, this analysis will have to be reconsidered.

The considered system is made by one gadolinium disk, which is cooled by the cooling water through the 2 mm gap on both sides (CASE 1 in *Figure 66*). Alternatively, it is possible to increase the yield by the positioning of another gadolinium disk next to the first one. However, in this case, the thermal load deposited on the second disk is much more important. Looking to the cross-sections of reference, for the production of Tb-152 is not worth to have a beam exit energy of less than 30 MeV as the cross-section is not convenient, for the production of Tb-155 instead is not worth to have a beam exit energy below 20 MeV as the thermal constraints will be very high and the cross-section not convenient. For this reason, one target of 4 mm of thickness followed by a gadolinium target up to 3 mm thick could be potentially considered (CASE 2 *Figure 66*). In each case, the targets are cooled by a water flow on both faces and they are fixed to the targetry system from the lateral surface.

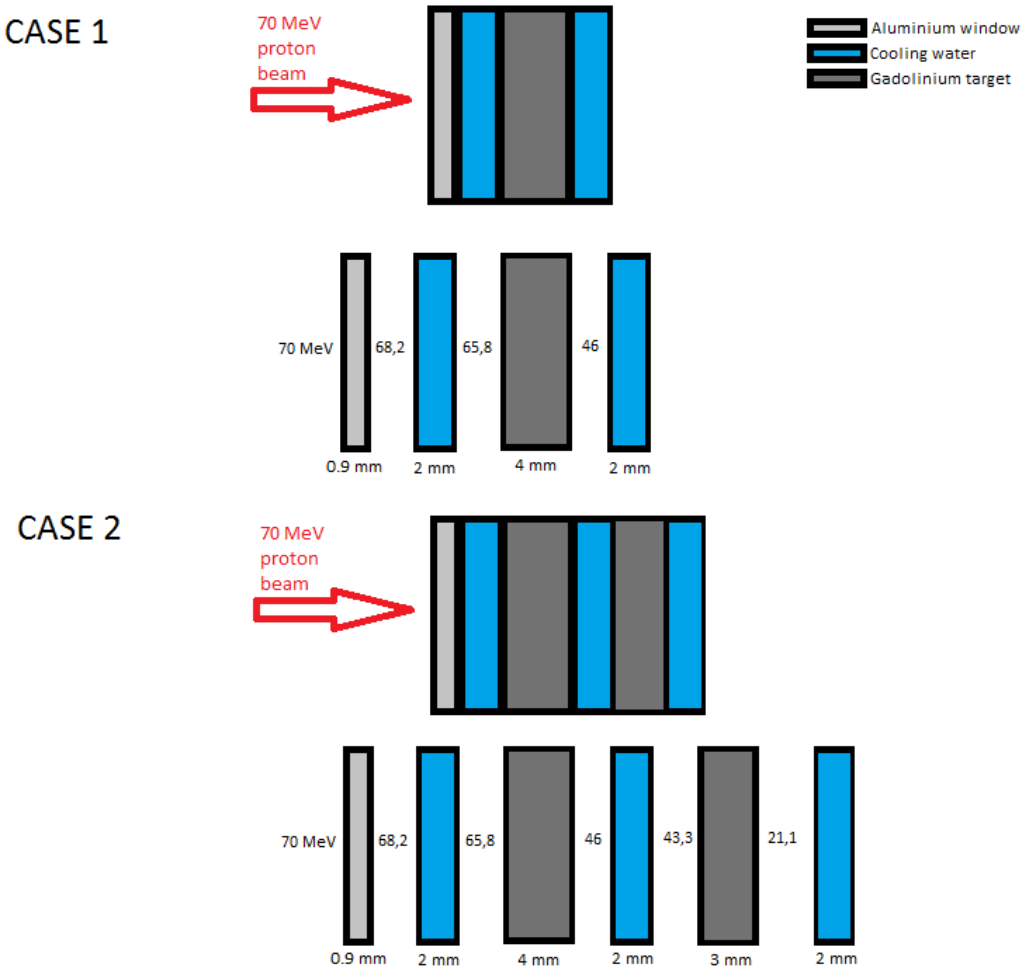

Figure 66: tested target breakout, two different configurations. Case 1 representing the use of one gadolinium target; Case 2 representing the use of two gadolinium targets in a row

4.3 Thermal and mechanical target resistance

When developing a target, it is of fundamental importance to guarantee the integrity of the target during the irradiation. Therefore, it is necessary to set up an iterative process to define the best target dimension for maximizing the production yield. As deeply explained in the Annex I, the study was divided in two parts: 1-D calculation and 3-D static simulation.

4.3.1 Static 1-D estimation

Considering the targetry shown as "CASE 1" in Figure 66, a thermal exchange coefficient of 30000 W/m^2K, are presented in Table 28 the temperatures reached in the target and the maximum temperature of the cooling water. The latter should be lower than the boiling point of the water at 15 bar (198.3 ºC). This shows the feasibility of the targetry system for an incident beam current between 50 and 100 µA, which is reasonable.

Table 28: temperature variation in cooling water and target with different proton beam currents with a thermal exchange coefficient of 30000 W/m2K.

Proton current (µA)	Maximum target temperature (°C)	Maximum water cooling temperature (°C)
100	417.9	215.9
50	218.9	72.9
10	59.6	30.4

4.3.2 Static 3-D simulation

The 1-D thermal calculation gave an idea on the thermal constraints and feasibility of the system. This is useful to develop a 3-D static simulation concentrated on the indications from the 1-D analysis. It was implemented in ANSYS mechanical workbench. The target disk has been simulated with a reduced geometry for optimizing the computational cost, respecting the symmetry of the system. Thus, a quarter of half thickness disk has been defined. A function has been written to take into account the ideal Gaussian shape of the incident proton beam. The function depends on the incident proton current. Different calculations have been made for different heat transfer coefficients in order to verify the behavior of the maximum temperature. This could be useful in case in future the cooling system will be modified, or one new cooling system must be developed in a new facility for such application.

Table 29: water cooling and target temperature for different beam currents and thermal exchange coefficients for the gadolinium target

Heat transfer coefficient (W/mK)	*beam current (µA)*	*T water (°C)*	*T max (°C)*
40000	100	192,7	820,1
	75	149,6	620,9
	50	106,4	420,8
	25	62,3	220,4
30000	100	248,2	871
	75	191,2	658,5
	50	134,2	445,9
	25	77,1	232,9
20000	100	356,5	969,1
	75	272,5	732,1
	50	188,4	495
	25	104,2	257,5
10000	100	663	1249,4
	75	502,4	942,4
	50	341,8	635,2
	25	180,9	327,6

Interpolating the data in *Table 29*, one can obtain the maximum beam current which induces a thermal load on the target casing leading to the heating of the water to its boiling point. Considering the nominal thermal exchange coefficient 34182 W/m^2/K, the maximum current is 88.3 µA. Considering around 10 % of safety margin, the beam current considered for the irradiation will be 80 µA.

The temperature profile inside the target which is irradiated by a 80 µA and 70 MeV proton beam is presented in Figure 67. It is possible to see that the maximum temperature reached in the center of the target is 681 °C, almost half of the melting point of gadolinium, which is a very good value. The maximum temperature at the interface between target and cooling water is 181 °C, which is lower than the boiling point of the water at 15 bar.

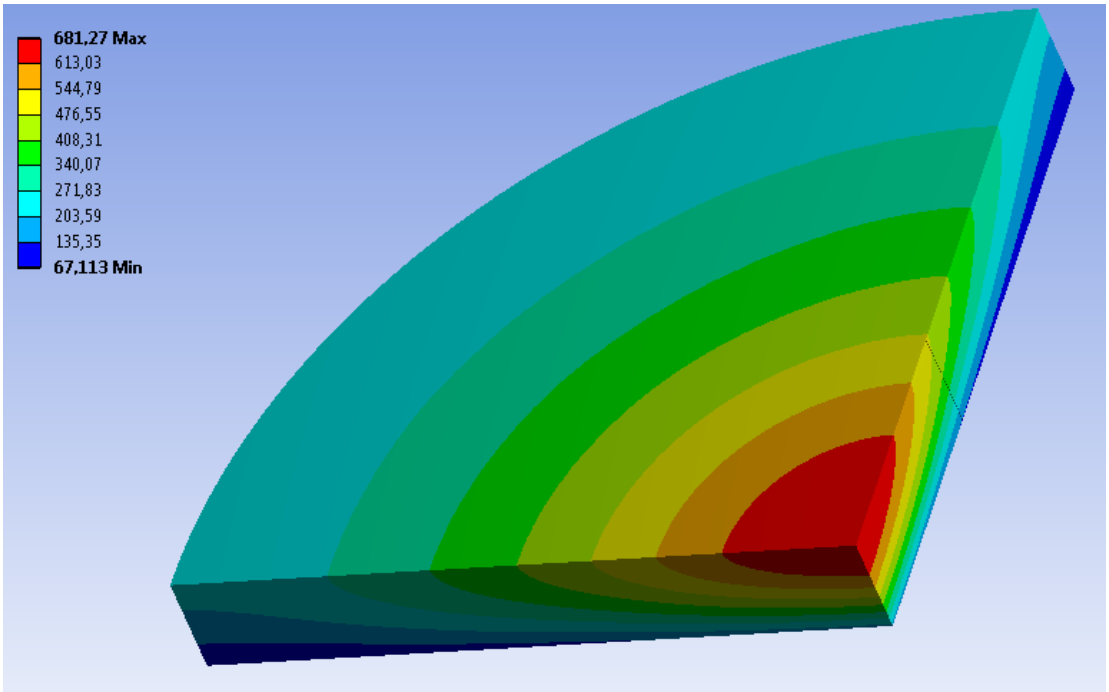

Figure 67: temperature profile of the natural gadolinium target irradiated with a 80 µA and 70 MeV proton beam

The mechanical resistance is evaluated with the total deformation and the Von Mises stress. In order to be conservative, the target is considered mechanically blocked on the lateral surface and free to expand/shrink in the beam direction. The results presented in the following figures shows the negligible swelling of the target, in the figure visible only thanks to the larger scale in use (5x). The maximum tensile strength of the material is 460 MPa, largely higher than the maximum strain in the most solicited point in the target which is 301 MPa.

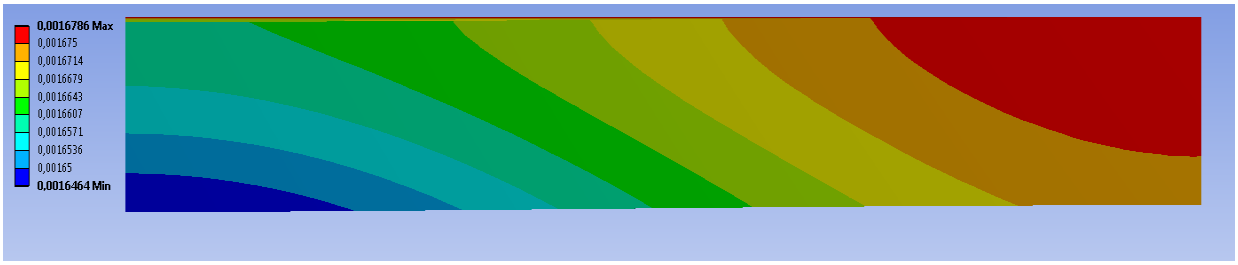

Figure 68: total deformation of the gadolinium target (m), the scale is amplified (5x)

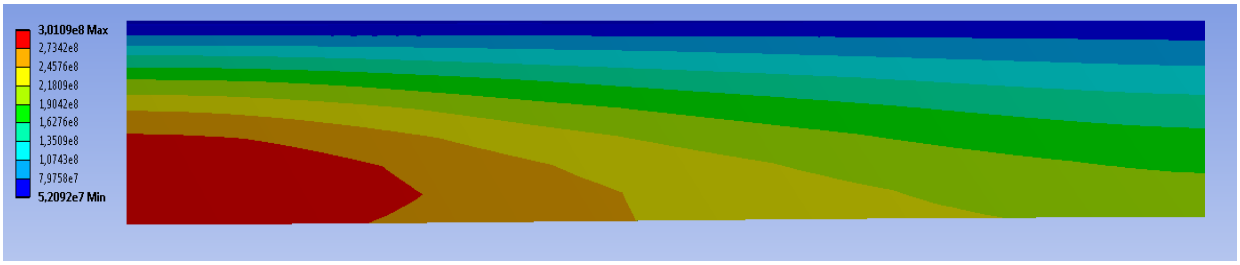

Figure 69: von Mises equivalent stress (Pa) of the target. The scale is amplified (5x)

4.4 Monte Carlo simulations for contaminant evaluation

With Monte Carlo simulations it is possible to predict the list of the contaminants produced from the interaction between the proton beam and the target. Calculations have been made with MCNPx software. It is based on theoretic models; therefore, the predicted contaminants can differ from the experimental ones. The list of contaminants has been obtained for a natural gadolinium target (CASE 1 *Figure 66*) irradiated with an incident proton beam of 70 MeV. The list is shown in the following table.

Table 30: list of all the radionuclides produced with a proton beam of 70 MeV in a natural gadolinium

Nuclide	***Half-life***	***Nuclide***	***Half-life***
Pm143	265 d	Pm144	363 d
Pm146	5.53 y	Sm144	Stable
Sm145	340 d	Sm146	≈ Stable
Sm147	≈ Stable	Sm148	≈ Stable
Sm149	Stable	Sm150	Stable
Sm151	90 y	Sm152	Stable
Eu145	5.93 d	Eu146	4.61 d
Eu147	24 d	Eu148	54.5 d
Eu149	93 d	Eu150	37 y
Eu150m	12.8 h	Eu151	≈ Stable
Eu152	13.53 y	Eu152m	9.3 h
Eu153	Stable	Eu154	8 y
Eu156	15.2 d	Eu157	15.2 h
Eu158	46 m	Eu159	18 m
Gd146	48.27 d	Gd147	38.06 h
Gd148	71 y	Gd149	9.28 d
Gd150	≈ Stable	Gd151	124 d
Gd152	≈ Stable	Gd153	240 d
Gd154	Stable	Gd155	Stable
Gd156	Stable	Gd157	Stable
Gd158	Stable	Gd159	18 h
Gd160	Stable	Tb147	1.64 h
Tb148	60 m	Tb149	4.12 h
Tb150	3.48 h	Tb151	17 h
Tb152	17 h	Tb153	2,3 d
Tb154	21 h	Tb155	5.3 d
Tb156	5.3 d	Tb157	71 y
Tb158	180 y	Tb159	Stable
Tb160	72.3 d	Dy154	≈ Stable
Dy158	Stable	Dy160	144 d

The table is useful to estimate the potential isobaric contaminants after mass separation.

For Tb-149 production, from this table, one can see that after the mass separation, no nuclides can be oxidized to reach the same mass of Tb-149. This is a remarkable advantage with respect to what is obtained at high energy using spallation process. Indeed, oxide contaminants produced in ISOLDE and MEDICIS as ^{133}LaO ($T_{1/2}$=3.9 h), ^{133}CeO ($T_{1/2}$=97 m) and ^{133}PrO ($T_{1/2}$=6.5 m) are quite abundant and lower the radionuclidic purity of the collected batches, requiring a post-chemical treatment. Common contaminants are Eu-149 ($T_{1/2}$=93 d) and Gd-149 ($T_{1/2}$=9.28 d), but for a cyclotron production the quantities should be lower.

For Tb-152 only Eu-152 is a radiocontaminant, also traces of stable Sm-152 and Gd-152 will be present in the collected batch. From the simulation, no particular contaminants are produced in the isobaric of Tb-155, except for the stable Gd-155. However, particular attention should be made on the detection of Eu-155 (4.7 y), which could be produced even if in the simulation results it was not present. Indeed for example the threshold energy for the main reaction leading the production of Eu-155, Gd-156(p,2p)Eu155, is E_{th}= 8.1 MeV.

4.5 Mass separation of cold terbium

In order to estimate the overall yield of the proposed method, it is fundamental to determine the experimental overall efficiency of stable terbium extraction with mass separation technology, before using the radioactive material. The separation of a known mass of stable terbium was performed in the offline laboratory at CERN. A mixture of stable terbium and gadolinium masses were used to check also the separation of both of them, verifying if there are suitable conditions for the preferential extraction of terbium rather than gadolinium. For this experiment MEDICIS target unit #675-M, the one dedicated to the following separation of external target from GIP ARRONAX at CERN-MEDICIS, was used. It consists of a conventional ISOLDE type target unit, with inside an empty target container and a rhenium surface ion source. A tantalum plug is used to close the tantalum target container, with a more conic shape than conventional plugs to allow its removal after the completion of the test and to reuse the target unit. A gas leak of 5.5E-4 mbar*l/s has been installed in the target, allowing the flexibility of the target in case in the future a gas leak inside the target will be needed. An example is the possible oxygenation of metallic gadolinium to enhance the evaporation of Tb atoms in TbO molecules while preventing the evaporation of metallic gadolinium. This will be tested as a back-up plan. For this experiment, as oxygen is not needed initially, a mixture of 5 noble gases (20% He, 20% Ne, 20% Ar, 20% Kr, 20% Xe) at 700 mbar is used. Its aim is just to fill the leak line.

The volumes of standard solutions (1 mg/ml with 5% HNO3, purchased from Alfa Aesar) used were 50 µl of gadolinium and 50 µl of terbium, which gives a ratio Tb:Gd atoms of 1:1, were deposited on a rhenium boat (Figure 70). The system is heated up to around 40 °C in order to evaporate the acid solution and deposit the gadolinium and terbium mixture. The boat is used only to prevent any contact between the sample and the tantalum container.

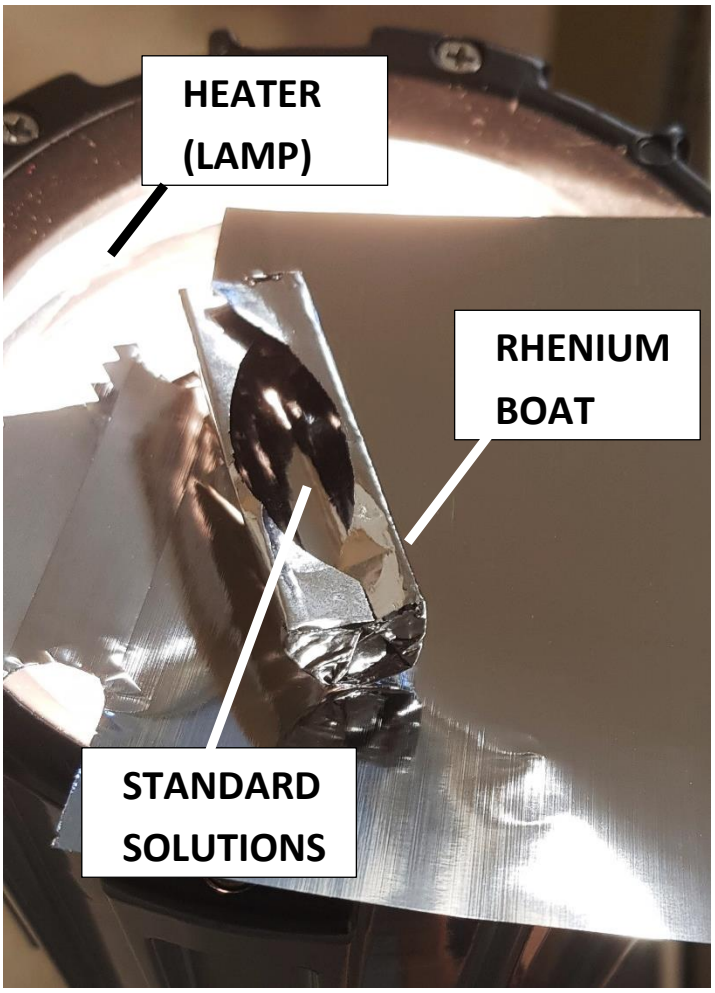

Figure 70: rhenium boat containing the standards solutions of gadolinium and terbium on the heater for the evaporation

After inserting the sample inside the target container, the target unit was positioned on the offline 1 front end. Once the front-end vacuum reached the order of 1E-6 mbar of magnitude, the ion source was heated up to around 2100 °C and the target container to 1100 °C. When it reached the temperature, the mass separator was calibrated. The first calibration was made on the optical components and the position of the extraction electrode for optimizing the extracted total beam. Then the first Faraday cup was removed and the mass separated beam optimized on mass 39 and 41, which are the masses of the potassium isotopes present in nature and always present inside the target as it can be present in the material and in the tools used for the target assembling. When the profile of the beam was optimized, the target container was gradually heated up. At around 1300 °C as the presence of cesium was quite important, a calibration of the beam shape was made on mass 133. Terbium begun to be released at around 1500 °C (corresponding parameters: line 330 A, target 400 A). At that temperature the vapor pressure of Tb is 8E-3 mbar, while the vapor

pressure for Gd is 4E-3 mbar, explaining why terbium is flowing out of the target slightly before gadolinium (90). Different mass scans were taken each around 50 A added on the target container to control the evolution of terbium and gadolinium release of their atomic and oxides ions.

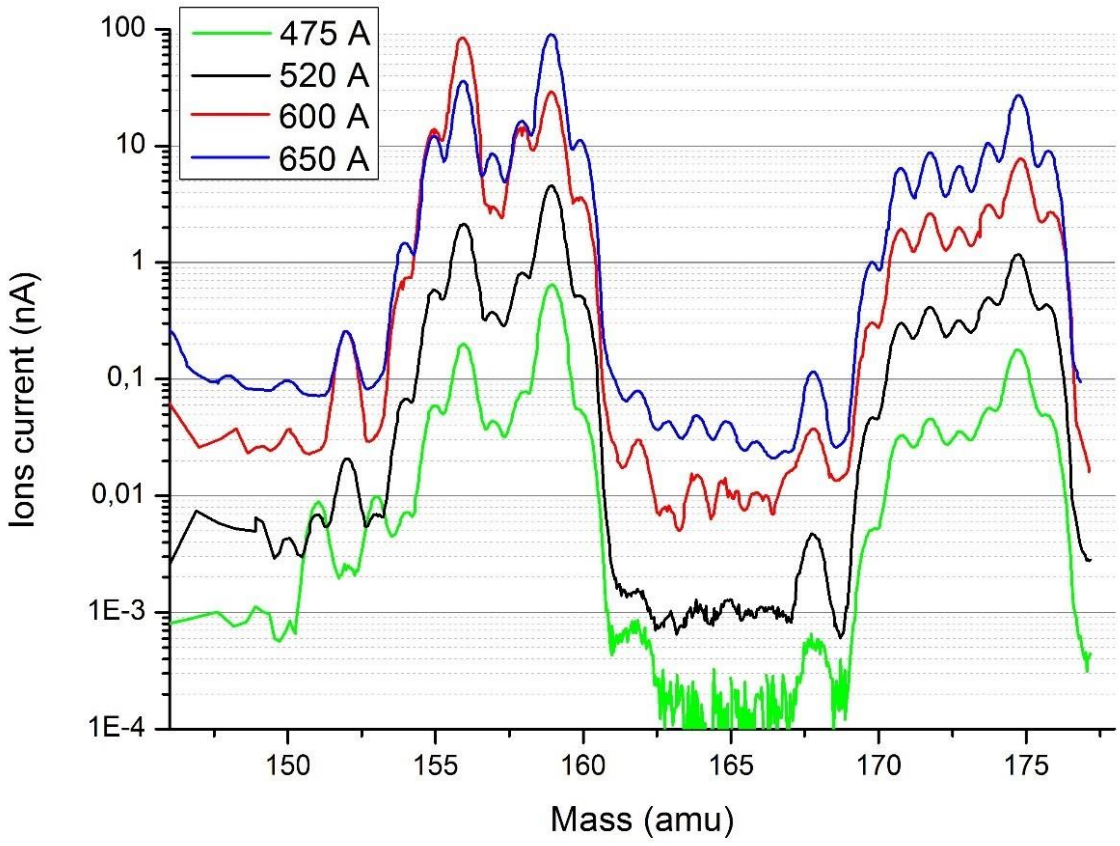

Figure 71: mass scans of the first experiment performed in terbium and gadolinium regions of atomic and oxide masses. The different scans presented have been made for different target container temperatures corresponding to the relative current applied.

From Figure 71 it is possible to see the behavior of the ion current for each mass in the region of terbium and gadolinium atomic and oxides ions. In correspondence to mass 156 and mass 158 affecting the measure of gadolinium, there is the presence of cerium oxide. It is clearly visible in the oxides region where the profiles of GdO and TbO are well defined. It has been found that its presence is systematic in the experiments involving rhenium ion source, therefore it could be a contaminant coming from the manufacturing of the ionizer. The atomic versus oxide release of terbium was almost constant during the experiment with the increase of temperature. The ratio is around 3:1 atomic ion to oxide ion. The same ratio for gadolinium ions instead is almost 1.5 during the whole experiment.

The total number of atoms of terbium corresponding to 50 µg are 1.89E17 atoms. After 5.7 hours of collection, 2.55E15 ions of atomic terbium of mass 159 were collected, resulting in an overall efficiency of 1.4 %.

A second run was performed in order to verify the effect of oxygen on terbium extraction efficiency. For this reason, the noble gases leak of the previous experiment was replaced by an oxygen flux leak set at the pressure of 700 mbar. The rhenium boat was left at the maximum temperature after the first run for one night. After that it was cleaned with an ultrasonic bath. In this way the quantity of atoms of terbium and gadolinium left in the boat should not affect largely the result, it could be neglected in first instance.

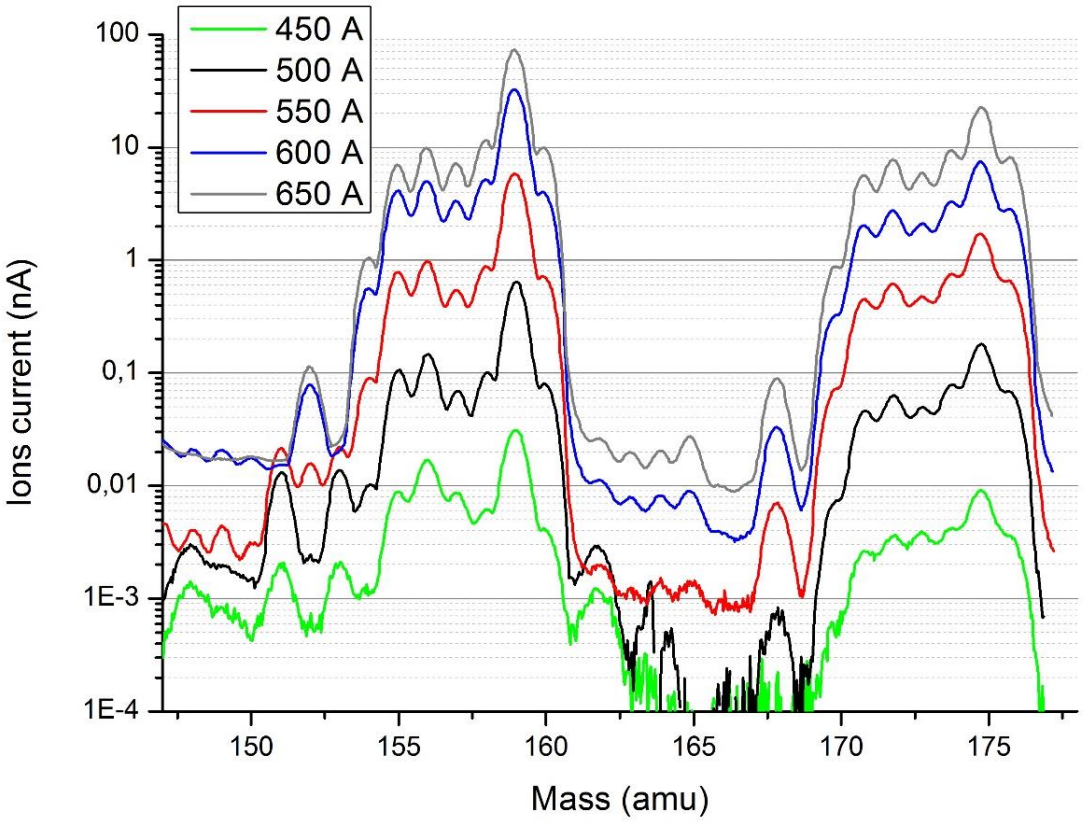

Figure 72: mass scans of the second experiment performed in terbium and gadolinium regions of atomic and oxides masses. The different scans presented have been made for different target containers temperatures corresponding to the relative current applied.

From Figure 72 it is possible to see the behavior of the ions current for each mass in the region of terbium and gadolinium atomic and oxide ions for the second experiment. Surprisingly no effect of the oxygen was detected. In this case the effect of cerium oxide was limited, therefore it could

derive from the target assembling and the degassing made during the first experiment drastically reduced it. The atomic versus oxide release of terbium was as for the previous experiment around 3:1 atomic ion to oxide ion. Similarly, a same ratio for gadolinium ions has been detected, around 1.5.

After 5.7 hours of collection, 3.55E15 atoms of mass 159 were collected, resulting in an overall efficiency of 1.9 %.

The error bars for the two experiments are difficult to determine. However, the main source of error is the estimation of the exact number of atoms inside the initial sample. As the second experiment could be largely affected by this error due to the reuse of the same boat, the result of the first experiment will be the one of reference.

4.6 Terbium laser ionization

Experimental tests for quantifying the benefit of laser in the mass separation process for terbium production have been performed. As described in the previous chapters (1.5.3.5 Laser ionization), experiments have been done at Johannes Gutenberg University of Mainz.

For the laser resonant ionization of terbium, different schemes have been compared, the 1+1' single scheme and a 2 steps scheme. Among all the possible schemes previously tested by LARISSA team, one scheme of each type has been chosen. Terbium was purchased by LARISSA team from Alfa Aesar in standard solution, which means Tb_4O_7 in 5% of HNO_3 with atomic terbium concentration of 1000 µg/ml. The solutions were reduced by a factor of 10 diluting 100 µl of solution with 900 µl of deionized water. The importance of having a limited amount of atoms is to have shorter test with shorter degassing time in order to redo the experiment several times in one week. From the previously made diluted solution of terbium, for each test 3 µl of solution were taken and deposited on a metallic foil. The foil was heated to around 40 degrees to let evaporate the acid solution allowing the sedimentation of the terbium salt on the foil. The 3 µl of terbium corresponds in this case to 1.15E15 terbium atoms per run. The metallic foils used were hafnium and zirconium foils. After the first runs with both of them, zirconium foils were chosen. The main reasons were the lower melting point allowing the use of the mass marker many times more than with hafnium foils, the lower cost, and the slightly better behavior as reductive material.

The selected wavelength for the 1+1' single step scheme was 406.27 nm. In the Figure 73 are represented the experimental points. Three measurements of the laser ionization efficiency have been performed and seemed to be consistent. The average efficiency value is 34.8%. The result is very promising and shows that good laser ionization efficiency can be achieved with only one laser available, as compared to the 1.4 % obtained with only surface ionization.

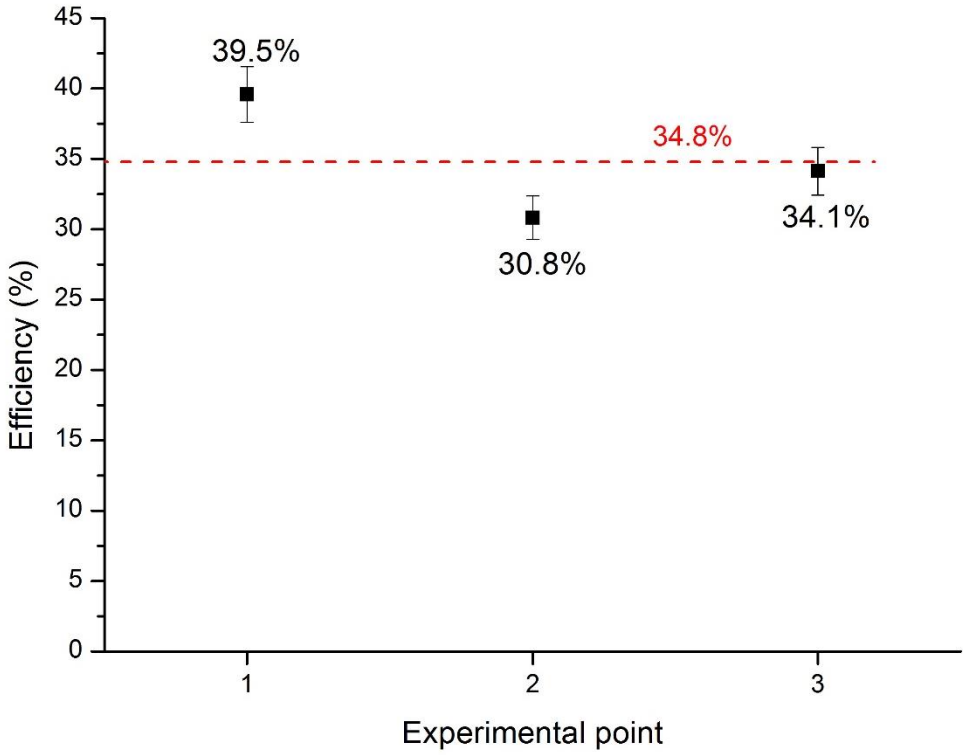

Figure 73: efficiency measurements for the 1+1' step scheme terbium laser ionization

However, the two-step scheme should be the one which will be routinely used in MEDICIS. For this experiment the chosen wavelengths are 432.76 nm for the first step and 410.86 nm for the second step. The terbium solution used was the same as for the 1+1' scheme study; in this case only zirconium foils were used. Results are presented in *Figure 74*, with comparison to the 1+1' scheme points obtained before (in blue squares).

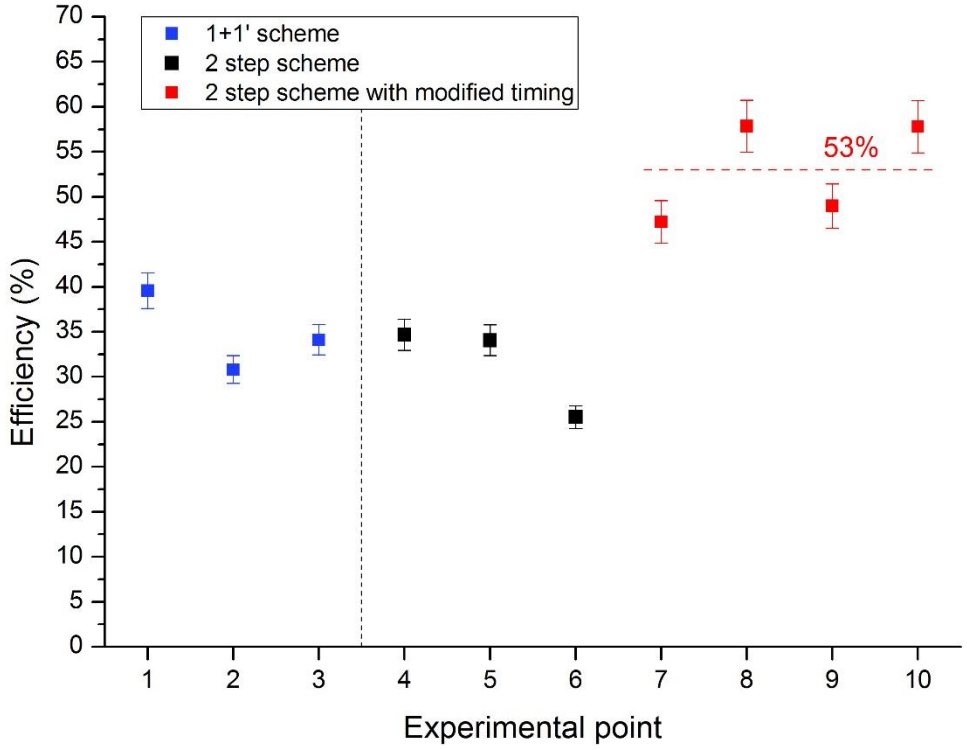

Figure 74: comparison of the 1 step scheme and 2 step schemes for terbium laser ionization efficiency

The first three measurements with the 2-step scheme were influenced by the non-optimized laser setting, in particular the timing of the two lasers. Therefore, after the optimization of the timing, the increase in the efficiency was remarkable as shown in Figure 74 in red squares. Taking in consideration only the experiments with the optimized timing, the average value for the laser ionization efficiency with the two-step scheme was 53%, which is very promising for the future development at MEDICIS.

Furthermore, in order to simulate the conditions of mass separation at CERN-MEDICIS from external targets, in particular the gadolinium target that will be irradiated at GIP ARRONAX cyclotron and mass separated at CERN-MEDICIS, a mixture of gadolinium and terbium standard solutions has been analyzed. The solution was properly prepared for this experience, with the same number of terbium atoms as the previous experiments, and a ratio of 50 between gadolinium atoms and terbium atoms.

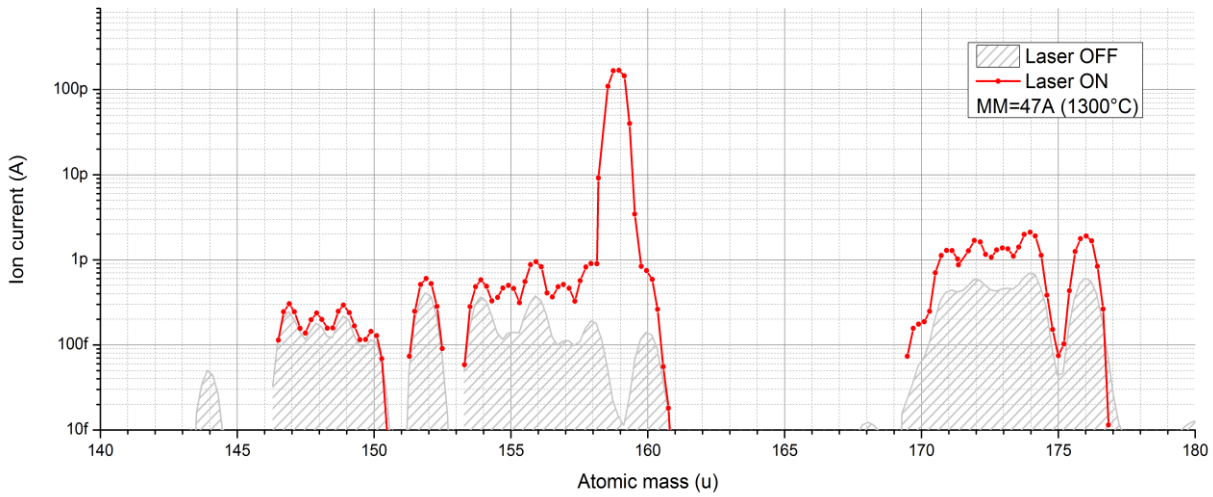

Figure 75: mass spectrum of the gadolinium terbium mixture (50:1) measurement with the mass marker at around 1300°C

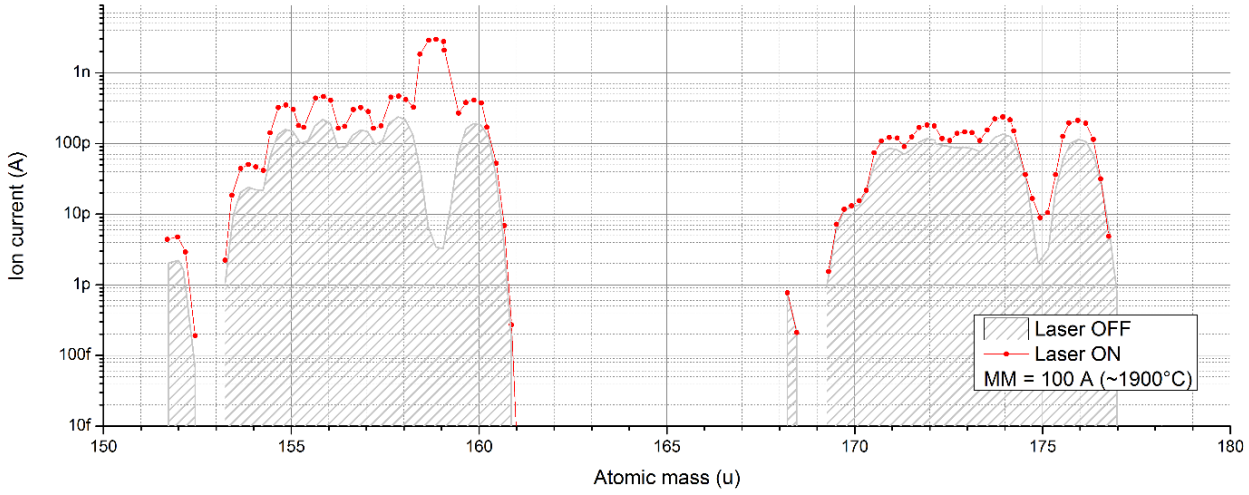

Figure 76: mass spectrum of the gadolinium terbium mixture (50:1) measurement with the mass marker at around 1900°C

As shown in the *Figure 75* and Figure 76 the selectivity of the laser for terbium ionization was very high, as well as the efficiency showing laser on/laser off ratio very high (between 1000 and 10000 depending on the temperature of the mass marker and therefore of the release of the element) for terbium and very low for gadolinium. The ratio of atomic versus oxide terbium is difficult to estimate without lasers as it is influenced by the larger presence of gadolinium. However, the ratio with laser on is around 1000. The ratio atomic versus oxide gadolinium seems dependent on the temperature. Indeed, at higher temperature the ratio is 1, whereas at lower temperature the oxide release is more important than the atomic one. The performed mass scans

showed a similar behavior compared to the one registered during the measurement at CERN, with a slight difference in the relative release ratio. The influence of the laser power is illustrated in Figure 77.

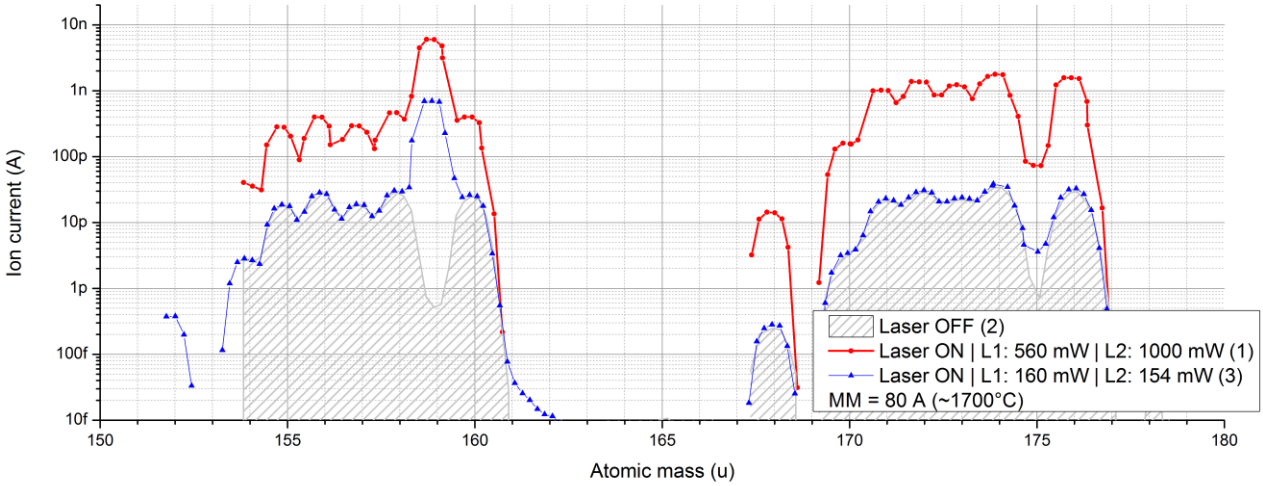

Figure 77: mass spectrum of the gadolinium terbium mixture measurement for different 2 steps laser powers, with the mass marker at around 1700°C

Combining these results with the measurement of the terbium solution only, the potential for the future development is very high. The first proof of principle of this method is foreseen for the beginning of 2019. It consists in the irradiation of a natural gadolinium target at ARRONAX cyclotron and the collection of Tb-155 at CERN-MEDICIS. The outcome will be useful to verify experimentally the yield achievable. Furthermore, it will be useful to extrapolate the data for the future production of Tb-152 and possibly Tb-149.

4.7 Proof of principle

The objective of the proof of principle for the production at ARRONAX cyclotron and the subsequent mass separation at CERN-MEDICIS is to produce Tb-155 as it is the longer-lived isotope within the considered ones. A natural gadolinium target with dimension of 25x25x0.025 cm^3 will be irradiated at ARRONAX cyclotron at the beginning of 2019. The irradiation parameters are 35 MeV and 50 µA proton beam for 5 hours, allowing the production of 149 MBq of Tb-155. Thus, this activity allow an easier handling and it is not too far from the target activities needed for the routine production (some GBq), good compromise for the optimization for the process. At EOB the target is opened in hot cell and transferred for the chemistry.

Once the target irradiated, it will be dissolved with HNO_3 1M and the chemical separation could be performed with the separation method internally developed in ARRONAX based on liquid/liquid extraction. This method has been chosen mainly due to its lower cost compared to other methods such as solid/liquid extraction. An aliquot of the gadolinium solution will be poured in a 5 ml

container, diluted and counted at gamma spectrometry in order to characterize and quantify the contaminants produced in target. This will give the experimental validation of the list of contaminants and their activities. The solution will be then deposited onto a rhenium support and then heated up to around 45 °C for evaporating the acid and deposit terbium mixture salt. Once evaporated the holder will be inserted into the target contained and it will be closed and prepared for the shipment. Once the target arrived in MEDICIS it could be installed on MEDICIS front end and the collection of Tb-155 could be performed

4.8 Conclusion

A new method of large-scale production of high specific activity terbium radionuclides is proposed, consisting in a gadolinium target irradiation at commercial cyclotron and mass separation to obtain very pure batches of non-carrier added radionuclides. The use of mass separation indeed, allow separating those terbium contaminants which cannot be separated with conventional chemical separation techniques. The theoretical development has been presented for the natural gadolinium target development, whereas further investigations will be necessary for the enriched target development for Tb-149 production. First tests with stable terbium showed the feasibility of mass separation, with low separation efficiencies. This can be overcome by the use of resonant laser ionization. It was showed that an improvement up to around 50% of the overall efficiency is possible. The first proof of principle of the production of terbium radionuclides will be performed during the first half of 2019. A very important milestone will be the experimental result on the yield produced at CERN-MEDICIS with the laser ionization added to the conventional mass separation technology.

CHAPTER-5

Target developments for large-scale production of scandium radionuclides

In this chapter a new large-scale production method is proposed for scandium radionuclides considering the irradiation of a target at ARRONAX cyclotron and the off-line mass separation at CERN-MEDICIS. In particular the production of the β- emitter Sc-47 is considered as the other diagnostics radionuclides are already available. All the theoretical steps from the target development to the achievable yield are illustrated. The first step for the feasibility study is the target definition. It is an iterative process which takes in account several parameters: availability of the material, cross-sections of the reactions of interest, achievable yields, cost of the material, target definition and thermal and mechanical resistance of the target.

5.1 Introduction

Scandium is the lightest transition metal belonging to the third group of the periodic table. It has hexagonal structure and under proper conditions it forms insoluble hydroxides, fluorides and oxalates, similarly to the lanthanides. (58) Scandium was discovered in 1879 by Lars Fredrik Nilson, a Swedish chemist, by separation from rare earth mixtures in euxenite and gadolinite. The name scandium derives from Scandinavia. It occurs in association with lanthanides in uranium ores and several minerals. The only known concentrated sources of this element are thortveitite, euxenite,

and gadolinite. The principal uses of scandium are in Sc-Al alloys for different applications such as structural parts in airplanes and in solid oxide fuel cells. Minor amounts of scandium are also used in variety of other applications including electronics, lasers, and lighting. Further uses are: in oxides as a catalyst and in making ceramic parts; in sulfates in very dilute aqueous solutions is used in agriculture as a seed treatment to improve the germination of corn, peas, wheat, and other plants. The abundance of scandium in the Earth's continental crust is remarkable, with average values of 31, 19, and 14 ppm for the lower, middle, and upper crust, respectively. (59)

Scandium has atomic number 21 and up to nowadays 23 isotopes are known, namely one stable Sc-45, six neutron-deficient and sixteen neutron-rich. (25) Among them, a triplet of isotopes raised interest for medical applications because of their physical properties suitable for theragnostics applications: Sc-43 for PET, Sc-44 for PET and $\beta^+\gamma$ imaging, Sc-47 β^- therapy. *Table 31* resumes the main physical properties of scandium radionuclides of medical interest.

Table 31: main physical properties of scandium radionuclides identified for medical applications

Radioisotope	Sc-43	Sc-44	Sc-47
Half-life	3.89 h	3.97 h	3.35 d
Decay mode	β^+ (88%)	β^+ (94%)	β^- (100%)
Main γ emission energy (keV)	373 (22.5%) 511 (176.2%)	511 (188.5%) 1157 (99.9%)	159 (68.3%)
Mean/max. β⁻ emission energy (keV)	N/A	N/A	143/441 (68.4%) 204/600 (31.6%)

Scandium radionuclides are raising increasing interest in medicine. This is mainly due to the theragnostic couples available, namely Sc-43/Sc-47 or Sc-44/Sc-47. Furthermore, the general opinion is that Sc-44 can be a diagnostic agent which could be potentially used in parallel or in place of Ga-68 as the diagnostic pair of radiolanthanides such as Lu-177. In this chapter the large-scale production of the theragnostic couple is analyzed with focus on the production of Sc-47, as the diagnostic radionuclides can already be produced in large quantities and high purity in small scale facility from calcium targets. The new production method is based on commercial high-energy and high current cyclotron irradiation, coupled with mass separation technology. ARRONAX cyclotron and CERN-MEDICIS mass separator are considered for the analysis.

5.2 Scandium Sc-47 production

The clinical application of Sc-47 is still far from ideal due to the lack of regular availability of sufficient quantities batches. However, the physical properties of Sc-47 are suitable for targeted radionuclide therapy of small tumors and cancer metastases. Indeed, from *Table 32* it is glaring that

the emissions from its decay are close to the clinically-established Lu-177. The main differences are the two-times smaller half-life and the higher branching ratio of the 159.4 keV gamma ray (68.3%), which can lead to better SPECT images efficiencies. Indeed, the gamma emission is comparable to Tc-99m one which is ideal for the actual SPECT camera technology.

Table 32: physical properties comparison between Sc-47 and Lu-177

Radioisotope	Sc-47	Lu-177
Half-life (days)	3.35	6.65
Mean/maximum β-	142.6/440.9 (68.4%)	47.7/177 (11.6%)
emissions (keV)	203.9/600.3 (31.6%)	111.7/385.3 (9%)
		149.3/498.3 (79.4%)
γ emissions (keV)	159.4 (68.3%)	112.9 (6.2%)
		208.4 (10.4%)

The production of Sc-47 in a commercial cyclotron with a proton beam up to 70 MeV can be pursued in two ways: irradiation of calcium targets or titanium targets. Other beam particles as deuterons or alpha are not considered in this case. The only calcium isotope that can lead to the production of Sc-47 is Ca-48 with the reaction 48Ca(p,2n)47Sc, although the natural composition of calcium isotopes doesn't allow a satisfactory production. Indeed, the natural abundance of Ca-48 is only 0.187%. For this reason, enriched calcium must be considered (Table 33) with a maximum enrichment level close to 100% and a very high price. For the second way, with the irradiation of titanium, the main reaction is 48Ti(p,2p)47Sc. In this case, Ti-48 is the most abundant titanium isotope therefore natural titanium can be considered as well as the use of enriched target. The comparison between the natural abundance and the maximum enrichment levels achievable for calcium and titanium isotopes are shown in Table 33 and Table 34 respectively.

Table 33: properties of calcium isotopes taken from Trace Sciences.

Isotope	***Natural Abundance***	***Max Enrichment Level***	***Chemical Form***
Ca-40	96.94%	99%	Carbonate, fluoride
Ca-42	0.647%	97%	Carbonate, oxide
Ca-43	0.135%	90%	Carbonate
Ca-44	2.086%	98%	Carbonate, oxide
Ca-46	0.004%	24%	Carbonate
Ca-48	0.187%	97%	Carbonate

Table 34: properties of titanium isotopes taken from Trace Sciences.

Isotope	***Natural Abundance***	***Max Enrichment Level***	***Chemical Form***
Ti-46	8.25%	97%	oxide, metal, chloride
Ti-47	7.44%	95%	oxide, metal
Ti-48	73.72%	99%	oxide, metal, chloride
Ti-49	5.41%	96%	oxide, metal
Ti-50	5.18%	90%	oxide, metal

From the previous tables one can see that enriched Ca-48 can be purchased only under carbonate form. Calcium carbonates are already used for the production of other scandium isotopes as Sc-44. In most of the cases, the carbonate powder is compressed in disks. On the other side natural and enriched titanium are available as a wide range of compounds. Nevertheless, the most interesting for targetry is the metallic form as it is more resistant and is a better conductor, allowing to perform target cooling in a easier way. The main differences between the properties of calcium carbonates and metallic titanium are resumed in the following table:

Table 35: properties comparison between natural titanium and calcium carbonate

Properties	***calcium carbonate***	***metallic titanium***
Density [g/cm³]	2.71	4.506
Melting point [°C]	1339	1668
Thermal conductivity [W/mK]	5.5	21.9
Decomposition temperature [°C]	840	-

In case of the use of calcium targets, particular attention must be paid to the decomposition temperature, as above that value gaseous release may happen from the target.

5.2.1 Cross-section of the reactions of interest

In order to decide which target material to choose, the cross-section of reference and the differences in term of achievable yields are compared. The theoretical cross-sections for the reactions of interest have been evaluated with Talys for comparison and they are reported in *Figure 78* and *Figure 79*. The curves are obtained using the default parameters included in TALYS. *Figure 78* shows the cross-section of the reaction Ca48(p,2n)Sc47 considering a 100 % enriched calcium Ca-48 target, whereas *Figure 79* shows the ones for natural titanium and enriched Ti-48 target material compared to the experimental values obtained from Garrido *et. al.* (2016). (91) No experimental data are available for the reaction Ca48(p,2n)Sc47 below 70 MeV. The only data published in literature refer to incident proton beam between 660 and 120 MeV. (92)

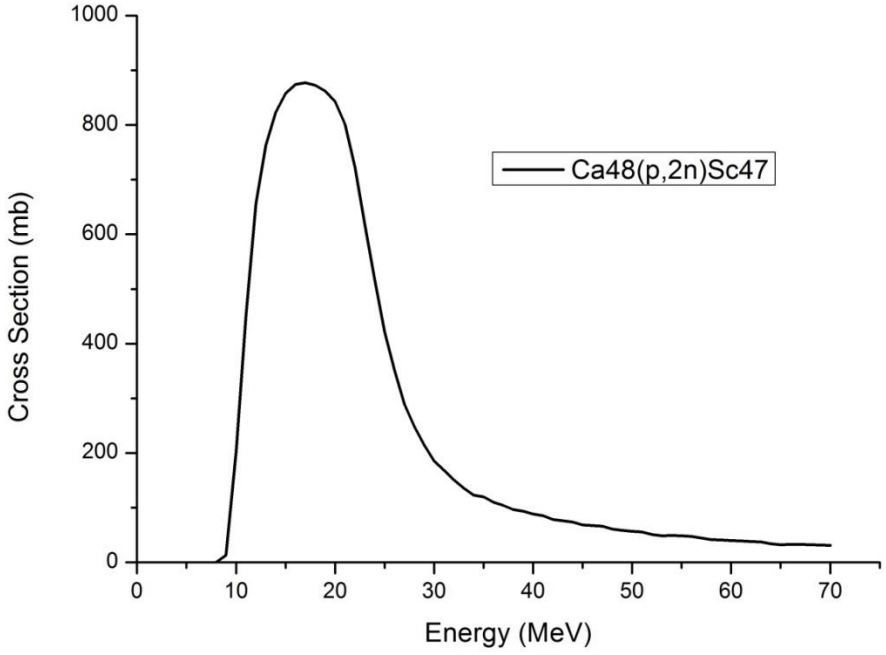

Figure 78: cross-section for the production of Sc-47 from enriched Ca-48 target.

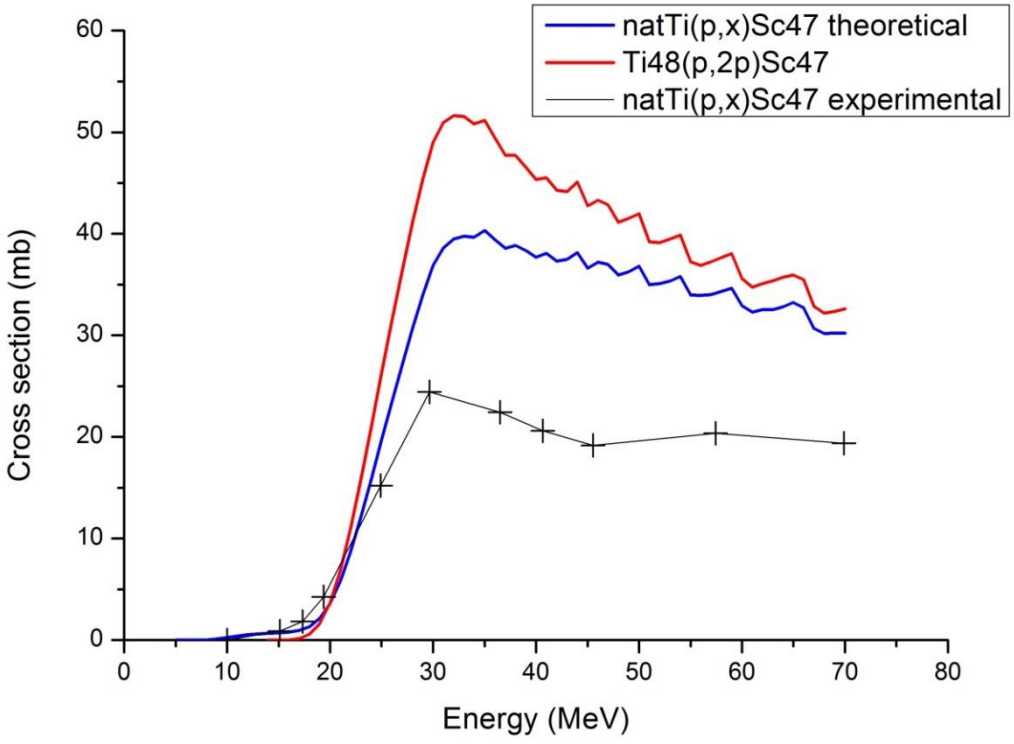

Figure 79: cross-section for the production of Sc-47 from natural titanium and enriched Ti-48 targets, compared with experimental results from Garrido et.al (2016) (91).

5.2.2 Yield comparison

With the presented cross-sections, a comparison of the achievable yield is made for evaluating which starting material to choose. The yield comparison shown in *Figure 80* and *Figure 81*, highlight that the use of enriched titanium induces a gain of 16 %. Thus, it doesn't justify the use of the more expensive enriched titanium Ti-48. For this reason only natural titanium is considered. An enriched Ca-48 target is favorable from the point of view of the production rate, in particular below 30 MeV. However, the target material is very expensive compared to the natural titanium and its availability could be an obstacle for the large-scale supply. Furthermore, the targetry is easier for natural titanium because it can be purchased in metallic foils with different thicknesses and shapes, while enriched calcium is present only under oxide or carbonate powder. For this reason, for this analysis natural titanium is chosen. However, looking to the comparison between the curve calculated with Talys with default parameters and the experimental values coming from Garrido et. al. (91) a factor 2 should be taken into account when considering theoretical cross-sections.

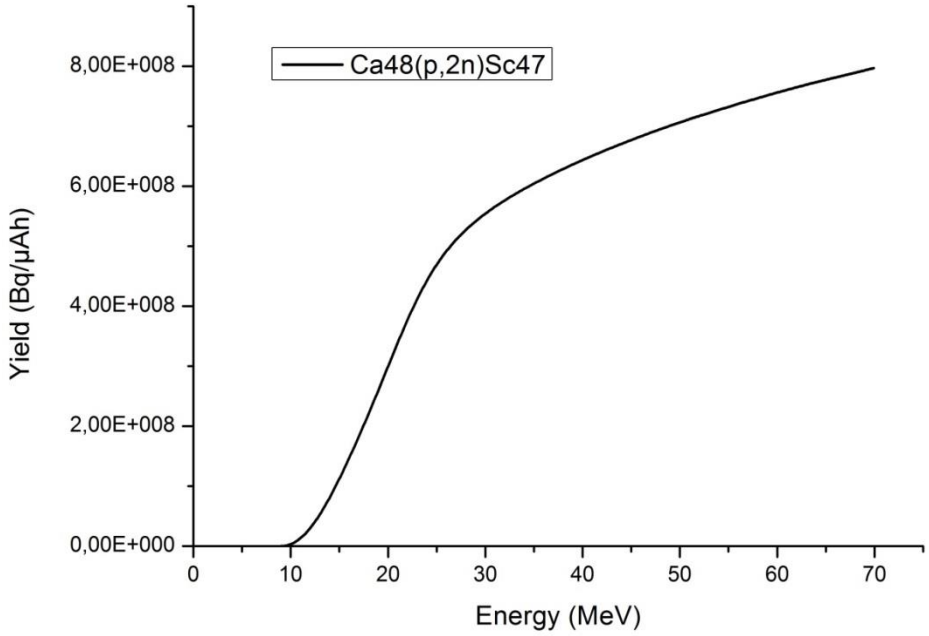

Figure 80: Sc-47 yield achievable from a 97% enriched Ca-48 target.

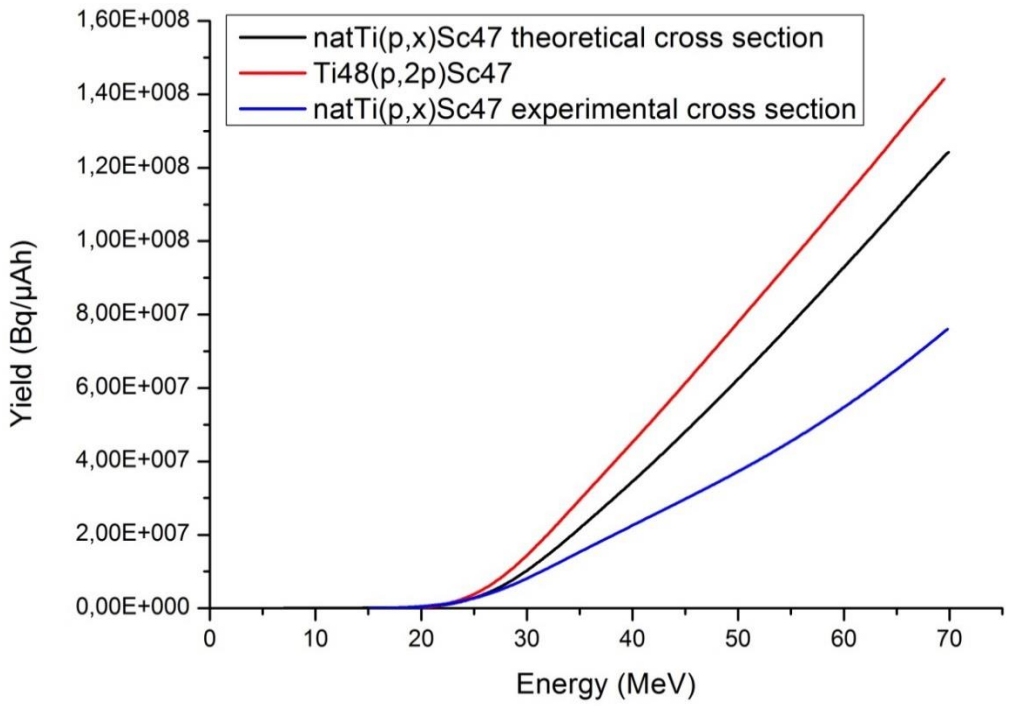

Figure 81: yield comparison for energies up to 70MeV for the production of Sc-47 from natural titanium and from 99% enriched Ti-48 targets. Experimental data are taken from Garrido et. al. (2016). (91)

5.2.3 Scandium diagnostic pair co-production

By Irradiation of a natural titanium target, several scandium radionuclides will be co-produced at the same time. The most interesting radionuclides are Sc-43 and Sc-44 that are used for diagnostic applications.

The mass separator at CERN-MEDICIS-PROMED has been commissioned with only one collection point, suitable for the collection of one radionuclide per collection and the priority is given to the production of Sc-47. However, as explained in the introductory chapter, it can potentially allow collecting three different radionuclides, because it can be set on three different masses for the collection in three collection chambers simultaneously. For this reason, yields of those radionuclides are evaluated in the following figure. For Sc-44g (half-life 3.97), it is considered the production of its metastable state Sc-44m (half-life 58.6 h), which decays 98.8% IT in Sc-44g and 1.2% β+ in stable Ca-44. Sc-44m can act as in-vivo generator of Sc-44g.

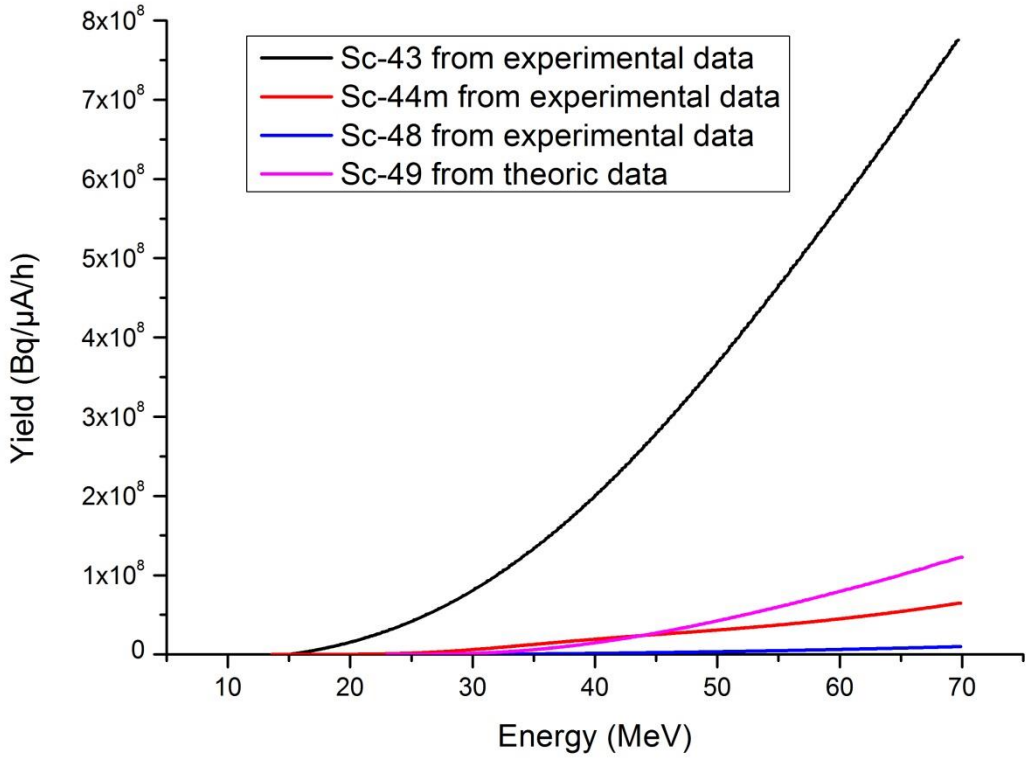

Figure 82: yield comparison between the co-products of Sc-47 interesting for medical application. Experimental data are taken from Garrido et.al. (2016) (91).

5.2.4 Target thickness

Considering the previously calculated yield for Sc-47, a target of natural titanium should be defined. The thickness should allow the interaction of the beam with the target in the range of 30-70 MeV. Determining the stopping power of a 70 MeV proton beam in a metallic titanium target with SRIM, it is possible to evaluate the projected range. The curve is presented in Figure 83. It is evident that around 10 mm of target thickness is needed in order to irradiate the target at the suitable conditions to maximize the production of Sc-47. Thus, it might be challenging to irradiate such thick target. Multiple thinner targets might be considered instead.

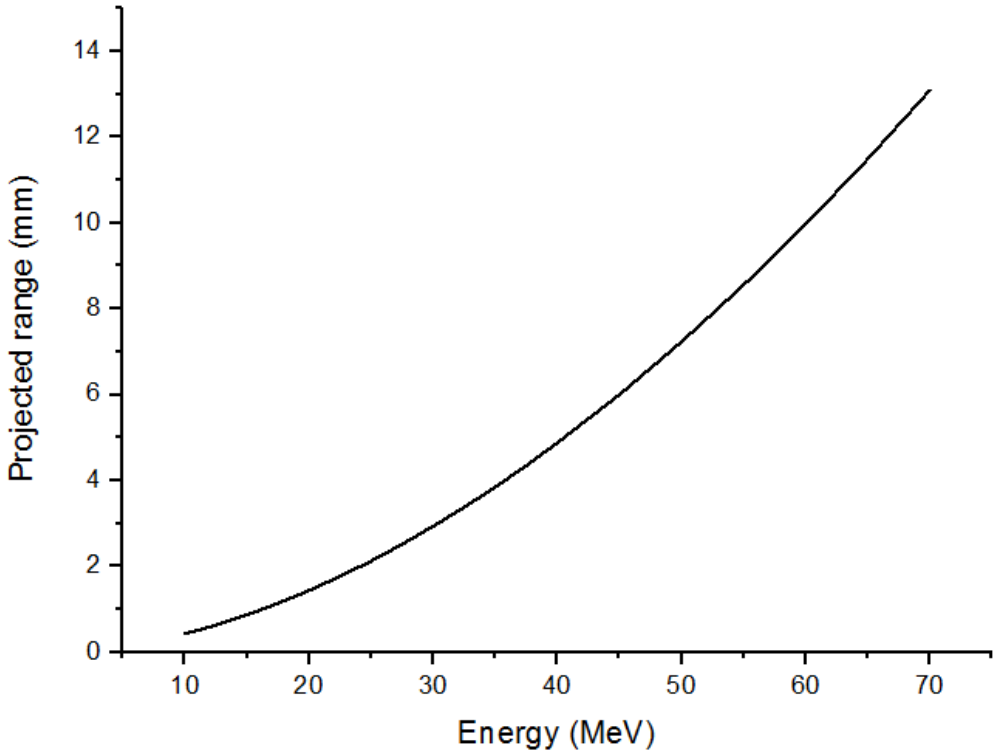

Figure 83: projected range of a proton beam incident on natural titanium target.

5.3 Target definition

Considering the target system used for natural gadolinium targets and their dimensions (4.2 Target definition: Tb-152 and Tb-155 production), the same geometry has been considered for natural titanium targets. However, in this case, considering the stopping power and the energy range of the incident beam with a 4 mm thick target, two targets in a row can be used due to the lower thermal load on the second disk compared to gadolinium and due to the suitable energy range for Sc-47 production. In *Figure 84* the breakout of the considered target system, with the respective incident proton energy for each layer, is presented.

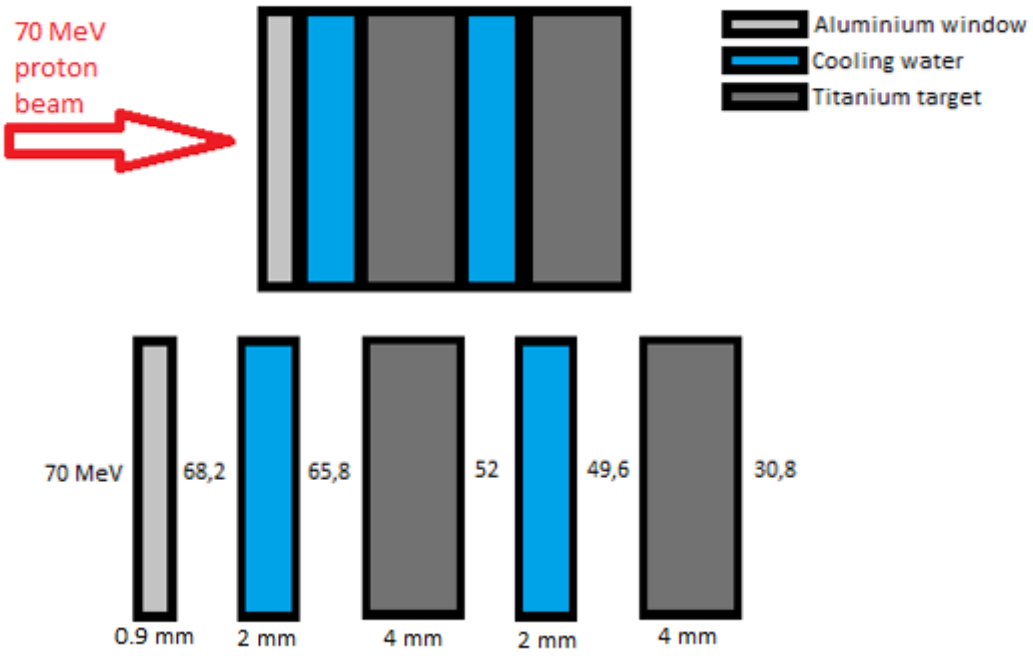

Figure 84: breakout of the targetry system considered with the incident proton beam energy for each layer

The considered target is simulated with Ansys simulations for the feasibility study and the definition of the nominal beam parameters.

5.3.1 Thermal and mechanical target resistance

As for the terbium production analysis described in the previous chapter, when developing a target, it is of fundamental importance to guarantee the integrity of the target during the irradiation. Therefore, it is necessary to set up an iterative process to define the best target dimensions for maximizing the production yield. This is explained in detail, in Annex I.

In this case, as two disks in a row are considered, only the second is simulated. Thus, the thermal power deposition is higher in the second disk because the slowing down of the beam is more important at lower incident beam energy.

5.3.1.1 1-D thermal evaluation

For a natural titanium target, the 1-D thermal evaluation gave the results presented in *Table 36*. The considered thermal exchange coefficient is h=30000 W/m^{2}K.

Table 36: 1-D thermal evaluation of titanium targetry for the production of Sc-47

Proton current (µA)	Maximum target temperature (°C)	Maximum water cooling temperature (°C)
100	522.7	232.1
50	271.3	125.5
10	10.1	41.1

5.3.1.2 Static calculation in 3-D

For the titanium targetry CFD study, only one disk has been analyzed, the second one seen by the beam. The disk has been simulated with a reduced geometry for optimizing the computational cost, respecting the symmetry of the system. Thus, a quarter of half thickness disk has been designed. Similarly, for what was done in case of gadolinium target in the previous chapter, a function has been written to take in account the ideal Gaussian shape of the incident proton beam. The function depends on the incident proton current.

Table 37: water cooling and target temperature for different beam currents and thermal exchange coefficients for titanium target

Heat transfer coefficient (W/mK)	**beam current (µA)**	**T water (°C)**	**T max (°C)**
40000	100	203,4	628,9
	75	160,5	426
	50	114,6	335,4
	25	67,3	177,7
30000	100	260,3	678,8
	75	204,4	466
	50	144,5	362,5
	25	82,2	191,3
20000	100	369,1	774,9
	75	288,8	543,3
	50	202,2	415,2
	25	111,1	217,5
10000	100	664,2	1039,9
	75	520,8	758,5
	50	362,5	563,1
	25	191,2	291,6

Interpolating the data of Table 37, the beam current corresponding to the thermal load induced on the target casing, the heating of the water to its boiling point, considering the nominal thermal exchange coefficient, is 81.2 µA. Considering around 10 % of safety margin, the maximum beam current considered for the irradiation will be 75 µA.

The temperature profile reached in the target is presented in Figure 85. The maximum temperature reached in the center of the target is 514 °C which is less than a third of the titanium melting point, meaning a very high safety margin. The maximum temperature at the interface target cooling water is 184 °C.

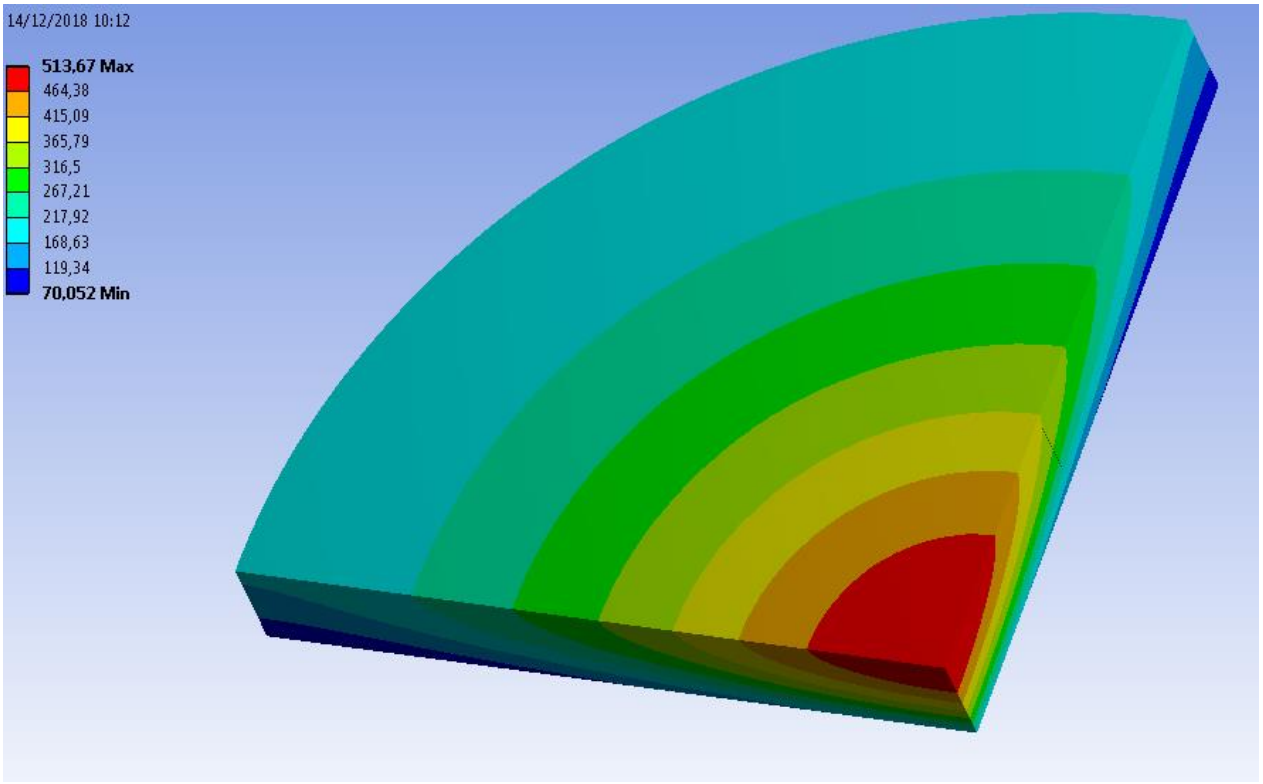

Figure 85: temperature profile for a titanium target irradiated with a 73 µA proton beam

The thermal simulation has been applied to the mechanical one. In Figure 86 is shown the total deformation of the target, in Figure 87 is represented the von Mises equivalent stress (Pa) of the target. Both figures are in higher scale (8.7x) in order to zoom and highlight the deformation. Indeed, the induced thermal power on the target leads to a negligible swelling of the latter. This can be seen only increasing the scale of the geometry significantly. Titanium has an ultimate tensile strength ranging from 275 to 590 MPa, and the measured maximum tensile strength is 570 MPa, meaning a possible non-elastic behavior of the target. Therefore, particular attention should be made on the mechanical characteristics of the material purchased if 75 µA are strictly needed. If not, it is suggested to lower to maximum beam current of 5% to 10%.

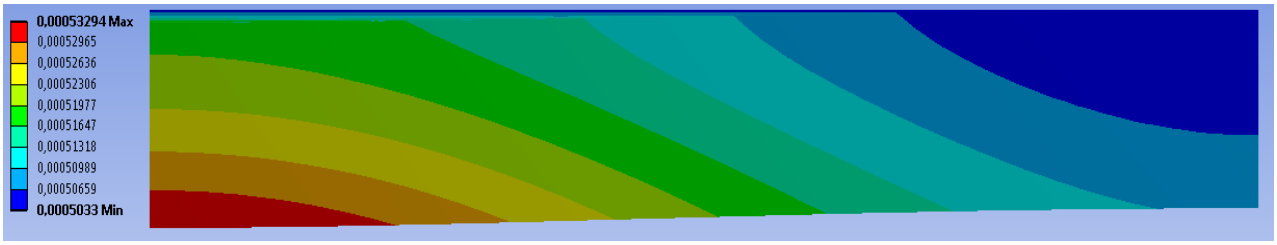

Figure 86: total deformation of the target (m). The scale is amplified (8.7x).

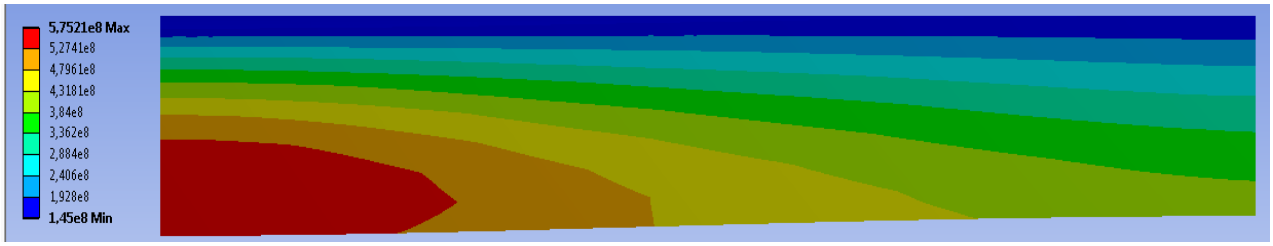

Figure 87: von Mises equivalent stress (Pa) of the target. The scale is amplified (8.7x).

5.3.1 Sc-47 production estimation

Monte Carlo simulations performed with MCNPx can estimate the list of the contaminants produced from the interaction between the proton beam and the target. MCNPx outputs will be analyzed with the tool Orihet which allows a quantitative and qualitative estimation considering the contaminants decay over time. The list of the radionuclides produced in-target considering the targetry system mentioned above with a 70 MeV proton beam is presented in Table 38.

Table 38: list of all the radionuclides produced with a proton beam of 70 MeV in a natural titanium target. For each radionuclide the theoretical activity EOB is calculated.

ELEMENT	***Half-life***	***Yield EOB (Bq/µAh)***
S-35	87 d	2,06E+03
Cl-36	3E+05 y	2,79E-02
Cl-39	56 m	6,25E+05
Ar-37	35 d	2,72E+05
Ar-39	269 y	1,73E+02
Ar-42	33 y	1,50E+01
K-38	7.6 m	2,50E+06
K-42	12 h	1,25E+08
K-43	22 h	1,67E+07
K-44	22 m	3,13E+06
Ca-41	9.9E4 y	7,92E+00
Ca-45	162 d	1,47E+06
Ca-47	4.5 d	8,88E+05
Sc-43	3.89 h	8,10E+08
Sc-44	3.97 h	9,66E+09
Sc-45m	318 ms	2,78E+01
Sc-46	**83.8 d**	**5,48E+07**
Sc-47	**3.34 d**	**5,29E+08**
Sc-48	43 h	8,77E+07
Sc-49	57 m	2,14E+08
Ti-44	60 y	1,97E+04
Ti-45	185 m	6,81E+09
V-47	32 m	3,22E+09
V-48	16 d	8,66E+07
V-49	330 d	1,25E+06

As one can notice from the contaminant list, several scandium isotopes are co-produced. The main constraint is given by Sc-46 that has 83.79 days of half-life. Indeed, whereas the other scandium contaminants can be separated or strongly reduced by setting some decay time, Sc-46 cannot be separated. Considering the target system mentioned above, the inlet energy in the target is 65.8 MeV and the outlet energy is 30.8 MeV. With those parameters, the yield ratio of Sc-46 over Sc-47 production is around 10%, given by Monte Carlo simulations starting from the theoretical cross section values. Starting from experimental cross sections values, one can obtain

9.9% that is in agreement with the simulations. For this reason, the mass separation system at CERN-MEDICIS is taken as reference for this analysis. Therefore, considering the extraction of atomic Sc-47, particular attention has been made on contaminants with mass 47. As V-47 has a very short half-life, the only contaminants are Ca-47 and stable Ti-47. For this reason, a first chemical separation has to be foreseen in order to reduce the contaminant number of atoms. Indeed, the aim is to reduce the ratio titanium/scandium in the target for improving the following mass separation. A ratio of at least around 10 has been targeted from previous experience of mass separation technique.

An example of yield and specific activity achievable is given in Table 39, considering 3.3 days of irradiation (one Sc-47 half-life), 70 MeV and 25 µA proton beam, 5% of mass separation efficiency (37). The specific activity values should then be compared to the theoretical specific activity of Sc-47 which is 31.1 TBq/mg.

Table 39: Sc-47 yield and specific activity achievable with 3.3 days of irradiation (one Sc-47 half-life), 70 MeV and 25 µA proton beam, 5% of mass separation efficiency

	Activity	Specific Activity
End Of Beam	1.185 TBq	65.8 MBq/mg
Post mass separation	29.6 GBq	30.6 TBq/mg

5.4 Conclusions

A new method of large-scale production of scandium radionuclides is proposed, in particular for Sc-47, consisting in natural titanium targets irradiation with commercial cyclotrons followed by the mass separation. Its use is considered to obtain very pure batches, as the major constrained is the co-production of Sc-46. The theoretical development of the targetry for the production of Sc-47 in commercial cyclotrons has been finalized. Before performing the proof of principle of the production method, some further investigations are suggested. The first one is the study of the mass separation of cold scandium from a stable scandium titanium mixture of standard solutions. The experimental efficiency numbers are needed to verify the feasibility of the process and the achievable yield. Furthermore, an experimental campaign for the resonant laser ionization efficiency of the system previously mentioned is needed. The two experiments will give the optimal setup for the first radioactive production at CERN-MEDICIS. Finally, a very important milestone will be the experimental result on the yield produced at CERN-MEDICIS with the laser ionization added to the conventional mass separation technology.

CHAPTER-6

Erbium Er-169 production

Erbium Er-169 is one of the most interesting radiolanthanides for new potential receptor-targeted β- therapy applications. Its main physical characteristics are low energy β- emissions and the low energy and very low intensity gamma rays. In this chapter the production of the first worldwide batch of very high specific activity Er-169 is presented. The result was achieved by adding the mass separation step, at CERN-MEDICIS, after the production of Er-169 in nuclear reactor, at ILL. The developments from the starting material selection to the further improvement needed are illustrated and discussed. A focus has been made on resonant laser ionization to improve the overall production yield. The illustrated complete production method could guarantee a large-scale supply of Er-169 for preclinical study first and potentially for future clinical supply.

6.1 Introduction

Erbium is a lanthanide which was discovered in 1843 by Carl Gustaf Mosander, Swedish professor in chemistry and pharmacy. He succeeded in separating the gadolinite in three compounds: yttria, erbia and terbia. Initially he named the rose oxide powder terbia, name who was years later inversed in erbia. (93) The name is coming from the Swedish village of Ytterby, near Stockholm, from which mine are deriving several elements' names. With the latest nomenclature it became Erbium as known nowadays. Later, Heinrich Bommer and Wilhelm Klemm were the first to isolate a metallic erbium powder sample in 1934.

In Earth's crust, erbium is as abundant as tantalum and tungsten, around 2.8 mg/kg and in seawater is around 0.9 ng/l. (94) Usually it occurs in a mixture of lanthanides. It is currently used for several applications: for photographic filters, rose spots in ceramic glazes or glasses, metal properties changer when alloyed with other metals as vanadium (it lowers the hardness and improves the malleability), amplifier in optic fibers. It has 6 isotopes in nature with the following abundances: Er-162 0.1%, Er-164 1.6%, Er-166 33.5%, Er-167 22.9%, Er-168 27.0%, Er-170 14.9%. Among erbium radionuclides, two of them have interesting physical properties for medical applications: Er-165 for Auger therapy and Er-169 for β^- therapy. Er-165 (10.3 hours of half-life) is one of the very few quasi-pure Auger electron emitter isotopes. (95) Whereas the properties of Auger electrons are suited for the local DNA damage of tumoral cells, as they are very low energy electrons which have high linear energy transfer (LET), they are still far from the clinical use. Er-169 is the longest lived among erbium radioisotopes with 9.39 days of half-life. It is an almost pure β^- emitter with few low energy and very low intensity gamma rays. The main physical characteristics are presented in the following table, compared to lutetium Lu-177, which is the β^- emitter of reference for the already available targeted radiotherapy (25).

Table 40: main physical properties comparison between Er-169 and Lu-177 (25).

Radioisotope	**Er-169**	**Lu-177**
Half-life (days)	9.39	6.65
Mean/maximum β^- emissions (keV)	98.27/342.9 (45%) 100.96/351.3 (55%)	47.7/177 (11.6%) 111.7/385.3 (9%) 149.3/498.3 (79.4%)
γ emissions (keV)	109.78 (1.3E-3%) 118.19 (1.4E-4%)	112.9 (6.2%) 208.7 (10.36%)
Mean/max. penetration in soft tissues	0.2/1 mm (96)	0.23/1.7 mm (97)

As showed in the table, Er-169 has lower energy and low intensity gamma rays. Whereas it is an advantage in terms of radioprotection, it is not possible to follow the treatment with gamma imaging. However, as all radiolanthanides, it can be coupled with a diagnostic radionuclide pair of trivalent elements, such as Ga-68 or Sc-44, for theranostics applications. The lower β^- energies instead, could be useful for specific small tumor treatment requiring lower electron energies to diminish as much as possible the deposition of their energy outside the tumor cells, preserving healthy tissues.

Due to its characteristics, it has already been used in medicine for radiosynovectomy (also called radiosynoviorthesis) of small joints such as finger joints. (96) Radiosynoviorthesis has been used since 1952 with the injection of pure or almost pure β^- emitters based radiopharmaceuticals.

Different isotopes are currently used for different sized joints depending on their physical characteristics, in particular the electron emission energy: Y-90 is used for knee joints while Re-186 for elbow and ankle joints. For targeting the joints, the radionuclides could be used as a colloid in citrate form. (96) For this application low specific activity of carrier-added Er-169 can be used. The radionuclide batches are currently produced in nuclear reactors irradiating highly enriched, up to 98.2%, Er-168 targets. The neutron capture reaction of the target material allow producing Er-169: Er168(n,γ)Er169. In Figure 88 the cross-section of reference, taken from TENDL 2017 database is given.

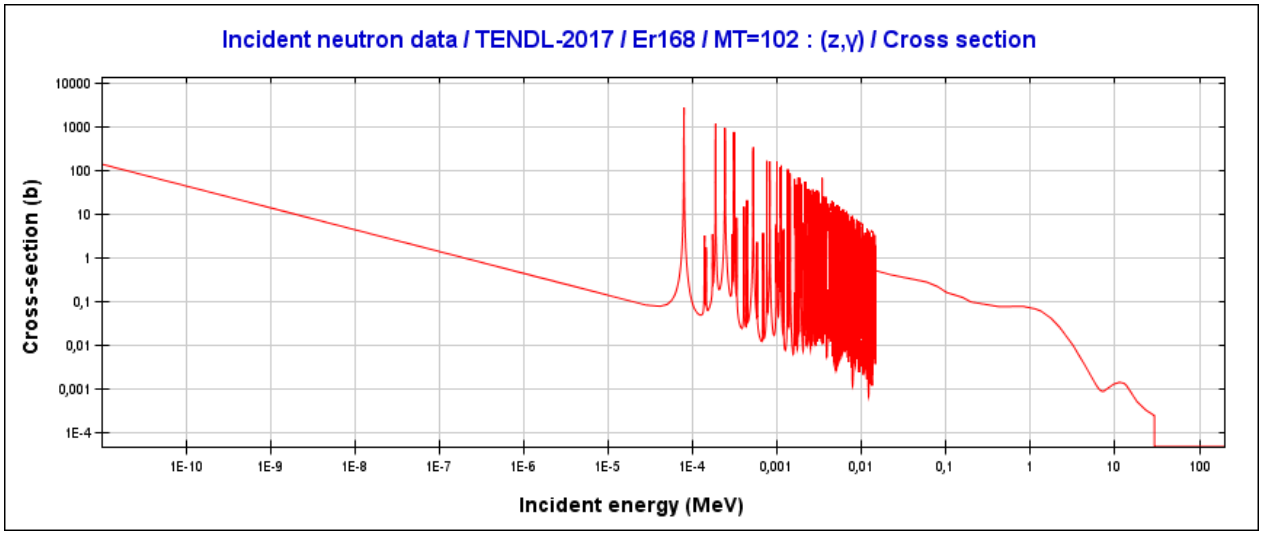

Figure 88 : neutron capture cross-section for the reaction Er168(n,γ)Er169. Data taken from TENDL 2017 database.

The rather small cross-section, 2.3 barns for thermal neutrons (2,5E-8 MeV), is a limit for the specific activity. Considering the neutron flux of 1.2E15 n/cm^2/s, achievable in a high-flux nuclear reactor such as ILL, and ten days of irradiation, the specific activity achievable is 4.8 GBq/mg according to the equation (9) (1.2.1.1 Specific activity). It corresponds to a ratio between Er-168 and Er-169 nuclides of 650 at end of irradiation. The dilution of Er-169 in stable erbium limits the benefits in receptor-targeted therapy as stable erbium will compete with the radioactive one for the radiolabeling. Therefore, higher specific activities are required. For improving the specific activities, Er-169 should be separated from stable erbium Er-168. As they are isotopes of the same element, conventional chemical separation processes could not be used. In this chapter the mass separation of a reactor irradiated enriched Er-168 target is proposed for the production of very high specific activity batches of Er-169 for the potential application in vectorized radiotherapy. The experiments performed to produce Er-169 at ILL's (Institute Laue Languevin) high flux nuclear reactor in Grenoble (France) combined with the mass separation of the irradiated samples at

CERN-MEDICIS will be discussed. The experimental campaign results are shown and the potential improvement of the system introducing the laser ionization to the mass separation will be analyzed.

6.2 Offline mass separation test with stable erbium

The first step is to determine the experimental overall efficiency of stable erbium extraction with mass separation technology. This will allow obtaining extrapolated yields values for production estimations. The separation of a known mass of stable erbium was performed in the offline laboratory at CERN. For this experiment MEDICIS target unit #631-M, the one dedicated to the following separation of Er-169 at CERN-MEDICIS, was used. It consists in a conventional ISOLDE type target unit, with inside an empty target container and a tungsten surface ion source. Usually a tantalum plug is used to close the tantalum target container, but with the high working temperatures it welds. This behavior is fine when the target is irradiated with CERN's proton beam because the target container has not to be opened once assembled. In our case as the target container has to be filled several times, the plug should be easily removable. Therefore, for guaranteeing the retrieval of the inserted samples a special graphite plug has been used.

The inserted sample consisted in erbium standard solution (1 mg/ml with 5% HNO_3) purchased from Alfa Aesar. A volume of 100 µl, which means 3.6E17 atoms of natural erbium, were poured on a graphite disk laid on a molybdenum boat. The boat is used only to prevent any contact between the sample and the tantalum container. Indeed, at very high temperatures graphite and tantalum could react. By means of a lamp, the sample was heated to evaporate the acid solution and deposit the erbium salt $Er(NO_3)_3$. The surface temperature of the solution was measured with a laser pyrometer and it resulted in a temperature of around 40°C. Graphite has been chosen for erbium separation because we thought it could improve the erbium release as it is a reductive material. It was not used for terbium because from past experiences graphite hindered the release of terbium. In the Figure 89 is shown the preparation of the sample.

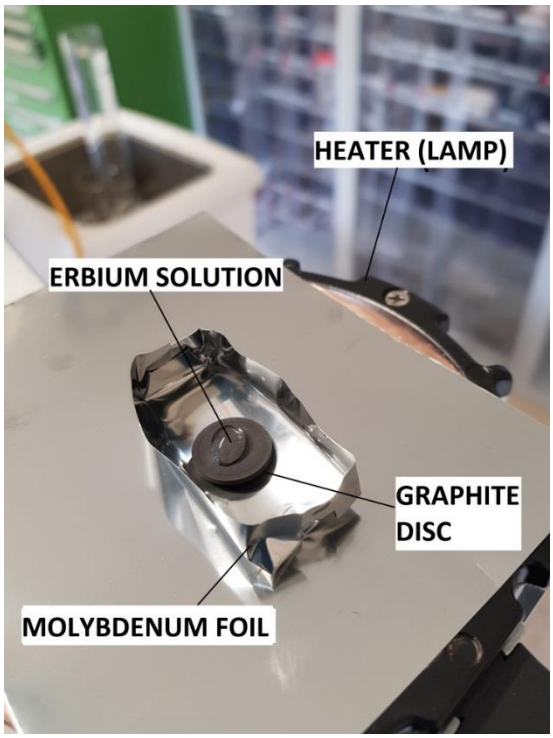

Figure 89: representation of the target used for the stable erbium separation test

After inserting the sample inside the target container, the target unit was positioned on the offline 1 front end. Offline 1 is an offline mass separator at CERN used for testing new targets and new targetry technologies before going online for irradiation in ISOLDE or MEDICIS. Once the front-end vacuum reached the order of magnitude of $1 * 10^{-6}$ mbar, the ion source was heated up to around 2100 °C. When it reached the temperature, the mass separator was calibrated. The first calibration was made on the Einzel lens and the position of the extraction electrode for optimizing the extracted total beam. Then the Faraday cup was removed and the mass separated beam optimized on mass 39 and 41, which are the masses of the potassium isotopes present in nature. When the profile of the beam was optimized, the target container was gradually heated up. Erbium begun to be released at around 1550 °C (corresponding parameters: line 330 A, target 425 A), with a vapor pressure at that temperature equal to $2 * 10^{-2}$ mbar. After that, the heating was stopped for optimizing once more the extracted beam in shape and magnitude. This because the mass 166 of the most abundant erbium isotope was selected for the run and it is far from the masses 39 and 41, meaning eventual slightly different settings. Then the target was heated to around 2100 °C. The separation was performed over 7.8 h collecting $3.147 * 10^{14}$ ions of Er-166. As it is 33.5% of the natural erbium, the initial number of Er-166 atoms in the sample were $3.6 * 10^{17} * 0.335 = 1.206 * 10^{17}$. The overall efficiency of the mass separation was consequently $\frac{3.147*10^{14}}{1.206*10^{17}} * 100 = 0.26\%$.

When reaching the maximum temperature in the target, there was a release current peak of 1.7 nA. Then as the temperature remained constant until the end of the measurement the release of Er-169 from the target exponentially decreased over time as expected. The ratio of atomic versus oxide release was 100, constant for the entire measurement. This signify that the efficiency loss due to the oxides formation is negligible.

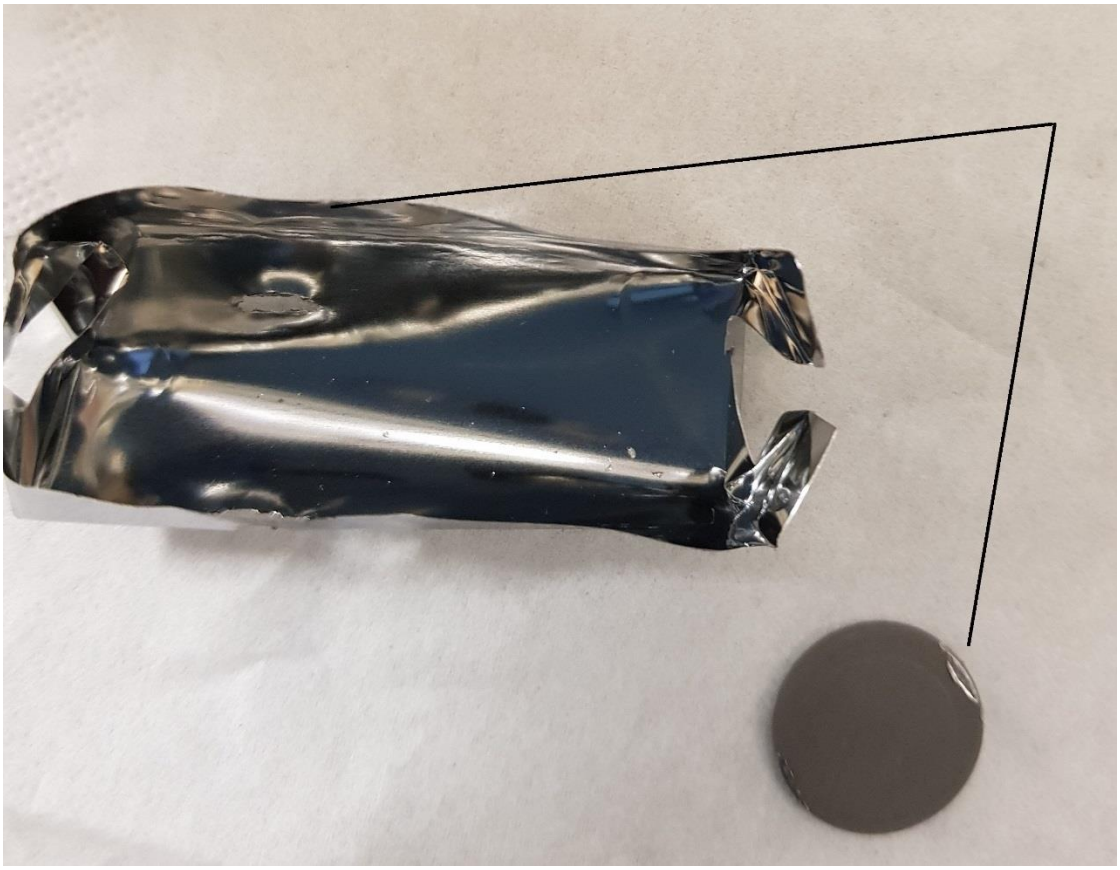

Figure 90: signs of the contact points graphite/molybdenum after being used at around 2100 °C.

Once the test was finished, the target was opened and the sample removed. It appeared that the contact points between graphite and molybdenum melted forming holes. (Figure 90) Therefore, a new system had to be studied for the final experiment. Several boat holder materials as molybdenum, tantalum, tungsten and rhenium have been simulated with the software HSC Chemistry 7.1. The aim was to find a material which does not react with graphite at high temperatures (around 2100 °C). The results showed that rhenium has the best behavior in high temperature environments as compared to the other materials. Indeed, it starts to react with graphite around 2150 °C. A thermal test was performed in the pump stand at CERN. It turned out that rhenium and graphite start to react and melt at the contact points between 2100 and 2200 °C, confirming simulations. Those temperatures are the usual maximum working temperatures at

MEDICIS. Therefore, the system composed by a graphite container laid on a rhenium holder was selected for the final experiment.

6.3 Material choice and NAA test

The best and most used way for producing Er-169 is the neutron activation of the enriched erbium Er-168 through the reaction Er-168(n,γ)Er-169. The market of highly enriched Er-168 was analyzed to buy the best target material. Several suppliers were contacted, then two different materials have been chosen based on the enrichment level, price and type and quantity of contaminants. One sample has been purchased from Isoflex and the other from Trace Sciences. Enriched erbium was purchased as oxide Er_2O_3, a pink powder. The isotopic composition comparison of the two materials is shown in Table 41.

Table 41: starting material characteristic

Company	**Isotopic composition (%)**					
	Er-162	Er-164	Er-166	Er-167	Er-168	Er-170
Trace Sciences	<0,06	<0,06	0,35	0,76	98,2	0,69
Isoflex	0,02	0,03	0,35	0,9	98	0,7

For each sample, a certificate of analysis was provided from the supplier (ANNEX-B). However, a first activation test has been performed in order to verify the contaminants type and quantity and compare them with each certificate of analysis. Particular attention was given to radiolanthanides having mass 169 and 153 because the atomic ion in the first case and the eventual oxide molecules in the second case have the same mass of the wanted radionuclide. They will be found in the isobar collected after the mass separation, lowering the achievable radionuclidic purity.

The test irradiation was performed at ILL at the external cold neutron beam line PF1b the first week of March 2017. For each starting material a quartz ampoule and a plastic ampoule (Eppendorf) were filled. For the comparison analysis, only the plastic ampoules are considered as their gamma spectrometry outcomes are more statistically consistent. Indeed, the quartz ampoules activation induced a higher background compared to the plastic ones. The parameters are described in Table 42.

Table 42: Irradiation parameters for Isoflex and Trace Sciences samples.

Material	**Isoflex**	**Trace Sciences**
Er_2O_3 mass	2 mg	4.1 mg
Start irradiation time	06/03/17 at 17.43	07/03/17 at 23.45
End irradiation time	08/03/17 at 8.30	08/03/17 at 8.30
Beam type	Cold neutrons	Cold neutrons
Beam flux [n/cm^2/s]	1.68E10	1.32E9
Irradiation time [h]	34h02	8h45

Due to the delay in the delivery of the Trace Sciences material, the irradiation time is different and the neutron flux is lower as the sample was positioned in a different cold neutrons irradiation spot. Furthermore, because of the concomitance of experiments in the same line, during the irradiation of Isoflex samples, the beam has been switched on and off several times. It results in an effective irradiation time of 34h02. No interruption to report for the irradiation of Trace Sciences samples. After the irradiation, the ampoules were left in the irradiation bunker for some hours to let very short-lived radionuclides decay. After that, they were taken out and counted on a germanium detector for gamma spectrometry several times in the following days. The importance of counting after several days is that the short-lived nuclides have decayed and the longer-lived isotopes can be detected more accurately. The software used for the acquisition and the analysis is Genie2000 (21). In the following tables are presented the gamma spectrometry results. The less-than sign in front of a number means that the number is an upper limit, therefore not directly detected but estimated as the minimum activity detectable for such nuclide for a given measurement.

Table 43 : detected radionuclides and other potential contaminants upper limits for the Isoflex material Eppendorf ampoule

DETECTED RADIONUCLIDES

Element	**radionuclide**	**parent nuclide mass (mg)**	**parent nuclide PPM**	**Comments**
Er	Er-171	1,2E-02 ± 1.9%		
	Er-169	2.04 ± 18%		
	Er-165	7.5E-04 ± 40%		
Dy	Dy-165		41	
Yb	Yb-169		2	
Gd	Gd-159		75	
Co	Co-60	4,8E-03		related to the ampoule
Na	Na-24	1,4E-03		related to the ampoule

OTHER POTENTIAL CONTAMINANTS

Element	**radionuclide**	**parent nuclide PPM upper limit**
Gd	Gd-153	< 10
Zr	Zr-95	< 428
Dy	Dy-157	< 4
	Dy-159	< 743
Ag	Ag-110m	< 28
Ca	Ca-47	< 86

Table 44: detected radionuclides and other potential contaminants upper limits for the Trace Sciences material Eppendorf ampoule

DETECTED RADIONUCLIDES

Element	*Radionuclide*	*parent nuclide mass (mg)*	*parent nuclide PPM*	*Comments*
Er	Er-171	2.6E-02 ± 8%		
	Er-169	3.67 ± 10%		
	Er-165	2.85E-04 ± 16%		
Tm	Tm-170		645	
Dy	Dy-165		57	
Yb	Yb-169		3	
	Yb-175		7	
Na	Na-24		422	related to the ampoule

OTHER POTENTIAL CONTAMINANTS

Element	*Radionuclide*	*parent nuclide PPM upper limit*
Lu	Lu-177	< 385
Ho	Ho-166	< 17
Tb	Tb-160	< 82
Ca	Ca-47	< 37
Gd	Gd-153	< 8
	Gd-159	< 707

No harmful contaminants have been detected in both starting materials. Less contaminants have been detected compared to the one present in both certificates of analysis. The main contaminant detected which could decrease the radionuclidic purity achievable having the same mass of Er-169 is Yb-169. In contradiction with Isoflex certificate of analysis (ANNEX-B) Yb-169 has been detected. The detected quantity of Yb-169 was even the same for both samples, considering a double mass irradiated for the Trace Sciences sample. Furthermore, Gd-153 could be found in the collection isobar in GdO ion after mass separation in very small quantities. Indeed, it comes from the neutron activation of Gd-152, which is the least abundant gadolinium isotope at 0.2%. Due to the lower content of the unwanted impurities, in particular ytterbium isotopes in Trace Sciences sample, it will be the chosen material.

6.4 First Er-169 production

The first irradiation of the chosen Trace Sciences enriched Er-168 sample, took place at ILL from the 13th to the 20th of April 2018. A quartz ampoule was filled with 3.4±1 mg of erbium oxide and

irradiated with an effective average thermal neutron flux of 1.2E+15 n/cm^2/s. After irradiation, the sealed irradiated ampoule needs to be opened for extracting the erbium powder for the mass separation. Once the ampoule is opened, the powder must be dissolved with an acid solution and then transferred on a support which is inserted in MEDICIS target unit. For this first test the Er-169 handling limitation at CERN-MEDICIS was 500 MBq, and at MEDICIS facility the radiochemistry laboratory was not yet completed. For this reason, the irradiated sample was sent to Hevesy Laboratory (Denmark) for processing and sent back to CERN. Together with Prof. M. Jensen a fume hood has been prepared, developing the procedure for the experiment. In Figure 91 the experimental setup is shown.

Figure 91: *on the left the experimental setup in the fume hood at Hevesy Laboratory (DK). On the right the evaporation of the erbium acid solution for the deposition on the graphite support*

When the radioactive sample arrived at Hevesy Lab, it was put inside the fume hood. Then the ampoule was cut with a Dremel. 1 M HNO_3 was used to dissolve the erbium oxide and transfer it from the ampoule to the support consisting in a graphite holder inserted in a rhenium boat. Then with a lamp, the solution was heated to around 40 °C, this allowed then the evaporation and the deposition of the solution on the holder. The sample was then packed and sent to CERN-MEDICIS. At CERN, the sample was extracted from the container and put inside the MEDICIS target unit, which was later positioned on the mass separator front end.

In order to calibrate the mass separator, two mass markers were put inside the target unit, one containing an excess mass of terbium, the other an excess mass of europium. Excess mass signifies a high enough mass of element, sufficient for the calibration of the target, usually around 100 µg. Finally, as the currents should be limited in the mass marker due to its small dimension, the

temperature reached were limited to around 1200-1300 °C. At that temperature, only europium allowed the calibration of the separator, as terbium did not evaporate at all. However, as at around 1600 °C erbium starts to be detected, from erbium isotopes profile the mass separator was calibrated once more and set to mass 169. Three gold foils, M24, M25 and M26 were positioned in the collection chamber. For this experiment a collimator of 10 mm was used. (Figure 92)

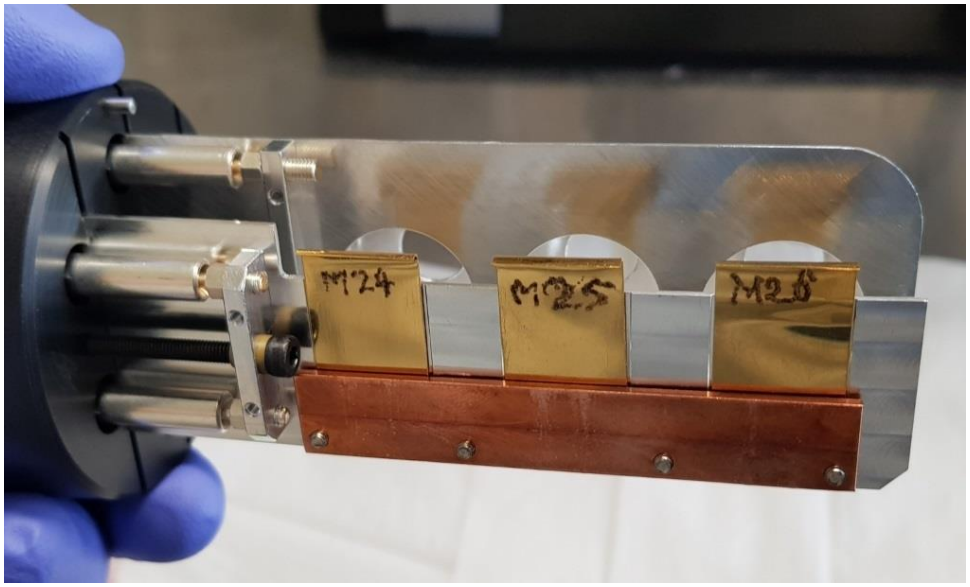

Figure 92: internal view of the collection box and the zinc coated gold collection foils used for the first Er-169 separation at CERN-MEDICIS

The first foil was needed for the finalization of the mass separator setup, while on M25 was implanted most of the collection. Because of a magnet fault, on M25 the collection lasted for only 3 hours from 10:00 to 13:00 the 23rd of May 2018. The current readout was not performing correctly, therefore it was not possible to estimate the number of atoms collected on the foils. The foil after the mass separation was removed from the collection chamber and sent to the gamma spectrometry detectors room. The analysis of the obtained spectrum showed that the foil contained around 70 kBq of Er-169 and 8 Bq of Yb-169, the isobaric contaminant with a ratio of 1.14E-4. It means that only 0.03% of the initial source has been collected on the foil. In order to determine the specific activity, the presence of Er-168 must be quantified. For this reason, an ICP-MS analysis will be performed once the atoms will be fully decayed. However, in order to demonstrate that higher activities can be produced, a second irradiation was scheduled.

6.5 Second Er-169 production

The second irradiation was originally foreseen from the 29th of June to the 9th of July 2018, but due to an unexpected stop of ILL reactor, the EOI was the 5th of July. A new quartz ampoule was

filled with 7±0.1 mg of erbium oxide and irradiated with an effective neutron flux of 1.2E15 n/cm^2/s. For this experiment the irradiated ampoule was shipped directly to CERN-MEDICIS where the target transfer was performed. One of the CERN-MEDICIS fume hoods (Figure 93) was equipped for the target transfer and a similar procedure as the one developed for the first experiment was applied.

Figure 93: erbium target transfer setup in MEDICIS fume hood

There were few differences from the first production: higher Er-169 in-target activity before mass separation (10 GBq), new design for the graphite holder (

Figure 94), no mass marker for the mass separator setup and correct readout of collection foil current (which was not working during the previous collection). Indeed, the mass marker were removed as the setup can be easily done following the spectrum of erbium. The mass 169 had been quickly identified and the beam easily optimized with the same parameters (Figure 95 and Figure 96). Good agreement had been found between the settings of the first and second collection (Figure 97).

Figure 94: graphite holder

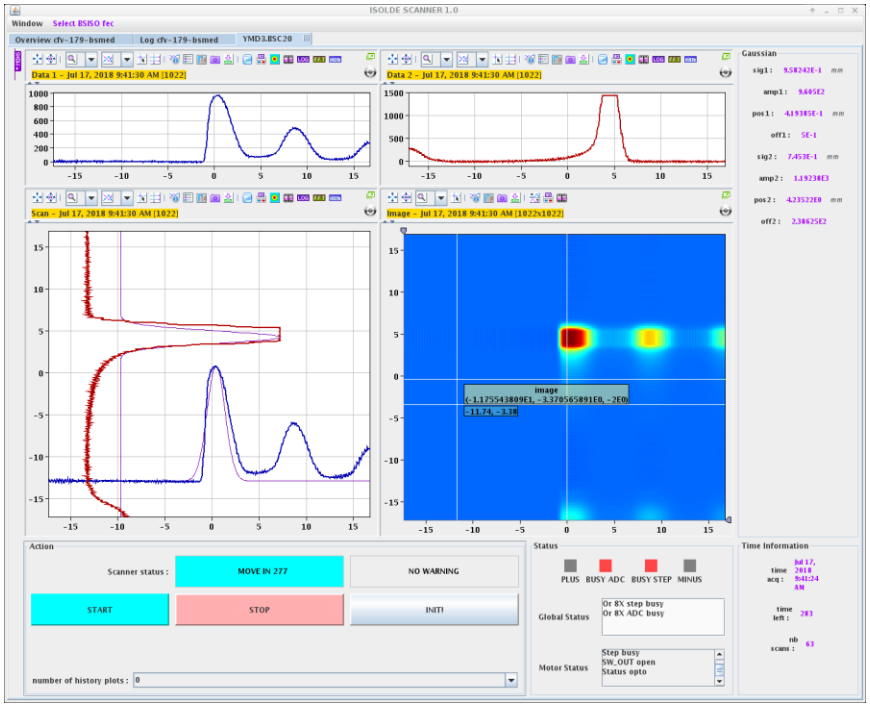

Figure 95: mass 169 beam profile before starting the collection before closing the right slits. Screenshots taken from MEDICIS software.

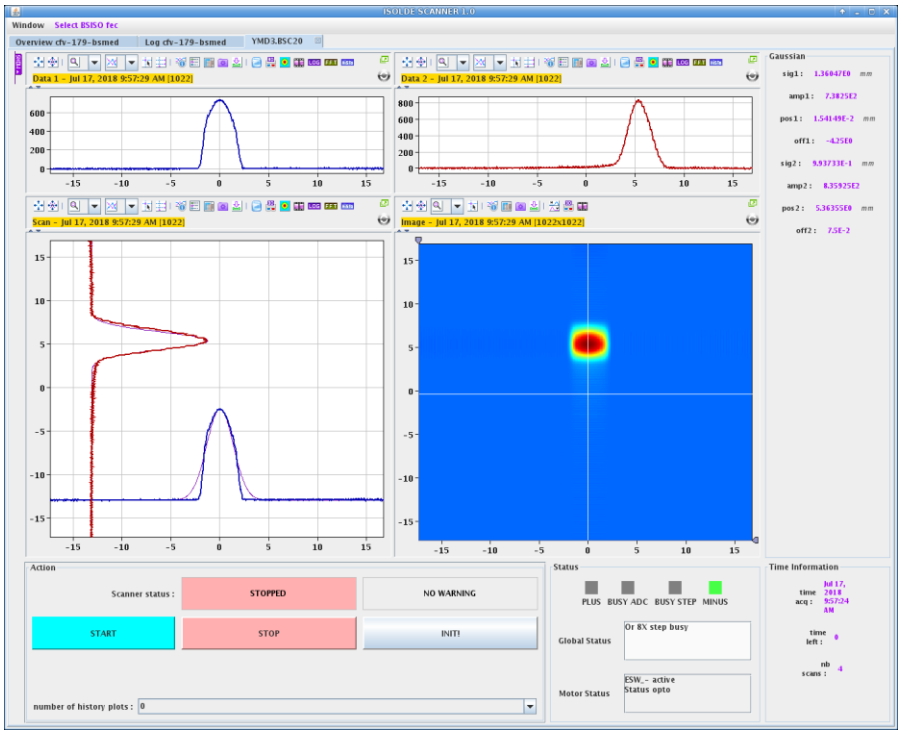

Figure 96: mass 169 beam profile before starting the collection before closing the right slits. Screenshots taken from MEDICIS software.

Figure 97: mass separator setup for erbium collection. Screenshots taken from MEDICIS software.

The collection started the 17th of July 2018 at 10:00 until the 18th of July 2018 at 10:00. The operating temperature was around 2000-2100 °C in the target container and the surface ion source. The readout of the current from the collection foils was in agreement with the Faraday cup and the collimator readout. The losses in the collimator were almost constant all along the collection oscillating around 7%. The ion current peak reached was 3.8 nA when the target container reached the maximum temperature, then the signal decreased exponentially accordingly. The number of atoms collected was 2.56E14. The gamma spectrometry analysis showed that were collected on the gold foil 18.2 MBq of Er-169 and 10.4 kBq of Yb-169, with a ratio of 5.71E-4. It is equivalent in number of atoms to 2.13E13 Er-169 atoms and 4.15E10 Yb-169 atoms. Subtracting to the total number of atoms implanted on the zinc-coated gold foil the atoms of Er-169 and Yb-169, the difference is assumed to be the number of atoms of Er-168. This because the quantity of Er-168 is almost three orders of magnitude higher than Er-169. Therefore, the beam profile at mass 168 is much broader and some atoms of Er-168 can be found in one side of the Gaussian profile at the mass 169 beam position.

The ratio of Er-168 over Er-169 atoms became 12 after the mass separation from the initial 850, meaning a gain of a factor 89. The specific activity was increased from 2.7 GBq/mg to 235 GBq/mg, closer to the theoretic specific activity which is 3 TBq/mg. The results can be confirmed when every radionuclide will be decayed through the ICP-MS test. However only 18 MBq of Er-169 were extracted from the 10 GBq of Er-169 present in the MEDICIS target container before mass separation. The overall efficiency was consequently 0.18%. The gamma spectrum of reference for this analysis is presented in ANNEX-C.

The obtained results referred to the first worldwide production of high specific activity Er-169. The proof of principle of the production of a usable dose was performed. Nevertheless, the production yield and the quality of the product can be improved. The first improvement is the reduction of Er-168 content, which can be achieved optimizing the position of the mass separator slit. The optimal position for the maximum reduction of stable erbium minimizing the Er-169 should be found. The second improvement needed, not in order of importance of the effect, is the increase of the extraction efficiency, as 0.18% is too low. In order to improve the extraction efficiency a better ionization efficiency is needed. This could increase the total beam of ions entering in the mass separator magnet, increasing the overall mass separation efficiency, therefore the total ions collected. For this reason, the integration of lasers in the mass separation process is considered.

6.6 Laser ionization study for erbium

As shown before, the conventional mass separation with the ionization of the atoms through a surface ion source the efficiencies are not favorable for large scale productions. One way to improve the efficiency of the process is to improve the atoms ionization. It is possible to selectively ionize erbium atoms from conveying lasers towards the ion source. The double effect of the ion source and laser will increase the ionization and extraction of the wanted radionuclides. As described for terbium in the dedicated paragraph, in order to test the possible gain with this feature, a study on the best laser ionization scheme and the possible improvements was performed. Experiments have been done at Johannes Gutenberg University of Mainz, in collaboration with LARISSA group under the supervision of Prof. Klaus Wendt. As it is a non-radioactive laboratory, the tests have been performed with stable erbium which is representative for the real case with radioactive Er-169.

Erbium oxide solution was purchased by Larissa group from Alfa Aesar in standard solution, which means Er_2O_3 in 5% of HNO_3 with atomic erbium concentration of 1000 µg/ml. The solution concentration was reduced by a factor of 10 diluting 100 µl of solution with 900 µl of deionized water. This allow reducing the number of ions for each experiment, shrinking the time needed for each run. From the erbium diluted solution, 3 µl of solution were taken and deposited on a zirconium foil. The heat generated by a lamp positioned over the foil allowed the evaporation and

sedimentation of the erbium solution on the foil. The 3 µl of erbium correspond in this case to 1.08E15 number of erbium atoms. For this experiment a two-step scheme has been selected from work previously done by LARISSA group and present in literature (98). The chosen wavelengths are 400.91 nm for the first step and 410.90 nm for the second step. For both steps the laser saturation power has been measured (Figure 98 and Figure 99). The laser power used for the experiment was then 70 mW for the first step and 250 mW for the second step.

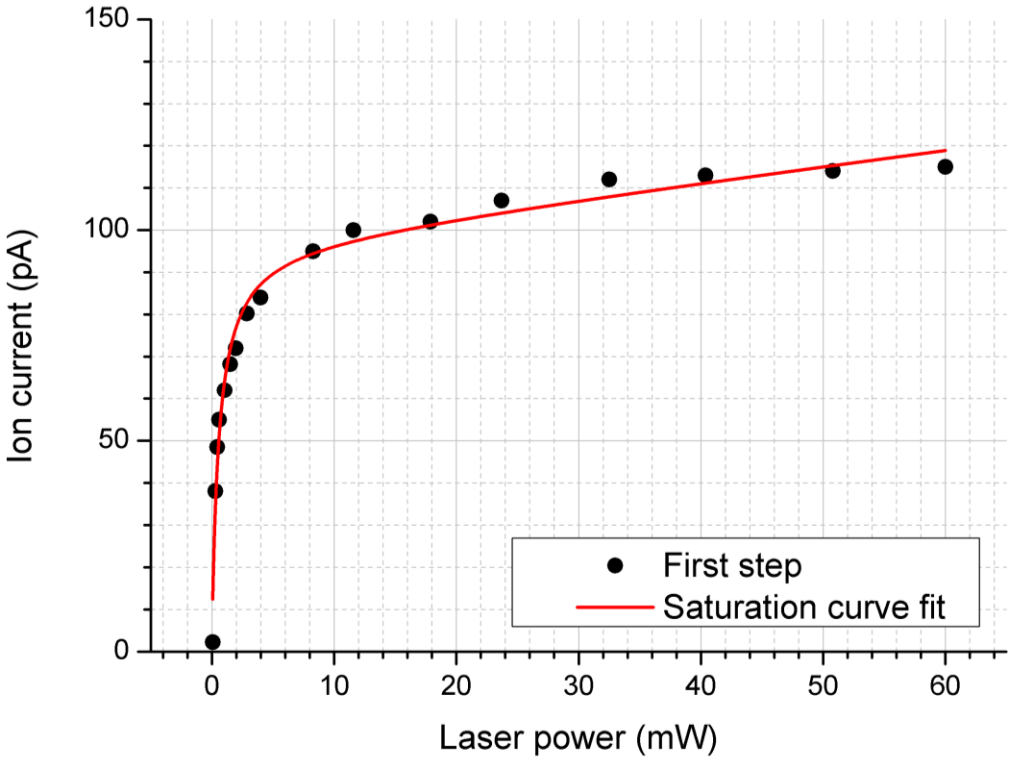

Figure 98: first step power saturation curve

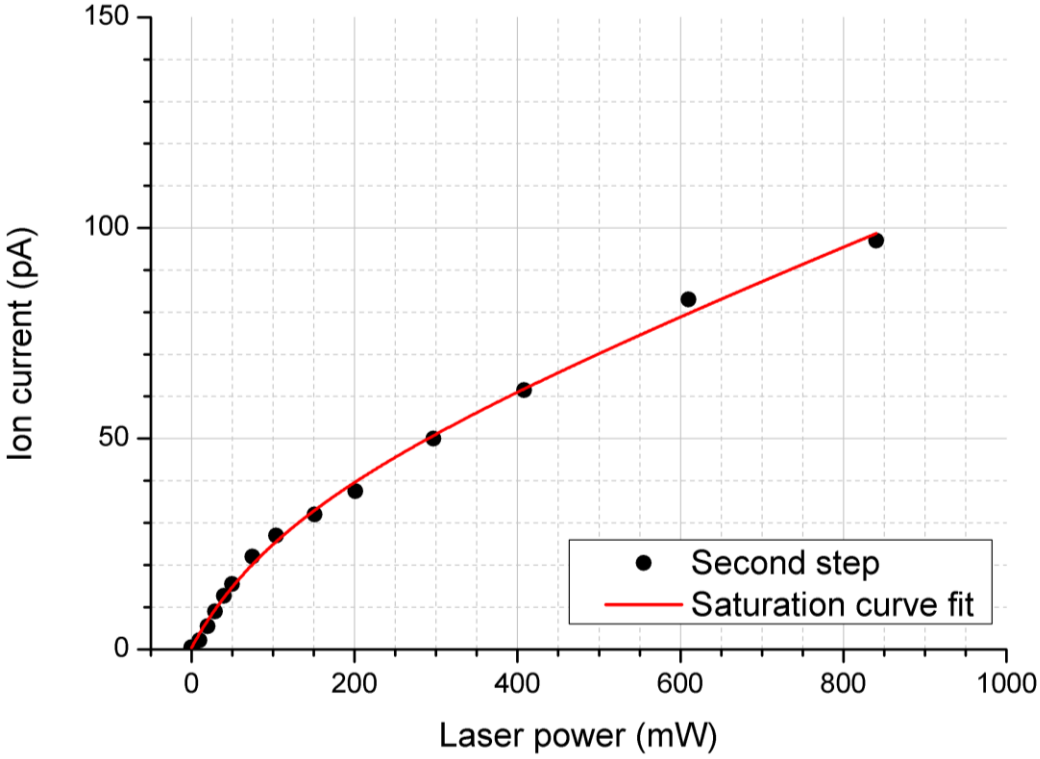

Figure 99: second step saturation curve.

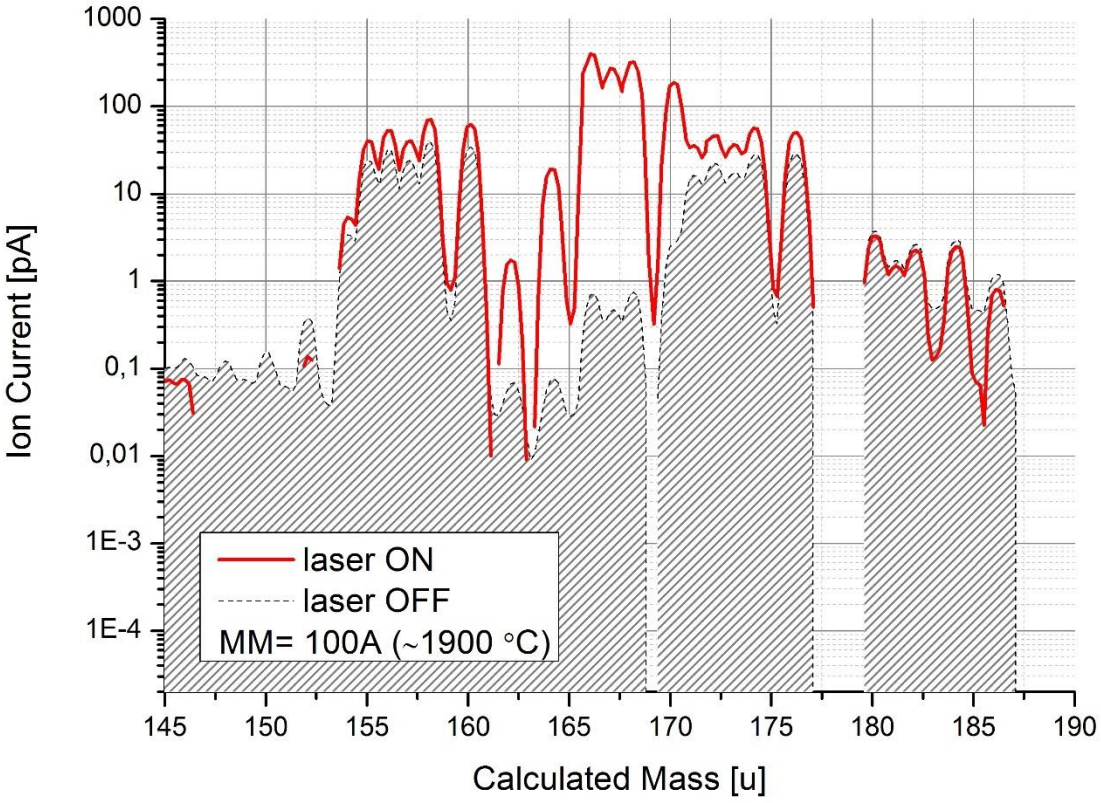

Figure 100: laser on laser off mass scan

In *Figure 100* an example of mass spectrum is given, taken from the final part of the second experiment. The ratio laser on / laser off was between around 1000 and 10000. All the erbium released was under atomic form, no erbium oxides were observed. The quite high presence of atomic gadolinium and gadolinium oxide do not interfere with the erbium separation measurement. Indeed, its nuclides mass range is from 152 to 160 and the oxides mass range 168 to 176, while the measurement was performed on mass 166.

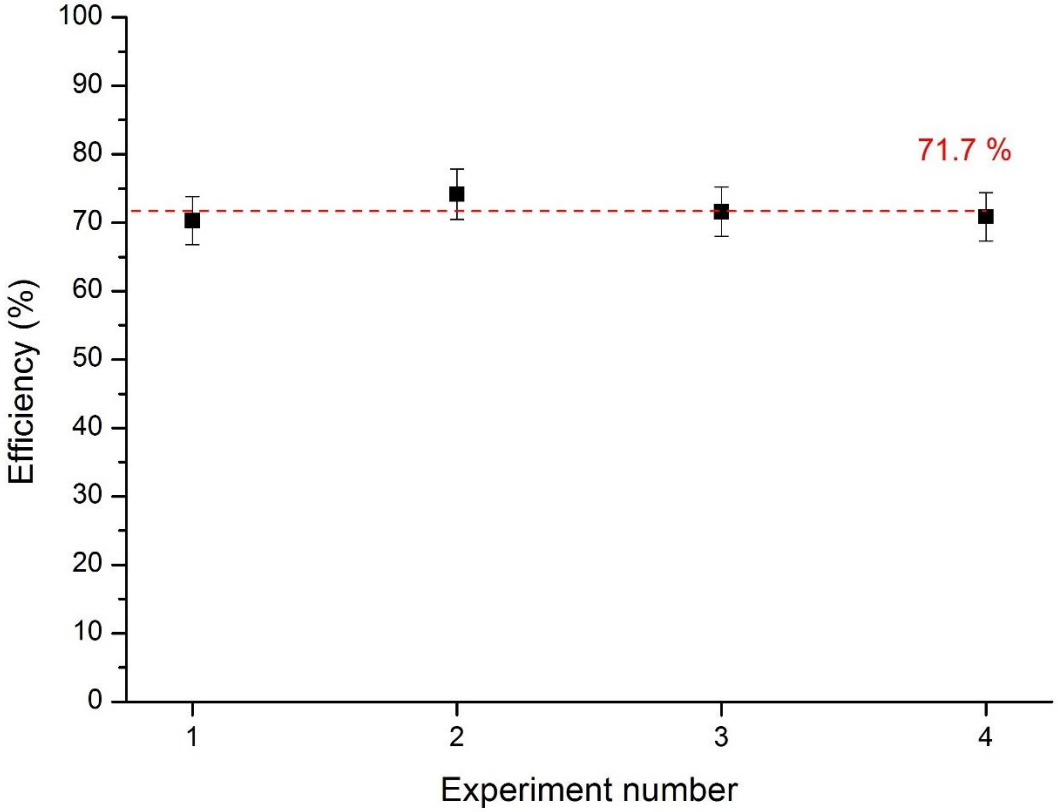

Figure 101: efficiency measurements for the 2-step scheme erbium laser ionization

Four laser ionization efficiency measurements have been performed (Figure 101) and seemed to be consistent within each other: (70.3±5%)%; (74.1±5%)%; (71.6±5%)%; (70.8±5%)%. The experimental error is estimated to be 5% from the literature (99), as conservative error, coming mainly from the determination of the exact number of erbium atoms inside the initial sample. The other sources of errors, as the Faraday cup readout, where considered negligible. The average efficiency, 71.7%, is very high and has never been achieved before. For this reason, after the first two measurements the results were questioned, and the other two experiments were repeated with different parameters. Solution 3 and 4 were prepared by two different people respects to the first two measurements. Furthermore, different pipettes have been used, the automatic and the manual ones, but the experiments 3 and 4 confirmed the first two runs.

A further cross check was done. It was decided to test the initial erbium standard solution used, for this reason a sample of solution was sent to GIP ARRONAX where the ICP-OES test were performed to verify the concentration of the solution. The outcome was 106 ppm (106 µg/ml) with non-detected lanthanides contaminants. It confirmed the correct dilution 1:10 of the starting erbium standard solution (1000 µg/ml) in water. The tests validate the efficiencies obtained.

This is an important milestone which asserts the large margin of improvements of the Er-169 production yields combining the conventional mass separation technology with the laser ionization. Extrapolating the results obtained at JGU Mainz to the experiments performed at CERN-MEDICIS a possible efficiency improvement of a factor around 397, from 0.18% to around 71.7% could be achieved. Future tests will be performed at CERN-MEDICIS once the laser installation MELISSA will be finalized (likely beginning 2019) in order to obtain the experimental values for the selected production process. This will allow verifying the experimental efficiency improvement factor for the production yields of Er-169, with the complete production process configuration.

6.7 Conclusions

Er-169 is an interesting isotope for receptor-targeted radiotherapy for its physical characteristics. However, it is not currently available with a sufficient specific activity because of the quite small cross-section (2.3 b) for the neutron activation reaction of enriched Er-168. This implies a high atom ratio of Er-168 over Er-169. In this chapter, the combined use of nuclear reactor production and mass separation is proposed to overcome this issue. Indeed, with the mass separation technology, the isotopes having a determined mass can be selectively isolated and collected. The experiments performed at ILL reactor and CERN-MEDICIS facility showed the feasibility of the production method. A specific activity improvement from 2.7 GBq/mg to 235 GBq/mg was obtained. It was the first worldwide production of high specific activity Er-169. Nevertheless, 18 MBq of Er-169 were extracted from the initial 10 GBq, resulting in an overall efficiency of 0.18 %, which is still too low. One method for further improving the specific activity is to optimize the position of the left slit maximizing the reduction of Er-168 atoms while minimizing the loss of Er-169 on the collection foil. The method identified for improving the efficiency, instead, consists in introducing the laser ionization in the mass separation process. This was studied at JGU Mainz with LARISSA group achieving excellent results. It was demonstrated the possibility to increase the overall mass separation efficiencies to around 70%. This means a potential improvement of the Er-169 extraction efficiency of a factor of 397. The finalization of MELISSA laser laboratory at CERN-MEDICIS by the first half of 2019 will allow verifying the experimental gain factor in the production yields of Er-169. In parallel, as it was shown that Er-169 can be produced and be available in quantities sufficient for preclinical studies, preclinical

trials could be performed starting from beginning of 2019 in collaboration with hospitals and research centers.

Conclusions and perspectives

The objective of the work performed in this thesis was to assess a new large-scale production method for innovative radionuclides having suitable physical properties for theranostics applications. In particular the production method has been analyzed for those radionuclides which no production routes are currently or constantly available. After a thorough selection process, radionuclides of terbium, scandium and erbium have been selected.

One of the chosen radionuclides identified for the production from commercial cyclotrons is Sc-47. It is a β^--emitter with 3.35 d of half-life. It can be used as therapeutic pair of the diagnostic radionuclide Sc-44, or alternatively Sc-43. Whereas the diagnostic scandium radionuclides are already produced with high purity and in large quantities, for Sc-47 a reliable, efficient and cost-effective production method for a very pure product is missing. The proposed production method consists in natural titanium targets irradiation with proton beams provided by commercial cyclotrons followed by the mass separation. Its use is considered to obtain very pure batches, as the major constrained is the co-production of Sc-46 which is a β^--emitter with longer half-life than Sc-47. The theoretical development of the targetry for the production of Sc-47 in commercial cyclotrons has been finalized. The target material, dimension and the irradiation parameters have been defined. Nevertheless, before performing the proof of principle of the production method, consisting in the irradiation of the titanium target at ARRONAX cyclotron followed by the mass separation at CERN-MEDICIS, some further investigations are suggested. The first one is the study of the mass separation of cold scandium from a stable scandium/titanium mixture of standard solutions. The overall mass separation efficiency should be studied initially considering the rhenium ion source as ionizer, as it presents theoretical higher ionization efficiencies. The obtained efficiency value is needed to verify the feasibility of the process and the yield achievable. Furthermore, an experimental campaign for the resonant laser ionization efficiency for scandium and scandium/titanium standard solutions mixture is needed. The two different experiments will give the optimal setup for the first radioactive production at CERN-MEDICIS. Finally, a very important milestone will be the experimental proof of principle of the yield produced at CERN-MEDICIS with the laser ionization added to the conventional mass separation technology.

Terbium offers a set of interesting radionuclides for a wide range of applications: Tb-149 (half-life 4.12 h) for alpha therapy, Tb-152 (half-life 17.5 h) for PET, Tb-155 (half-life 5.32 d) for SPECT and Tb-161 (half-life 6.89 d) for β^- therapy. Whereas non-carrier-added Tb-161 can be produced in reactor through the decay of Gd-161 produced by neutron activation of enriched Gd-160, the lack of a reliable production route for the other three radionuclides hinders their potential future

use in clinic. In this work, the gadolinium target irradiation with proton beams provided by commercial cyclotrons is considered for their production.

The first step was to perform experiment at Arronax cyclotron in order to evaluate the experimental cross-section of the reaction of interest from the irradiation of proton beam from 58 MeV to 70 MeV of natural gadolinium target. The main objective was to overcome the lack of data for the production of Tb-149. The cross-section for the production of the other terbium radionuclides have been evaluated too, resulting in agreement with the few experimental values already present in literature. This confirmed the very low cross-section for the production of Tb-149 from natural gadolinium, therefore enriched material should be considered. The challenge in using enriched material is to find a suitable method to make a target which can be irradiated with high beam currents. Electrodeposition of enriched gadolinium has been investigated. This will be the way pursed for further developments at ARRONAX.

For the production of Tb-152 and Tb-155 natural gadolinium can be considered instead. Nevertheless, the irradiation with a 70 MeV proton beam will induce the co-production of several terbium radionuclides having similar if not longer half-life, requiring a physical separation method. Thus, the mass separation of the irradiated gadolinium target is considered to obtain very pure batches of non-carrier added radionuclides. The target material, dimension and the irradiation parameters have been defined. Furthermore, experiments for the mass separation of stable terbium and stable gadolinium have been performed, obtaining around 1.4% of overall efficiency by using rhenium surface ionizer as ion source. In order to increase this value, resonant laser ionization added to the mass separation was considered. From experiments conducted at JGU Mainz with LARISSA group, promising results were obtained, with a potential improvement of the overall mass separation efficiency up to around 50%. The first proof of principle of the proposed production method will be tested during the first half of 2019. A very important milestone will be the experimental result on the radionuclides yield produced at CERN-MEDICIS with the laser ionization added to the conventional mass separation technology. If the experimental efficiencies will be confirmed, high yields could be obtained in the future, making routinely available the considered terbium radionuclides for medical applications.

Finally, the combined use of nuclear reactor production and mass separation is proposed to overcome the low specific production of some carrier-added lanthanides. In particular, in this work the production of very high specific activity Er-169 has been analyzed. Er-169 (half-life 9.39 d) is an almost pure β^- emitter with low energy electrons emission and few low energy and very low intensity gamma rays. It can be produced in reactors through the neutron activation of Er-168, which is one of the 6 natural erbium isotopes. Er-168 is commercially available at around 98% enrichment level; however, the cross-section of the reaction is quite low, resulting in a production of Er-169 diluted in high amount of stable Er-168. Thus, the only way to separate the

two nuclides is a physical method. Therefore, the use of mass separation technology is considered. The experiments performed at ILL nuclear reactor and CERN-MEDICIS facility showed the feasibility of the production method. It consists in an irradiation of enriched Er-168 at ILL followed by the mass separation of the irradiated sample at CERN-MEDICIS. The successfully performed proof of principle corresponded to the first worldwide production of such high specific activity Er-169. A specific activity improvement from 2.7 GBq/mg to 235 GBq/mg was obtained. Nevertheless, 18 MBq of Er-169 were extracted from the initial 10 GBq, resulting in an overall efficiency of 0.18 % by using tungsten surface ionizer as ion source, which is still far from ideal. Based on the first experiments, some improvements have been identified for the future improvement of the considered production method. One is to optimize the position of the left slit maximizing the reduction of Er-168 atoms while minimizing the loss of Er-169 on the collection foil. The method identified for improving the efficiency, instead, consists in introducing the laser ionization in the mass separation process.

Indeed, part of the work has been developed at JGU Mainz with LARISSA group achieving excellent results on resonant laser ionization of stable erbium. It was demonstrated the possibility to increase the overall mass separation efficiencies to around 70%. This means a potential improvement of the Er-169 extraction efficiency of a factor of 397. The finalization of MELISSA laser laboratory at CERN-MEDICIS by the first half of 2019 will allow verifying the experimental gain factor in the production yields of Er-169. In parallel as it was shown that Er-169 can be produced and be available in quantities sufficient for preclinical studies, preclinical trials could be performed starting from beginning of 2019 in collaboration with hospitals and research centers.

Bibliography

1) O. Glasser, *W. C. Roentgen and the discovery of the Roentgen rays,* American Journal of Roentgenology Diagnostic Imaging and Related Sciences, 165 (1995) 1033-1040.

2) A. Assmus, *Early History of X Rays,* Beam Line , 25 (1995) 10–24 .

3) W. C. Röntgen, *On a new kind of rays,* Nature, 53 (1896) 274-277.

4) M. Sklodowska-Curie, *Recherche sur le substances radioactives,* Doctoral thesis, Ecole Politecnique Paris, 1901.

5) Musée Curie (coll. ACJC), https://lejournal.cnrs.fr/articles/marie-curie-portrait-intime, visited on 11/2018.

6) H. N. Wagner, *A Personal History of Nuclear Medicine,* Springer, 2006.

7) S. F. Keevil, Physics and medicine: a historical perspective. *Physics and Medicine 1,* 379 (2011) 1517–24.

8) P. Curie, H. Becquerel. *Action physiologique des rayons du radium,* C.R.T. 132 (1901) 1289-1291.

9) G. C. de Hevesy, *Marie Curie and Her Contemporaries,* J. Nuc. Med. Techno., 24 (1996) 273-279..

10) P. Radvanyia, J. Villain. *The discovery of radioactivity*, C. R. Physique, 18 (2017) 544–550.

11) F. Soddy, The radio-elements and the periodic law. *The chemistry of the radio-elements.* 1914.

12) I. Curie, F. Joliot, *Artificial production of a new kind of Radio-Element,* Nature, 10 (1934).

13) S. Modoni, N. Urban, L.Mansi, *The Discovery of technetium-99m and iodine-131* .

14) B. R. Martin, *Nuclear and Particle Physics,* John Wiley & Sons Ltd, 2006. ISBN-13: 978-0-470-01999-3.

15) W.R. Leo, *Techniques for Nuclear and Particle Physics Experiments - A How-to-Approach,* Springer-Verlag, 1994.

16) http://eduweb.site/karlsruher-nuklidkarte-18.html, visited on 02/2019

17) Physics open lab. http://physicsopenlab.org/2016/02/15/beta-radioactivity/, visited on 10/2019.

18) C. Duchemin, *Étude de voies alternatives pour la production de radionucléides innovants pour les applications médicales,* PhD thesis, 2015.

19) A. Einstein, *On the theory of light production and light absorption,* Annalen der Physik, 20 (1906) 199-206.

20) G. Reilly, D. Nelson, Gamma-Ray Interactions with Matter, *Passive Nondestructive Analysis of Nuclear Materials.* 1991.

21) Canberra, http://www.canberra.com/products/detectors/germanium-detectors.asp, visited on 09/2019.

22) Ortec. LVis 2.0. Counting laboratory application manager - software for gammavision-32. https://www.ortec-online.com/products/application-software/lvis, visited on 09/2019.

23) J., Fitzgerald, *Fitzpeaks Gamma Analysis and Calibration Software version 3.66,* User Guide and Technical Manual version 3.63, 2007.

24) GENIE2000. Genie 2000 Gamma Analysis Software, http://www.canberra.com/fr/produits/radiochemistry_lab/genie-2000-software.asp, visited on 09/2019.

25) Brookhaven National Laboratory. National nuclear data center, https://www.nndc.bnl.gov/nudat2/chartNuc.jsp, visited on 09/2019.

26) Nucleonica. https://nucleonica.com/, visited on 08/2019.

27) IAEA. *Manual for reactor produced radioisotopes.* 2003.

28) OECD, NEA. *2017 Medical Isotope Supply Review: 99Mo/99mTc Market Demand and Production Capacity Projection 2017-2022,* The Supply of Medical Radioisotopes, 2017.

29) F. Poirier, S. Girault, S. Auduc, C. Huet, E. Mace, J.L. Delvaux, F. Haddad *The C70 ARRONAX And Beam Lines Status,*Proceedings of IPAC2011, 2011.

30) M. J. Dresser, *The Saha-Langmuir Equation and its Application,* Journal of Applied Physics, 19-1 (1967).

31) U. Köster, *Resonance ionization laser ion sources,* Nuclear Physics A, 701 (2002) 1-4.

32) M. Manzolaro *et. al., Ionization efficiency estimations for the SPES surface ion source,* Nuclear Instruments and Methods in Physics Research B , 317 (2013) 446–449.

33) P. V. Cuong, *Development of a New Surface Ion-Source And Ion Guide in the ALTO Project,* PhD thesis, 2009.

34) R. Middleton, *A Versatile High Intensity Negative Ion Source,* Nuclear Instruments and Methods, 214 (1983) 139-150.

35) *R.* Kirchner*, On the termoionization in hot cavities*, Nuclear Instruments and Method in Physics Research A, 292 (1990) 203-208.

36) National Institute of Standards and. NIST Atomic Spectra Database Ionization Energies Form, https://physics.nist.gov/PhysRefData/ASD/ionEnergy.html, visited on 11/2019.

37) R. Augusto *et. al.*, *CERN-MEDICIS (Medical Isotopes Collected from ISOLDE): A New Facility,* Applied Science, 4 (2014) 265-281.

38) J. A. Paisner, *Atomic Vapor Laser Isotope Separation.* Paisner, Applied Physics B , 46 (1988) 253-260.

39) T. R. Mazur, B. Klappauf, M. G. Raizen*, Demonstration of magnetically activated and guided isotope separation,* Nature Physics, 10 (2014) 601–605.

40) V. Gadelshin, *Preparation of Laser Isotope Separation for the Nuclear Medical Project – MEDICIS.* 2016.

41) C. Lang, D. Habs, K. Parodi, P.G. Thirolf*, Sub-millimeter nuclear medical imaging with high sensitivity in positron emission tomography using b+g coincidences,* Journal of Instrumentation, 9 (2014).

42) K. Nedunchezhian *et. al., Boron Neutron Capture Therapy - A Literature Review.* J Clin Diagn Res, 10 (2016).

43) N. Sunthraralingam *et. al.*, Chapter 14 : basic radiobiology. *Review of Radiation Oncology Physics : A Handbook for Teachers and Students.* 2009.

44) R. M. de Kruijff, H. T. Wolterbeek, A. G. Denkova*, A Critical Review of Alpha Radionuclide Therapy - How to Deal with Recoiling Daughters?,* Pharmaceuticals, 8 (2015) 321-336.

45) ORNL ramps up production of key radioisotope for cancer-fighting drug. ORNL *press release.* May 2018.

46) C. Muller *et. al.*, *A unique matched quadruplet of terbium radioisotopes for PET and SPECT and for α- and β- radionuclide therapy: an in vivo proof-of-concept study with a new receptor-targeted folate derivative,* J Nucl Med, 53 (2012) 1951.

47) R. Levine, E. P. Krenning*, Clinical History of the Theranostic Radionuclide Approach to Neuroendocrine Tumors and Other Types of Cancer: Historical Review Based on an Interview of Eric P. Krenning by Rachel Levine,* J Nucl Med, 58 (2017) 3S-9S.

48) J. G. Hamilton, M. H. Soley*, Studies in Iodine Metabolism by the Use of a New Radioactive Isotope of Iodine,* American Journal of Physiology, 127 (1939) 3.557.

49) B. E. Hertz, K. E. Schuller, *Saul Hertz, MD (1905-1950): A Pioneer in the Use of Radioactive Iodine*, Endocrine Practice - hystorical vignette, 16 (2010).

50) Advanced Accelerator Applications Receives US FDA Approval for LUTATHERA® for Treatment of Gastroenteropancreatic Neuroendocrine Tumors, *Advanced Accelerator Applications Press release,* 2018.

51) IAEA. *Cyclotron Produced Radionuclides: Physical Characteristics and Production Methods Technical,* technical report, 2009.

52) S.W. Zielhuis *et. al.*, *Production of GMP-grade radioactive holmium loaded poly(L-lactic acid) microspheres for clinical application,* International Journal of Pharmaceutics 311 (2006) 69-74.

53) S. Vosoughi *et. al.*, *Production of no-carrier-added Ho-166 for targeted therapy purposes,* Iran J Nucl Med 25 (2017) 15-20.

54) K. Abbas *et. al., Development of an accelerator driven neutron activator for medical radioisotope production,* Nuclear Instruments and Methods in Physics Research A, 601 (2009) 223–228.

55) Brookhaven National Laboratory. *EXFOR Systems Manual.* 1999. report BNL-NCS-63330.

56) A. J. Koning, S. Hilaire, M. Duijvestijn, *Talys-1.2, A nuclear reaction program,* User manual, 2009.

57) M. Sitarz, Radionuclide Yield Calculator, http://www.cyclotron-nantes.fr/spip.php?article373.

58) F. Habashi, Scandium. *Metall.* 62 (2008).

59) I. M. Samson, M. Chassé, Scandium (Sc), *W.M. White (Ed.) Encyclopedia of Geochemistry, Encyclopedia of Earth Sciences Series,* Springer International Publishing, 2016.

60) C. Müller *et. al., Promising Prospects for 44Sc/47Sc-Based Theragnostics: Application of 47Sc for Radionuclide Tumor Therapy in Mice*, Journal of Nuclear Medine, 20 (2014) 1658-64.

61) M. Mamtimin, F. Harmon, V. N. Starovoitova, *Sc-47 production from titanium targets using electron linacs,* Applied Radiation and Isotopes, 102 (2015) 1–4.

62) K. DeLorme *et. al., Production potential of Sc-47 using spallation neutrons at the Los Alamos Isotope Production Facility,* Journal of Nuclear Medicine, 55 (2014).

63) L. F. Mausner *et. al., Scandium-47: A replacement for Cu-67 in nuclear medicine therapy with beta/gamma emitters,* Journal of Nuclear Medicine, 40 (2000) 43-45.

64) L. F. Mausner *et. al., Radionuclide Development at BNL for Nuclear Medicine Therapy,* Appl. Radiat. lsot., 49 (1998) 285-294.

65) IAEA, http://cra.iaea.org/cra/stories/2015-09-30-F22053-New_Emerging_Radionuclides.html, visited on 10/2019.

66) *G. Deng, Terbium glows green,* Nature Chemistry, 10 (2017).

67) E. G. Moore *et. al.*, *From Antenna to Assay: Lessons Learned in Lanthanide Luminescence,* Acc Chem Res, 2009.

68) J. Kaleta *et. al.*, *Magnetomechanical properties of Terfenol-D powder composites,* Solid State Phenomena, 154 (2009).

69) R. P. Baum *et. al.*, *Clinical evaluation of the radiolanthanide terbium-152: first-in-human PET/CT with (152)Tb-DOTATOC,* The Royal Society of Chemistry, 2017.

70) C. Müller *et. al.*, *Alpha-PET with terbium-149: evidence and perspectives for radiotheragnostics*, EJNMMI Radiopharmacy and Chemistry, (2016) 1:5.

71) N. Dmitriev *et. al.*, *Lanthanides in Nuclear Medicine: Preparation of 149Tb by Irradiation with Heavy Ions*, Radiochemistry 44 (2002).

72) B. J. Allen *et. al.*, *Production of terbium-152 by heavy ion reactions and proton induced spallation,* Applied Radiation and Isotopes, 54 (2001).

73) C. Vermeulen *et. al.*, *Cross-sections of proton-induced reactions on natGd with special emphasis on the production possibilities of Tb152 and Tb155,* Nuclear Instrument and Methods in Physics Research B, 275 (2012) 24-32.

74) IAEA, Monitor reactions 2017, https://www-nds.iaea.org/medical/monitor_reactions.html, visited on 08/2019.

75) Y. T. Mironov*, Features of investigation excitation function of nuclear reactions on internal beam synchrocyclotron,* Conf. Nucl. Spectrosc. Nucl. Struct, 9 (2001) 276.

76) J. F. Ziegler. *The stopping of energetic light ions in elemental matter,* J. Appl. Phys / Rev. Appl. Phys., 85 (1999) 1249–1272.

77) W. S. Kleeven, *Energy definition for extracted beams in the C70 cyclotron,* IBA report, 2009.

78) Goodfellow, www.goodfellow.com, visited on 07/2019.

79) Nuclear Energy Agency, Java-based Nuclear Data Information System 4.0., https://www.oecd-nea.org/janis/, visited on 09/2019.

80) S. Y. F. Chu *et. al.*, The Lund/LBNL Nuclear Data Search, Version 2.0, February 1999, http://nucleardata.nuclear.lu.se/toi/, visited on 09/2019.

81) M.B. Challan *et. al.*, *Excitation Functions of Radionuclides Produced by Proton Induced Reactions on Gadolinium Target,* 6th Conference on Nuclear and Particle Physics, 2007.

82) S. N. Dmitriev *et. al.*, *Lanthanides in Nuclear Medicine: Preparation of 149Tb by Irradiation with Heavy Ions,* Radiochemistry, 44 (2002).

83) R. Salminem, *Geochemical Atlas of Europe,* IUGS/IAGC Global Geochemical Baseline, 2005.

84) R. Pullicino, K. Das, *Is it safe to use gadolinium-based contrast agent in MRI?*, J R Coll Physicians Edinb, 47 (2017) 243–6.

85) Z. Khan*, Influence of gadolinium on the microstructure and mechanical properties of steel and stainless steel,* The Journal of The Southern African Institute of Mining and Metallurgy, 112 (2012).

86) G. F. Steyn *et. al., Cross-sections of proton-induced reactions on 152Gd, 155Gd and 159Tb with emphasis on the production of selected Tb radionuclides,* Nuclear Instrument and Methods in Physics Research B, 319 (2014) 128-140.

87) R. Formento Cavaier *et. al., Terbium Radionuclides for Theranostics Applications: A Focus On MEDICIS-PROMED.*, Physics Procedia, 90 (2017) 157-163.

88) Z. Kovacs *et. al.*, *Preparation of thin gadolinium samples via electrodeposition for excitation function studies,* J Radioanal Nucl Chem, 307 (2016) 1861–1864.

89) P. Liu *et. al., Electrodeposition of Gd-Co film on organic bath,* Electrochimica Acta 45 (2000) 2147-2152.

90) Vapor Pressure Calculator,

https://www.iap.tuwien.ac.at/www/surface/vapor_pressure, visited on 07/2019.

91) E. Garrido *et. al.*, *New excitation functions for proton induced reactions on natural titanium, nickel and copper up to 70 MeV,* Nuclear Instruments and Methods in Physics Research B, 383 (2016) 191–212.

92) I. Levenberg, V. Pokrovsky, I. Yutlandov, *Simple nuclear reactions on Ca48 induced by high energy protons,* Nuclear Physics, 41 (1963).

93) S. Cotton, Lanthanide and Actinide Chemistry, John Wiley & Sons Ltd, 2006.

94) P. Patnsik, *Handbook of inorganic chemicals,* 2003.

95) D. V. Rao *et. al., Radiations emitted in the decay of 165Er: A promising medical radionuclide,* Medical Physics, 4 (1977) 177-186.

96) J. Farahati *et. al.*, *Post-radiosynovectomy imaging of Er-169 using scintigraphy and autoradiography,* Clinical Case Reports, 5 (2017) 1048–1050.

97) J. J. Zaknun *et. al.*, The joint IAEA, EANM, and SNMMI practical guidance on peptide receptor radionuclide therapy (PRRNT) in neuroendocrine tumours, Eur J Nucl Med Mol Imaging, 40 (2013) 800–816.

98) D Studer *et. al.*, RIS in dysprosium and erbium for scheme development and determination of the first ionization potential, LA3NET Laser Ion Sources Workshop, 2016.

99) T. Kron *et. al., High efficiency resonance ionization of palladium with Ti:sapphire lasers,* J. Phys. B: At. Mol. Opt. Phys. 49 (2016).

ANNEX-A

Computational Fluid-Dynamics applied to target development

For producing radionuclides, different combinations of target materials, facilities and beam types and energies could be exploited. In order to optimize the beam irradiation parameters, it is necessary to infer the impact of the thermal power deposition induced by the beam on the target. A fluid cooling system should guaranty the thermal power removal from the irradiated target. The induced thermal stress should be thoroughly analyzed because this could induce problems in the targetry and in the cooling system. Indeed, a too high temperature induced on the target could provoke the target fusion or boiling of the cooling fluid. This should be avoided as the phase changing of the fluid dramatically decrease the thermal exchange coefficient of the fluid itself, impeding the correct thermal power removal. Furthermore, the thermal stress can cause a mechanical stress in the target. If the stress is higher than the maximum stress affordable for a target, it can undergo to a rupture. Thus, depending on the targetry system adopted it could cause a irradiation stop and beam line damages if the target is the interface between beam line vacuum and fluid cooling; it could strongly contaminate the cooling system; it could contaminate the environmental area causing the stop of the activity for a period depending on the radionuclides involved.

In this work, Ansys and Ansys Fluent have been used to estimate the maximum temperatures reached in the target and the mechanical integrity of the latter for a given targetry configuration. This is performed for different irradiations conditions for determining the optimal irradiation parameters which maximize the production yield while controlling the fluid temperatures at reasonable values.

The study is conducted for a solid target system water cooled to find the best condition to avoid boiling at all for the cooling water being below its boiling temperature. For this reason, only one phase turbulent fluid flow simulations have been considered. The boiling point of the water at the working pressure 15 bar is estimated to be 198.3 ºC from the water phase diagram.

A.1 Reynolds number

For determining whether the flow is in turbulent or laminar regime the dimensionless number of Reynolds (Re) should be evaluated. It is the ratio of inertial forces to viscous forces. Laminar

flow occurs at low Re where viscous forces are dominant and is characterized by smooth and constant fluid motion; turbulent flow occurs at high Re and is dominated by inertial forces, which tend to produce chaotic eddies and vortices. The conventional ranges are usually: Re<2100 for laminar flow, Re>4000 for turbulent flow, and 2100≤Re≤4000 representing the transition zone. In this zone the flow becomes turbulent, but it is still not completely developed. The number of Reynolds is defined as follow:

$$Re = \frac{\rho v D}{\mu} = \frac{v D}{\nu} \qquad \text{(A-1)}$$

Where ρ is the density of the fluid in kg/m^3, v is the velocity of the fluid in m/s, D is the characteristic dimension of the system (in this case the hydraulic diameter) in m, μ is the dynamic viscosity of the fluid in kg/m/s, ν is the kinematic viscosity of the fluid in m^2/s.

A.2 Prandtl number

Another important dimensionless number is the number of Prandtl (Pr). It is the ratio of molecular momentum and thermal diffusivities. Small values of the Prandtl number indicate the dominancy of the thermal diffusivity, whereas with large Pr values the momentum diffusivity dominates the behavior of the fluid. It is defined as follow:

$$Pr = \frac{c_p \mu}{k} \qquad \text{(A-2)}$$

Where c_p is the specific heat of the fluid at constant pressure in J/kgK, k is the thermal conductivity in W/mK, μ is the dynamic viscosity of the fluid in kg/m/s.

A.3 Nusselt number

Nu is Nusselt number, which is the ratio of convective to conductive heat transfer which are parallel within them and perpendicular to the mean fluid flow. A small value of Nu close to 1 corresponds to laminar flow, whereas larger Nu corresponds to turbulent flow. It is defined as follow:

$$Nu = \frac{h * D}{k} \qquad \text{(A-3)}$$

Where h is the convective heat transfer coefficient in W/m^2/K, k is the thermal conductivity in W/mK, D is the characteristic dimension of the system (in this case the hydraulic diameter) in m.

A.4 Dittus-Boelter correlation

For estimating the heat transfer coefficient one empirical correlation can be used, depending on the characteristics of the system. In this work, the Dittus-Boelter correlation has been considered. Thus, this correlation is usually used for turbulent flows with no phase change.

Furthermore, it is consistent for limited fluid difference of temperature and viscosity, which is the case. The validity conditions of the equation are:

- $0.6 \leq Pr \leq 160$
- $Re \geq 10000$
- $L/D \geq 10$

The Dittus-Boelter correlation is given by:

$$Nu = 0.023\, Re^{0.8}\, Pr^{0.3} \qquad \text{(A-4)}$$

Prandtl number's exponent can be 0.4 for fluid heating and 0.3 for fluid cooling, in this case 0.3 has been considered.

A.5 ARRONAX targetry

In this work different target materials for radionuclides production have been studied. One common solid targetry system has been considered for all the applications considered. (*Figure 102*, Figure 103)

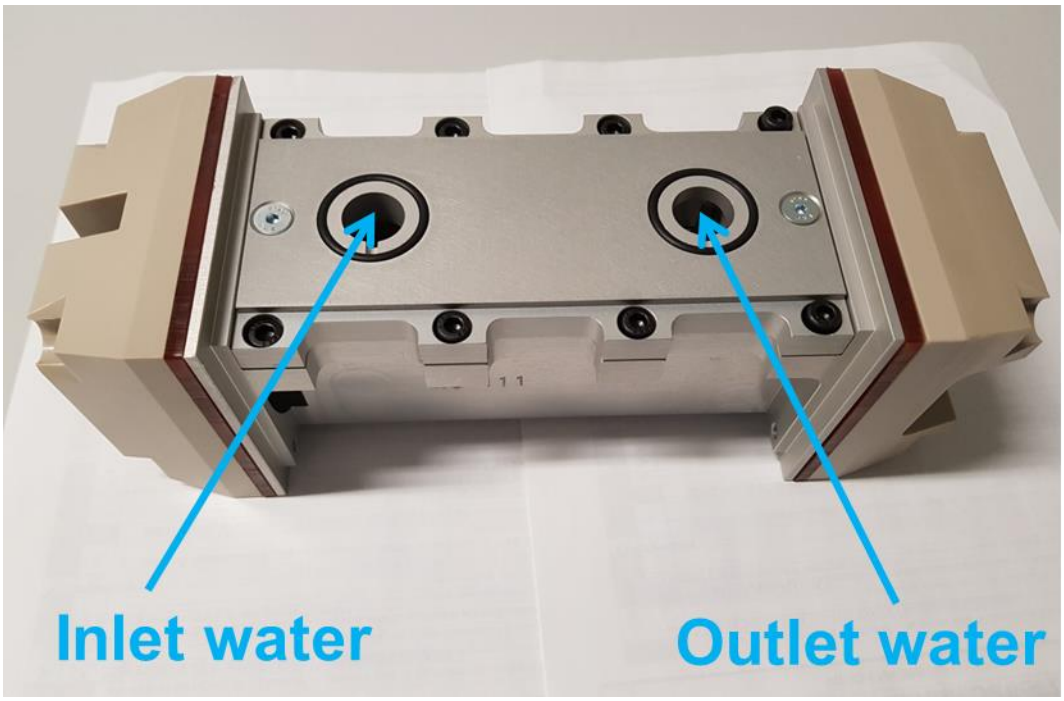

Figure 102: rabbit used for the irradiations at GIP ARRONAX

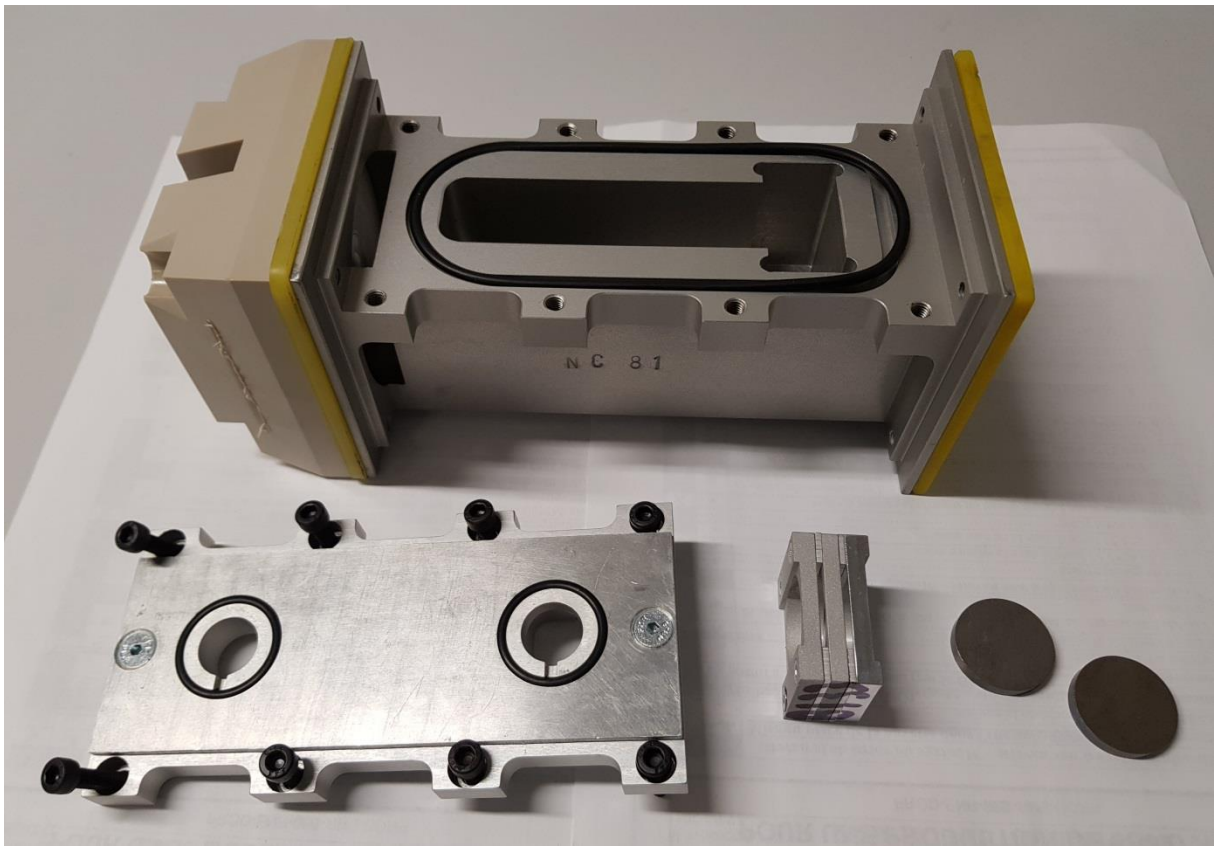

Figure 103: breakout of the rabbit system: in the top the base of the system, on the bottom left the closing cap, in the bottom center the target holder, in the bottom right the targets to be irradiated.

In the following table are presented the main parameters of the cooling water circuit in the targetry system (Figure 103) at GIP Arronax.

Table 45: cooling water circuit parameters at GIP Arronax

	Value	***Unit***
Flow rate	0,41	kg/s
Conduct dimensions	2.00E-3	m
	2.60E-2	m
Area conduct	5.20E-5	m^2
hydraulic diameter	3.71E-3	m
Water velocity	7,16	m/s
Water pressure	20	bar
Pressure drop	5	bar

The hydraulic diameter is the characteristic dimension considered for the heat flux exchange. It is given by $D_h = \frac{4A}{p}$ where A is the cross-sectional area of the fluid flow and p its perimeter.

As shown in Table 47 Pr and Re conditions are respected for Dittus-Boelter equation. Only the third condition, L/D>10, should be better discussed. Indeed, if one considers as wall length only the irradiated target zone the ratio is 7, in any case close to 10. If instead one considers the entire length of the conduct, the ratio is higher almost 20, therefore respecting the conditions of validity of the equation. As for the equation the properties of the fluid should be taken at $(T_w + T_b)/2$, considering the bulk temperature T_b= 20 ºC and assuming the wall temperature (T_w) at 180 ºC close to the boiling point, the properties listed in the following table are taken for water at 100 ºC.

Table 46: water cooling physical date used for the analysis

Fluid physical data		
kinematic viscosity	1,00E-06	m^2/s
dynamic viscosity	0,001	Pa*s
heat transfer coefficient	0,6	W/mK
Density	1000	kg/m3
specific heat	4180	J/kgK

Considering the water properties in Table 46 and the Dittus-Boelter equation the obtained dimensionless number are presented in Table 47. They lead to a calculated heat transfer coefficient of h=34182 $W/m^2/K$.

Table 47: dimensionless numbers

Number	**Value**
Re	26601.6
Pr	25.9
Nu	211.6

The study of the thermal and mechanical behavior of the considered targetry system can be divided in three steps: 1-D calculations, 3-D static simulation, 3-D dynamic simulation.

A.6 1-D calculations

A first indication on the temperatures ranges reached both in the target and in the cooling system for different target thicknesses and thermal coefficient exchanges is made in 1-D. This gives the order of magnitude of the maximum temperature reached in the target, allow having a

first approximation on the feasibility of the identified possible targetry systems and beam parameters. Thus, it will allow focusing the simulations on few cases for deeper analysis. For simplifying the 1-D calculations, the beam profile is assumed constant and not as the ideal Gaussian profile. The volumetric heat generation q in W/m^3 in the target is defined as follows:

$$q = \frac{\Delta E * \phi}{S * th} \qquad \text{(A-5)}$$

Where ΔE is the beam energy loss in the target in MeV, ϕ is the beam current in μA, S is the surface of the target in m^2 and th is the thickness of the target in m. Considering the target symmetry and a negligible variation of the deposited volumetric power inside the target, only half thickness is considered to estimate the temperature in the hottest spot, the target center. In order to evaluate the temperature of the target and the cooling water, conductive and convective heat transfer are considered. The two main equations describing the system are the Fourier's law of heat conduction and the Newton's law of cooling

$$q = \frac{\lambda}{th^2}(T_w - T_b) \qquad \text{(A-6)}$$

$$q = \frac{h}{th}(T_t - T_w) \qquad \text{(A-7)}$$

Where λ is the thermal conductivity of the target material in W/mK, T_b is the bulk temperature of the unperturbed cooling water in K. T_w is the temperature of the water in contact at the target wall, T_t is the maximum temperature reached in the center of the target.

From the Newton's law of cooling, on can obtain the temperature of the water in contact at the target wall, given by:

$$T_w = T_b + \frac{q * th}{h} \qquad \text{(A-8)}$$

Where h is the convective heat transfer coefficient in W/m^{2}K. The maximum temperature T_t of the target is given by:

$$T_t = T_w + \frac{th}{\lambda} * (q * th) \qquad \text{(A-9)}$$

A.7 Ansys and Ansys-Fluent simulations

Considering the resulting feasible targetry systems from 1-D calculations, 3-D simulations are performed to thoroughly analyze the nominal working conditions. For the static and dynamic 3D thermal and mechanical stress evaluation of the considered geometry, the Computational Fluid-Dynamics (CFD) solvers ANSYS and ANSYS-FLUENT respectively have been used in this work. They are solvers based on the finite volume method. This implies the discretization of the simulated geometry into a finite set of control volumes. The general transport equations are solved on this set of control volumes, in particular:

- Continuity equation (conservation of mass): the mass rate entering a system is equal to the mass rate leaving the system plus the accumulation of mass within the system.

$$\frac{\delta\rho}{\delta t} + \nabla \cdot (\rho v) - 0 \qquad \text{(A-10)}$$

Where ρ is the density, t is the time, v is the fluid velocity vector.

- Momentum equation (conservation of momentum): The rate of change of momentum of an object is directly proportional to the resultant force applied and is in the direction of the resultant force.

$$\frac{\delta\rho \boldsymbol{V}}{\delta t} = -(\nabla \cdot \rho \boldsymbol{V})\boldsymbol{V} - \Delta P + \nabla \cdot \tau + \rho g \qquad \text{(A-11)}$$

Where $\frac{\delta\rho V}{\delta t}$ is the increase rate of momentum per unit volume, $(\nabla \cdot \rho V)V$ is the rate of momentum gain for convection per unit volume, ΔP is the pressure force on the element per unit volume, $\nabla \cdot \tau$ is the rate of momentum gain by viscous transfer per unit volume, ρg is the gravitational force on the element per unit volume.

- Energy equation (conservation of energy): for a stationary volume element through which a pure solid is flowing the conservation of energy is given by

$$\frac{\delta\rho(u+0.5V^2)}{\delta t} = -\nabla \cdot \rho \boldsymbol{V}(u + 0.5V^2) - \rho q''' + \rho(\boldsymbol{V}g) - \nabla \cdot P\boldsymbol{V} + \nabla \cdot (\tau \cdot \boldsymbol{V}) + q''' \qquad \text{(A-12)}$$

Where u is the internal energy, $\frac{\delta\rho(u+0.5V^2)}{\delta t}$ is the gain rate of energy per unit volume, $\nabla \cdot \rho \boldsymbol{V}(u + 0.5V^2)$ is the rate of energy input per unit of volume by convection, $\rho q'''$ is the rate of energy input per unit of volume by conduction, $\rho(\boldsymbol{V}g)$ is the rate of work gain on fluid per unit of volume by gravitational forces, $\nabla \cdot P\boldsymbol{V}$ is the rate of work gain on fluid per unit of volume by pressure, $\nabla \cdot (\tau \cdot \boldsymbol{V})$ is the rate of work gain on fluid per unit of volume by viscous forces, q''' is the source term.

Combining the three conservation equations it is possible to obtain the formulation of the Eulerian equation, referred to the fluid element analysis:

$$\frac{\delta}{\delta t}\int_V \rho\phi dV + \oint_A \rho\phi V \cdot dA = \oint_A \Gamma_\phi \nabla\phi + \int_V S_\phi dV \qquad \text{(A-13)}$$

Where the first term is the unsteady term, the second is the convective term, the third term is the diffusion term and the last is the heat generation term. In this equation, ϕ is 1 for continuity conservation, u for x-momentum conservation, v for y-momentum conservation, w for z-momentum conservation, h for energy conservation.

The partial differential equations are discretized into a system of algebraic equations, which are then solved numerically to render the solution field.

A.8 Meshing

The process of representing a physical domain with the finite elements method is known as meshing and the resulting set of elements is known as the finite element mesh. The meshing must be refined until the solution of a simulation converges to the exact solution. The mesh should be accurately defined and optimized depending on the geometry and the aim of the specific analysis. For example, whereas for CFD simulations tetrahedral meshes can give a suitable description of the system for solving the system of equations, for mechanical analysis parallelepiped meshes must be preferred; however, when the simulations include different results a compromise should be found to satisfy the criteria of the convergence of each solution and the optimal quality of the mesh.

A.9 Ansys calculation

Certain steps in formulating a finite element analysis of a physical problem are common to different kind of analyses such as structural, heat transfer, fluid flow. These steps are embodied in commercial finite element software packages, such as ANSYS, and are the following:

- Preprocessing: The preprocessing step is the definition of the model. It is a crucial step as a perfectly computed finite element solution is of no value if applied to the wrong problem. It includes the definition of the geometric domain of the problem, the element types to be used, material properties, the elements connectivity, loadings and physical constraints.
- Solution: During the solution phase, the software assembles the governing algebraic equations in matrix form and computes the unknown values of the primary field variables. The computed values are then used by back substitution to compute additional, derived variables, such as reaction forces, element stresses and heat flow.
- Postprocessing: The postprocessing is the analysis and evaluation of the solution results. A postprocessor software could process the results for sorting, printing, and plotting selected results from a finite element solution. Examples of features are the equilibrium check, production of color-coded plots, animations of dynamic model behavior. Whereas solution data can be manipulated many ways in postprocessing, the most important objective is to determine whether the solution results are physically reasonable or not.

In this work, the evaluation on the static heat transfer 3D simulation has been made. The considered geometry was a quarter of half-thickness target disk. It could have been further reduced the volume, however it has been chosen as it reduces by one eighth the computational cost and it is easier to mesh compared to smaller geometries. The main aim of this step is to determine the irradiation conditions and to verify the mechanical integrity of the target coupling

the static CFD simulation with the static mechanical simulation. Based on the 1-D calculations previously obtained, different irradiation conditions have been tested.

The following step is to develop a dynamic 3-D CFD simulation. Thus, simulating the turbulent fluid flow inside the targetry system will allow a more accurate analysis. This will allow also studying solutions for ameliorating the thermal power transfer in order to increase as much as possible the incident beam power deposition, maximizing the achievable yield of the produced radionuclides.

A.10 Parameters used for Ansys simulations

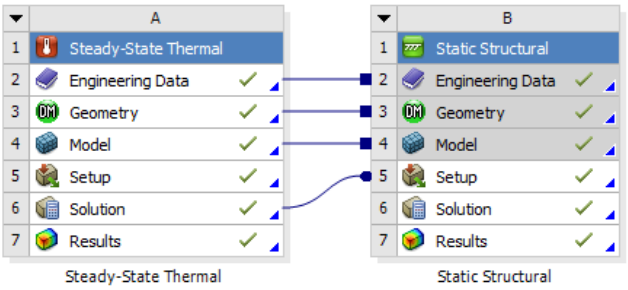

Figure 104: Ansys workbench model used for static 3-D simulations

Material Field Variables	Table	
Density	7901	kg m^-3
Isotropic Secant Coefficient of Thermal Expansion		
Coefficient of Thermal Expansion	9,4E-06	C^-1
Isotropic Elasticity		
Derive from	Young's Modulus and Poisson's Ratio	
Young's Modulus	55000	MPa
Poisson's Ratio	0,26	
Bulk Modulus	3,8194E+10	Pa
Shear Modulus	2,1825E+10	Pa
Isotropic Thermal Conductivity	10,9	W m^-1 C^-1

Figure 105: engineering material data used for natural gadolinium target simulations

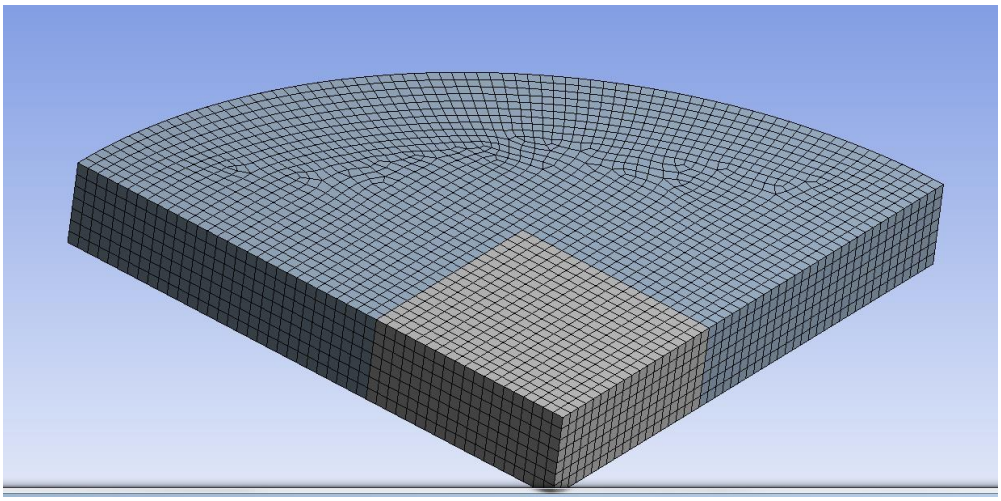

Figure 106: mesh of the disk considered for the static 3-D simulations. This mesh presents the best quality ratio compromise between thermal and mechanical simulations

ANNEX-B

Enriched Er-168 certificates of analysis

	Composition (PPM)	
Element	Trace Sciences	Isoflex
Al	30	100
Ag		10
W		40
TI		40
Mn		40
Ca	30	300
Zr		100
Cr	100	40
Cu	40	30
Dy	700	1000
Fe	10	500
Ni		250
Gd	500	1000
Mo		30
V		30
Ho	400	
K	60	
Lu	1300	
Mg	90	300
Na	40	
Pb	50	100
Si	40	200
Sn	100	30
Tm	1100	

Tb	600	
Co		100
Yb	400	
Y		30
Bi		30

ANNEX-C

Erbium Er-169 gamma spectrometry analysis

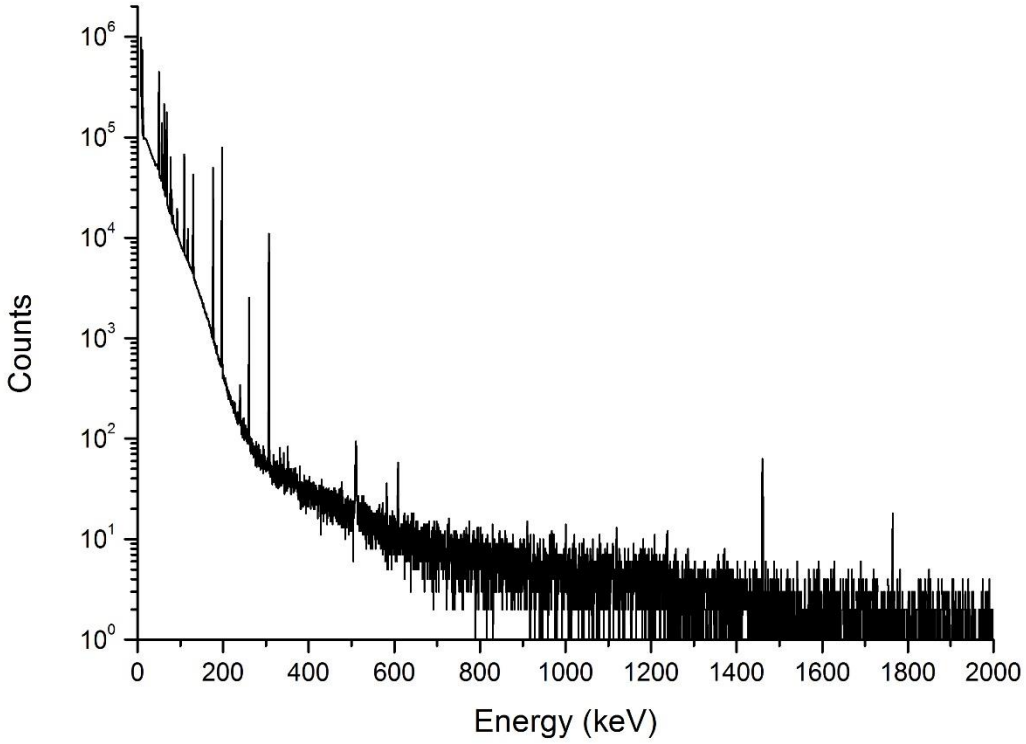

Figure 107: Gamma spectrum taken from the analysis of the mass separated collected sample at MEDICIS after the erbium production of the 17/07/18. The spectrum has been taken from GENIE2000 software.

The presented gamma spectrum in *Figure 107* refers to the analysis of the sample from the 17/07/18 erbium Er-169 production. The analysis was performed with GENIE2000 and the outcome was 18.2 MBq of Er-169 and 10.4 kBq of Yb-169. The gamma ray energies and intensities used for the identification and the quantification of the radionuclides present in the analyzed sample, are resumed in the following table.

Table 48: Gamma ray energies and intensities used for the identification and the quantification of the radionuclides present in the 17/07/18 erbium collection sample

Nuclide	***Half-life***	***γ-ray energy (keV)***	***γ-ray intensity***
Er-169	9.39 d	109.78	0.0013 %
		118.19	0.00014 %
Yb-169	32 d	109.78	17.36 %
		118.19	1.87 %
		130.52	11.38 %
		177.21	22.32 %
		197.96	35.93 %
		307.74	10.05 %

UNIVERSITE MATIERE BRETAGNE MOLECULES LOIRE ET MATERIAUX

UNIVERSITÉ DE NANTES

Titre : Production de radionucléides innovants pour des applications théranostiques utilisant des cyclotrons commerciaux ou des réacteurs nucléaires couplés avec la séparation en masse

Mots clés : théranostiques, séparation en masse, terbium, erbium, scandium

Résumé : En médicine nucléaire, la pureté du produit final est très importante. Souvent les contaminants peuvent être chimiquement éliminés. Néanmoins, cette technique n'est pas appropriée quand les contaminants proviennent du même élément. Dans ce cas, seulement des processus physiques peuvent être utilisés. La séparation en masse est l'un de ces procédés. Le but de ce travail de thèse au sein du projet MEDICIS-PROMED est de déterminer la faisabilité de la production de radionucléides innovants pour des applications théranostiques. Cela au travers de l'utilisation de cyclotrons commerciaux ou de réacteurs nucléaires, couplées avec la séparation en masse développée au CERN-MEDICIS. Au laboratoire JGU de Mayence (Allemagne) afin d'améliorer les rendements de séparation en masse nous avons étudié l'apport de l'ionisation laser dans l'objectif de la combiner avec la séparation en masse. Ainsi le développement d'une méthode alliant ces processus de séparation physique donne accès de manière industrielle à des produits à très hautes activités spécifiques et très pures, qui n'étaient pas disponibles en quantités suffisantes. Des radionucléides du scandium et du terbium ont été identifiés pour la production en cyclotrons et l'Er-169 pour la production en réacteurs. Le développement des cibles appropriées à la production industrielle a été réalisé pour les premiers deux éléments. En parallèle, nous avons réalisé la première production mondiale d'Er-169 à très haute activité spécifique en combinant le réacteur nucléaire de l'ILL et le séparateur en masse de CERN-MEDICIS. Les améliorations envisagées ainsi que les perspectives futures seront présentées et discutées.

Title : Innovative radionuclides production for theranostics applications from commercial cyclotrons and nuclear reactors coupled with mass separation technology

Keywords : Theranostics, mass separation, terbium, erbium, scandium

Abstract : In nuclear medicine, batches purity is of key importance. Contaminants coming from the irradiation can be often removed using chemistry. However, this technique does not work when contaminants corresponds to isotopes of the same element. In this case, only physical processes can be used. One technique is the mass separation, but it suffers from low process efficiency and it is thus limited to research. The aim of this work, within MEDICIS-PROMED project, is to determine the feasibility of producing innovative radionuclides for theranostics applications. Thus, using a commercial cyclotron, or in alternative a nuclear reactor, coupled with the mass separation technology developed at CERN-MEDICIS. Work was also performed at JGU of Mainz (DE) on laser ionization technique. Combined to mass separation, it improves the efficiency of the overall process. The developed production method will allow producing high purity and high specific activity batches; it can make available those radionuclides which are not currently produced in sufficient quantities. Radionuclides of scandium and terbium have been identified for the production in cyclotrons, while Er-169 has been identified for the production in reactors. For the first two elements, the scheme from target development to large-scale production has been studied. In parallel, we have performed the first ever production of very high specific activity Er-169 using ILL reactor and CERN-MEDICIS mass separator. Future improvements needed, as well as future perspectives of this production method, will be presented and discussed.